Universidad de Valencia
DEPARTAMENTO DE FÍSICA ATÓMICA
MOLECULAR Y NUCLEAR

INSTITUTO DE FÍSICA CORPUSCULAR

Beam Halo Collimation and Induced Wakefield Studies for Future Linear Colliders: the ATF2 Case
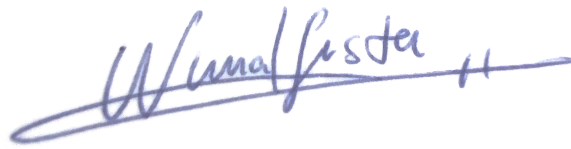
TESIS DOCTORAL EN FÍSICA

Nuria Fuster Martínez

Abril de 2017

Supervised by:

Dr. Ángeles Faus-Golfe

Declaración:

Esta tesis es el resultado de mi propio trabajo, excepto cuando se hace referencia explícita al trabajo de otros, y no ha sido presentado para ninguna otra calificación en esta u otro Universidad.
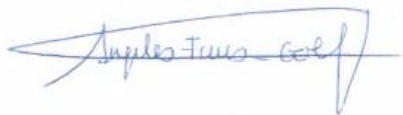
Fdo. Nuria Fuster Martínez

Dra. ÁNGELES FAUS GOLFE,

CERTIFICA:

Que la presente memoria *Beam Halo Collimation and Induced Wakefield Studies for Future Linear Colliders: the ATF2 Case* ha sido realizada bajo su dirección en el Departamento de Física Atómica Molecular y Nuclear de la Universidad de Valencia por Nuria Fuster Martínez y constituye su Tesis Doctoral.

Y para que así conste, se firma el presente certificado

Fdo: Dra. Ángeles Faus Golfe

El trabajo descrito en esta tesis se ha llevado a cabo en el **Instituto de Física Corpuscular** (IFIC) en Valencia, España.

El IFIC es un centro mixto del Consejo Superior de Investigaciones Científicas (CSIC) y de la Universitat de València. En Julio de 2015 recibió la acreditación **Severo Ochoa** (SEV-2014-0398) que le distingue como Centro de Excelencia. Dicha acreditación reconoce la excelencia y las contribuciones científicas que realizan los centros y unidades a nivel nacional e internacional, su impacto empresarial y social y su capacidad para atraer talento.

To my mother, my father, my sister and my brother.

Aknowledgements

Resumen

Introducción y objetivos

La Física de Partículas ha hecho grandes progresos en el estudio de las leyes de la naturaleza al nivel más fundamental. El descubrimiento del bosón de Higgs, acompañado por muchos otros resultados experimentales, ha confirmado el Modelo Estándar en escalas de energías más allá de las previamente exploradas. Estos resultados plantean nuevas preguntas sobre el origen de la masa de las partículas elementales y sobre el papel del bosón de Higgs en la teoría más fundamental que subyace en el Modelo Estándar. El descubrimiento del bosón de Higgs es el inicio de un importante programa de trabajo para medir las propiedades de la partícula con la precisión más alta posible para probar la validez del Modelo Estándar y buscar nueva física en la frontera de energía exploradas. El Gran Colisionador de Hadrones (*Large Hadron Collider*, LHC) se encuentra en una posición única para lograr estos objetivos. El aumento de la luminosidad de la máquina con el fin de recoger diez veces más datos que en el diseño inicial es una prioridad que se llevará a cabo alrededor del 2030 con el objetivo de explotar el potencial del LHC.

Existe consenso en la comunidad de Física de Altas energías de que la siguiente generación de aceleradores en la escala de energías del TeV debe ser un colisionador electrón-positrón, complementario al LHC. Un acelerador con estas condiciones permitiría estudiar las propiedades del bosón de Higgs y otras partículas con una precisión sin precedentes. Se están evaluando dos posibles colisionadores lineales en el rango del TeV para colisionar electrones con positrones: el *International Linear Collider* (ILC) y el *Compact Linear Collider* (CLIC). Aunque la tecnología CLIC está adquiriendo un grado de madurez enorme, la tecnología del ILC es una solución ya madura para un rango de energía de hasta 1 TeV. En febrero del 2013, el *International Committee for Future Accelerators* (ICFA) tomó la decisión de que los dos proyectos comenzaran a trabajar juntos bajo un esfuerzo único denominando el projecto como *Future Linear Collider* (FLC). Además, en los últimos años, la viabilidad de un prosible colisionador circular en el rango de energías del TeV se está evaluado en otros dos proyectos: el *Future Circular Collider* (FCC-ee) [27] y el *Circular electron positron Collider* (CepC) [28].

Un desafío técnico importante para el FLC es la colisión de haces de partículas con una talla vertical de unos pocos nanómetros (requerida para alcanzar la luminosidad de diseño). Este objetivo presenta tres retos claves: la producción de haces con una

emitancia muy pequeña, la viabilidad de preservar la emitancia durante la aceleración, el transporte y la focalización final del haz, y la capacidad de focalizar un haz de nanómetros en el punto de interacción (*Interaction Point*, IP). Con el fin de evaluar las tecnologías necesarias para el desarrollo de los FLCs se necesitan instalaciones con aceleradores. Aquí en esta tesis nos centramos en la *Acceleration Test Facility* 2 (ATF2) que es una línea de extracción que utiliza el haz extraído del anillo de amortiguamiento (*Damping Ring* (DR)) de la *Acceleration Test Facility* (ATF) en el *High Energy Accelerator Research Center Organization* (KEK) de Japón. ATF fue construida para crear haces con una emitancia pequeña, y tuvo éxito en la obtención de una emitancia que cumple los requisitos del ILC. Por su parte, ATF2 fue construido con el objetivo de demostrar dos importantes requerimientos del ILC: la producción de haces con un tamaño nanométrico utilizando un sistema de focalización final como el del ILC y la capacidad de producir haces con una estabilidad del orden del nanómetro. Concretamente las dos metas de ATF2 son: primero lograr un tamaño vertical del haz de 37 *nm*, y la segunda lograr una estabilidad del haz del orden del nanómetro en el IP. La distribución de un haz de partículas se caracteriza por una parte más densa llamada *core* y una parte menos densa llamada halo, formada por aquellas partículas que tienen una trayectoria y/o energía muy desviada respecto de la nominal. Las partículas que forman el halo se rigen por una dinámica no lineal y pueden interaccionar con los componentes del acelerador y generar partículas secundarias. Estas partículas secundarias, puede degradar la señal de los detectores o los dispositivos de diagnóstico utilizados para medir las propiedades del haz limitando el funcionamiento y los experimentos de los aceleradores. Para controlar y reducir el halo de partículas y las pérdidas no deseadas a lo largo de la máquina se diseñan los sistemas de colimación. El diseño de tal sistema, es un complejo equilibrio entre la eficiencia que se requiere y el impacto de los *wakefields* inducidos que pueden comprometer la luminosidad del haz y la estabilidad. Los *wakefields* son un efecto que se debe a la interacción del campo generado por el haz de partículas con las paredes del conducto por el que circula. El efecto de los *wakefields* es más intenso en transiciones abruptas con aperturas pequeñas. Es importante controlar este efecto porque puede inducir variaciones en la órbita y aumentar el tamaño del haz y la emitáncia degradando en consecuencia, la luminosidad.

En ATF2, se observó que los fotones generados por la interacción del halo de partículas con el último imán de la línea (BDUMP) podían estar limitando la precisión y la estabilidad del *Shintake monitor* (IPBSM) utilizado para medir la talla del orden de unas decenas de nanómentro en el IP. Este monitor, mide la modulación de fotones producidos debido a la inteacción de un láser con el haz de lectrones. Los fotones producidos en el BDUMP pueden mezclarse con los relacionados con la medida de la talla del haz limitando la precisión de la medida. Con el objetivo de reducir estos fotones se instaló un estrechamiento del conducto por el que circula el haz llamada *Tapered beam pipe* (TBP) con una media apertura fija de 8 *mm*. Esta estructura desmostró interceptar parte del halo de partículas mejorando las medidas del IPBSM sin embargo no permite ajustar la profundidad de colimación a mas de 18 σ_y de forma simétrica. Uno de los dos objetivos principales de esta tesis consiste en el estudio de diseño de viabilidad, construcción, instalación, puesta en marcha y experimentos de eficiencia y medidas de los *wakefields* de un sistema de colimación vertical para ATF2. El objetivo principal del sistema de colimación desarrollado para ATF2 es reducir los fotones de fondo en la última región de la línea que a partir de ahora llamaremos Post-IP. El segundo obje-

tivo de esta tesis consiste en la realización de un estudio detallado de los *wakefields* inducidos por dicho sistema en el contexto de estudios de *wakefields* para ATF2 y los FLCs. En este marco, hemos realizado un estudio sistemático comparativo entre cálculos analíticos, simulaciones, estudios de *tracking* y medidas experimentales del impacto de los *wakefields* inducidos por el sistema de colimación vertical de ATF2. Estos estudios son de gran importancia para el futuro diseño de los sistemas de colimación del FLC.

Discusión de los resultados

Estudios de eficiencia de un sistema de colimación para ATF2

La eficiencia y la viabilidada de un sistema de colimación betatrónico y de energía para ATF2 se han estudiado mediante simulaciones de la dinámica y trayectoria del halo de partículas para diferentes modelos de halo, localizaciones y ópticas, utilizando el código de seguimiento MADX-PTC [80]. Del análisis de los resultados obtenidos concluimos que:

- Con respecto a la eficiencia en la reducción de los fotones generados en el BDUMP con el fin de mejorar la precisión del IPBSM, se demostró que se necesita **un sistema de colimación betatrónico vertical** con apertura media de 5 *mm* correspondiente a una profundidad de colimación de 15 σ_y.

- La **mejor ubicación** encontrada para el sistema de colimación vertical está en s = 60.69 *m* entre los cuadrupolos $QD10BFF$ y $QM11FF$ donde tenemos un máximo de $\beta_y = 7487.51$ *m*, la diferencia de avance de fase entre el sistema de colimación vertical y el BDUMP es $\Delta\phi_x^{BDUMP-C} = 1.483$ [2π] y $\Delta\phi_y^{BDUMP-C} = 1.493$ [2π] y el espacio libre disponible es de aproximadamente 0.8 *m*.

- También se estudió la eficiencia de un sistema de colimación betatrónico y de energía con el fin de reducir la distribución horizontal del halo de partículas en el contexto de los estudios y medidas de electrones Compton de segundo orden con el recientemente instalado sensor de diamante (DS). En este caso, los estudios demostraron que el sistema de colimación horizontal es más eficiente que el sistema de colimación de energía.

- En este caso, la **ubicación más eficiente** encontrada está en s = 63.02 *m* entre $QD10AFF$ y $QF9BFF$ con un máximo de $\beta_x = 157.02$ *m* con una diferencia de avance de fase entre el sistema de colimación horizontal y el DS de $\Delta\phi_x^{DS-C} = 1,493$ [2π] y $\Delta\phi_y^{DS-C} = 1,499$ [2π] y un espacio libre disponible de 0.7 *m*. Sin embargo, este sistema **no es útil por el momento porque el nivel actual de *pickup* del sensor de diamante (DS)** es demasiado alto y no permite las medidas de los electrones Compton de segundo orden. Por esta razón, el resto de esta tesis se centra en el diseño, estudio detallado de *wakefields*, construcción, instalación, puesta en marcha y primeras medidas experimentales de un sistema de colimación de halo vertical.

Implicaciones y estudio de wakefields en el diseño de un sistema de colimación vertical para ATF2

En el capítulo 3 se presentan los estudios de diseño de las *jaws* del colimador. Las *jaws*, son las dos piezas centrales que se insertan en la trayectoria de las partículas del halo. En la Fig. 1 se puede ver el modelo de las *jaws* utilizado en los estudios de diseño, con los parámetros geométricos estudiados indicados. La geometría y el
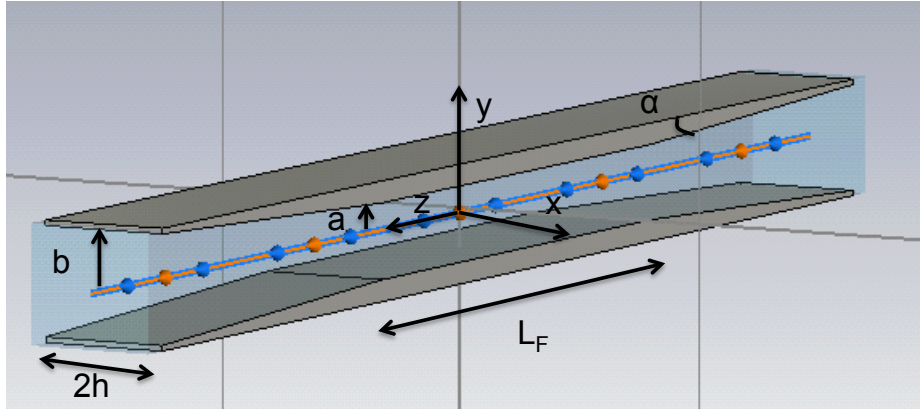
Figure 1: Modelo geométrico de las *jaws* utilizado en los estudios de diseño.

material de estas piezas tiene que optimizarse para minimizar los *wakefields* inducidos. El espacio disponible considerado en el diseño del sistema de colimación es de 0.6 *m*. Teniendo en cuenta este espacio disponible, sólo se puede utilizar alrededor de 0.3 *m* para las *jaws* porque también se necesita espacio para la pieza que hace de transición entre el coducto del acelerador y las *jaws*. **La transición de esta parte** tiene que ser **lo más suave posible** ($\alpha <<$) para no introducir *wakefields* adicionales. La parte plana del colimador tiene que ser capaz de absorber la cascada EM producida por un electrón de 1.3 *GeV* para que el sistema sea eficiencte en la minimización de la emisión de partículas secundarias. Como resultado de los estudios presentados en este capítulo, **cobre** resultó ser el **mejor candidato** porque requiere de una longitud menor para absorber la casaca EM producida por electrones de 1.3 *GeV* y además es un buen conductor y por tanto induce un nivel de *wakefield* menor. Desde el punto de vista de la supervivencia del sistema se ha estimado el incremento de **temperatura** debido a la potencia disipada por el haz de partículas y debido al impacto directo de un paquete de partículas (10^{10} electrones). El resultado de los cálculos muestra un impacto **insignificante**, por lo que concluimos que el sistema no necesita refrigeración. En el estudio del impacto de los *wakefields*, hemos calculado con CST PS el impacto de otras dos estructuras (una cavidad de referencia y la TBP) instaladas en ATF2, cuyo impacto fue estudiado con detalle en estudios anteriores. Para cada estructura hemos calculado el *wakefield kick*, un factor que caracteriza la intensidad de los *wakefields* inducidos en promedio. Para la cavidad de referencia hemos obtenido un *wakefield kick* de $\kappa_y^{CST\ PS}$ = 0.079 *V/pC/mm* mientras que para el TBP el valor es de $\kappa_y^{CST\ PS}$ = 0.005 *V/pC/mm*, en ambos casos hemos considerando un haz desplazado verticalmente 1 *mm*. Estos cálculos los hemos realizado considerando un langitud del paquete de partículas de 7 *mm* que corresponde al valor de diseño de ATF2. Observamos una diferencia de un orden de magnitud entre la intensidad de los *wakefields* inducidos por estas dos estructuras. En nuestro diseño para reducir el impacto de los *wakefields* inducidos

hemos considerado un ángulo de transicin tan pequeño como el espacio disponible y las restricciones mecánicas nos lo han permitido. Si se considera una parte plana de la parte central del sistema de colimación de 100 *mm* de cobre, el espacio disponible y las restricciones mecánicas conllevan a un ángulo de transicin de 3 °. Para estas especificaciones, el impacto de los *wake fields* al cerrar el colimador una media apertura de 8 *mm* es de $\kappa_y^{CST\ PS} = 0.006\ V/pC/mm$, valor que es comparable con el impacto de la TBP. Con el sistema de colimación descrito necesitamos considerar una apertura media de 3 *mm* para qu ese induzcan unos *wake fields* del orden de magnitud del impacto inducido por la cavidad de referencia. En cuanto a la apertura del sistema de colimación hemos elegido un sistema retráctil que permite ajustar dicha apertura en función del modo de oparación de la máquina **entre 3 y 12** *mm*. Estas especificaciones fueron dadas al ingeniero del LAL como punto de partida para la realización del diseño mecánico del sistema de colimación de halo vertical para ATF2.

Además, en el capítulo 3, se ha estudiado el impacto de los *wake fields* inducidos por el sistema de colimación vertical en la dinámica del haz mediante simulaciones de seguimiento con el código de *tracking* PLACET. Decidimos utilizar este código de *tracking* porque tiene implementado un módulo que permite calcular la contribución dipolar y cuadrupolar de los *wake fields* inducidos por un sistema de colimación. Este módulo se basa en modelos analíticos. También es posible implementar el *wake potential* calculado mediate simulaciones EM. El *wake potential* caracteriza como evolucionan los *wake fields* en la estructura al paso del haz de partículas. Aunque es posible hacer esta implementación, por falta de tiempo esto no se ha realizado en esta tesis. Con el fin de validar los resultados obtenidos con el código de *tracking* PLACET se comparó la variación de la órbita y del tamaño del haz debido a los *wake fields* inducidos por el colimador obtenidos con PLACET con el cálculo de la propagación lineal del *wake field kick* calculado con CST PS. Sin embargo, al comparar los resultados, se encontraron algunas discrepancias en un orden de magnitud. Se realizó un estudio detallado y se encontró que la fuente de las discrepancias estaba en la definición de los límites del cálculo analítico relevantes para el caso de ATF2. El problema se resolvió y el programa se ha modificado en consecuencia en una nueva versión del código de seguimiento PLACET (v1.0.1) [43]. La nueva versión de PLACET (v1.0.1) se utilizó para estudiar el efecto de los *wake field* inducidos en la órbita de ATF2 y el tamaño del haz en el IP. La conclusión a la que llegamos con estos estudios es que para una media apertura de 5 *mm* del sistema de colimación vertical y un desplazamiento del haz de partículas de 0.5 *mm* respecto del centro del colimador, el impacto en la órbita en el IP es aproximadamente del 13 % del tamaño del haz vertical en el IP. Considerando el mismo caso que para el impacto en la órbita, el impacto en el incremento del tamaño del haz vertical en el IP es aproximadamente del 10 %.

Simulaciones realistas sobre la efieciencia del sistema de colimación de halo vertical para ATF2

La eficiencia del sistema de colimación vertical se ha estudiado también de forma más realista utilizando el código de *tracking* BDSIM. BDSIM nos permite realizar **simulaciones de seguimiento** teniendo en cuenta la posible **regeneración del halo del partículas** y la emisión de partículas secundarias. Los resultados de estos estudios se presentan en el capítulo 4. Si bien a partir de simulaciones con **MADX-PTC** con-

cluimos que la media apertura del sistema de colimación necesaria era de **5** *mm* para evitar pérdidas en la entrada del BDUMP, los resultados obtenidos con **BDSIM** muestran que **4** *mm* son necesarios. En BDSIM se considera la longitud del imán y eso tiene un impacto en la profundidad de colimación necesaria para cumplir los objetivos del sistema. Con BDSIM también se calculó la energía depositada en el colimador por las partículas que absorbe. El número máximo de pérdidas debe mantenerse por debajo de 0.4 % de la intensidad nominal del haz, valor fijado por el sistema de seguridad y control de radiaciones de ATF2. Si consideramos que la intensidad nominal del haz es 10^{10} electrones, el límite de seguridad en ATF2 es del orden del *mW*. Para una media paertura de 5 *mm* del sistema de colimación las pérdidas están por debajo de 0.001 % de la intensidad nominal del haz de ATF2 y la potencia perdida es del orden de μW.

Construcción, calibración e instalación de un sistema de colimación vertical para ATF2

Una vez caracterizada la ubicación, la eficiencia y el impacto de los *wakefields*, el siguiente paso en el diseño del sistema de colimación vertical consistió en realizar el diseño mecánico en 3D. Este trabajo fue realizado por S. Wallon miembro del departamento de aceleradores del Depacc en el LAL. Los parámetros descritos en el capítulo 3 (cobre, $\alpha = 3$ ° y $L_F = 100$ *mm*) resultado de la optimización de las *jaws* se dieron como parámetros de entrada a S. Wallon. El diseño fue inspirado en experiencias anteriores [110] y en un diseño preliminar de los sistemas de colimación para el ILC [40]. En el capítulo 5, se presenta el diseño mecánico 3D final y los cálculos EM 3D relacionados que se realiazaron para refinar la elección del material de la parte de transición entre las *jaws* y el conducto del acelerador por donde circulan las partículas. Además, el impacto de los *wakefields* de la estructura completa se calcularon con CST PS para investigar la contribución de todo el sistema. **Cerca de un 15-30 % de diferencia se observa en el cálculo realizado con CST PS del sistema completo y de sólo las** *jaws*. Las piezas se limpiaron y montaron en el LAL, labor que fue realizada por S. Wallon. Además, se calibraron y alinearor las piezas centrales del colimator y se realizó un test de vacio en el laboratorio. En marzo del 2016 se instaló el sistema de colimación vertical en ATF2. El autor de esta tesis llevó a cabo las primeras pruebas experimentales en marzo del 2016. Cuatro turnos se dedicaron a comprobar el funcionamiento y control del sistema de colimación vertical. Los objetivos principales de estas pruebas fueron verificar y calibrar el sistema de control y medir la alineaciń del sistema respecto del haz. También realizamos en estos primeros experimentos una primera tanda de medidas de la eficiencia del sistema de colimación. Observamos una reducción de los fotones de fondo cuando el sistem de colimación vertical se cierra a una media apertura de más de 6 *mm*, resultados que está deacuerdo con las simulaciones realizadas con MADX-PTC y BDSIM. Además, se midió **con un scáner de alambre y el sensor de diamante (DS)** el corte producido por el colimador en la distribución vertical del halo de partículas. El corte observado experimentalmente es compatible con las simulaciones.

Estudios experimentales con el sistema de colimación vertical de ATF2

En el capítulo 6, se presentan los estudios experimentales realizados por el autor de

esta tesis durante los meses de mayo, octubre, noviembre y diciembre del 2016. Se midió el impacto de los *wakefields* en la órbita del haz inducidos por el sistema de colimación vertical, así como la eficiencia del sistema de colimación vertical bajo diferentes condiciones del haz y de la máquina.

En la Tabla 1 se presenta un resumen de las medidas del *wakefield kick* en comparación con los cálculos analíticos y las simulaciones numéricas.

Medidas del *wakefield kick* 2016			
Parameter	Units		
a	$[mm]$	4.00 ± 0.01	3.00 ± 0.01
Scan range	$[mm]$	$\pm1.00 \pm 0.01/\pm2 \pm 0.01$	$\pm1 \pm 0.01$
N	$[\times10^{10}]$	$>0.80\pm0.06$	0.75 ± 0.05
σ_z	$[mm]$	$8.6\pm0.6< \sigma_z <9.1\pm0.6$	8.6 ± 0.6
$\kappa_y^{analytic}$	$[V/pC/mm]$	0.033	0.059
$\kappa_{y,jaws}^{CSTPS}$	$[V/pC/mm]$	0.033	0.059
$\kappa_{y,transition}^{CSTPS}$	$[V/pC/mm]$	0.037	0.066
$\kappa_y^{averaged}$	$[V/pC/mm]$	0.040 ± 0.004	0.070 ± 0.006

Table 1: Resumen y comparación de las medidas de *wakefields* realizadas en el 2016.

El *wakefield kick* medido está de acuerdo con las simulaciones numéricas realizadas con CST PS para el modelo realista. La precisión de comparación se encuentra al nivel del 10 %. La diferencia entre las medidas y el cálculo analítico es de aproximadamente un 15 %. Este impacto puede ahora escalarse a la longitud del paquete de partículas del ILC, para ver las implicaciones de este tipo de sistemas en el contexto del ILC.

El sistema de colimación vertical fue diseñado con el objetivo principal de reducir los fotones de fondo en la región final de ATF2. La eficacia se ha medido utilizando el *background monitor* y el *IPBSM Cherenkov monitor*. La eficiencia se ha medido también en comparación al efecto de la TBP que actúa como un sistema de colimación pero con una apertura fija. A partir de estas medidas llevadas a cabo durante los meses de marzo, mayo, octubre y noviembre de 2016, concluimos que el sistema de colimación vertical instalado en ATF2 es eficiente en reducir los fotones de fondo en la última sección del accelerador. Definimos la eficiencia relativa, *Relative Photon Collimation Efficiency* ($\Delta\gamma CE$), como:

$$\Delta\gamma CE = 100\left(1 - \frac{\Delta\gamma_{w\ coll}^{BDUMP-WINDOW}}{\Delta\gamma_{w/o\ coll}^{BDUMP-WINDOW}}\right) \tag{1}$$

donde $\Delta\gamma_{w\ coll}^{BDUMP-WINDOW}$ son los fotones generados entre la entrada del BDUMP y la ventana para fotones del IPBSM con el sistema de colimación cerrado a una cierta apertura y $\Delta\gamma_{w/o\ coll}^{BDUMP-WINDOW}$ sin sistema de colimación.

La eficiencia relativa, $\Delta\gamma PCE$, medida en cada uno de los periodos se comparan en la Fig. 2 donde además en rojo indicamos los resultados obtenidos en las simulaciones realizadas con BDSIM. La reducción relativa de los fotones de fondo, ($\Delta\gamma CE$), es de aproximadamente 60-80 % para el sistema de colimación vertical cerrado a 3 *mm* y **las medidas son consistentes** en los tres **diferentes periodos de ejecución**. Además, la reduccin de los fotones generados en el BDUMP se calculó utilizando **BDSIM** en
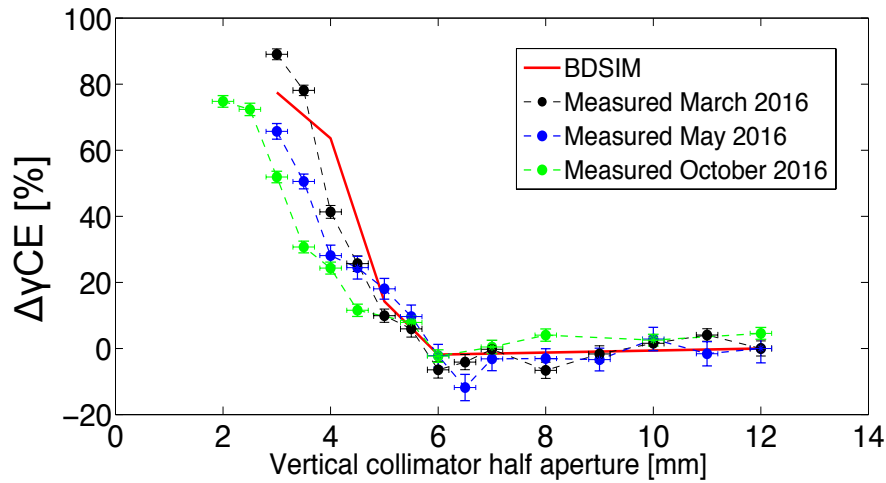
Figure 2: Comparación de la medidas realizadas en marzo, mayo y octubre 2016 de la eficiencia del sistema de colimación con los resultados obtenidos en las simulaciones realizadas con BDSIM.

función de la apertura del sistema de colimación vertical, los resultados obtenidos son relativamente consistentes con las medidas.

También se ha estudiado la eficiencia del sistema de colimación para distintas intensidades del haz de partículas, distintas presiones en el DR y distintas ópticas. En estas medidas observamos que el nivel de fondo aumenta para altas intensidades, altas presiones en el DR y para el conocido modo de operación $low - \beta$ que correpsonde a $(10\beta_x \times 0.5\beta_y)$. Para lograr el mismo nivel de fotones de fondo no se observa ningún cambio en la profundidad de colimación necesaria con distintas presiones de vacío, pero para **diferentes intensidades y para distintas ópticas la profundidad de colimación tiene que ser ajustada**. La TBP funcionaba como un sistema de colimación pero limitada a un corte máximo simtrico de 18 σ_y para un haz pasando por el centro de esta estructura. Para lograr el mismo impacto, el sistema de colimación vertical tiene que estar cerrado entre 5-6 *mm* correspondiente a 15-18 σ_y. **Una profundidad de colimación simétrica menor de 18 σ_y solo es posible con el sistema de colimación vertical**. En febrero del 2017, la TBP fue reemplazada por una cavidad de RF con el fin de realizar experimentos de compensación de *wakefields* y **el sistema de colimación vertical fue operado con éxito como el principal sistema de colimación**.

Conclusiones

Pérdidas de partículas del haz en zonas no deseadas puede limitar el funcionamiento y los experimentos en los aceleradores. Con el fin de controlar y reducir el halo de partículas y las pérdidas en zonas no deseada a lo largo del acelerador, se necesitan los sistemas de colimación de halo. El diseño de dichos sistemas es un complejo equilibrio entre la **eficiencia** requerida y **los** *wakefields* inducidos que pueden comprometer la luminosidad del haz y la estabilidad. En este contexto, en la primera parte de esta tesis hemos realizado un estudio de diseño de viabilidad, construcción, instalación,

puesta en marcha y experimentos de un sistema de colimación vertical para ATF2 con el objetivo principal de reducir los fotones de fondo en el Post-IP. En la segunda parte de la tesis hemos utilizado el sistema de colimación vertical the ATF2 para realizar un estudio detallado de los *wakefields* inducidos por tal sistema en el contexto de estudios de *wakefields* para ATF2 y FLCs. Hemos realizado un **estudio sistemático de comparación** del *wakefield kick* entre **cálculos analíticos, simulaciones numéricas y medidas**.

En cuanto al tema de **colimación de halo**, mediante simulaciones de *tracking* llegamos a la conclusión de que el sistema más eficiente para reducir las pérdidas en el BDUMP es un sistema de colimación betatrónico vertical. Por lo que el resto de la tesis se centro en desarrollar dicho sistema. Se utilizó el código de *tracking* **MADX-PTC y BDSIM** para estudiar la eficiencia del sistema de colimación vertical. Si bien a partir de simulaciones con **MADX-PTC** concluimos que la apertura necesaria era de **5** *mm* para evitar pérdidas en la entrada del BDUMP, los resultado de las simulaciones más realistas con **BDSIM** mostraron que necesitamos cerrar el colimador hasta **4** *mm*. Con BDSIM también calculamos la reducción de los fotones de fondo en el Post-IP en función de la apertura del sistema de colimación vertical para luego compararla con las medidas experimentales. El sistema de colimación vertical fue construido y probado en laboratorio del LAL e instalado en ATF2 en Marzo del 2016. Después de algunas pruebas de funcionalidad y calibración realizadas en marzo de 2016 se llevó a cabo un programa experimental por el autor de esta tesis para medir la eficiencia del sistema de colimación. La eficiencia del sistema de colimación vertical fue demostrada. Además, las medidas son consistentes con las simulaciones de BDSIM. También se comparó la eficiencia del sistema de colimación vertical con la de la TBP. La TBP se utilizaba como una especie de sistema de colimación pero limitado a una profundidad máxima de colimación de 18 σ_y para un haz que pasa por el centro de este dispositivo. Para lograr el mismo impacto, el sistema de colimación vertical tiene que estar cerrado a una media apertura de entre 5-6 *mm* correspondiente a 15-18 σ_y. **Una profundidad de colimación simétrica menor que 18** σ_y sólo es posible con el **sistema de colimación vertical**. En febrero de 2017, con el fin de realizar nuevos experimentos de *wakefields* una cavidad radiofrecuéncia (RF) se colocó en lugar de la TBP y **el sistema de colimación vertical es ahora utilizado como el principal sistema de colimación**.

El otro tema principal de la tesis consiste en **un estudio detallado y sistemático de los** *wakefields* **inducidos por el sistema de colimación vertical**. La geometría y el material de las *jaws* se ha optimizado para reducir los *wakefields* inducidos por el sistema. Se realizó un estudio detallado de como reducir el impacto de los *wakefields* y los parámetros resultantes son los siguientes: **una parte plana central de 100** *mm* **de cobre**, con un **ángulo de 3** ° y un **apertura variable entre 3 y 12** *mm*. Para estas especificaciones, el impacto de los *wakefields* del sistema de colimación vertical es un factor 2 mayor que el de la TBP (con un bajo impacto de *wakefields*) y un factor 4 inferior al de la cavidad de referencia (con un alto impacto de *wakefields*). Estas especificaciones fueron dadas al ingeniero del LAL como el punto de partida para la realización del diseño mecánico del sistema.

El impacto de los *wakefields* **en la dinámica del haz** se ha estudiado utilizando el **código de seguimiento PLACET**. Se encontraron algunas discrepancias entre los re-

sultados obtenidos con PLACET (v1.0.0) y la propagación lineal del *wakefield kick* calculado numéricamente con CST PS en un orden de magnitud. El motivo de las discrepancias se estudió con detalle y se encontró que la fuente de las discrepancias estaba en la definición de los límites del cálculo analítico relevantes para el caso ATF2. El problema fue resuelto y el programa ha sido modificado en consecuencia en una nueva versión PLACET (v1.0.1) [43], versión utilizada para continuar con los estudios de ATF2. Los resultados finales de estas simulaciones se resumen en la Tabla. 2. Estos estudios analíticos y numéricos fueron completados con un programa

Sistema de colimación vertical de ATF2							
$I = 0.9 \times 10^{10}$, $\sigma_z = 9$ *mm*, $\Delta y^c = 0.5$ *mm* and $(10\beta_x \times 1\beta_y)$ optics V5.2							
BDSIM (V0.91) and PLACET (v1.0.1)							
[*mm*]	[%]		[*V/pC/mm*]			[*nm*]	
a	$\Delta\gamma PC^{BDSIM}$	$\Delta\gamma PC^{medido}$	$\kappa_y^{analitico}$	$\kappa_y^{CST\ PS}$	κ_y^{medido}	$\Delta\sigma_y^{*,PLACET}$	$\Delta y^{*,PLACET}$
5	15	15	0.015	0.017	—	4.5	6.5
4	60	35	0.033	0.037	0.040±0.004	6.2	11.1
3	78	70	0.059	0.066	0.070±0.006	9.9	21.6

Table 2: Resumen del funcionamiento del sistema de colimación vertical de ATF2.

experimental llevado a cabo durante 2016 con el objetivo principal de medir el impacto de los *wakefields* inducidos por el sistema de colimación vertical en la órbita. Estas medidas se realizaron con el objetivo principal de investigar el **modo de operación óptimo** del sistema de colimación vertical instalado en ATF2 en términos de eficiencia y *wakefield* y realizar un estudio sistemático de comparación entre **cálculos analíticos, simulaciones numéricas y medidas**. Estos estudios son cruciales para el futuro diseño del sistema de colimación del FLC porque existen **discrepancias en el** *wakefield kick* **descrito en los distintos modelos analaíticos**, en los modelos implementados **en los códigos de** *tracking* y **entre simulaciones y medidas experimentales** (ESA (SLAC) 2001-2007 [36]). Además, existen **diferentes modelos analíticos** (inductivos, intermedios, difractivos) dependiendo de la geometría del colimador y del haz y cuando los parmétros del problema están **cerca de los límites los calculos no son precisos**. En mis estudios realicé un estudio de comparación sistemático incluyendo simulaciones numéricas con CST PS y medidas. Además, los modelos analíticos **solo describen las** *jaws* y en nuestro estudio, las simulaciones numéricas y las medidas se han realizado para la estructura completa. Concluimos que **las medidas experimentales estan de acuerdo con las simulaciones numéricas** con el error experimental asociado. La diferencia entre las medidas y el cálculo analítico que tiene en cuenta solo la parte central del sistema, es de aproximadamente un 20 %. Además, observamos una diferencia entre simular solo la parte central y todo el sistema de colimación vertical de aproximadamente un 15-30 %. Finalmente, en la Tabla- 2 se presenta un resumen de la eficiencia y *wakefields* inducidos para distintos modos de operación del sistema de colimación vertical de ATF2.

Abstract

In the framework of the design studies for Future Linear Colliders (FLCs) to explore the fundamental laws of nature in the TeV energy scale the ATF2 facility was constructed to address two major challenges of the International Linear Collider (ILC): focusing the beam to the nanometer scale using ILC-like Final Focus System (FFS) and proving nanometer beam stability. Undesired background due to beam halo hitting the beam pipe of some machine components could limit the performance and experiments of the accelerators. In order to control the beam halo and the losses in the machine the beam halo collimation systems are necessary. The design of such a systems is a complex balance between the efficiency needed, the wakefields induced which can compromise the beam luminosity and stability and the self-preservation.

In ATF2, background photons generated in the Post-IP showed to be limiting the performance of the Post-IP diagnostics. There was no dedicated beam halo collimation system in ATF2 although some apertures and a Tapered beam Pipe (TBP) installed in the high β region were intercepting part of it. In this context, in the first part of this thesis, we have performed a feasibility design study, construction, installation, commissioning and first experimental measurements of a single vertical collimation system for ATF2 with the main objective of reducing the background photons in the Post-IP. The vertical collimation system was installed in March 2016 and the efficiency measured and compared with realistic simulations. In 2017 February run, the TBP was removed, and the vertical collimation system operated as the main collimation system.

In the second part of this thesis, we have used the ATF2 vertical collimation system to perform a detailed study of the wakefields induced by such a system. We have performed a systematic benchmarking study between analytical calculations, numerical simulations and measurements of the wakefield kick induced by the ATF2 vertical collimation system in order to define an optimum operation mode in terms of efficiency and wakefields. These benchmarking studies contribute to the understanding of the applicability of the tools used to estimate such effect being crucial for the design of the FLC collimation systems.

Contents

Introduction to beam halo collimation and induced wakefields in Future Linear Colliders (FLCs)

1.1 General concepts in collimation for Linear Colliders (LCs)

High energy accelerators have been used in the past decades in High Energy Physics (HEP) to explore the most fundamental laws of nature. The experiments carried out in the past 50 years in HEP validate the predictions of the Standard Model (SM). However, this theory does not include the gravitational force and does not well describe some phenomenon, such as the dark matter. The Particle and Accelerator Physics community are evaluating the feasibility of higher energy colliders to test the SM at unprecedented energies. Such accelerators are becoming very complex and costly machines and a big effort is being made in the accelerator physics and technology field in order to provide feasible solutions.

Colliders are very complex machines made of different subsystems. In general, a linear collider is composed of particle sources in order to generate the particles beams, a Damping Ring (DR) where the beam emittance is reduced to the design value, a linear accelerator (LINAC) where the beam passes through a chain of radiofrequency (RF) acceleration structures in order to achieve the desired energy and the Beam Delivery System (BDS) where the beam is prepared and guided to the Interaction Point (IP). A scheme layout of half a linear collider can be seen in Fig. 1.1 [1]. The BDS is further divided into two other sub-systems: the collimation system and the Final Focus System (FFS). The collimation system is located with the main objectives of removing the particles that can cause unacceptable background in the Interaction Region (IR) and to protect the machine against miss-steered energy particles. A collimation system is typically composed of several blocks of matter, called jaws, which are inserted into the beam pipe to intercept the particles with a large betatron amplitude and a large energy deviation with respect to the nominal one. These jaws have to be located in strategic places from the optics point of view in order to be efficient. Furthermore, again to be efficient, the collimation system jaws have to be placed very close to the beam, due to this fact the system will induced wakefields that could compromise the beam stability
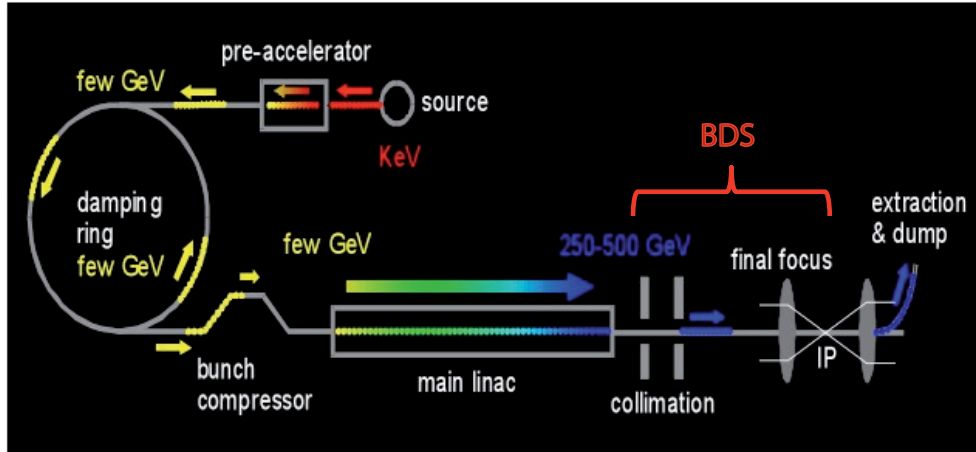
Figure 1.1: Conventional half linear collider layout.

and luminosity. Wakefields are the Electromagnetic (EM) fields resulting from the interaction of the beam EM fields with the collimation system walls. The strength of the wakefields induced by the collimation system depends on its geometry and material. This fact, makes the optimization essential for wakefield minimization. In addition, the design of the collimation system material is crucial to ensure its survivability, which is especially challenging for high energy and high intensity colliders. Summarizing, the design of a collimation system is a complex balance between the efficiency in removing undesired particles, emittance dilution due to wakefields and self-preservation.

In this chapter, we introduce the basic collimation concepts and studies involved in the design of a collimation system. At the end of the chapter, the collimation system of the two LC projects, the International Linear Collider (ILC) [2] and the Compact Linear Collider (CLIC) [3], are described.

1.1.1 Beam halo in LCs

The particle beam distribution generated in the accelerator source system is characterized by a high-density part called the beam core. This high beam density region is surrounded by a low-density distribution of particles called the beam halo formed by particles with a large betatron amplitude and a large momentum error with a different beam dynamics behavior. Losses that originate from the beam halo hitting the accelerator components can lead to activation and damage of these elements, degrading the quality of the beam as well as creating undesired background in the particle physics detectors. The understanding of the beam halo formation and control is essential for high energy and high intensity FLCs. There are many mechanisms of formation, which depends on the type of machine and on the nature of the particle beam. In this work we focus on linear machines used to accelerate electrons. In this case, the main beam halo driven mechanism are [4, 5]:

- **Beam-gas Coulomb scattering**. The particles of the beam can interact with the Coulomb potential created by the residual gas particles. The incident beam particles will suffer a betatron amplitude deflection (elastic scattering) or energy

variation (inelastic scattering). Particles with a final large betatron amplitude and energy deviation with respect to the nominal one will form part of the beam halo.

- **Intrabeam scattering**. This effect describes the interaction of the EM fields of the particles in the beam itself, which results in momentum variation and can push particles from the core into the beam halo region. In particular, this effect is important in DRs where the emittances are reduced.

- **Collective instabilities (wakefields)**. The wakefield effect due to the EM interaction of the beam with the beam pipe may also change the betatron amplitude and energy of the particles and increase the number of particles in the beam halo region.

- **Optics-related effects and misalignments**. Optics mismatches, coupling, dispersion, magnet field errors induced by small misalignments and power supply jitter can also enhance the beam halo density.
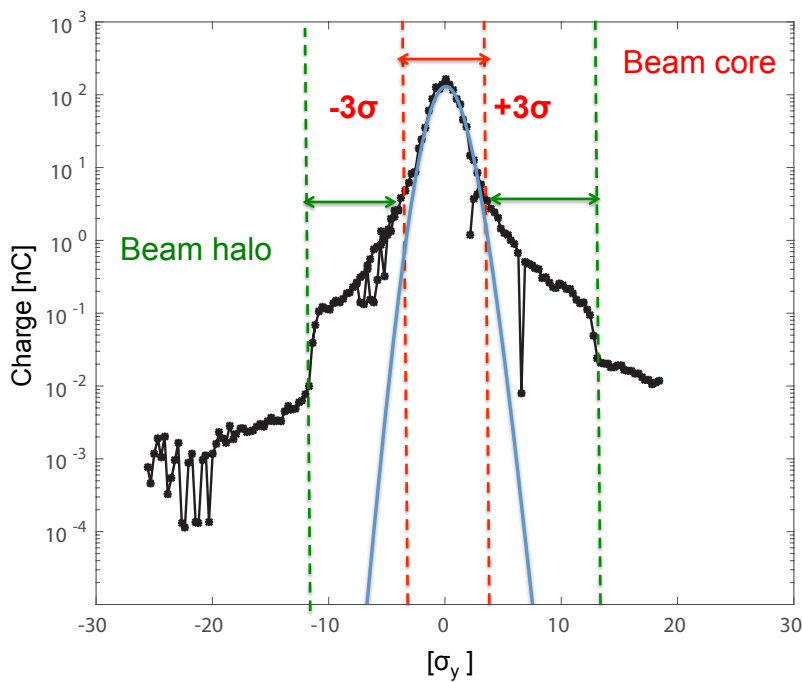
Figure 1.2: Vertical beam halo distribution measured in the Accelerator Test Facility 2 (ATF2) in March 2016 [6]. Beam-halo limit depicted at $\pm 3\sigma$ and beam core fitted with a Gaussian distribution.

In electron linear machines, the beam core usually follows a Gaussian distribution but the distribution of the beam halo is not well known and it constitutes an important field of research. It is very difficult to give one and simple definition for the beam halo since its formation is beam and machine dependent. Measurements are required in most of the cases and the limit separation between core and halo comes directly from

observation. For a Gaussian-like beam the core-halo separation is usually defined around $\pm(3,4)\,\sigma$ of the particle distribution as illustrated in Fig. 1.2. Recent studies [7, 8] proposed a new method to determine the separation between the core and beam halo based on a study of the space charge force which is density dependent. In this method the core-halo limit is defined as the point in the distribution where the EM space charge field changes abruptly. This change corresponds to the abrupt change of the second derivative of the particles distribution parametrization. The method has been tested for different beam halo models for both electron and proton machines and verified experimentally. The method has been shown to be important in the cases where the beam halo differs dramatically from a Gaussian like beam, in particular, in order to characterize the beam halo distribution in high-energy proton machines. In 2013-2014 a beam halo measurement campaign with wire scanners was carried out in the ATF2 facility [9, 10] and this new method to define the core-halo limit was applied to these measurements with a resulting core-halo limit around $\pm(3,4)\,\sigma$.

An understanding of the beam halo formation constitutes a complex study, which is very important for the good performance of FLCs. In order to reduce and control the beam halo collimation systems have to be installed in the accelerators. In the following sections, we will give a description of the design issues of such a systems.

1.1.2 Collimation depth and location issues

In general, the design of the collimation system for any FLC is a complex balance between the following conditions:

- The choice of the geometric aperture and location should guarantee a good cleaning efficiency of the beam halo without introducing intolerable wakefields, which can compromise the beam stability and degrade the luminosity.

- The regeneration of the beam halo due to beam particles scattering at the collimation should be limited.

- The material of the collimation system jaws has to be robust enough in order to survive the impact of a full train of bunches.

The most important parameter of a collimation system is the **collimation depth**. The collimation depth determines how much we need to close the collimation system to reduce the generation of background in the region of interest and avoid losses in other components outside the collimation section.

The transverse position of a particle at a given longitudinal location, s, can be described by a **betatron component**, x_{β_x} and y_{β_y}, describing the betatron oscillations of the trajectory, and a **dispersion component**, $x_D(s)$ and $y_D(s)$, describing the deviation of the orbit with respect to the reference orbit for off-momentum particles as:

$$x, y(s) = x_{\beta_x}, y_{\beta_y}(s) + x_{D_x}, y_{D_y}(s) = \sqrt{\epsilon_{x,y}\beta_{x,y}(s)} + D_{x,y}(s)\sigma_E \tag{1.1}$$

where $\beta_{x,y}$ is the betatron function, $\epsilon_{x,y}$ is the geometric emittance, σ_E is the energy spread and $D_{x,y}$ is the dispersion function.

To eliminate the particles with a large betatron amplitude and with a large energy deviation with respect to the nominal trajectory and energy, two collimation systems are

needed: **the betatron collimation system** and **the energy collimation system**. A conventional collimation system (betatron or energy) consists in pairs of spoilers and absorbers as shown in Fig. 1.3 in the particular case of the vertical plane. In this configuration, the spoilers are installed first with a smaller aperture (a_y) and longitudinal length (L_F) than the absorbers. The main objective of the spoilers is to increase the beam angular divergence by multiple Coulomb scattering to decrease the transverse density of the incident beam halo into the absorber. The absorbers are longer jaws with larger apertures, which have to absorb the beam halo particles efficiently minimizing the emission of secondary particles.

Beam halo

Beam
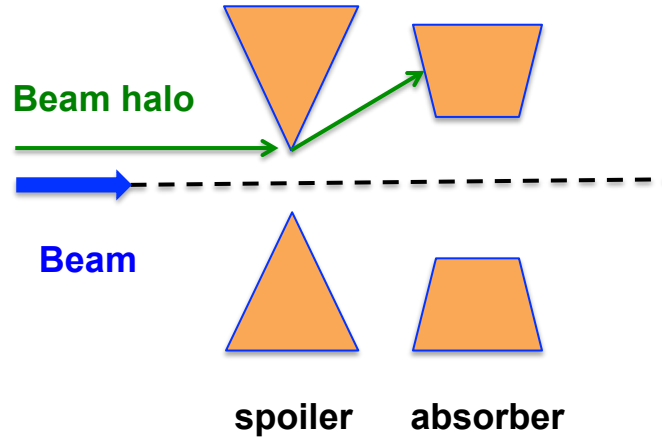
spoiler   **absorber**

Figure 1.3: Conventional collimation system scheme illustrated in the vertical plane.

In order to collimate the full phase space, $(x, x', y, y', z, \sigma_E)$, several collimation stages composed of spoilers and absorbers located at specific optics locations are needed. In the following, we will briefly describe the optic considerations and collimation depth definition for each kind of collimation: betatron and energy, but only considering one collimation stage for each degree of freedom. Details about the optimized optics for a more complex collimation system considering two stages for each degree of freedom can be found in [11].

The betatron collimation system

The betatron collimation system aims to reduce the transverse beam halo distribution in order to protect the accelerator components outside the collimation system from beam halo losses. One of the main goals of the betatron collimation system in LCs is to reduce the background created in the IR due to the beam halo hitting the beam pipe or due to the emission of Synchrotron Radiation (SR) in the Final Doublet (FD) from particles with a large betatron amplitude. The most important concept in the design of the betatron collimation system is the **betatron collimation depth**, $N_{x,y}$, defined for a fixed transverse collimation system half aperture, $a_{x,y}$, in units of the transverse beam size, $\sigma_{x,y}$, as:

$$N_{x,y} = \frac{a_{x,y}}{\sigma_{x,y}} = \frac{a_{x,y}}{\sqrt{\epsilon_{x,y}\beta_{x,y} + (D_{x,y}\sigma_E)^2}} \tag{1.2}$$

In the case of pure betatron collimation, the collimation system is usually located in a region with zero transverse dispersion, $D_{x,y}$, in order to collimate only the geometric component of the trajectory, x_{β_x} and y_{β_y} (see Eq. (1.1)). A location with high $\beta_{x,y}$ function is also convenient because at this location the beam sizes are larger and for a given collimation depth the aperture of the collimation system required will be higher. Furthermore, a higher geometric aperture will induce less wakefields as will be explained in more detail in chapter 3. Having the betatron collimation system in a place where the $\beta_{x,y}$ function is large also implies a lower density of particles interacting with the collimation system jaws, which will be important for the survivability of the collimation system. In this case, the collimation depth, $N_{x,y}$, is given by:

$$N_{x,y} = \frac{a_{x,y}}{\sigma_{x,y}} = \frac{a_{x,y}}{\sqrt{\epsilon_{x,y}\beta_{x,y}}} \qquad (1.3)$$

In the particular case of LCs, the betatron collimation depth is usually defined as the aperture needed such that the SR photons generated by the beam halo in the FD pass cleanly through the IR without being intercepted by the IR apertures. The photons generated in the FD could be due to the interaction of the beam halo with the IR geometric apertures and due to the emission of SR of large betatron amplitude particles when they are strongly focused into the IP. In Fig. 1.4 a conventional scheme of the IR of a LC is depicted with a collimation system indicated. The mask located to protect the FD. The detector, the FD and the IP are also illustrated for the vertical plane.
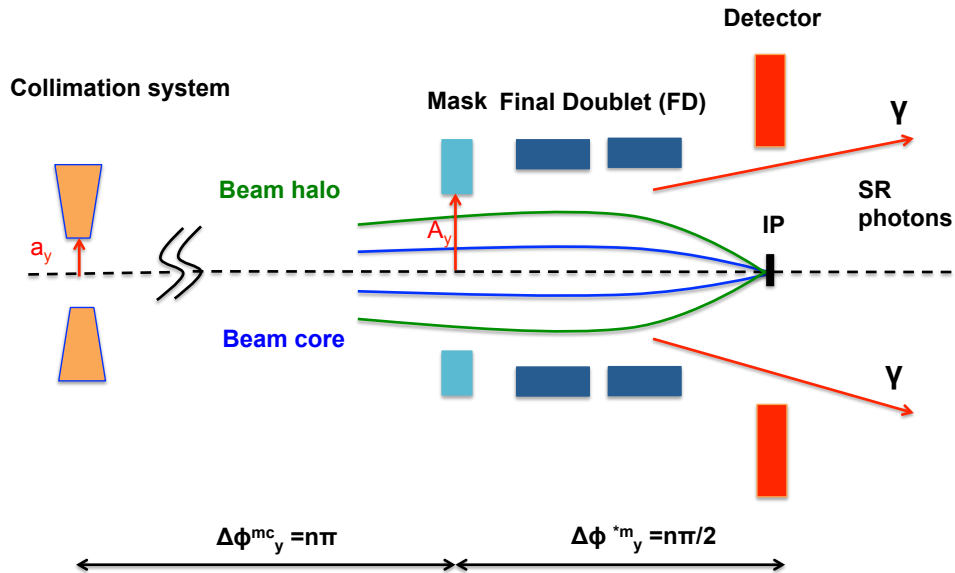
Figure 1.4: IR scheme illustrated fo the vertical plane.

In a first approximation, considering only the photons generated due to the interaction of the beam halo particles with the mask, **the betatron collimation depth can be estimated using the transport matrix formalism** (more details can be found in the Annex 1). Let's consider the mask depicted in Fig. 1.4 with a vertical half aperture A_y

as the collimation target. The phase space at the collimation system location, $X^c(s_0)$, is related to the phase space at the mask location, $X^m(s)$, by the first order transport matrix, $R(s, s_0)$, as:

$$X^m(s) = R(s, s_0)X^c(s_0) \tag{1.4}$$

where X=$(x, x', y, y', z, \sigma_E)$ is the 6D particle trajectory coordinates.

In the particular case of having a pure betatron collimation system, without considering the dispersion and in an uncoupled scenario the vertical coordinates will be transported as the following:

$$\begin{pmatrix} y^m \\ y'^m \end{pmatrix} = \begin{pmatrix} \sqrt{\frac{\beta_y^m}{\beta_y^c}}(\cos \Delta\phi_y^{mc} + \alpha_y^c \sin \Delta\phi_y^{mc}) & \sqrt{\beta_y^m \beta_y^c} \sin \Delta\phi_y^{mc} \\ \frac{(\alpha_y^c - \alpha_y^m)\cos \Delta\phi_y^{mc} - (1+\alpha_y^c\alpha_y^m)\sin \Delta\phi_y^{mc}}{\sqrt{\beta_y^m \beta_y^c}} & \sqrt{\frac{\beta_y^c}{\beta_y^m}}(\cos \Delta\phi_y^{mc} - \alpha_y^m \sin \Delta\phi_y^{mc}) \end{pmatrix} \begin{pmatrix} y^c \\ y'^c \end{pmatrix} \tag{1.5}$$

The vertical coordinates at the mask location can be expressed as:

$$y^m = \sqrt{\frac{\beta_y^m}{\beta_y^c}} \left[\cos \Delta\phi_y^{mc} + \alpha_y^c \sin \Delta\phi_y^{mc} \right] y^c + \left[\sqrt{\beta_y^m \beta_y^c} \sin \phi_y^{mc} \right] y'^c \tag{1.6}$$

$$y'^m = \left[\frac{(\alpha_y^c - \alpha_y^m)\cos \Delta\phi_y^{mc} - (1 + \alpha_y^c\alpha_y^m)\sin \Delta\phi_y^{mc}}{\sqrt{\beta_y^m \beta_y^c}} \right] y^c +$$
$$+ \sqrt{\frac{\beta_y^c}{\beta_y^m}} \left[\cos \Delta\phi_y^{mc} - \alpha_y^m \sin \Delta\phi_y^{mc} \right] y'^c \tag{1.7}$$

In order to collimate first the betatron amplitude, y^m, we locate the collimation system in a maximum of the β function ($\beta_y^c = \beta^{max}$). At this location $\alpha_y^c = 0$ and the angle distribution is in a minimum. Under these considerations Eq. (1.6) can be simplified as:

$$y^m = \left[\sqrt{\frac{\beta_y^m}{\beta_y^c}}(\cos \Delta\phi_y^{mc}) \right] y^c + \left[\sqrt{\beta_y^m \beta_y^c} \sin \phi_y^{mc} \right] y'^c \tag{1.8}$$

From Eq. (1.8) we can deduce that to directly shadow the aperture of the mask with the geometrical aperture of the collimation system we should locate the collimation system with a phase advance difference with respect to the mask location of $\Delta\phi_y^{mc} = n\pi$ (n being an integer).

Furthermore, using the inverse matrix of Eq. 1.5 (see Annex 1 for more details) and considering a phase advance between the mask and the collimation system of $\Delta\phi_y^{mc} = n\pi$, we can calculate the collimation half aperture, a_y, required to have a maximum amplitude at the mask location of A_y as:

$$a_y = A_y \sqrt{\frac{\beta_y^c}{\beta_y^m}} \tag{1.9}$$

Then, we need to collimate the angle, y'^m. For that, an additional spoiler/absorber pair has to be installed. Usually the optics of the collimation system is designed to be periodic with maximums and minimums of the β function separate by a phase advance

of $\Delta\phi = \pi/2$. Considering a periodic section and the amplitude collimation system located at a maximum of β_y, to collimate y'^m the collimation system has to be located at a phase advance with respect to the amplitude collimation system of $\Delta y^{s2s1} = n\pi/2$ in order to be more efficient. In Fig. 1.5 this concept is illustrated.
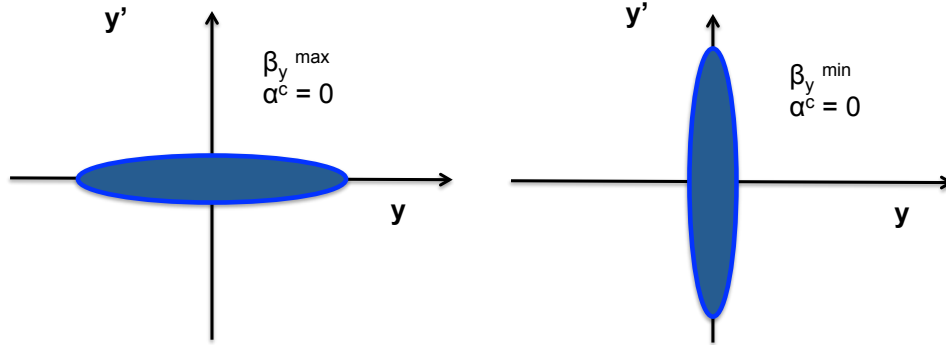
Figure 1.5: (yy') phase space in a maximum (left) and a minimum (right) of the β function.

This first order calculation can be used to estimate the collimation system aperture needed for a given background source. But in order to design the collimation system, this calculation has to be done for each possible emission point in the IR or other relevant possible sources along the beamline. In order to perform these calculations for all possible sources, tracking codes have to be used that include also higher order transport elements as well as the interaction of the particles with the collimation system jaws. These facts, could modify the final betatron collimation depth required by the machine.

One collimation system stage is usually composed of one spoiler and one absorber. Figure 1.6 shows an example of an efficient way of placing the collimation system jaws to collimate the vertical plane $(y-y')$ considering the FD as the collimation target. In this example, circular collimation system jaws have been considered and only one stage per degree of freedom. The first vertical spoiler cleans the region $(N_y\sigma_y \leq |y|)$ and at $\pi/2$ phase advance the other spoiler cleans the region $(N_y\sigma_y \leq |y'|)$. The same arrangement with horizontal spoilers can be used to clean the horizontal phase space.

Typical collimation systems consist of circular or rectangular jaws. Which geometry is used depends on the vertical and horizontal beam size ratio. If we have a circular beam, circular collimation systems can be used but if we have a flat-like beam $(\sigma_x \gg \sigma_y)$ rectangular jaws are a better option in order to collimate the vertical and the horizontal planes independently.

In a first approximation, considering the collimation system as black absorbers (we do not consider here the interaction of the particles with the block of material), if we have a round beam and use circular collimation systems the collimation depth is covered using one collimation stage per degree of freedom (amplitude and angle) as it is illustrated for the vertical plane in Fig. 1.7 (top left). However, in the case of having a flat-like beam we have to use rectangular collimation systems and using only two collimation stages (one for y and the other for y') some particles will remain in the region $(\pm N_y\sigma_y \sqrt{2})$ as it is illustrated in Fig. 1.7 (top right in green) and will propagate along
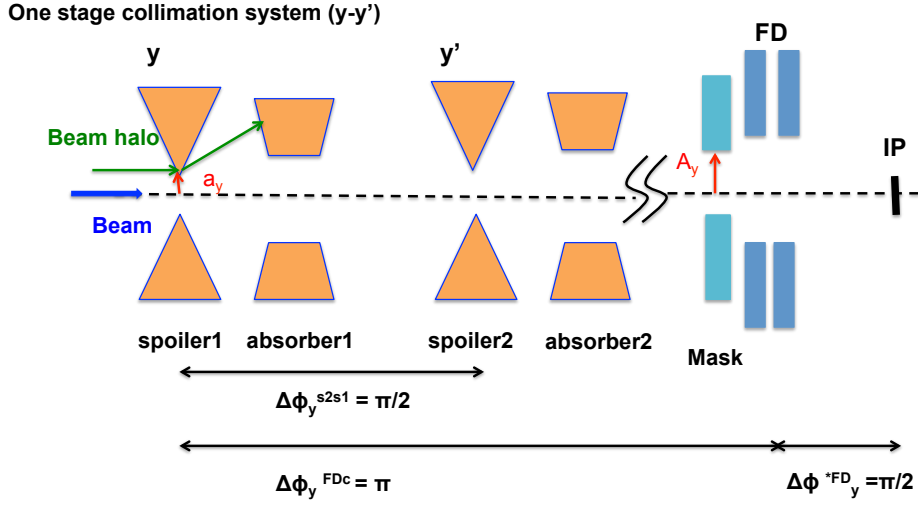
Figure 1.6: Conventional collimation system scheme illustrated in the vertical plane.

the beamline. In order to solve this problem we have two possible solutions: to reduce the collimation system jaws half aperture to ($\pm N_y \sigma_y / \sqrt{2}$) (see Fig. 1.7 (bottom a)) or to add a third collimation stage located at a proper phase advance ($\Delta\phi_y^{s2s1} = \pi/4$) (see Fig. 1.7 (bottom b)). The first solution will be limited by the wakefields induced by the collimation system (stronger for smaller geometric apertures) and the second solution will be limited by the space and cost of the collimation system.

The energy collimation system

As introduced in this section, also energy collimation is required due to the dispersion component of the particle's trajectory. The **energy collimation depth** is defined by the required collimation aperture needed to avoid backgrounds caused by particles with a high-momentum errors. The energy collimation system must protect the accelerator from the linac's failure modes. This system must intercept miss-steered energy beams, protecting the magnets in the BDS or other important equipment. Momentum errors can be generated in the main linac if the beam is injected with the wrong phase or with the wrong charge. As for the betatron component the collimation depth can be defined as:

$$N_{x,y} = \frac{a_{x,y}}{\sigma_{x,y}} = \frac{a_{x,y}}{\sqrt{\epsilon_{x,y}\beta_{x,y} + (D_{x,y}\sigma_E)^2}} \tag{1.10}$$

The energy collimation system has to be located in a region with dispersion, where the dispersion component of the particles trajectory, $x_D(s)$ or $y_D(s)$, of Eq. (1.1), dominates. If not, particles with a low betatron function but with very off-momentum may still survive the collimation system and cause undesired background. Tracking simulations are required to estimate the energy collimation depth introducing off-energy particles. The transport matrix formalism can be used to illustrate the phase space transport along the machine taking into account the dispersion function. Following the same example as for the betatron case, let's consider the mask as the energy collimation target. In the same way, the phase space at the collimation system location,

Circular collimators   **Rectangular collimators**
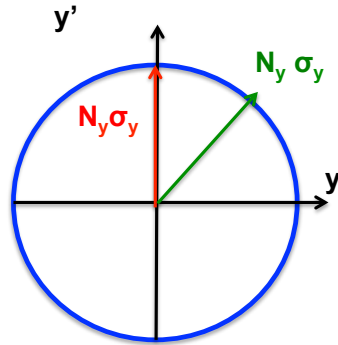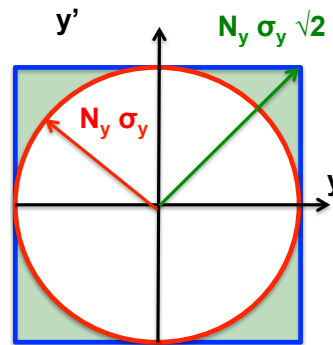
Rectangular collimators
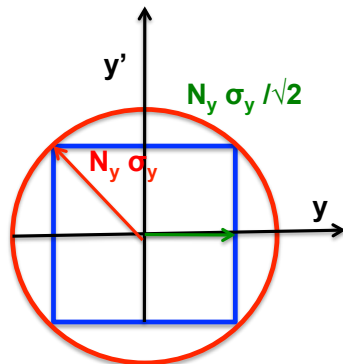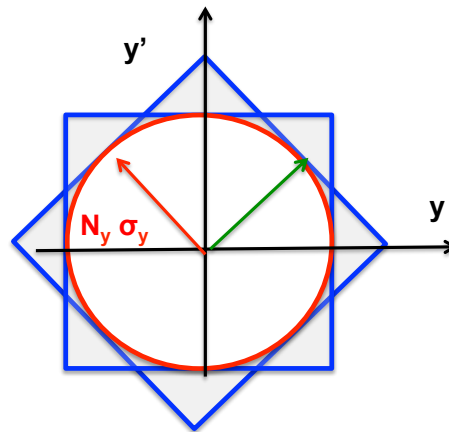
Required collimation depth: $N_y \, \sigma_y$

■ Particles transmitted

Figure 1.7: Circular (left) and rectangular (right) collimation system cleaning phase space region (top). Possible solutions for the case of considering a rectangular collimation system geometry to cover the full $(y - y')$ variable phase space for a given betatron collimation depth (bottom).

$X^c (s_0)$, is related to the phase space at the mask location, $X^m (s)$, by the transport matrix, $R(s, s_0)$, as defined in the Eq. (1.4), but in this case the transport matrix has to include the elements characterizing the dispersion function along the machine. Usually the horizontal plane is considered when performing energy collimation since the dispersion in this plane is orders of magnitude higher than the vertical one. In the following example, we will consider the horizontal plane. For the uncoupled case, the horizontal coordinates taking into account the elements of the transport formalism

characterizing the dispersion will be transported as following:

$$
\begin{pmatrix} x^m \\ x'^m \\ (\Delta p/p)^m \end{pmatrix} =
\begin{pmatrix}
\sqrt{\frac{\beta_x^m}{\beta_x^c}}(\cos \Delta\phi_x^{mc} + \alpha_x^c \sin \Delta\phi_x^{mc}) & \sqrt{\beta_x^m \beta_x^c} \sin \Delta\phi_x^{mc} & D_x^c \\
\frac{(\alpha_x^c - \alpha_x^m)\cos \Delta\phi_x^{mc} - (1+\alpha_x^m \alpha_x^c)\sin \Delta\phi_c^{mc}}{\sqrt{\beta_x^m \beta_x^c}} & \sqrt{\frac{\beta_x^c}{\beta_x^m}}(\cos \Delta\phi_x^{mc} - \alpha^m \sin \Delta\phi_x^{mc}) & D_x'^c \\
0 & 0 & 1
\end{pmatrix}
\begin{pmatrix} x^c \\ x'^c \\ (\Delta p/p)^c \end{pmatrix}
\quad (1.11)
$$

Where the dispersion function in a magnet is described by:

$$
D_x^c(s) = S(s) \int_0^s \frac{1}{\rho(t)} C(t) dt - C(s) \int_0^s \frac{1}{\rho(t)} S(t) dt \quad (1.12)
$$

where $S(s)$ and $C(s)$ are the transport matrix elements, R_{11} and R_{12}, respectively, from
Eq. (1.11) and $\rho(t)$ is the bending radius of the magnet.
The horizontal coordinates at the collimation system are transported as:

$$
x^m = \sqrt{\frac{\beta_x^m}{\beta_x^c}} \left[\cos \Delta\phi_x^{mc} + \alpha_x^c \sin \Delta\phi_x^{mc} \right] x^c + \left[\sqrt{\beta_x^m \beta_x^c} \sin \phi_x^{mc} \right] x'^c + D_x^c(\Delta p/p)^c \quad (1.13)
$$

$$
x'^m = \left[\frac{(\alpha_x^c - \alpha_x^m)\cos \Delta\phi_x^{mc} - (1 + \alpha_x^m \alpha_x^c)\sin \Delta\phi_x^{mc})}{\sqrt{\beta_x^m \beta_x^c}} \right] x^c +
$$
$$
+ \sqrt{\frac{\beta_x^c}{\beta_x^m}} \left[(\cos \Delta\phi_x^{mc} - \alpha_x^m \sin \Delta\phi_x^{mc}) \right] x'^c + D_x'^c(\Delta p/p)^c \quad (1.14)
$$

The required energy collimation depth, for the given background source with horizon-
tal half aperture A_x will be given by:

$$
A_x > \sqrt{x^{m2} + x'^{m2}} \quad (1.15)
$$

The energy collimation depth in our example is given by the maximum momentum
error accepted without generating background at the given background source. Parti-
cles with momentum error higher than this value have to be collimated by the energy
collimation system. Tracking codes have to be used to estimate the energy collimation
depth and the required collimation system geometric aperture.
Typically, only one energy collimation system stage collimating in one plane (usually
the horizontal one as explained) is required. This is due to the fact that usually it is
enough to collimate the first-order energy dispersion. For that reason, rectangular jaws
are used and the scheme is based on one spoiler and one absorber as illustrated in Fig.
1.6.

1.1.3   Collimation efficiency

In order to quantify the efficiency of the a collimation system for a given defined aper-
ture **the single collimation system cleaning efficiency**, η^i, is defined as the fraction of
halo particles lost at the collimation system, N^i, over the total losses in the beamline
N_{Total}, as:

$$
\eta^i = \frac{N^i}{N_{Total}} \quad (1.16)
$$

A perfect beam collimation system should provide 100% cleaning efficiency avoiding the losses in other locations outside the collimation system.

If instead of having one collimation system we have several, **the total collimation system cleaning efficiency** will be defined as:

$$\eta^{Total} = \frac{\sum_i N^i}{N_{Total}} \tag{1.17}$$

In some particular cases it is useful to define **the local cleaning efficiency** for a given background source as:

$$\eta^i_{local} = 1 - \frac{N^i_{w\ coll}}{N^i_{w/o\ coll}} \tag{1.18}$$

where $N^i_{w\ coll}$ are the particles lost at the given background source with the collimation system and $N^i_{w/o\ coll}$ are the particles lost at the background source without a collimation system.

1.1.4 Multi-stage collimation concept

Single-stage collimation systems (one pair of spoiler/absorber per degree of freedom) have been proven to reach efficiencies on the order of 97-99% but in some machines as for example in accelerators operating with Superconducting (SC) cavities where losses lead to quenches of the magnets, higher collimation efficiency and control of the losses are required. Multi-stage collimation systems are designed in these cases. Usually 2 or 3 stages of betatron and energy spoilers/absorbers are considered. The first collimation stage has the smallest apertures. The second collimation stage has to absorb the secondary halo and the EM shower produced in the first collimation stage. At this stage the apertures of the collimation systems are usually higher that the ones in the first collimation stage. Furthermore, in some cases, a tertiary collimation stage is also installed closer to the IP to absorb the tertiary halo and the EM shower produced at the second collimation stage. In addition, passive protection collimation systems with a fixed half aperture are added to protect some sensitive elements in the beamline. In Fig. 1.8 this concept is illustrated.

1.1.5 Advanced collimation technologies for LCs

In order to assure the survivability of the collimation system in high-intensity and high-energy linear colliders the development of new collimation technologies may be required. Some advanced collimation technologies are being developed to be included in the spoiler/absorber scheme. Some of these advanced techniques are described in the following:

- **Consumable collimation systems** [12]
  In this case, the spoilers are made by a pair of wheels. The wheels rotate changing the damage surface presented to the beam. After a complete rotation of the wheel the spoiler needs to be replaced. This collimation technology was first proposed for the Next Linear Collider (NLC) design and it has also been considered for the FLC. In Fig. 1.9 a first prototype for the NLC is shown.
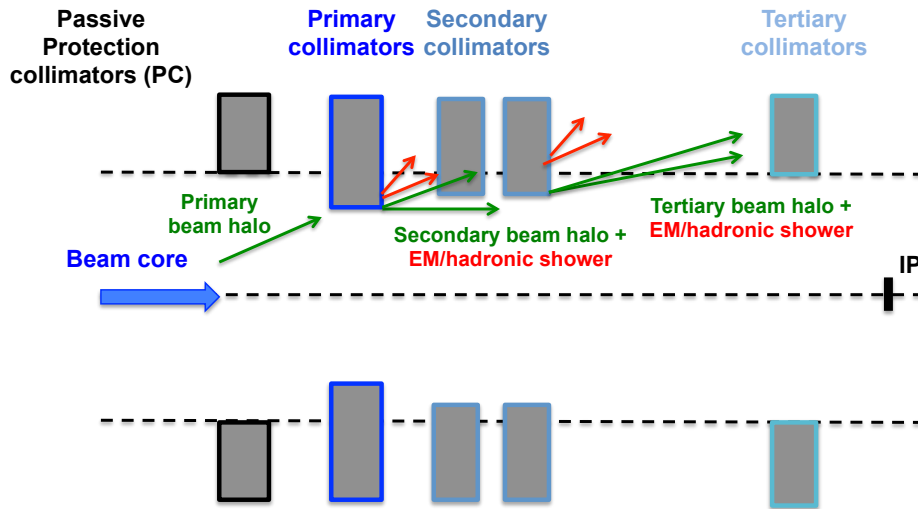
Figure 1.8: Multi-stage collimation scheme concept.
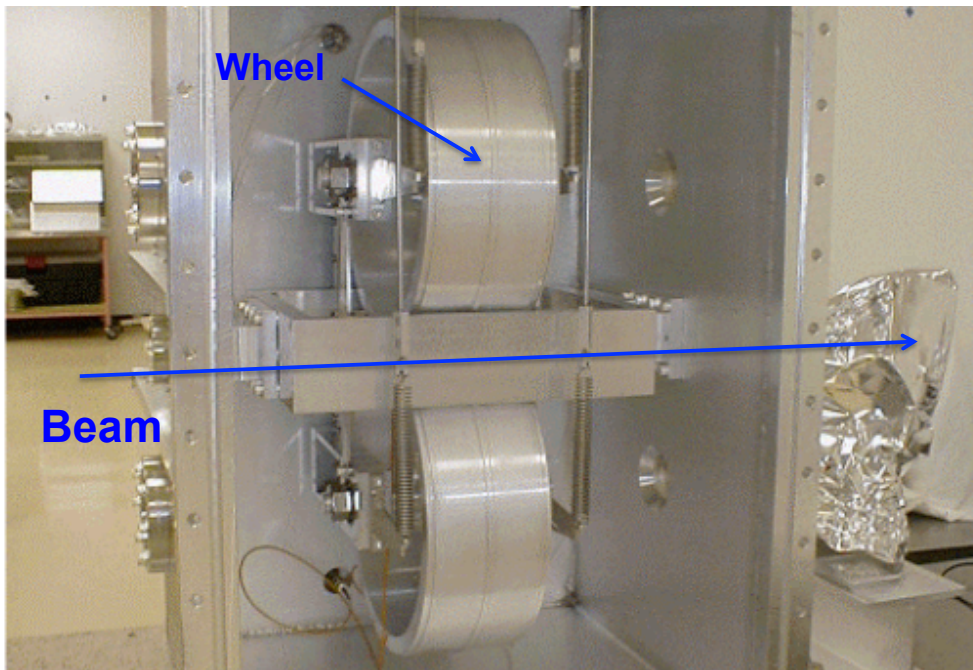
Figure 1.9: Consumable collimation system prototype successfully tested at the Stanford Linear Collider (SLC) at SLAC.

- **Repairable collimation systems** [12]

  The repairable spoiler is a new technique in which the spoiler can be operated even if the damage occurs for each beam pulse. The mechanical idea is the same as the one for the consumable collimation systems but in this case, the wheel is in contact with a tank of frozen liquid metal. The damage surface of the wheel is repaired when it enters into contact with the solidifying metal.

Then the solidified surfaced is rolled flat with smoothing rollers. The basic scheme is shown in Fig. 1.10. In this case, the main constraint is to find a good metal candidate with low vapor pressure at melting point and low toxicity. Molybdenum rollers and a bath of liquid Tin have been demonstrated to be a good candidate. The development of this technology is not essential for FLC but it might allow a reduction in size and cost of the collimation system allowing the reduction of the collimation stages required.
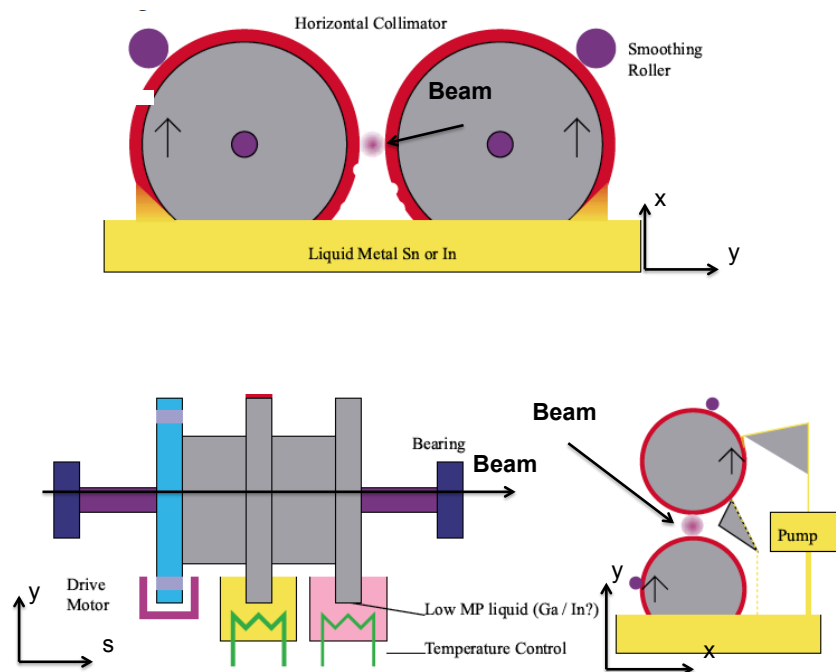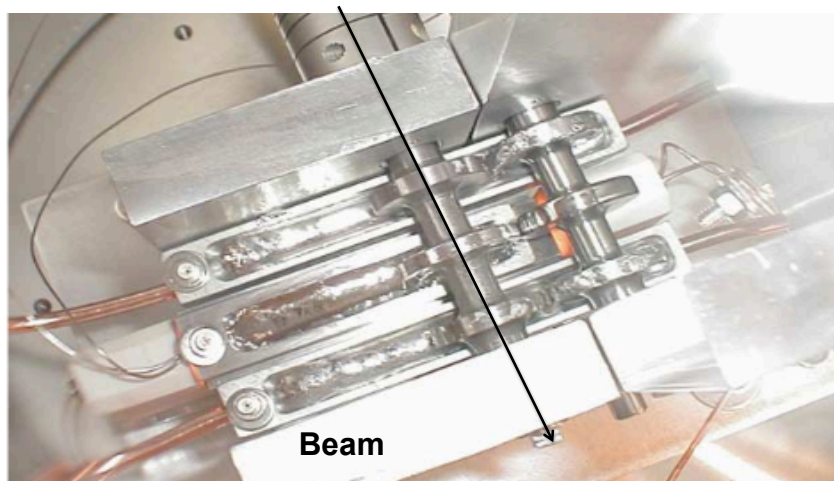
Figure 1.10: Repairable collimation concept scheme (top) and prototype tested at SLC at SLAC (bottom).

- **Nonlinear collimation [13, 14]**

  The basic concept of this system consists in adding non linear elements to blow up the beam size and particles amplitude at the collimator location, so that the collimation system jaws can be located further away from the nominal orbit (reducing the wakefields) and the beam density at the collimation system is decreased (for survival of such a system). Then a second non-linear element is placed at a phase advance distance of π with unit magnification to cancel geometric aberrations. A basic layout is shown in Fig. 1.11. The main advantages with respect to mechanical spoilers is that this collimation technique can not be damaged by high intensity beams and will not induce wakefield kicks which can cause emittance dilution. For the NLC a scheme based on two skew sextupoles and tail-folding octupoles was studied and it is also being evaluated for the FLC.
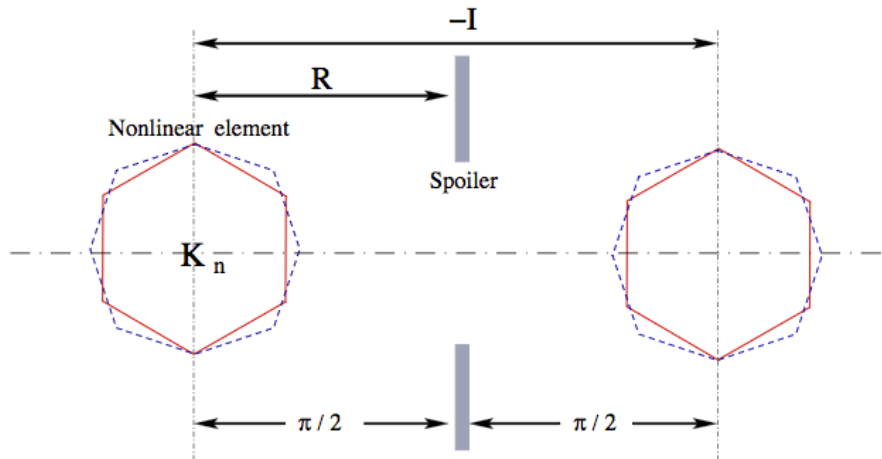
Figure 1.11: Non linear collimation scheme [13].

1.2 Collimation system wakefields effect

The wakefield effect due to collimation systems could be very important since these devices have to be very close to the beam in order to efficiently clean the beam halo. Analytical models have been developed for simple geometries in order to estimate the collimation system wakefield's impact. These models are valid under some approximations and provide information about the dependence of the wakefields on the collimation system geometry (like the minimum half aperture, a, and the tapered angle, α) and some beam parameters (like the bunch length, σ_z). However, for a more accurate calculation numerical simulations have to be performed using 3D EM solvers, such as, for example the Computer Simulation Technology Particle Studio (CST PS) [15]. Furthermore, the impact on the beam orbit and beam size has to be evaluated to quantify the implications of this effect. The impact on the beam dynamics can be calculated by linear transport of the wakefield kick, previously estimated using analytical models or numerical simulations, and using tracking codes, such as the tracking code

PLACET [16, 17]. In this section, we introduce the basic definitions to understand the wakefield effects and the impact of them on the beam dynamics. Later, in chapter 3, the particular case of a rectangular tapered collimation system is described in detail.

1.2.1 Basic definitions

A charged particle moving at a speed close to the speed of light carries EM fields perpendicular to the particle direction of motion with opening angle $1/\gamma$, where γ is the relativistic factor. These EM fields interact with the surrounding beam pipe and due to variations in the cross-sectional shape of the vacuum chamber and the finite conductivity of the materials of the walls these EM fields change and induce the so-called wakefields. The wakefields from particles in a bunch can affect other particles in the same bunch (**single-bunch wake**) and also particles in subsequent bunches (**bunch-to-bunch wake**). In Fig. 1.12 the wakefield effect is illustrated considering a two-particle model with an offset in the vertical plane. The horizontal plane can be treated in the same way. A first particle (**driving particle**) with a vertical offset with respect to the center of the structure, y_d, induces EM fields that will disrupt the dynamics of the second particle (**test particle**) with a vertical offset, y_t.
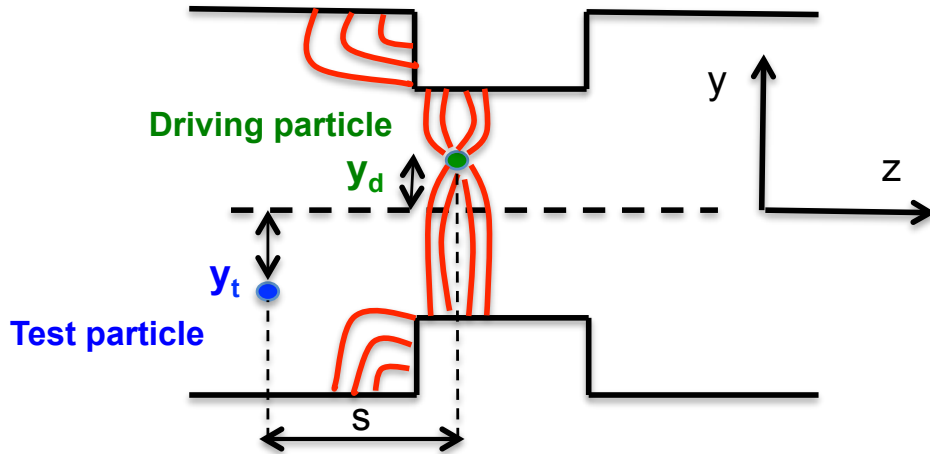
Figure 1.12: Two particle model wakefield effect scheme considering the effect on the vertical plane.

Since the longitudinal and transverse beam motion in an accelerator machine are decoupled, two effects on the test particle can be distinguished due to the longitudinal and transverse forces induced, F_L and $\vec{F}_T$, respectively. Integrating F_L and $\vec{F}_T$ along the structure length in the longitudinal axis, s, the two effects on the test particle are described by the longitudinal, $w_L(z - z')$, and the transverse, $\vec{w}_T(x_d, x_t, y_d, y_t, z - z') = (w_x, w_y)$, **wake functions** given respectively as [18]:

- An energy loss (longitudinal)

$$w_L(z - z') = \int_0^L F_L(z - z', s)|_{z-z'>0} \, ds \qquad (1.19)$$

- A transverse deflecting kick (transverse)

$$\vec{w}_T(x_d, x_t, y_d, y_t, z - z') = \int_0^L \vec{F}_T(x_d, x_t, y_d, y_t, z - z', s)|_{z-z'>0} \, ds \qquad (1.20)$$

where $F_L(z - z', s)$ and $\vec{F}_T(x_d, x_t, y_d, y_t, z - z', s)$ are the longitudinal and transverse components of the Lorentz force acting on the test particle and T stands for the vertical and horizontal plane (x, y). These two forces depend on the transverse position of the driving particle (x_d, y_d), on the transverse position of the test particle (x_t, y_t), on the longitudinal position of the test particle (s) and on the distance between the particle which drives the wake and the test particle $(z - z')$ (see Fig. 1.12). Due to the causality principle these wake functions can not propagate in front of the driving particle therefore $w_L(z - z') = 0$ and $w_T(x_d, x_t, y_d, y_t, z - z') = 0$ for $z - z' < 0$. Furthermore, the transverse and the longitudinal wake functions are related as a consequence of the Panofsky-Wenzel theorem [19] as:

$$\frac{\partial \vec{w}_T}{\partial s} = \frac{1}{\Delta T} \vec{\nabla} w_L \qquad (1.21)$$

This theorem is derived from the Lorentz equation using the general relations of the EM theory. These relations state that in order for a transverse deflection kick to occur, there must be a transverse variation of the longitudinal kick imparted by the EM fields of the system.
The wake functions normalized by the charge q of each particle (and in the case of the transverse plane also normalized to the transverse offset of the driving particle, T_d) are called **wake potentials**, W_L and $\vec{W}_T$, and are defined as following:

$$W_L(z - z') = \frac{w_L(z - z')}{q^2} \qquad (1.22)$$

$$\vec{W}_T(x_d, x_t, y_d, y_t, z - z') = \frac{1}{T_d} \frac{\vec{w}_T(x_d, x_t, y_d, y_t, z - z')}{q^2} \qquad (1.23)$$

where $W_L(z - z')$ is the longitudinal wake potential usually expressed in units of V/pC and in $V/pC/mm$ when it is normalized by the length of the structure given in mm; and $\vec{W}_T(x_d, x_t, y_d, y_t, z - z') = (W_x, W_y)$ is the transverse wake potential expressed in units of $V/pC/mm$ and in $V/pC/mm^2$ when it is normalized by the length of the structure. In general, we assume that the wake functions, $\vec{w}_T$, can be approximated by a power series expansion in the transverse cross sectional plane as:

$$\vec{w}_T(x_d, x_t, y_d, y_t, z - z') = \sum_{i,j,k,l,m=0}^{n} \vec{w}_{T,m} x_d^i x_t^j y_d^k y_t^l \qquad (1.24)$$

If the vacuum beam surroundings have reflectional symmetry around the transverse planes, the transverse wake function vanishes in the center of the structure $x_d = x_t = y_d = y_t = 0$. In addition, if we consider small offsets of the test and driving particles (only the linear terms of the expansion) and no coupling between the x and y planes,

the wake functions can be described as the sum of two contributions (one depending on the driving particle offset and the other on the test particle offset) as [20]:

$$w_x(x_d, x_t, y_d, y_t, z - z') \approx w_x^{dip}(z - z')x_d + w_x^{quad}(z - z')x_t \qquad (1.25)$$

$$w_y(x_d, x_t, y_d, y_t, z - z') \approx w_y^{dip}(z - z')y_d + w_y^{quad}(z - z')y_t \qquad (1.26)$$

where $w_{x,y}^{dip}(z - z')$ and $w_{x,y}^{quad}(z - z')$ are the dipolar and quadrupolar components respectively.

For a bunch of particles the dipolar component leads to coherent oscillations of the bunch as a whole and the quadrupolar component leads to oscillations that depends on the position of each individual particle as emittance growth. In this case, (x_t, y_t) stands for $\Delta x, \Delta y$ and the horizontal and vertical displacement of each individual particle in the bunch (x_d, y_d) as (x, y) (see Fig. 1.13). For a bunch of particles, the wake potential felt by a particle situated at a longitudinal position $(z - z')$ within the density distribution is given by the integral of the wake function over all possible distances $(z - z')$ between this particle and the particles situated ahead satisfying the causality principle as following:

$$W_L(z) = \frac{1}{q^2} \int_{-\infty}^{z} \rho(z) w_L(z - z') dz' \qquad (1.27)$$

$$\vec{W}_T(x, \Delta x, y, \Delta y, z) = \frac{1}{q^2 T_d} \int_{-\infty}^{z} \rho(z) \vec{w}_T(x, \Delta x, y, \Delta y, z - z') dz' \qquad (1.28)$$
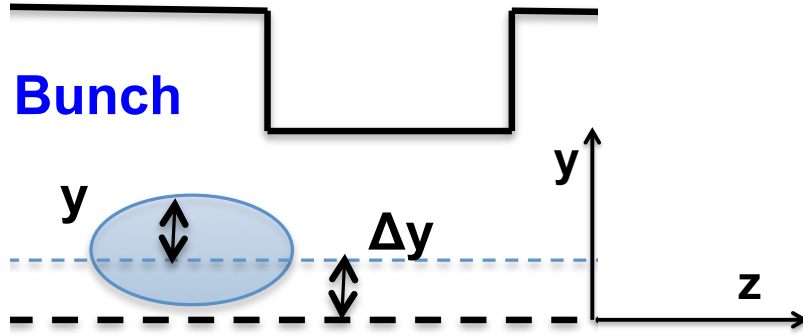
Figure 1.13: Schematic illustration of an offset bunch traversing a non uniform beampipe

In order to quantify the wakefield impact for a bunch of particles the wake potential is averaged over the bunch charge distribution, $\rho(z)$. The resulting quantities are the so-called **wakefield kicks**:

$$\kappa_{loss} = \int_{-\infty}^{+\infty} \rho(z) W_L(z) dz \qquad (1.29)$$

$$\kappa_T = \int_{-\infty}^{+\infty} \rho(z) \vec{W}_T(x, \Delta x, y, \Delta y, z) dz \qquad (1.30)$$

where κ_{loss} is the **energy loss kick factor** and κ_T is the **transverse kick factor**.
The longitudinal, $Z_L(\omega)$, and transverse, $\vec{Z}_T(\omega)$, impedances are defined as the Fourier transform of the **wake functions** as:

$$Z_L(\omega) = \int_{-\infty}^{+\infty} w_L(z)e^{-i\omega z/c}dz \qquad (1.31)$$

$$Z_T(x, \Delta x, y, \Delta y, \omega) = \int_{-\infty}^{+\infty} \vec{w}_T(x, \Delta x, y, \Delta y, z)e^{-i\omega z/c}dz \qquad (1.32)$$

And the wake functions can be calculated from the inverse Fourier transform of the impedance as:

$$w_L(z) = \frac{1}{2\pi} \int_{-\infty}^{+\infty} Z_L(\omega)e^{-i\omega z/c}d\omega \qquad (1.33)$$

$$\vec{w}_T(x, \Delta x, y, \Delta y, z) = \frac{1}{2\pi} \int_{-\infty}^{+\infty} \vec{Z}_T(x, \Delta x, y, \Delta y, \omega)e^{-i\omega z/c}d\omega \qquad (1.34)$$

where ω is the frequency.
Two main factors will influence the transverse wakefield effect induced by an accelerator component: **the geometry** and **the material**. For the analytical calculations two contributions to the **total transverse kick factor**, κ_T, are distinguished depending on the origin of the effect: the geometric one, κ_T^g, and the resistive one, κ_T^r. The geometric contribution is due to a geometric change of the beam pipe seen by the beam and the analytical models are developed under the assumption of infinite material conductivity. In the resistive model, the conductivity of the material is finite and the fields are integrated in transverse symmetric sections. The total κ_T factor is then calculated by adding up both contributions as:

$$\kappa_T = \kappa_T^g + \kappa_T^r \qquad (1.35)$$

1.2.2 Transverse wakefield's beam dynamics impact

The wakefield impact induced by a wakefield source will lead to beam orbit oscillations and beam size and emittance growth. In this section, we present the basic formulas that can be used to estimate these dynamic effects.
First, we will described the impact **on the orbit** given by the wakefield kick, $\kappa_{x,y}^i$, from a given wakefield source. The wakefield kick is calculated in the Eq. (1.30) taking into account only the first order wake function of the Eq. (1.26) referred to as the dipolar component. The wakefield kick induced by this given wakefield source, $\kappa_{x,y}^i$, with a horizontal or vertical beam offset, $\Delta(x, y)^i$, will deviate the bunch of particles at the wakefield source location by an angle $\Delta(x', y')^i$, given by:

$$\Delta(x', y')^i[rad] = \frac{r_e N_e}{\gamma}\kappa_{x,y}^i[mm^{-2}]\Delta(x, y)^i = \frac{eq}{E}\kappa_{x,y}^i[V/pC/mm]\Delta(x, y)^i \qquad (1.36)$$

where N_e is the number of particles in the bunch, r_e is the classical electron radius in mm, $\Delta(x, y)^i$ are the beam offsets from the collimation system axis in mm, eq is the beam charge in pC and E the energy of the beam in eV. Notice here that the wakefield kick, $\kappa_{x,y}^i$, is usually calculated in units of mm^{-2} or $V/pC/mm$. In each case it has to be multiplied by a different factor in order to express it in units of rad as defined in the

Eq. (1.36).

In order to estimate the wakefield's impact at a certain location, the wakefield kick given in Eq. (1.36) can be transported to the location of interest using the first order transport matrix formalism (see Annex 1 for more details). In the following, we will focus on the impact at the IP denoted by *, however, the formulas can be applied to any place of interest. The horizontal and vertical position difference with and without wakefield source at the IP can be estimated as:

$$\Delta(x,y)^* = \sqrt{\beta_{x,y}^i \beta_{x,y}^*} \sin \Delta \phi_{x,y}^{*i} \Delta(x',y')^i \qquad (1.37)$$

where $\beta_{x,y}^i$ is the betatron function at the wakefield source location, $\beta_{x,y}^*$ is the betatron function at the IP, $\Delta \phi_{x,y}^{*i}$ is the betatron phase advance difference between the wakefield source and the IP and $\Delta(x',y')^i$ is defined in Eq. (1.36).

If instead of having one wakefield source we have several, it is useful to define a jitter amplification factor, $\mathcal{A}$, to sum the impact of all wakefield sources and compare it with the orbit jitter budget of the machine. This calculation has to be performed in order to evaluate if the wakefields induced in the machine are, or are not, acceptable to preserve the beam stability.

For a given wakefield source, using Eq. (1.36) in units of beam size and beam divergence, $\sigma_{x,y}^i$ and $\sigma_{x',y'}^i$ respectively, we find the following relation:

$$m_{x,y}^i \sigma_{x',y'}^i = C \kappa_{x,y}^i n_{x,y}^i \sigma_{x,y}^i \qquad (1.38)$$

where $n_{x,y}^i$ is the orbit jitter at the wakefield source location in units of beam sizes, $m_{x,y}^i$ is the wakefield source induced angular jitter in units of angular divergence, $\kappa_{x,y}^i$ is the wakefield source induced wakefield kick and C is the normalization factor which depends on the units of the kick factor defined in Eq. (1.36). Then, the jitter amplification factor for a given wakefield source, $\mathcal{A}^i$, is defined as the ratio $m_{x,y}^i/n_{x,y}^i$ as:

$$\mathcal{A}_{x,y}^i = \frac{m_{x,y}^i}{n_{x,y}^i} = C \kappa_{x,y}^i \frac{\sigma_{x,y}^i}{\sigma_{x',y'}^i} \qquad (1.39)$$

If the wakefield source is placed near a maximum of the β function in a region with zero dispersion, **the betatron amplification factor**, $\mathcal{A}_{\beta_{x,y}}^i$, can be calculated as:

$$\mathcal{A}_{\beta_{x,y}}^i = C \kappa_{x,y}^i \beta_{x,y}^i \qquad (1.40)$$

where we have considered that with a maximum of β function the angular divergence stands for $\sigma_{x',y'} = \sqrt{\epsilon_{x,y}/\beta_{x,y}}$. Then, it is possible to combine the corresponding effect of the different wakefield sources at the IP by summing their contributions and taking into account the corresponding phase advances, $\Delta \phi_{x,y}^{*i}$, introduced in Eq. (1.37) as:

$$\mathcal{A}_{\beta_{x,y}}^{Total} = \sum_i \mathcal{A}_{\beta_{x,y}}^i \sin \Delta \phi_{x,y}^{*i} \qquad (1.41)$$

Furthermore, if the wakefield source is located at a location with $D_{x,y}^i \neq 0$ some transverse jitter is generated which is proportional to the energy jitter. This effect on the energy jitter induced by the transverse wakefields can be expressed as:

$$n_{x,y}^i \sigma_{x',y'}^i = C \kappa_{x,y}^i D_{x,y}^i \sigma_E \qquad (1.42)$$

where only the dispersion component of the trajectory to the beam size has been considered. Then, for a given wakefield source **the energy jitter amplification factor**,
$\mathcal{A}_\delta^i$, can be defined as:

$$\mathcal{A}_\delta^i = \frac{n_{x,y}^i}{\sigma_E} = C\kappa_{x,y}^i \frac{D_{x,y}^i}{\sigma_{x',y'}^i} \qquad (1.43)$$

The energy amplification factors has to be summed by taking into account the phase
advance difference, $\Delta\phi_{x,y}^{*i}$, introduced in Eq. (1.37) as:

$$\mathcal{A}_\delta^{Total} = \sum_i \mathcal{A}_\delta^i \sin \Delta\phi_{x,y}^{*i} \qquad (1.44)$$

The wakefields induced by the wakefield source i will also induce a change **on the
beam size**, due to the **longitudinal change of the EM fields induced**. As can be seen
in Eq. (1.28), the wake potential depends on the coordinate z. This effect is illustrated
in Fig. (1.14).
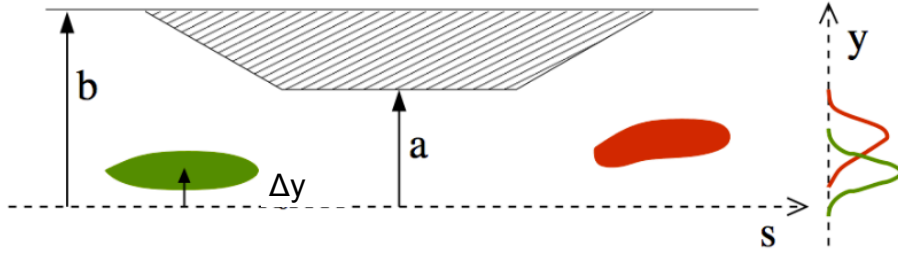
Figure 1.14: Beam size growth effect due to the wakefields induced in a non uniform
beam pipe. In the right side, the projections of the beam sizes in the vertical plane for
the beam before (green) and after (red) feeling the wakefield impact are depicted [21].

The beam size, $\sigma_{x,y}^*$, taking into account the wakefields induced by the wakefield
source i, can be estimated as:

$$\sigma_{x,y}^{*2} = \sigma_{0x,0y}^{*2} + \sigma_{\Delta(x',y')^i}^2 \qquad (1.45)$$

where $\sigma_{0x,0y}^*$ is the beam size at the IP without taking into account the wakefields and
$\sigma_{\Delta(x',y')^i}$ is the variance of Eq. (1.36) given by:

$$\sigma_{\Delta(x',y')^i} = C\sigma_{\kappa_{x,y}^i} \qquad (1.46)$$

where the variance of centroid kicks, $\sigma_{\kappa_{x,y}^i}$, due to the variation the wake potential,
$W_{x,y}^i(z)$, in the longitudinal plane (see Eq. (1.28)) can be calculated as:

$$\sigma_{\kappa_{x,y}^i} = \sqrt{< W_{x,y}^i(z) - \kappa_{x,y}^i >^2} = \left[\int_{-\infty}^{+\infty} (W_{x,y}^i(z) - \kappa_{x,y}^i)^2 \rho(z)dz \right]^{\frac{1}{2}} \qquad (1.47)$$

where $\kappa_{x,y}^i$ is the wakefield kick factor of Eq. (1.30) for the given wakefield source and
$\rho(z)$ is the bunch distribution.

The wakefields will also have an impact **on the emittance**. In the following, we will derive the formula to estimate the emittance growth at the IP due to a wakefield source [21]. The statistical definition of the vertical emittance is given by:

$$\epsilon_x = \sqrt{<(x-\bar{x})^2><(x'-\bar{x}')^2> - <(x-\bar{x})(x'-\bar{x}')>^2}$$
$$\epsilon_y = \sqrt{<(y-\bar{y})^2><(y'-\bar{y}')^2> - <(y-\bar{y})(y'-\bar{y}')>^2} \tag{1.48}$$

where $\bar{x}$, $\bar{y}$, $\bar{x}'$ and $\bar{y}'$ are the average horizontal and vertical position and angle. The second moments of the particle distribution (taking into account the wakefields induced) can be expressed in terms of the Twiss functions as:

$$<(x-\bar{x})^2> = \epsilon_x\beta_x^i \qquad\qquad <(y-\bar{y})^2> = \epsilon_y\beta_y^i$$
$$<(x'-\bar{x}')^2> = \sigma_{\Delta(x')^i}^2 + \epsilon_x\gamma^i \quad <(y'-\bar{y}')^2> = \sigma_{\Delta(y')^i}^2 + \epsilon_y\gamma^i \tag{1.49}$$
$$<(x-\bar{x})(x'-\bar{x}')> = -\epsilon_x\alpha_x^i \qquad <(y-\bar{y})(y'-\bar{y}')> = -\epsilon_y\alpha_y^i$$

The emittance growth due to the impact of the wakefields can be found substituting Eq. (1.49) into Eq. (1.48) is by:

$$\frac{\Delta\epsilon_{x,y}}{\epsilon_{0x,0y}} = \frac{\epsilon_{x,y} - \epsilon_{0x,0y}}{\epsilon_{0x,0y}} = \sqrt{1 + \frac{\beta_{x,y}^i\sigma_{\Delta(x',y')^i}^2}{\epsilon_{0x,0y}}} - 1 \tag{1.50}$$

where $\epsilon_{x,y}$ and $\epsilon_{0x,0y}$ correspond to the emittance with and without a wakefield source, respectively, and the other parameters have been previously defined.
For a Gaussian bunch distribution the solution of Eq. (1.47) gives $\kappa_{x,y}^i/\sqrt{3}$. If we consider small emittance dilution cases $\Delta\epsilon_{x,y} \ll \epsilon_{0x,0y}$ the Taylor expansion of Eq. (1.50) gives the following approximation:

$$\frac{\Delta\epsilon_{x,y}}{\epsilon_{0x,0y}} \approx \frac{1}{2}\frac{\beta_{x,y}^i}{\epsilon_{x,y}}\left(\frac{1}{\sqrt{3}}C\kappa_{x,y}^i\Delta(x,y)^i\right)^2 = \frac{1}{2}\frac{\beta_{x,y}^i}{\epsilon_{x,y}}\left(\frac{1}{\sqrt{3}}C\kappa_{x,y}^in_{x,y}\sigma_{x,y}^i\right)^2 = (0.4n_{x,y}^i\mathscr{A}_{\beta_{x,y}^i}^i)^2 \tag{1.51}$$

where the definition of the jitter amplification factor in Eq. (1.40) has been used.
These formulas can be used for a first estimation, giving the order of magnitude of the impact that a given wakefield source has on the beam dynamics at a certain location. In a realistic scenario the wakefield impact has to be evaluated numerically using 3D EM solvers as CST PS [15] to compute the wake potential. This wake potential calculation has to be implemented in a tracking codes, such as PLACET [16], to perform more realistic and complete studies of such effects for all relevant wakefield sources in the beamline.

1.3 Collimation system material analysis

The collimation system has to be able to tolerate the heat load of the beam passing through without being damaged, as well as to survive the impact of a train of errant bunches. The instantaneous temperature rise is difficult to estimate analytically, however a reasonable estimation of the maximum allowable temperature rise could be done by taking into account the mechanical fracture temperature, the melting temperature

and the vapor pressure temperature of the jaws material. In this section, we will briefly introduce the definition of these three temperatures and the three main mechanisms that will contribute to the temperature rise: the electric field breakdown, the beam energy deposition by the induced image current induced and the collimation system-beam interaction mechanisms.

1.3.1   Jaw rise temperature limit

If the temperature of the collimation system jaws increases up to a certain value the jaws will be damaged. In order to choose the appropriate material for the required beam conditions criteria can be adopted based on the melting temperature, mechanical fracture temperature and material vapor pressure temperature. The three characteristic temperatures are described in the following [22]:

- **The melting temperature** is the point at which the material changes state from solid to liquid at atmospheric pressure. The maximum allowed temperature rise without melting in units of Kelvin is given by:

$$\Delta T_{melt} = 0.7 T_{melt} - T_{room} \tag{1.52}$$

    where $T_{room} = 293.15K$ is the room temperature and the 0.7 is an empirical factor [22].

- **The mechanical fracture temperature** is the temperature at which the material breaks and it is defined in units of Kelvin as:

$$\Delta T_{fail} = \frac{\epsilon \sigma_{uts}}{\alpha_T Y} \tag{1.53}$$

    where α_T is the thermal expansion coefficient, σ_{uts} is the ultimate tensile strength of the material (maximum tension supported by the material), ϵ is an empirical factor with an experimental value of 1.5, and Y is the Young's modulus (relation between the stress (force per unit area) and strain (proportional to the deformation)).

- **The material vapor pressure temperature** is the temperature at which the surface of the material can evaporate. The temperature of this process represents a higher limit than the melting and fracture temperature.

A safe limit is usually adopted based on the the three temperatures introduced, as $\Delta T_{limit} = min[\Delta T_{melt}, \Delta T_{fail}]$. The value of ΔT_{melt} and ΔT_{fail} for some typical collimation system materials are shown in Table 1.1 along with the radiation length and the conductivity for each material. These properties will be used in other sections.
Notice from Table 1.1 that Cu which has the highest conductivity (thus minimizes wakefields), has the lower ΔT_{melt} and ΔT_{fail}. In FLCs a miss-steered beam with a power on the order of MW could produce an instantaneous power density deposition on the order of GeV/mm^2. In order to design a collimation system to fulfill the requirements of the FLCs one possible solution that it is being evaluated to reduce wakefields and survive the impact of a single errant bunch consists of jaws made of C or Ti with a coating of Cu.

Material	ΔT_{melt} [K]	ΔT_{fail} [K]	σ [S/m]	X_0 [cm]
Be	792	174	2.5×10^7	35.28
C	2382	19000	1×10^5	19.32
Ti	1060	274	2.4×10^7	3.56
Cu	656	88	5.9×10^7	1.44
W	2285	149	2×10^7	0.35

Table 1.1: ΔT_{melt}, ΔT_{fail}, conductivity σ and radiation length, X_0, for some typical collimation system materials.

1.3.2 Rise Temperature mechanism

The temperature rise will be driven by three main collimation system-beam interaction mechanisms: electric field breakdown, the image current heating and direct energy deposition by beam-matter interaction [22]:

- **Electric field breakdown**
  This mechanism of material heating is based on the interaction of the high electric field carried by the beam with the surface of the jaws. If the electric field is high enough it can produce an electric discharge resulting in a heat damage. This phenomenon has to be avoided because it can damage the surface of the jaws and this surface deformation could lead to an increase in wakefields induced by the collimation system.

- **Image current heating**
  The interaction of the EM field carried by the beam with the beam pipe produces image currents in the jaws surface, resulting in an increase of the surface temperature. Even if the field is not high enough to produce breakdowns this interaction results in an increase of the jaw temperature that has to be controlled. Considering the impact in the vertical plane, different cases can be distinguished depending on the **distances between the center and the wall of the structure**, a, in comparison with the **beam size**, σ_y. The same calculations are applicable to the horizontal case changing y by x. The analytical formulas derived to estimate the energy deposited in the jaws by the image current are [23]:

  - **For a $>> \sigma_y$** the beam is far from the collimation system wall surface and the beam can be considered as a point-like beam. The energy density deposited by a beam with charge Q and bunch length σ_z is given by:

  $$E_{D,single} = \frac{Z_0 c}{2\pi} \frac{Q^2}{\sigma_z^2} \frac{1}{4\pi^2 r^2} \qquad (1.54)$$

  - **For a $\geq \sigma_y$** a miss-steered beam can get close to the collimation system surface and the approximation of a transverse point-like beam is not longer valid. The maximum deposited energy density is estimated to be a factor 4 larger than the value estate in Eq. 1.54 in [23].

  - **For a $\leq \sigma_y$** part of the bunch penetrates the collimation system block and other processes such as radiation heating, which are commented on next,

will start to be important and will contribute to the temperature rise. In this
case, the maximum energy deposition can be estimated as:

$$E_{D,single} = \frac{Z_0 c}{2\pi} \frac{Q^2}{\sigma_z^2} \frac{f_{max}^2(\sigma_y/\sigma_x)}{4\pi^2 \sigma_x \sigma_y} \tag{1.55}$$

where it is assumed that the collimation is performed in the vertical plane
and the function $f_{max}(v)$ is given approximately by:

$$f_{max}(v) \approx \sqrt{\frac{1}{2\pi}} \frac{ln(1 + \pi v)}{\sqrt{v}} \tag{1.56}$$

The impact of a single beam is described by the above equations but in addition
one needs to estimate **the impact of a train of bunches**. In order to increase
luminosity in FLC a high repetition rate is demanded. The main issue of the
estimation is to calculate the diffusion distance, which takes into account how
much of the energy deposited is dissipated when the second bunch arrives. The
diffusion distance is a function of the material and it is given by:

$$y_{heat} = \sqrt{Kt_{train}/c_p} \tag{1.57}$$

where K is the thermal diffusion coefficient, c_p is the specific heat capacity
which gives the resulting temperature change of the object for a given heat added
and t_{train} is the duration of one bunch train. Taking into account this value the
multi-bunch energy density deposited can be estimated as:

$$E_{D,train} = E_{D,single} N_p \frac{\delta_e}{y_{heat} \sqrt{\pi}} \tag{1.58}$$

where $E_{D,single}$ is the single-bunch energy deposited from Eq. (1.54) and Eq.
(1.55), N_p is the number of bunches per train and δ_e is the effective skin depth
that characterizes the layer of the material where the energy is deposited defined
as:

$$\delta_e = \Gamma(3/4) \sqrt{2\rho\sigma_z/c\mu} \tag{1.59}$$

where ρ is the resistivity of the material of the surface, μ is the magnetic perme-
ability of the collimation system surface, σ_z is the bunch length and $\Gamma(3/4) =$
0.43291174.

- **Energy deposition by direct beam-matter interaction**
  When the beam penetrates in the jaws, the particles of the beam interact with
  the material of the jaws. As in our case all the work focuses on electron beams,
  only the important interactions between electrons and matter are described in
  this section.
  Depending on the energy of the electrons different interaction mechanisms are
  present. A summary of the different processes is depicted in Fig. 1.15 for elec-
  trons interacting with lead.

  - **At low energies** $< 10\ MeV$: the electrons primarily lose energy by ioniza-
    tion, resulting in soft X-rays, which are absorbed within short distances.

- **At energies around** 1 *MeV*: at this energy other processes can also contribute to the energy loss, such as, the Moller scattering, Bhabha scattering and positron annihilation. Electron and positron scattering is considered as ionization when the energy per collision is below 0.255 MeV, and as Moller (electrons) or Bhabha (positrons) scattering when it is above.

- **At high energies** > 10 *MeV*: the electrons predominantly lose energy in matter by bremsstrahlung. The photons generated by bremsstrahlung can interact with matter and produce electron-positron pairs. This process is commonly called an EM cascade.
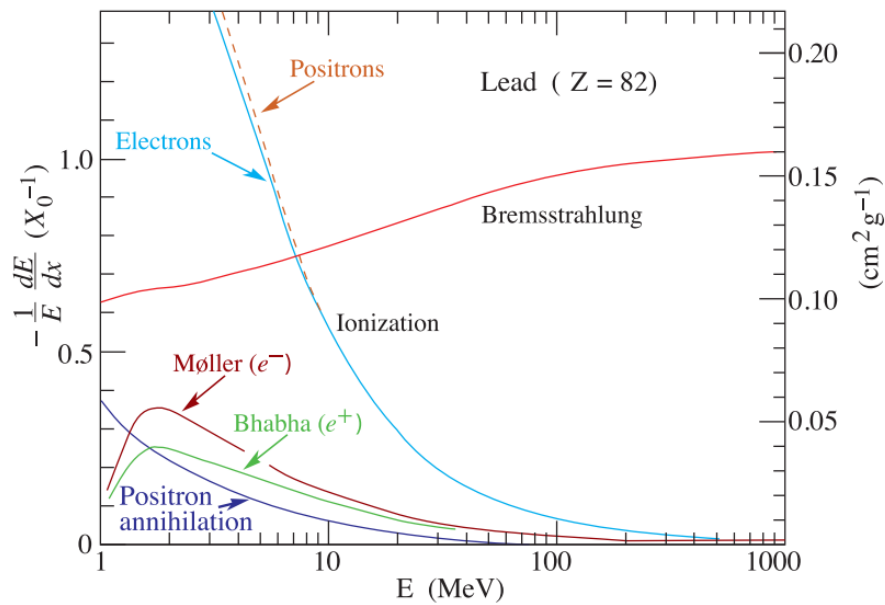
Figure 1.15: Energy deposited per unit of radiation length as a function of the incident electrons energy for all possible interaction mechanisms. Values of the energy deposited in units of $cm^2 g^{-1}$ are shown as an example for lead (right scale).

In order to determine the required length of the collimation system jaws to stop the EM cascade generated by high-energy electrons, a simple model can be used as described in the following. The energy after crossing z thickness of the medium can be calculated as:

$$E(z) = E_0 e^{-\frac{z}{X_0}} \tag{1.60}$$

where X_0 is defined as the radiation length corresponding to the distance traveled by the particle when it has lost 63% of the initial energy, E_0. The critical energy, E_C is defined as the energy at which the bremsstrahlung energy loss rate is equal to the ionization loss rate. $E_C \approx 610 MeV/(Z + 1.24)$ in the case of a solid and liquid target material and $E_C \approx 720 MeV/(Z + 0.92)$ in the case of gases, where Z is the atomic number.

In this model, the material is divided in layers of thickness t (see Fig. 1.16). In each layer, each particle produced will generate another two particles with
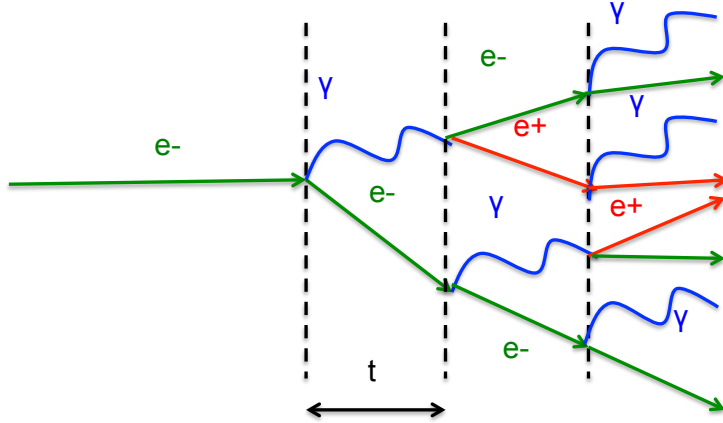
Figure 1.16: EM cascade scheme.

energy E. The total number of particles produced will be $N(t) = 2^{t/X_0}$ with
energy $E(t) = E_0/2^{t/X_0}$. The shower will stop when $E < E_c$. The corresponding
maximum depth taking into account the Eq. (1.60) will be:

$$z_{max} = X_0 \frac{1}{\ln 2} \ln\left(\frac{E_0}{E_c}\right) \qquad (1.61)$$

where z_{max} represents the length of the material needed to stop the EM cascade.
The number of radiation lengths needed can be calculated using Eq. (1.62), as:

$$n = z_{max}/X_0 = \frac{1}{\ln 2} \ln\left(\frac{E_0}{E_c}\right) \qquad (1.62)$$

1.4   FLC in the HEP landscape: ILC and CLIC

In July 2012, scientist at the Large Hadron Collider (LHC) [26] announced the discov-
ery of the Higgs boson [24, 25], the last missing elementary particle predicted by the
SM. In October 2013, Peter Higgs and François Englert were awarded with the Nobel
prize in Physics in recognition of their work on the Higgs mechanism. The LHC, the
largest and most powerful accelerator in the world, is a 27 km ring built at CERN using
the exiting Large Electron Positron (LEP) tunnel successfully commissioned in 2008.
With the advent of the LHC the HEP and Accelerators Physics community reached a
consensus on the **next step towards Future Colliders (FCs)** in order to extend, im-
prove and complement the LHC discoveries as well as explore the physics in a new
range of energies. The HEP community strongly agreed that the most suitable option
for the FC is an electron positron collider. Colliding such elementary particles provides
cleaner collisions with better know initial states and less background in the detectors
than colliding composite particles, such as protons.
Within this context, in June 2015 the Accelerator Physics community has produced a
Technical Design Report (TDR) presenting the matured technology, design and con-
struction plan for the International Linear Collider (ILC) [2]. Alongside this, the Com-
pact Linear Collider (CLIC) collaboration has worked out a Conceptual Design Report

(CDR) [3] published in 2012 demonstrating the feasibility of a different acceleration technology for the LCs. For several years, the particle physics community has been developing the ILC and the CLIC projects. In February 2013, the International Committee for Future Accelerators (ICFA) decided that the two projects should start to work together under a unique LC effort, collaborating on the technical issues that are common to both, providing direction for research and development on both accelerator technologies. This new structure for LCs development is a strong signal of the globally integrated nature of particle physics. Furthermore, in recent years, the feasibility of circulars TeV colliders is also being evaluated in two other projects: the Future Circular Collider electron positron (FCC-ee) [27] and the Circular electron positron Collider (CepC) [28].

In this chapter, we will discuss in a "simplistic" way, **the main challenging goals on the design of a high luminosity and high energy electron positron LC**. Then, we will introduce the two FLC projects: **ILC** and **CLIC**.

One of the main issues to make a project reliable is the cost. High energy colliders demand an efficient RF system in order to keep the electric power required under control. In linear machines there is no strong contribution from Synchrotron Radiation (SR) losses as in circular colliders, since the SR lost per turn is:

$$\Delta E \approx \frac{E^4}{\rho^2 m^4} \tag{1.63}$$

where E is the nominal energy of the beam, ρ is the radius of the accelerator circumference and m is the mass of the particle. However, in a linear machine, the beam must be accelerated to the required energy on each pulse of the machine and it is not possible to slowly increase the energy as in circular machines. The desired particles's energy is achieved by putting one cavity after another. Therefore the cost of reaching the desired energy in the linear colliders is subject to the the RF systems efficiency in transferring the energy to the beam and the construction costs.

Apart from **the center-of-mass-energy**, **the luminosity** (defined as the ratio between the event rate and the cross section for a given event), is the other key parameter in FLCs experiments. In linear colliders the instantaneous luminosity is defined as:

$$L = H_D \frac{N_b^2}{4\pi\sigma_x\sigma_y} n_b f_r \tag{1.64}$$

where H_D is a correction factor representing the combined effect of an **"hourglass"** (change of the beta function in the longitudinal direction over the collision region) and **disruption enhancement factor** (due to the force that the two colliding bunches exert on each other including the pinch effect and the bremsstrahlung), N_b is the number of particles per bunch (here the two colliding bunches have been considered to have the same number of particles), n_b is the number of bunches per pulse, $\sigma_{x,y}$ is the transverse beam size and f_r is the linac repetition rate.

The correction factor, H_D, is defined as the ratio between the effective luminosity (resulting from the beam-beam interaction) and the geometric luminosity. This factor can not be calculated analytically because of the non-linearity of the the beam-beam interactions but it is however a function of the disruption parameter, $D_{x,y}$. This parameter quantifies the more general beam-beam effect and represents a relative change in the

impact cross-section collision of the two beams due to the trajectory bend caused by the EM fields created by the opposite beam. The disruption factor is defined as [1] :

$$D_{x,y} = \frac{\sigma_z}{f_{x,y}} = \frac{2r_e N \sigma_z}{\gamma \sigma_{x,y}(\sigma_x + \sigma_y)} \tag{1.65}$$

where σ_z is the *rms* of the longitudinal bunch length, $f_{x,y}$ is the effective focal length of the beam in the transverse plane. If $D_{x,y}$ is small, the beam acts as a thin lens. In contrast, if $D_{x,y} \gg 1$ the focal length is shorter than the bunch length increasing the pinch effect which increases the luminosity. However, too big $D_{x,y}$ will also lead to strong beam instabilities in the presence of small beam offsets, degrading the luminosity. The enhancement factor can be estimated as a function of the disruption factor based on fits to simulations as:

$$H_{x,y} = 1 + D_{x,y}^{1/4} \left(\frac{D_{x,y}^3}{1 + D_{x,y}^3} \right) \left[ln(\sqrt{D_{x,y}} + 1) + 2ln \left(\frac{0.8\beta_{x,y}}{\sigma_z} \right) \right] \tag{1.66}$$

Furthermore, **the luminosity can be expressed in terms of the center-of-mass-energy**, E_{CM}, substituting the power of the beam given by $P_{beam} = n_b N_b E_{CM} f_r = \eta_{RF} P_{RF}$ in Eq. (1.64) as:

$$L = \frac{1}{4\pi E_{CM}} (\eta_{RF} P_{RF}) \left(\frac{N_b}{\sigma_x \sigma_y} H_D \right) \tag{1.67}$$

where P_{RF} is the RF power and η_{RF} is the efficiency of the RF system.

Achieving high luminosity in LCs is very challenging. Linear machines are one pass devices so each bunch only collides once. This fact results in a repetition rate factor smaller than in the case of circular machines where the beam performs many cycles. In order to have luminosities in linear machines comparable to those it is possible to achieve in circular machines we need to reduce the transverse beam size in the IP dramatically to the order of *nm*, four order of magnitude smaller than the vertical beam size at the LHC collision point. This requires strong focusing low-β and the chromatic and the geometric aberrations have to be cancelled very accurately. Furthermore high intensity beams means having to deal with strong beam-beam effects and tight vibration tolerances. However, both transverse planes can not be reduced at the same time, because of the energy loss by bremsstrahlung, δ_{BS}, which can be estimated as:

$$\delta_{BS} \approx 0.86 \frac{er_e^3}{2m_0 c^2} \left(\frac{E_{CM}}{\sigma_z} \right) \frac{N_b^2}{(\sigma_x + \sigma_y)^2} \tag{1.68}$$

Therefore, in a compromise between the increase of luminosity proportional to $(\sigma_x \sigma_y)^{-1}$ and the increase of the disruption factor proportional to $(\sigma_x + \sigma_y)^{-1}$, a **"flat" like beam** with big aspect ratio $\sigma_x / \sigma_y \gg 1$ is considered as a possible solution. If we consider a "flat" beam solution, the bremsstrahlung is only a function of the horizontal beam size as:

$$\delta_{BS} \approx 0.86 \frac{er_e^3}{2m_0 c^2} \left(\frac{E_{CM}}{\sigma_z} \right) \frac{N_b^2}{(\sigma_x)^2} \tag{1.69}$$

As a consequence, the horizontal beam size can be fixed for an acceptable energy loss by bremsstrahlung and combining Eq. (1.67) and Eq. (1.69) the luminosity scaling

law with the key LC parameters can be expressed as:

$$L \propto \frac{\eta_{RF} P_{RF}}{E_{CM}^{2/3}} \frac{\sqrt{\delta_{BS}} \sigma_z}{\sigma_y} H_D \qquad (1.70)$$

From Eq. (1.70) we see the luminosity increases with the bunch length, σ_z, however the "hourglass effect" has to be taken into account here. The vertical β function and the bunch length are constrained by the relation $\sigma_z^* \leq \beta_y^*$. When this condition is not satisfy the luminosity is reduced due to the "hourglass effect". Considering the limit in order to maximize the luminosity and writing the vertical beam size in terms of the vertical emittance, the final **LCs luminosity scaling law** is given by:

$$L \propto \frac{\eta_{RF} P_{RF}}{E_{CM}} \frac{\sqrt{\delta_{BS}}}{\epsilon_{y,N}} H_D \qquad (1.71)$$

From Eq. (1.71) we observe that flat beams with small vertical emittances while keeping an acceptable RF power and energy loss by bremsstrahlung maximize the luminosity. Active research is ongoing to achieve high energy and high luminosity in LCs and some of the collaborations involved in the research are introduced in this section.

1.4.1 International Linear Collider (ILC)

The ILC is a proposed electron and positron collider consisting of two linear accelerators that face each other (see Fig. 1.17). The ILC is intended to collide some 10 billion of electrons and positrons, toward each other at nearly the speed of light. The ILC accelerator complex consists of two high energy SC LINACs to accelerate the particles from 5 GeV to 250 GeV, a BDS to prepare the high energy beams for collision and separate the spent beams, two Damping Rings (DR) for preparation of low emittance beams and an injector system for the electrons (the positrons will be produced using the high energy electrons beam for synchrotron radiation via an undulator and a conversion target). The accelerating technology is based on SC accelerator cavities, operating at temperatures near absolute zero and with an average gradient of 31.5 MV/m. Stretching approximately 31 kilometers in length, the beams will collide with a center-of-mass energy of 500 GeV (upgraded to 1 TeV). A schematic layout of the ILC can be seen in Fig.1.17 and the main beam parameters in the Table 1.2. Detailed information can be found in [2].

Beam Test Facilities are required for critical technical demonstrations, including accelerating gradient, precise beam handling and beam dynamics. In each case, the R&D facilities are used to mitigate critical technical risks. To demonstrate the industrialization of the Superconducting RF technology and its application in a linear accelerator, the European X-Ray Laser Project (XFEL) has been constructed in DESY Hamburg now operating an electron linac where it is possible to run close to reference design gradients with nominal ILC beams. In this context also the STF facility at KEK in Japan, is working on SC technology R&D.

An important technical challenge of the ILC is the collision of extremely small beams of a few nanometers in size. The latter challenge has three distinct issues: creating small emittance beams, preserving the emittance during acceleration and transport,

focusing the beams to nanometers and colliding them. The Accelerator Test Facility (ATF) at the High Energy Accelerator Research Center Organization (KEK) was built to create small emittance beams, and succeeded in obtaining an emittance that almost satisfies the ILC requirements. The ATF2 facility, which uses the beam extracted from the ATF damping ring, was constructed to addresses two major challenges of the ILC: focusing the beams to a nanometer scale using an ILC-like final focus and providing nanometer stability. The activities being carried out in this facility are described in more detail in chapter 2.

Another key issue in the R&D of the ILC is the design of Damping Rings (DR) needed to achieve the ultra-low emittance (vertical of 2 pm) required. In this framework, three areas of study have been identified: developing methods to suppress the electron cloud instability and its impact on ultra-low emittance beams, undertaken mainly at the Cornell Electron-Positron Storage Ring Test Accelerator (CersTA); the demonstration of the ultra-low vertical emittance operation; and the demonstration of fast injection/extraction system undertaken in ATF.

The main parameters of these facilities are summarized in Table 1.3.

Parameters	Unit	CLIC	CLIC	ILC
Center-of-mass-energy, E_{CM}	[GeV]	500	3000	500
Luminosity, L	[$cm^{-2}s^{-1}$]	2.3×10^{34}	5.7×10^{34}	1.8×10^{34}
Repetition rate, f_{rep}	[Hz]	50	50	5
Bunch length, σ_z	[μm]	70	44	300
Number of bunches per train, N_b		354	312	1312
Acceleration gradient, G_a	[MV/m]	80	100	31.5
Charge per bunch	[nC]	6.8	3.72	3.2
Beam size at IP, σ_x^*/σ_y^*	[nm]	200×2.26	45×1	474×5.9

Table 1.2: ILC and CLIC main parameters.

Facility	Purpose	Host lab
XFEL [29]	Main Linac/SC	DESY (Germany)
STF at KEK [30]	Main Linac/SC	KEK (Japan)
Accelerator Test facility (ATF) [31]	Damping Ring	KEK (Japan)
Cornell Test Accelerator [32]	Damping Ring	Cornell (USA)
Accelerator Test Facility 2 (ATF2) [10]	Beam Delivery System	KEK (Japan)

Table 1.3: ILC test facilities around the world.

ILC collimation system

The ILC collimation system is located after the diagnostic section in the BDS. First, we have the betatron collimation system and after, in a region with horizontal disper-
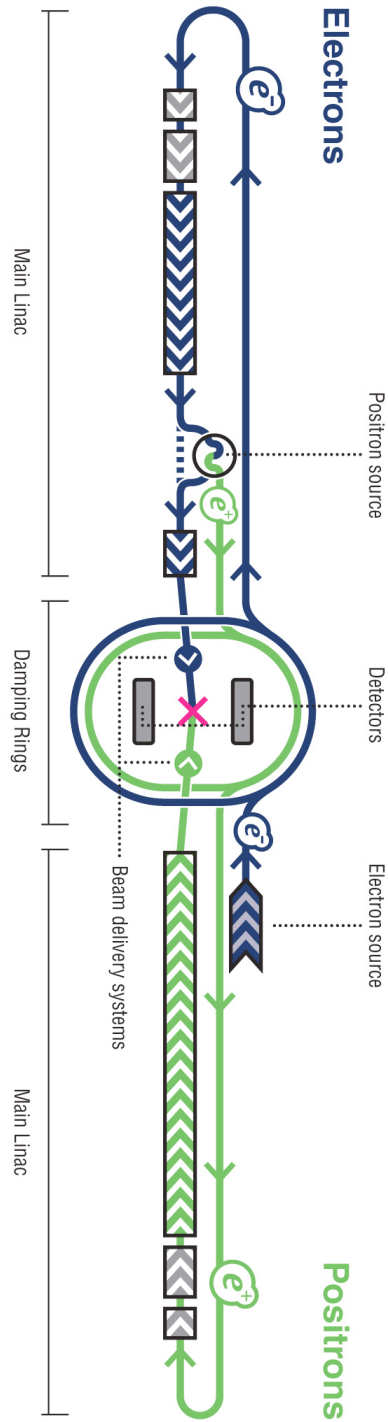
Figure 1.17: ILC schematic layout.
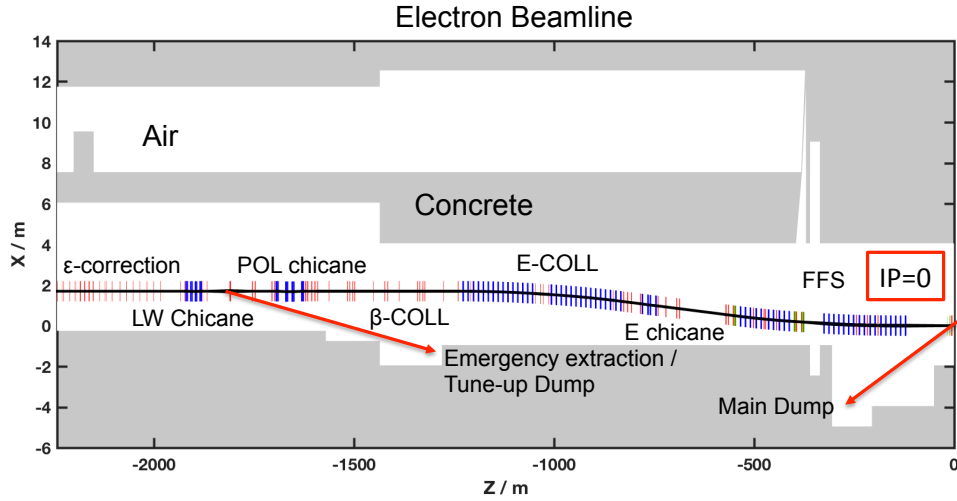
Figure 1.18: ILC tunnel layout of the BDS.

sion, the energy collimation system as it is illustrated in Fig. 1.19.

As explained in the first section of this chapter, the **betatron collimation depth** of the betatron collimation system is determined from the condition that the SR must pass through the IR without being intercepted by the components in this region. An scheme of the IR is shown in Fig. 1.20 where the last two betatron spoilers and the energy spoiler are depicted. In order to satisfy this condition the required betatron depth estimated **for a 500** GeV **center-of-mass-energy and** $L^* = 4.5$ m and 2 $mrad$ crossing angle configuration (distance between the FD and the IP) is **18** σ_x **(horizontal plane) and 87** σ_y **(vertical plane)** [**?**]. Different L^* values are being studied for the FFS of the ILC and each configuration requires a different collimation depth. More information can be found in recent studies at [33]. The betatron collimation system is formed of four pairs of spoilers/absorbers (two in phase ($n\pi$) with the FD and the other two in phase ($n\pi$) with the IP) with a minimum half aperture of 0.3 mm in the vertical plane and 0.4 mm in the horizontal one. In Table 2 of the Appendix 2 the design optics and geometry values for the ILC collimation systems jaws are shown. These values have been taken from the last lattice version ILC2015b for the nominal beam energy of 500 GeV.

The **energy collimation depth** for ILC is **estimated to be about** $\pm 1 - 1.5\%$, which means that the energy collimation system has to absorb beam particles with an energy $\pm 1 - 1.5\%$ different with respect to the nominal one. This value ensures that miss-steered beams will hit the energy spoilers or will pass all the way thought the IP without impacting on the betatron collimation system and other geometric apertures in the beamline for all the cases studied. The minimum half aperture of the energy collimation system is 3 mm and in Table 2 of the Appendix 2 the design ILC optics and geometry values for the jaws are reported for the 500 GeV scenario.
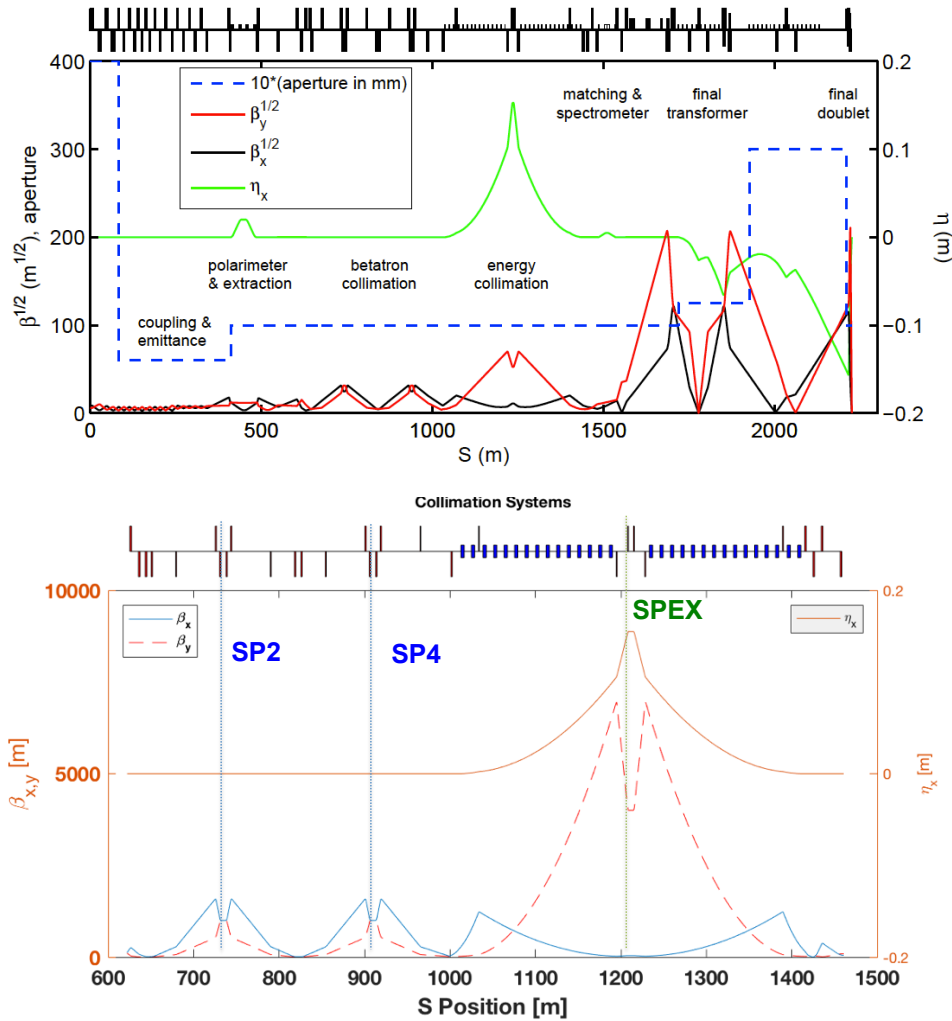
Figure 1.19: ILC optics of the BDS (top) and zoom of the collimation section (bottom).

ILC collimation system wakefield issues

Beam halo collimation is a trade off between efficiency and wakefields. Some studies have been done in order to evaluate the wakefield impact of the ILC collimation system based on analytical models [34] and tracking simulation codes [35]. However, the parameters of the ILC collimation systems in some cases sit close to the applicability limits of the analytical models in the case of geometric wakefields. Benchmarking between models and simulations (numerical and tracking) is essential to refine the ILC collimation system design. Experiments were made in End Station B to study the impact of the geometry and materials of the rectangular jaws on the induced wakefields [36–39]. In these experiments discrepancies between models and measurements of about a factor 2-3 were observed for some jaw geometries. These experiments gave quantitative information about how to reduce the wakefield effect of a collimation system by tapering the structure and minimizing the angle and flat part however
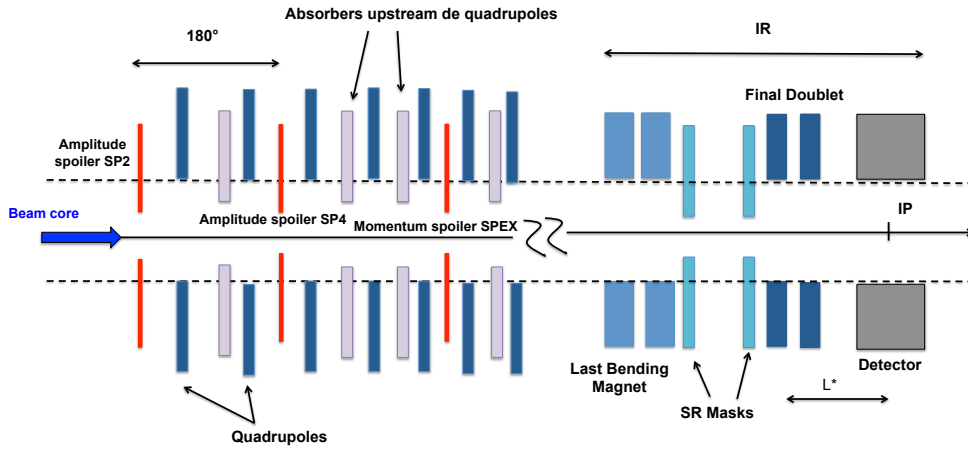
Figure 1.20: ILC collimation system concept scheme.

benchmarking between theoretical models and measurements for rectangular tapered jaws is at the level of a factor 2 difference in some cases. The results of these experiments were used to draw a first preliminary mechanical design of a collimation system prototype for the ILC [40]. For a more accurate estimation of the wakefield impact of such a device, it is crucial to perform benchmarking studies between analytical calculations, simulations and measurements.

The main subject of this thesis consists in the study of a collimation system designed and installed in the ATF2 facility with a mechanical design inspired by a preliminary design for the ILC spoilers. A detailed wakefield study of the rectangular collimation system has been performed by means of analytical calculations and 3D EM simulations. Furthermore, the impact on the beam dynamics has also been studied using the tracking code PLACET and the linear transport of the kick calculated with the EM solver CST PS [6, 41, 42]. Some discrepancies were observed when comparing the results of these two methods to evaluate the impact of the wakefields induced by the collimation system on the beam dynamics. The source of the discrepancies was further investigated and the problem fixed in a new version of the tracking code PLACET [43]. Furthermore, the wakefield impact has been measured experimentally and compared with analytical calculations and numerical simulations. The work in modeling and measuring the wakefield effect and the discussion of the results will contribute to the understanding of the applicability of the tools used. These results have to be scaled to the ILC scenario and the study of its implications will be crucial for the ILC collimation system design.

1.4.2   Compact Linear Collider (CLIC)

The aim of CLIC is basically the same as ILC but in the 0.5 to 3 TeV energy range. The CLIC study is focused on the design of a LC with a colliding center-of-mass energy of 3 TeV and a luminosity of 2×10^{34} $cm^{-2}s^{-1}$ by developing a novel technology of Two Beam Acceleration (TBA) based on normal conducting travelling-wave accelerating structure. The CLIC accelerator complex is based on a two beam scheme, where the necessary power for acceleration of the main beam is provided by the deceleration

of a high-intensity second electron beam, the drive beam, which runs parallel to the main beam. The power is transferred to the main beam by Power Extraction Transfer (PET) structures. CLIC consists of two main high energy LINACs to accelerate the particles from $9\,GeV$ to $1.5\,TeV$, the drive beam system (parallel to the main beam), the BDS to prepare the high energy beams for collision, an electron and positron injector system and the corresponding dumping system. CLIC is supposed to operate at a frequency of $12\,GHz$ and with very high electric gradient of $100\,MV/m$ to keep the total length about $48\,km$. The scheme of the CLIC layout is shown in Fig.1.21 and the main beam parameters are shown in Table 1.2. More information about CLIC can be found in [3]. Two facilities have been built at CERN aiming to demonstrate the feasibility of the CLIC working principle and related technology and instrumentation as summarized in Table 1.4. The CLIC Test Facility CTF3, built at CERN by an international collaboration, aims at demonstrating the feasibility of the CLIC scheme of multi-TeV e+e- linear collider. It is meant to demonstrate the technical feasibility of the key concepts of the novel CLIC RF power source, e.g., generation of high-charge, high-frequency electron bunch trains by beam combination in a ring using transverse RF deflectors and operation with a fully-loaded drive-beam accelerator. CTF3 will also be used to test CLIC critical components and in particular will provide the $12\,GHz$ RF power needed to test the main beam accelerating structures at the nominal gradient and pulse length ($100\,MV/m$ for $140\,ns$). As result of this work the Conceptual Design Report was published in October 2012. Furthermore, the XBOXs have been built in order to test and perform R&D of warm RF technology.

Facility	Purpose	Host lab
CTF3 [44]	Two beam acceleration technique and instrumentation	CERN
XBOXs [45]	Main Linac/warm	CERN

Table 1.4: CLIC test facilities.

CLIC collimation system

In the CLIC collimation baseline the betatron collimation is located after the energy collimator. This configuration is the main difference between the ILC and CLIC collimation system design and this is due to the fact that in CLIC the miss-steered energy beams due to failures in the acceleration system are expected to be more frequent. Therefore, in this case, the energy collimation system is placed after the diagnostic section in an area of non-zero dispersion and the betatron one is placed as it is illustrated in Fig. 1.22. The **betatron collimation depth** of the betatron collimation system is determined from the condition that the particles goes trough the IR without creating SR. In order to satisfy this condition the required betatron depth estimated for **a 3000** GeV **center-of-mass-energy** is **14** σ_x **(horizontal plane) and 83** σ_y **(vertical plane)**.The betatron collimation system design is formed of four pairs of spoilers/absorbers (two in phase ($n\pi$) with the FD and the other two in phase ($n\pi$) with the IP) with a minimum half aperture of $0.1\,mm$ in the vertical plane and $0.1\,mm$ in the horizontal one.
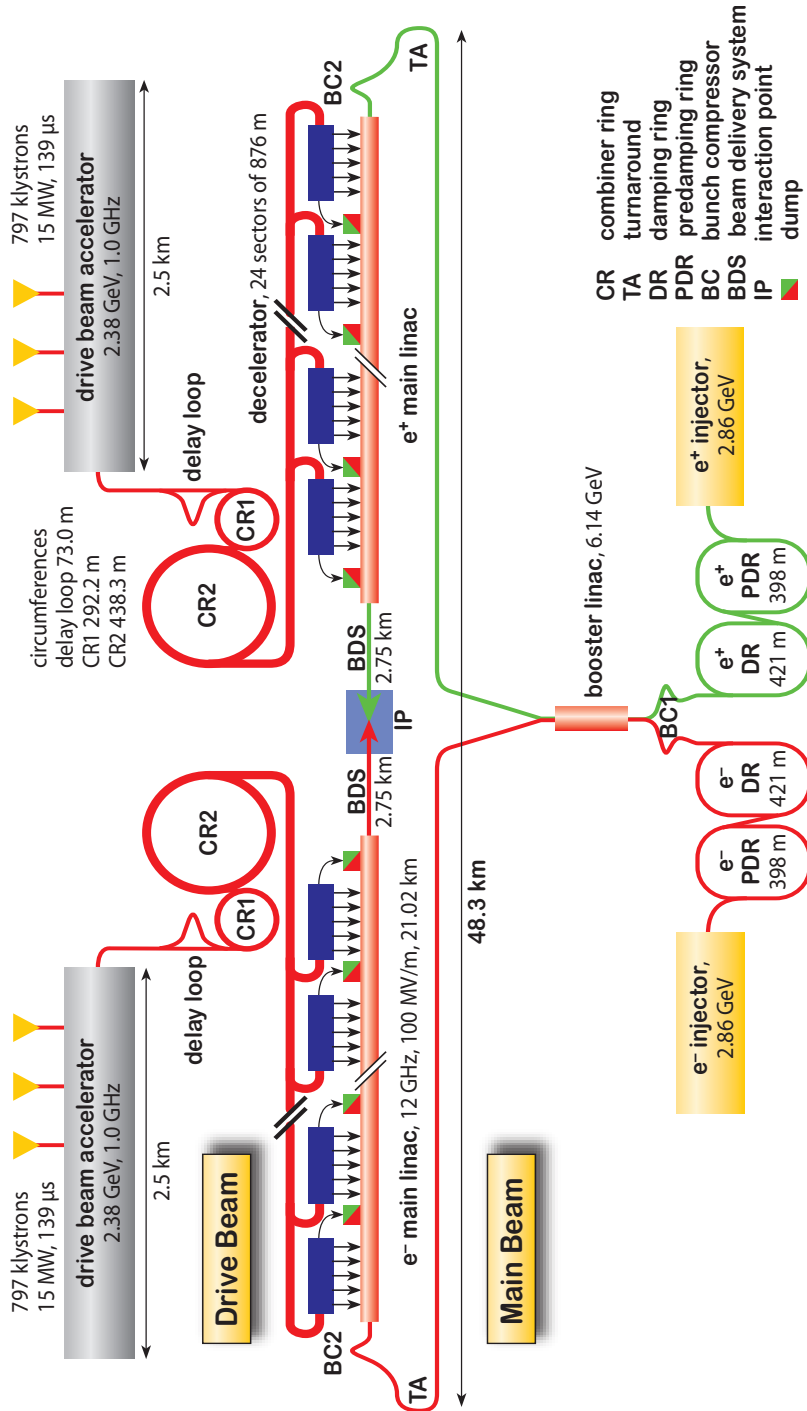
Figure 1.21: CLIC schematic layout.

More information can be found in [46]. The **energy collimation depth** for CLIC is estimated to absorb particles with an energy spread of **about** $\pm 1 - 1.5\%$. This value ensures that miss-steered beams will hit the energy spoilers or will pass all the way thought the IP without impacting on the betatron collimation system for all the cases studied. The minimum half aperture of the energy collimation system is 3.5 *mm*. The design optics and geometry values for the CLIC collimation systems jaws are shown in Table 3 of the Appendix 2.

CLIC collimation systems wakefield issues

As for the ILC collimation system, the collimation system's wakefield impact has to be carefully studied. The studies being performed for the ILC collimation system regarding analytical models, simulations and measurements benchmarking are also useful for the understanding of the CLIC collimation case. However, one has to take into account the CLIC beam parameters, as the energy and bunch length will lead to higher wakefields. Some first calculations can be found in [47].
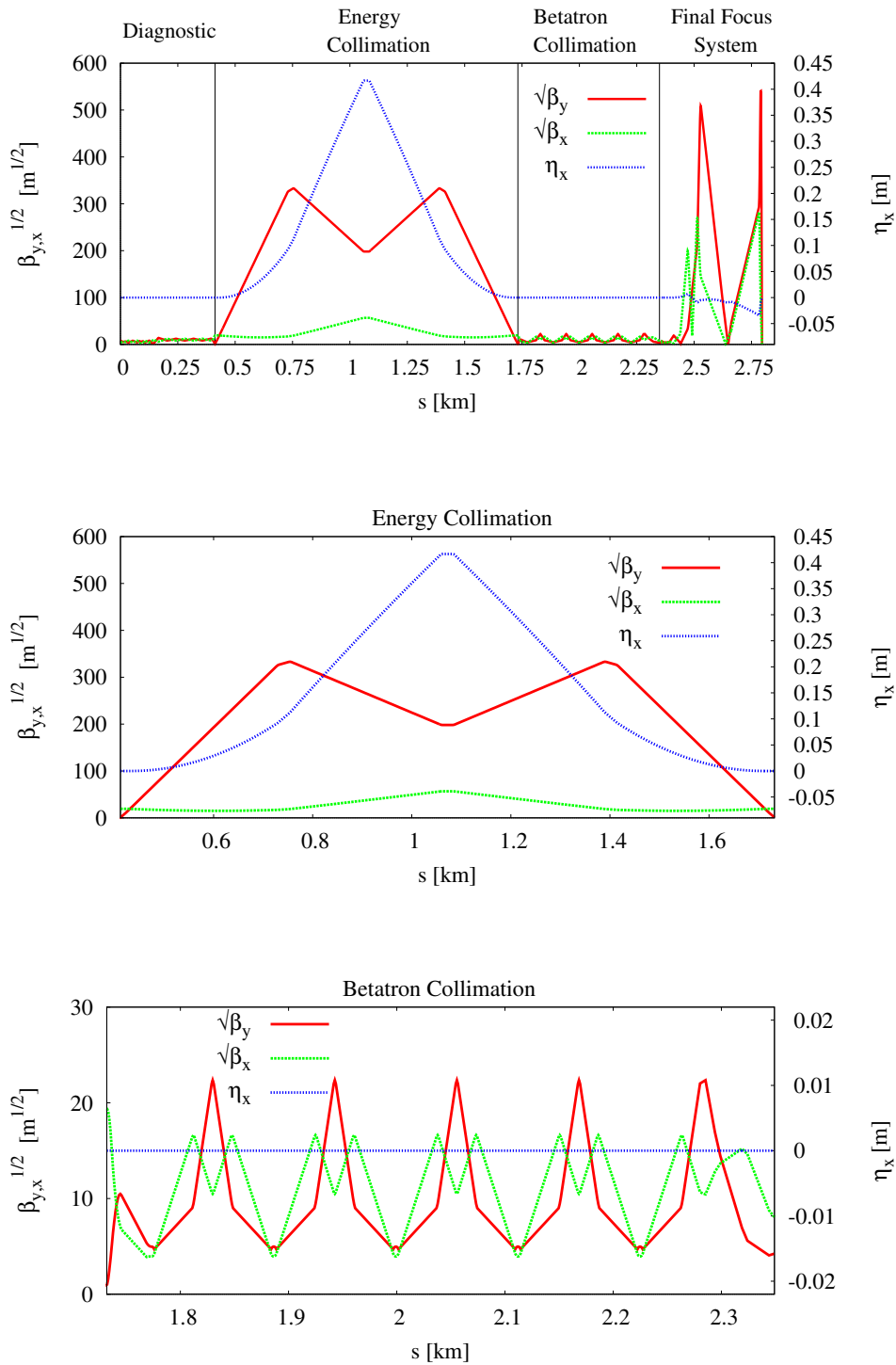
Figure 1.22: CLIC BDS optics for the complete BDS (top), energy collimation section (middle) and betatron collimation section (bottom) for the 3 TeV scenario and $L^* = 4.3$ m (nominal one).

Chapter 2

Optics, tracking simulations and efficiency studies of beam halo collimation at ATF2

2.1 Introduction

The ATF facility [31] at KEK was built in order to create electron beams satisfying the ILC requirements with very small emittances. The ATF accelerator has been successfully operated and has a world record in creating small emittance beams of high quality in both, single and multi-bunch operation modes. The typically measured emittance is of 2 *nm rad* × 12 *pm rad*, horizontal and vertical, respectively. The ATF facility was extended to include an extraction beamline with an ILC-type FFS in 2005 [10]. At the ATF2, there was initially no real collimation system for the beam halo, although physical apertures at various locations along the beamline could intercept some of it. The main subject of this thesis consists in the study of a dedicated beam halo collimation system for the ATF2 with the main goal of reducing the background photons in the IP and post-IP region. Betatron and energy collimation have been studied. The effectiveness of the collimation system has been studied by means of tracking simulations and loss map studies. At the end of this section, the results of these studies are discussed and the most efficient collimation solution proposed.

2.2 ATF/ATF2 test facility

The ATF accelerator facility (see Fig. 2.1) uses an S-band RF gun to generate the electron beam. Then, the electron beam is accelerated in an S-band linac to 1.3 *Ge*V and injected into the DR which has a circumference of 140 *m* where the small emittances are achieved. In normal operation mode, the beam is extracted from the DR and delivered to the Extraction Line (EXT) with 1.6 *nC* charge at 3.12 *Hz* and typically measured emittance of 2 *nm* rad × 12 *pm rad* in the horizontal and vertical, respectively. The ATF2, following ATF, is divided into 3 sections. First, we have the EXT line with the diagnostics where the beam is measured and prepared for being driven

into the FFS. The FFS forms the second section starting with the matching quadrupoles followed by the optics that focus the beam into the IP. The last section is the Post-IP where some diagnostics are located. The ATF2 beamline contains seven dipoles, three septa, 49 quadrupoles, five sextupoles, four skew sextupoles, 25 corrector magnets and two recently installed octupole magnets [48]. The basic layout of the ATF2 facility is shown in Fig. 2.2.

2.2.1 ATF2 goals and recent achievements

The ATF2 facility was built with the following two main goals:

- **Goal 1**: Optics design validation of the FFS local chromaticity correction scheme and achievement of a vertical beam size at the IP of 37 *nm*.

- **Goal 2**: Nanometer beam stabilization including hardware and beam handling technologies development.

The ATF2 facility is a continuation of the successful work archived at the Final Focus Test beam (FFTB) at SLAC built in 1993, where a 70 *nm* vertical beam size was measured [49,50]. The experience at the FFTB provided crucial progress on the knowledge of the factors that limit the smallest beam size we can make in a stable and reliable manner. Following the research performed in the FFTB, ATF and ATF2, were built to continue on the research to establish the technologies associated with producing very small emittance beams. At the ATF2, the design and operation of the FFS local chromaticity correction scheme have been successfully tested for the first time [51]. Furthermore, all the work being done in the ATF2 is providing more experience on the operation and stabilization of nanometer beams and the required hardware and correction techniques.
The tunability of the nanometer beam has been intensively studied at the ATF2. The FONT (Feedback On Nano-second Timescales) project was set up to research, design and test an intra-train beam-based feedback system to achieve and maintain nanobeam collisions, and therefore high luminosity, at FLCs. This feedback system is being tested and developed at the ATF2 aiming for the reduction of the orbit jitter to the *nm* level. Recently, the feedback system using 2 stripline Beam Position Monitors (BPMs) and 2 kickers resulted in a 600 *nm* level beam stabilization [52]. Using one Cavity-BPM (C- BPM) and one kicker the system stabilizes the beam at the level of 75 *nm* [53]. In addition, non linear knobs have been implemented in the tuning procedure in order to control and optimize non linear effects. All this effort has resulted in the demonstration of the new local chromaticity correction scheme and a 44 *nm* vertical beam size measured at the IP. A summary of the history on the minimum vertical beam size measured is shown in Fig. 2.3 (top) and the repeatability along 3 days of ATF2 operation in April 2014 (bottom) [54].
Furthermore, there are other on-going *R&D* accelerator projects at the ATF2, including very low-β studies for CLIC [55], ground motion feedback studies [56], beam halo control, measurement and modeling [57] and the development of a new ODR/OTR diagnostic station with resolution down to a few μm [58].
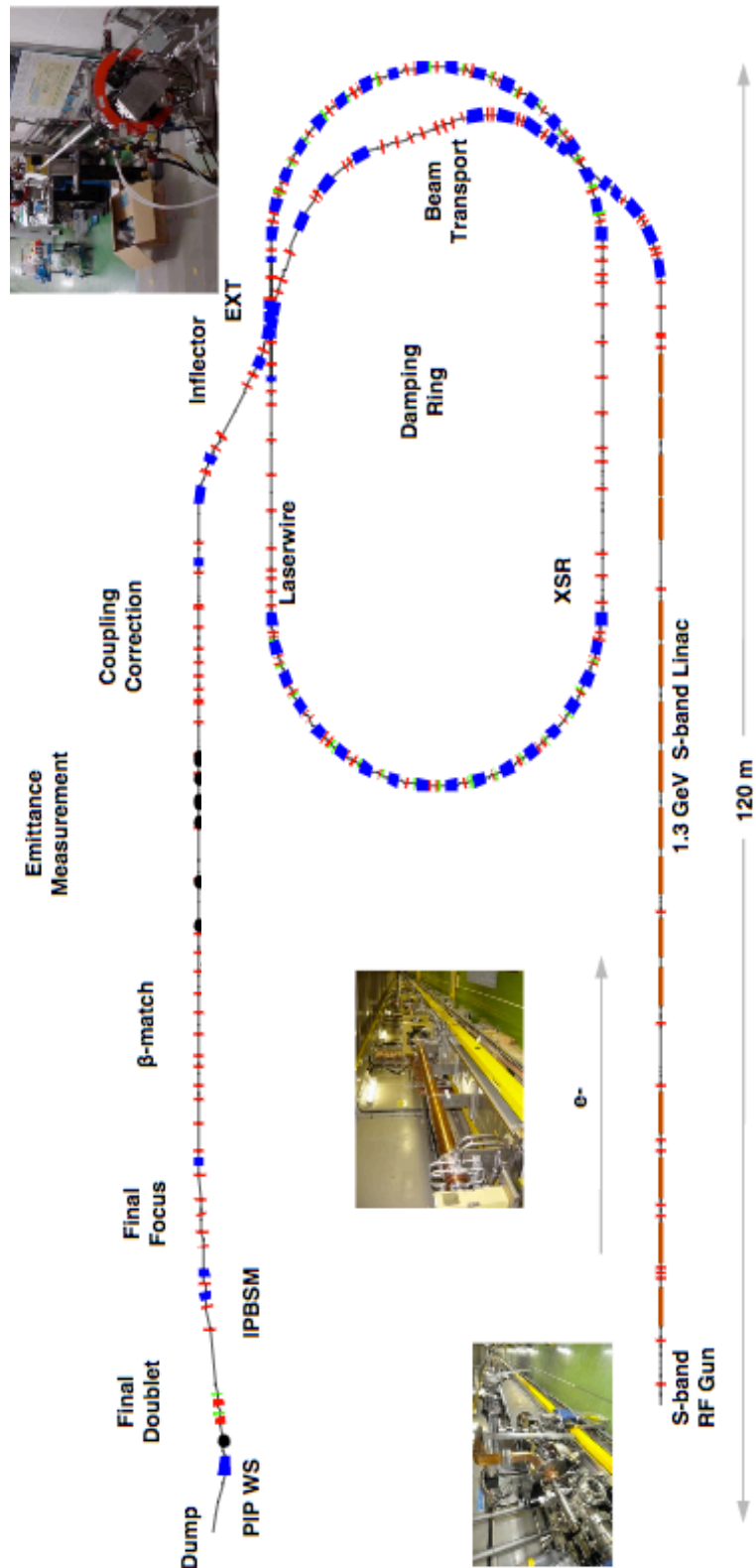
Figure 2.1: ATF accelerator facility.
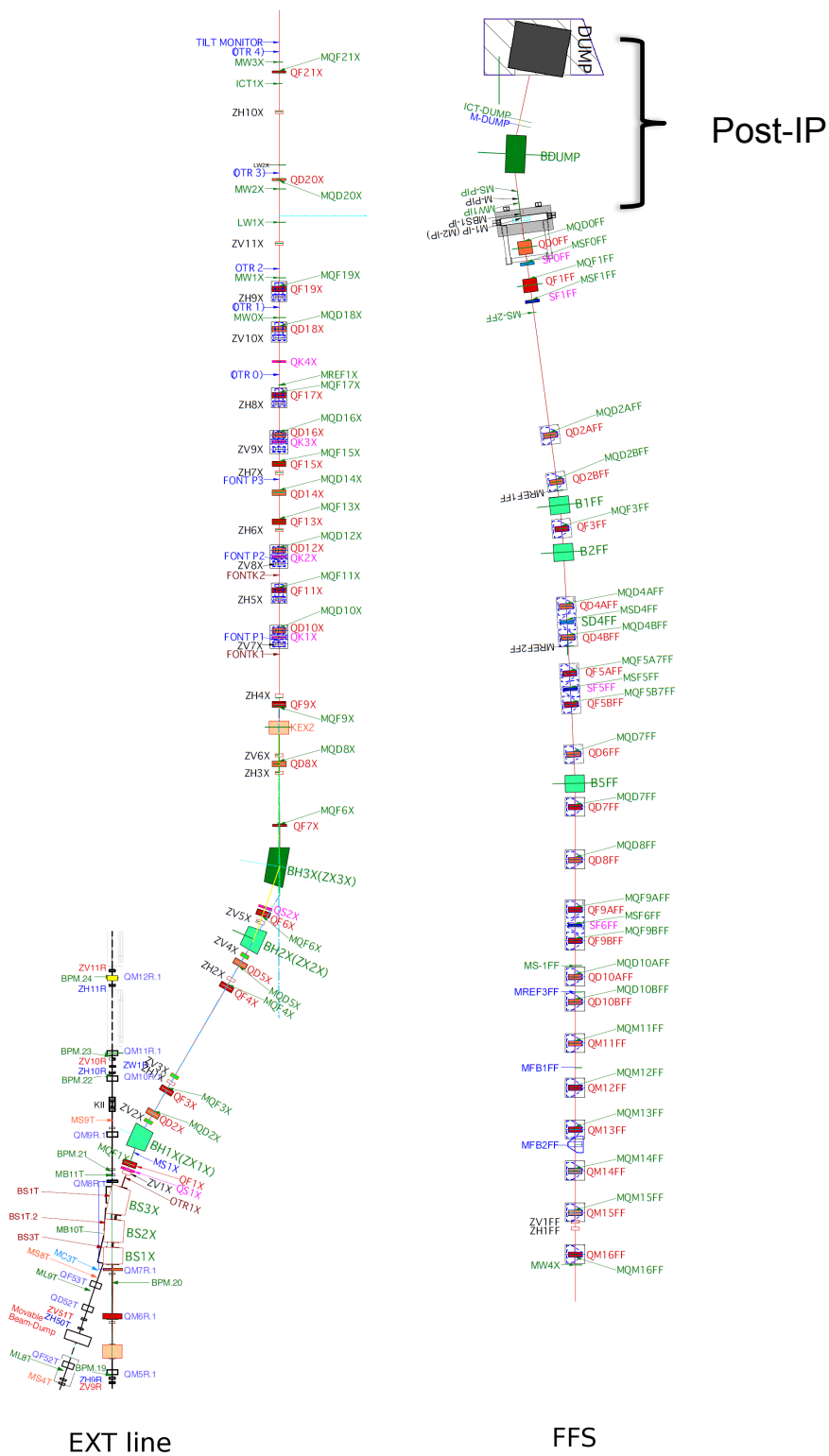
Figure 2.2: ATF2 layout with the EXT line (left), the FFS and the Post-IP (right) sections.
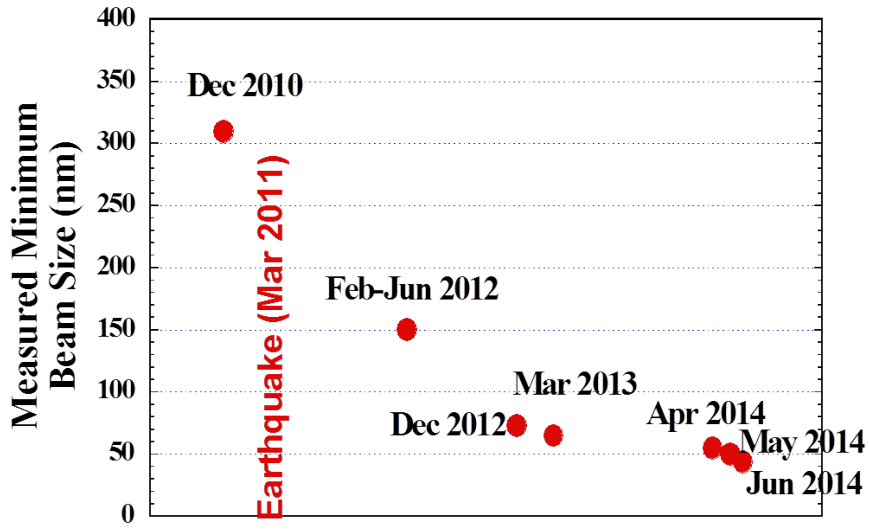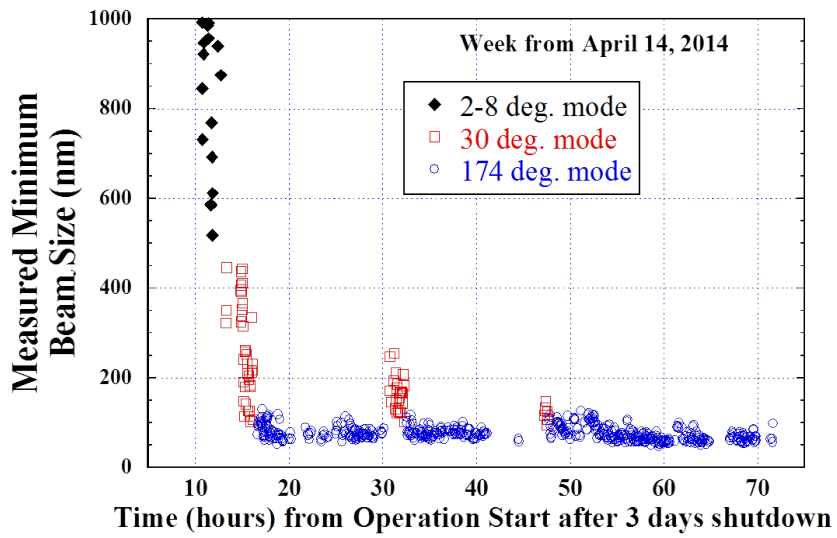
Figure 2.3: ATF2 minimum vertical beam size measurement history (top) and repeatability along 3 days of ATF2 operation in April 2014 (bottom).

ATF2 and ILC FFS comparison

The FFS of the ATF2 facility was built to be similar to the ILC FFS. Despite the difference on the electron beam energy between the ILC and the ATF2 they have some features in common which are being evaluated in the ATF2. The natural chromaticity and relative beam energy spread are similar for both machines and the proposed chromaticity correction scheme for ILC was implemented in the ATF2 and successfully tested. Furthermore, most of the magnetic tolerances, jitter vibration and power supply stabilization are comparable when the ATF2 machine is operated at 10 times the nominal β_x^* and the nominal β_y^* at the IP ($10\beta_x^* \times 1\beta_y^*$) [59]. Another common feature is the required beam monitor position resolution for beam stabilization at the *nm* level for both accelerator machines. The comparison of the main beam parameters between the ATF2 and the FFS of the ILC are summarized in Table 2.1.

Name	ATF2	ILC	Units
Beam energy, E	1.3	500	[GeV]
Bunch population, N_b	$1\ 10^{10}$	$1-2\ 10^{10}$	
Bunch length, σ_z	7	0.3	[mm]
Energy spread, σ_ϵ	0.08	0.07	[%]
Normalized emittance, $\gamma\epsilon_{x,y}$	5/0.03	10/0.035	[μm.rad]
$\beta_{x,y}^*$	4/0.1	11/0.48	[mm]
$\sigma_{x,y}^*$	9000/37	474/5.9	[nm]
Natural vertical chromaticity, ξ_y	10000	9400	

Table 2.1: ATF2 nominal beam parameters in comparison with the ILC FFS ones for the ($10\beta_x^* \times 1\beta_y^*$) optics.

Some aspects make the ATF2 operation more difficult than the ILC one, as for example, the development of a diagnostic device for measuring the *nm* vertical beam size at the virtual IP. In the ATF2 a monitor with *nm* resolution has been developed while in the ILC the beam-beam collisions could be used. In addition, the ATF2 bunch length is about 7 *mm*, which is much longer than the ILC design value and this restricts the low resonant frequency needed for the C-BPMs to work properly. Furthermore, the ATF2 building is not underground and its performance is more sensitive to temperature fluctuations and ground motion. A ground motion feed-forward feedback is being investigated, aiming at reduction of the beam jitter caused by the dynamic displacement of the quadrupoles. A high correlation between the position of the sensor and beam motion has been archived by mounting the sensors directly on the quadrupoles and using high-pass filtering. The success of the ground motion feedback system development will be important for ILC FFS [56] in which the effect will be severe due to its longer FFS.

In the contrast, there are some aspects crucial for the good performance of the ILC that can not be evaluated at the ATF2, such as, the time variation beam effects and wakefields coming from the linac since the ATF2 linac is much shorter than the ILC one.
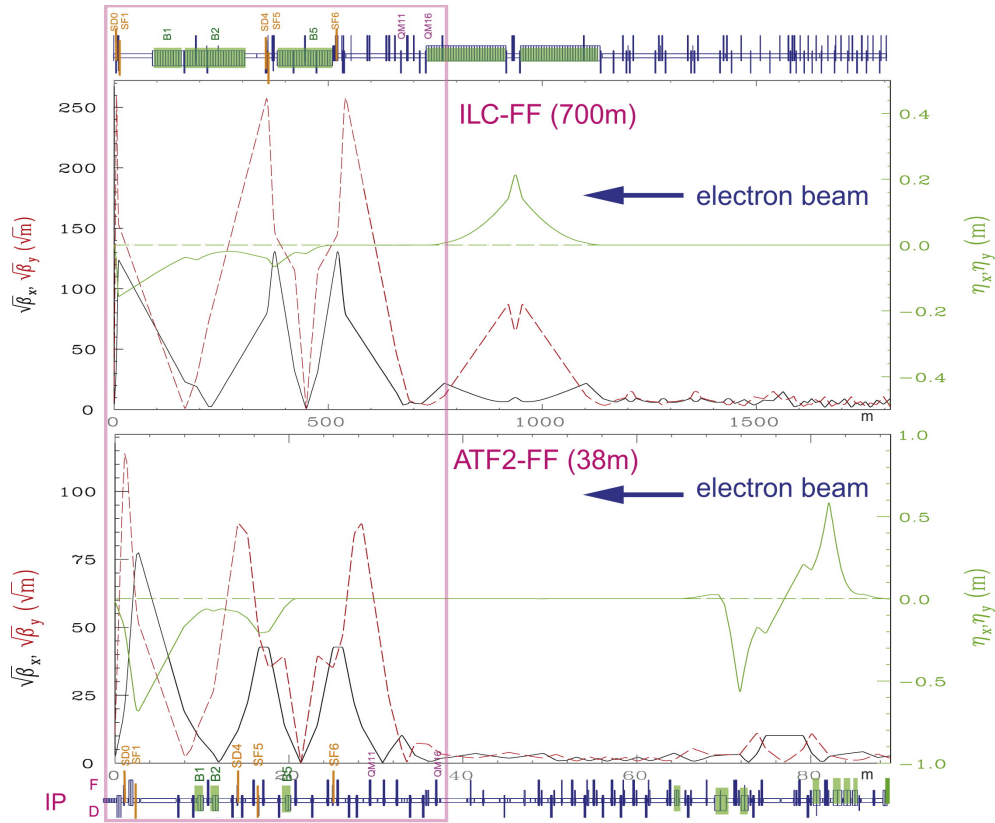
Figure 2.4: ATF2 and ILC FFS optics comparison. The different optic elements are depicted: the dipole magnets (in green), the quadrupoles (in blue), the sextupoles (in yellow) and the matching quadrupoles (in pink).

2.2.2 ATF2 diagnostics

One important contribution to the success of the ATF2 performance and also part of its R&D program is the research of the state-of-the-art diagnostics applicable for FLCs. Diagnostic devices have been developed and optimized to satisfy the ATF2 requirements, such as, the beam size monitor to measure the nanometer vertical beam size at the IP (the Shintake monitor) and the very precise beam position monitors and feedback system (BPMs system and FONT). In addition, in the ATF2 a multi-OTR system was installed in the EXT line for emittance and coupling measurements as well as a Post-IP wire scanner for beam size measurements. There is some further R&D instrumentation recently installed, such as, two Diamond Sensors (DSs) for beam halo measurements in the Post-IP, and a new ODR/OTR station for beam size measurements installed in the FFS with lower resolution than the OTR system installed in the EXT line. In the following, we will describe the basics of these devices.

Shintake monitor (IPBSM) [60, 61]

The first Shintake monitor tested was built and operated at the FFTB at SLAC [50]. An improved unit was installed in the ATF2. This monitor is based on the measurement of

the photons produced by the interaction of a fringe laser pattern with the electron beam. The Compton photons generated in this interaction are detected in an downstream gamma monitor. The beam size can be inferred from the number of Compton photons measured by moving the laser fringe pattern showing a modulation of photon counts. This modulation measured is defined as:

$$M = \frac{N_{max} - N_{min}}{N_{max} + N_{min}} \tag{2.1}$$

where N_{max} is the maximum number of photons measured and N_{min} the minimum number of photons measured. The relation between the modulation and the vertical beam size is the following:

$$\sigma_y = \frac{1}{k_y} \sqrt{\frac{1}{2} ln \left(\frac{C |\cos \theta|}{M} \right)} \tag{2.2}$$

where θ is the laser crossing angle, C is a correction factor (taking into account the error sources inherent to the IPBSM monitor) and $k_y = \pi/d$ is the wavelength of the laser where d represents the fringe pitch determining the beam size range that can be measured (see Fig. 6.25 bottom) defined as:

$$d = \frac{\lambda}{2 \sin(\theta/2)} \tag{2.3}$$

where λ is the laser wavelength.

The monitor consists in a laser mounted on a complex optic table (see Fig. 6.25 top and middle) that guide the laser towards the electron beam and allows you to change the crossing angle of interaction between the laser and the beam.

This monitor has three different operation modes made by adjusting the crossing angle between the interfering laser and the beam: 2° to 8° (continuously variable), 30° and 174°. This allows us to measure of the vertical beam size from a few micrometers to a theoretical minimum value of 20 *nm* respectively (see Fig. 6.25 bottom). The gamma detectors are located after the last bending magnet (BDUMP) that separates the photons from the electron beam. First a CsI detector was used until recently a new detector based on the Cherenkov phenomenon was installed in order to be used in a multi-bunch operation mode due to its faster response. The two IPBSM detectors available are:

- **IPBSM CsI detector**

  This gamma detector is made of CsI(Ti) scintillator divided up into four 40 *mm* layers and a large 290 *mm* back bulk layer. Incident photons are transformed into scintillation light which enters the Photomultipliers (PMTs) coupled to each layer. This multi-layer design separates signal and background by taking advantage of their difference on the energy spectrum (15 *MeV* for signal vs 53 *MeV* for background). Furthermore, in order to increase the signal to noise ratio photon collimators are installed in front of the detector to reduce the background photons that could be generated in the Post-IP region (this is explained in more detail in the next section, see Fig. 2.16).
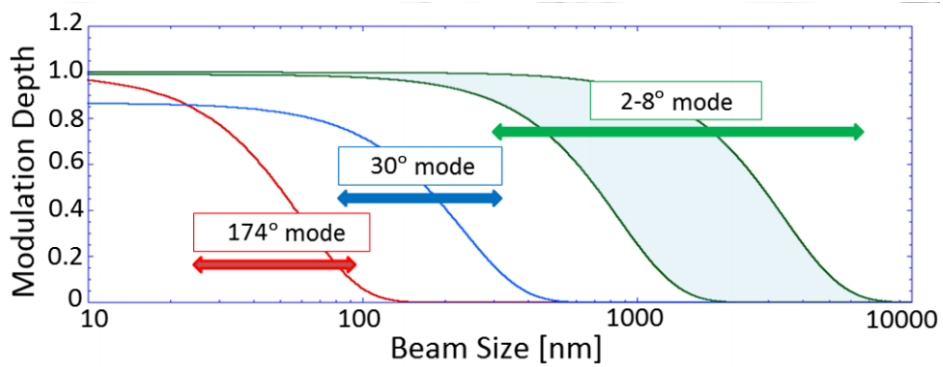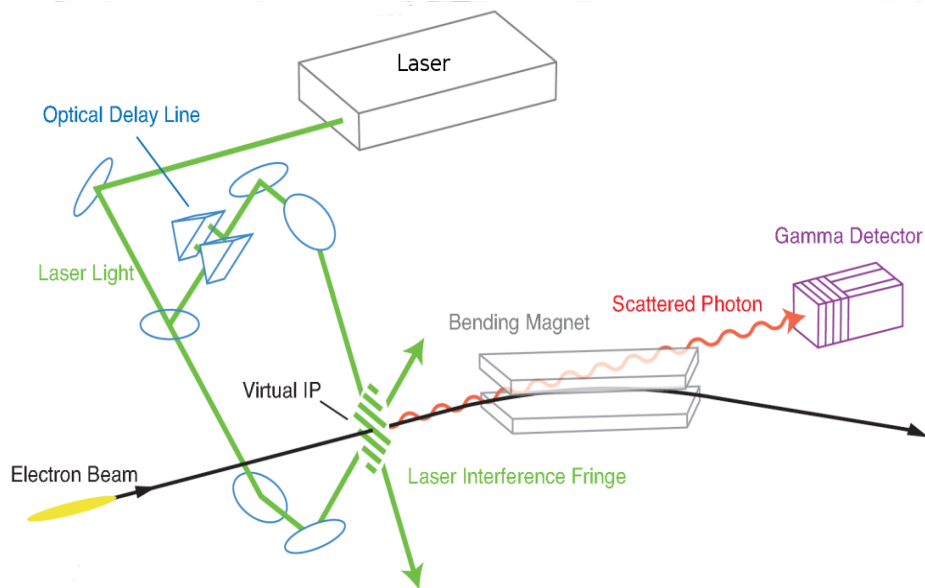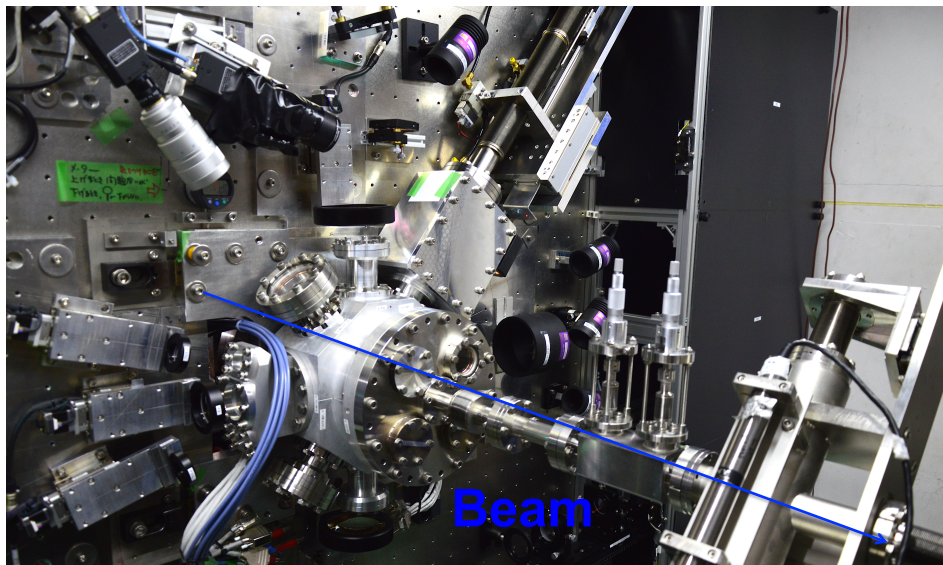
Figure 2.5: Real optic table (top), IPBSM scheme (middle) and modulation depth as a function of beam size for the three different IPBSM operation modes (bottom).

- **IPBSM Cherenkov detector**
  This detector is an upgrade of the CsI (Ti) detector developed to operate in the ATF2 two-bunch operation mode. This monitor was installed in 2015. This detector has a faster response and uses the light emitted when a charged particle passes through a material with a velocity greater than the phase velocity of the light traveling in this material.

BPM system

In the ATF2, the beam orbit is monitored with different BPMs based on different technologies that we will describe in the following:

- **Stripline BPMs** [62]
  Fig. 2.6 shows a typical stripline BPM, which consists of four metal strips or pick-ups connected to wires that extend outside the structure and are grounded. If the beam does not pass through the center of the monitor, there is a potential difference generated between the strips. This signal allows us to determine the offset of the beam. Three stripline BPMs are located in the EXT line with a resolution of 300 *nm* for a bunch charge of 0.5×10^{10} electrons (see Fig. 2.9). These BPMs are part of the FONT system, which will also be described in more detail in this section. In addition there are other 10 stripline BPMs used to measure the orbit in the EXT line.
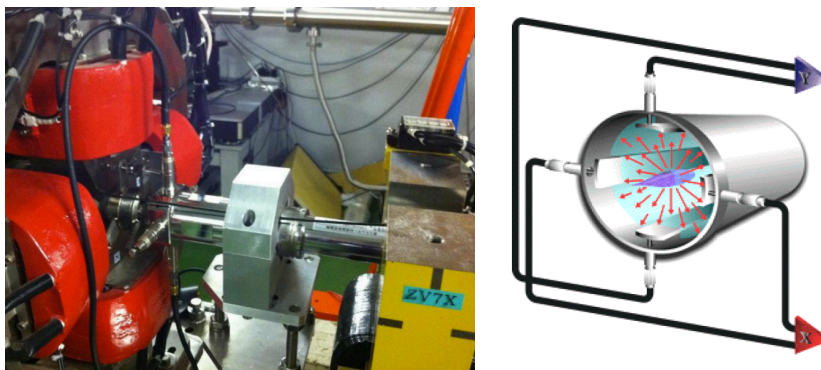
Figure 2.6: Stripline BPM installed in ATF2 (left) and principle scheme (right).

- **Cavity BPMs** [63]
  A cavity BPM is based on the induced EM fields within a resonant cavity when the beam passes trough. The cavity is designed to resonate at the bunching frequency of the beam. There are a large number of modes at which the EM fields within the cavity can resonate, the magnitudes of each of these modes of oscillation depend on a number of factors, including beam trajectory and the dimensions of the cavity. The two most important modes for beam position measurements are the monopole mode and the dipole mode. A cross-section of a cavity BPM showing the electric fields for the TM010 (monopole) and TM110 (dipole) modes is shown in Fig. 2.7 (right). The fundamental mode driven by
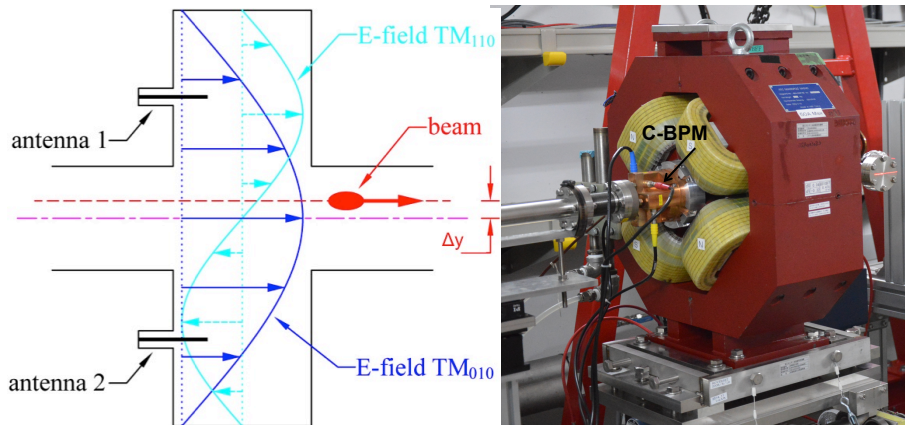
Figure 2.7: C-BPM concept (left) and real system mounted in the ATF2 beamline
(right).

the bunched beam within the cavity is the monopole mode. However, from the
point of view of a beam position measurement, the mode of choice is the dipole
one. The amplitude of the dipole mode depends linearly on the transverse beam
offset from the cavity center, and it is zero for a beam centered within the cavity.
By contrast, the monopole mode is excited most strongly for a centered beam
and has no such linear amplitude dependence. Therefore, one usually designs
the cavity to be able to couple out the dipole mode whilst ignoring or damping
out the monopole mode. This can be done, for example, by using a filter with a
narrow bandwidth on the output to select only the frequency of the dipole mode.
Then, the signal could be measured by using an antenna. A scheme of a C-BPM
can be seen in Fig. 2.7 (left). In Fig. 2.9, the locations of the thirty seven C-
band and four S-band BPMs in the ATF2 are depicted. From the thirty seven
C-BPMs, five C-BPMs ($MREF1X$, $MREF1FF$, $MREF2FF$, $MREF3FF$ and
$MFB2FF$) are operated in the monopole mode which is charge dependent in or-
der to normalize the measurements of the the other BPMs charge independent.
The cavity BPMs are attached to the quadrupoles and are labeled with the name
of the quadrupole plus a prefix M. Notice that in the ATF2 the quadrupoles are
named as Q(D/F)N(FF/X), where D indicates defocusing in the horizontal plane,
F is focusing on the horizontal plane, FF refers to the FFS, X refers to the EXT
line and N is an integer number. The C-BPMs are design to operate using the
dipole mode (TM_{110}) with a corresponding working frequency of 6.422 GHz.
The S-BPMs work with the same dipole mode but at 2.888 GHz. The C-BPMs
have circular geometric aperture with a half radius of 10 mm. These apertures
are one of the smallest apertures in the beamline. These devices introduce a sig-
nificant wakefield impact that has been carefully studied in the ATF2, including
measurements and simulations [64, 65].

- **IPBPMs** [66]
  In the IP region, three rectangular cavity BPMs were installed in order to mea-
  sure the beam trajectory in the IP region with nm precision, for tuning and feed-
  back system development. The system consists in three cavities installed inside

a vacuum chamber fixed to the IPBSM optical table. Inside, two blocks are separated: one before the IP (with two BPMs named as IPA and IPB) and a second block with the third BPM (named as IPC) after the IP. These cavities resonate in TM_{210} and TM_{120} modes at a frequency of 5.7 GHz and 6.4 GHz in the horizontal and vertical planes respectively. The IPBPM system before (left) and after (right) installing in the ATF2 beamline can be seen in Fig. 2.8.
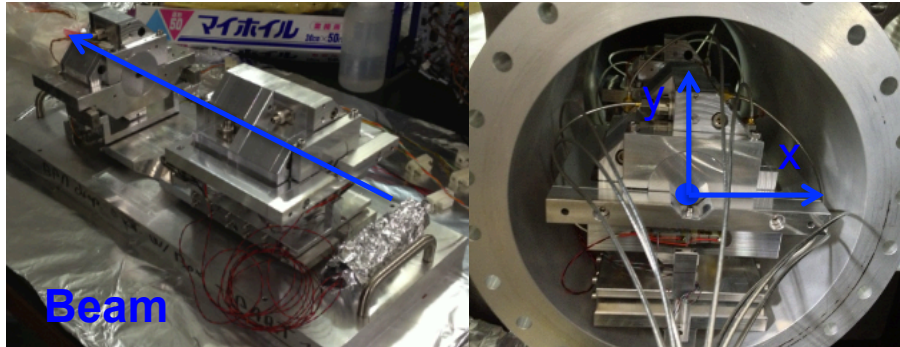
Figure 2.8: IPBPM system before (left) and after (right) installing into the ATF2 Post-IP beamline.

FONT system [52, 53, 67]

The FONT beam-based, intra-train feedback system has been designed to provide beam stability at single-pass accelerators. Two FONT feedback systems have been commissioned at the ATF2 aiming to reduce the orbit beam jitter. The accelerator is operated with two-bunch trains with a bunch separation of around 200 ns. The position of the first bunch is measured with a BPM and the second bunch is corrected by the use of a dipole kicker. The first system consists in two stripline beam position monitors (BPMs) used to characterize the incoming beam position and angle, and two kickers used to stabilize the beam. The location of the BPMs and kickers used by this system are depicted in the right part of Fig. 2.10 corresponding to the ATF2 EXT line. A resolution of about 300 nm has been measured for the stripline BPMs and when operating the feedback system, a factor 3 reduction in position jitter is observed. The second system uses one high-resolution cavity BPM ($IPBPMA/B/C$) with a fast decay time of around 20 ns designed to allow multiple bunches to be resolved. A BPM resolution of about 50 nm has been measured and the IP feedback system has been used to stabilize the beam position to the 75 nm level. The corresponding configuration in the IP region is illustrated in the left side of Fig. 2.10.

Multi-OTR system [68–71]

The Optical Transition Radiation (OTR) monitor system is based on the transition radiation (TR) phenomenon. The radiation is produced by a charge passing through an interface of two media with different dielectric constants. The EM field that a moving particle carries with it is media dependent. When the particle approaches and crosses the interface, the field reorganizes itself. In the reorganizing process, it emits TR. In
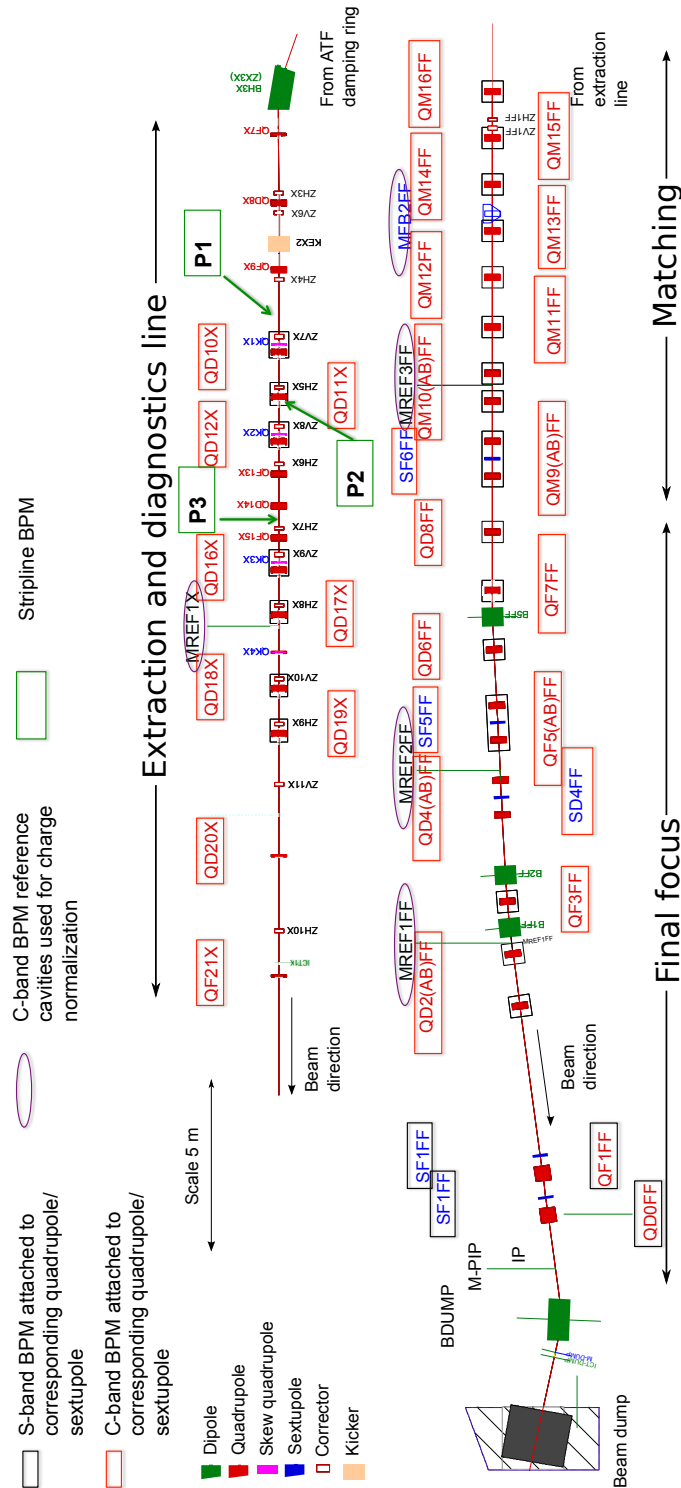
Figure 2.9: Stripline BPMs and C-band and S-band cavity BPMs location in the ATF2 beamline [63].
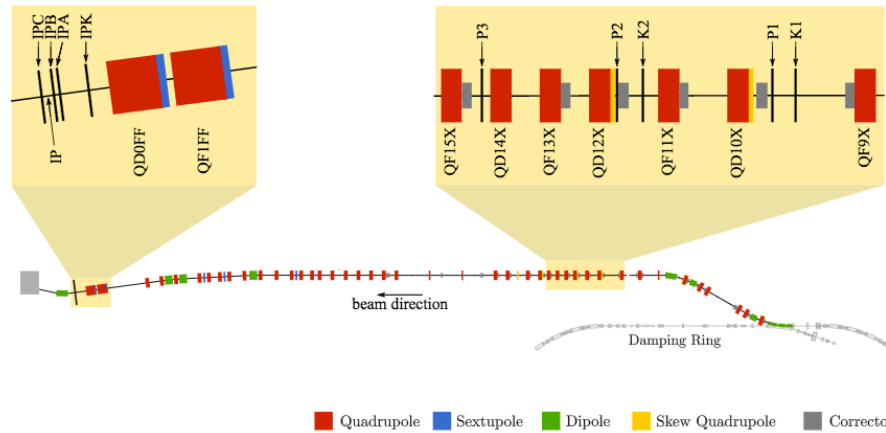
Figure 2.10: FONT system in ATF2.

Fig. 2.11, we can see the angular distribution of the emitted TR for different incoming energies. We can see how it increases with incoming energies and how the peaks are located at $\theta \approx 1/\gamma$ (where γ is the relativistic Lorentz factor). The basic scheme of an OTR monitor can be seen in Fig. 2.11. A metallic foil is inserted to intercept the beam and a CCD camera registers the emitted light. The target is normally inserted at $45°$ with respect to the beam path so that the light is emitted orthogonal to the beam pipe and can be collected by an optical system. Since it is normally outside the beam pipe it is necessary to have a vacuum sealed window to let the radiation pass through. The linearity between the number of OTR photons and the number of particles in the beam, assuming Gaussian beams, allows you to adjust a Gaussian function to the image in order to infer the beam size. The ATF2 multi-OTRs system consists of four OTR stations installed in the diagnostics section of the EXT line of the ATF2. Each individual system measures the vertical and horizontal beam sizes with a resolution of $2\,\mu m$ in less than a minute. With the vertical and horizontal beam size measurements the vertical and horizontal emittances are reconstructed. These stations are used in the ATF2 tuning process to verify the emittances and measure the $x - y$ coupling.

Post-IP wire scanners at ATF2 [72]

The Post-IP WS is located at 75 cm downstream of the IP to perform vertical and horizontal beam size measurements. The beam is scanned by the wire and the photons generated by bremsstrahlung are detected by a photon detector installed downstream. This detector is a plastic scintillator detector connected to a PMT (named as background monitor) located at the same location as the photon detector used for the IPBSM. A picture of this device can be seen in Fig. 2.12. The total length of the wire scanner is around 150 mm and the distance between two wire centers is 10 *mm*. The wire scanner is installed with an angle of $45°$ to the beam line to enable a simultaneous scan in the two transverse axes (horizontal and vertical). The *X* and *Y* wires are used for horizontal and vertical measurements respectively. The *U* wire, which is $45°$ to the *X* and *Y* wire is used to measure the correlation between horizontal and vertical mea-
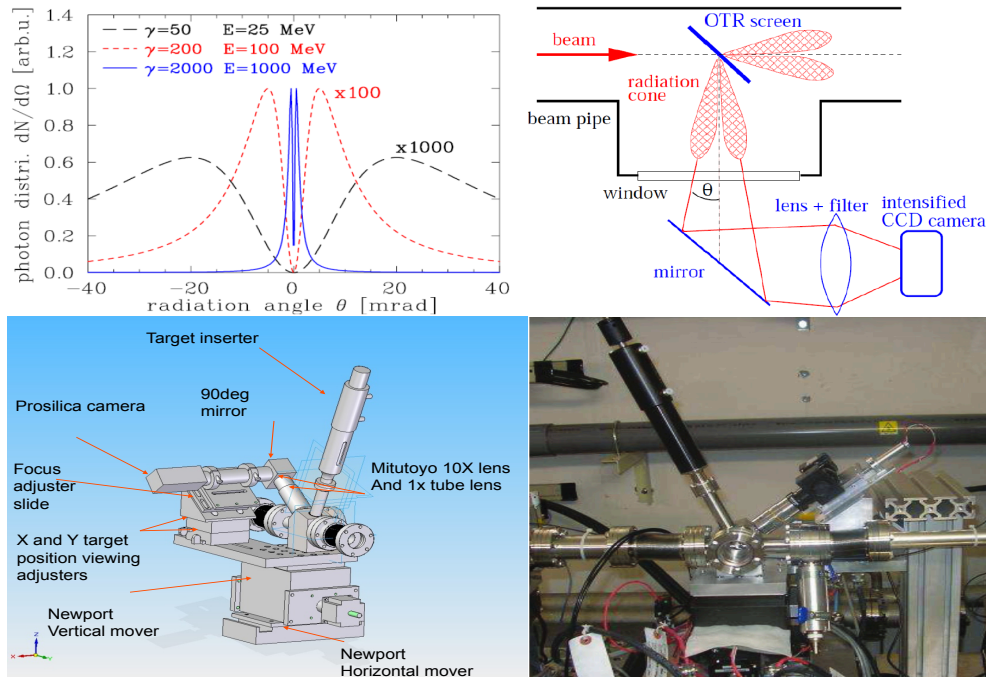
Figure 2.11: Angular distribution of the emitted TR light and conceptual scheme (top), real 3D mechanical design and one of the four OTR monitors installed in ATF2 (bottom).

surements. In addition, two 10 μm tungsten wires with $+10°$ and $-10°$ tilt relative to the *X* direction are used to measure the tilt angle of the beam profile. The resolution of the system is given by the diameter of the wire. In the horizontal plane the resolution is about 50 μm while for the vertical plane three wires with different diameters were installed with corresponding resolution of: 7, 10, 50 μm to measure different vertical beam sizes.

Diamond Sensor (DS) [57, 73]

In December 2014, an in vacuum horizontal DS was installed in the Post-IP beamline for horizontal beam and beam halo measurements with high dynamic range. In addition, in June 2015 a vertical unit was installed. The sensors are composed by four strips of diamond: two strips for beam halo scanning with dimensions 1.4 *mm* $\times$ 4 *mm*, and other two for beam core measurements with dimensions 0.1 *mm* $\times$ 4 *mm*. These strips constitute a piece of diamond with two electrodes attached in two of the opposite surfaces. When the particles go through the diamond, electron-hole pairs are generated due to ionization processes. Then, a voltage is applied to the electrodes on the surface of the diamond and an electric field is created in the bulk of the diamond. Under the force of this electric field, the electrons and holes start to move and this movement induces a current on the electrodes. This signal induced is collected. These devices have been successfully used to measure the vertical and horizontal beam sizes. The vertical and horizontal beam halo have also been measured with a dynamic range of 10^5. Although this is already enough dynamic range for beam halo research the dynamic range
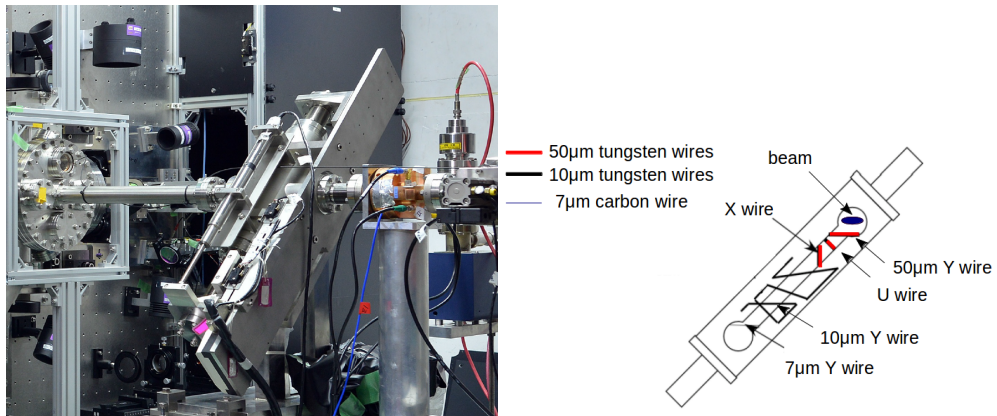
Figure 2.12: Post-IP wire scanner (left) and wires scheme (right).

archived is far from the design value of 10^8 due to the current pick up signal. With the current set up and a dynamic range of 10^5 the beam halo formation and parametrization is being investigated by means of measuring the beam halo distribution as a function of different beam conditions and different DR vacuum pressures [74].
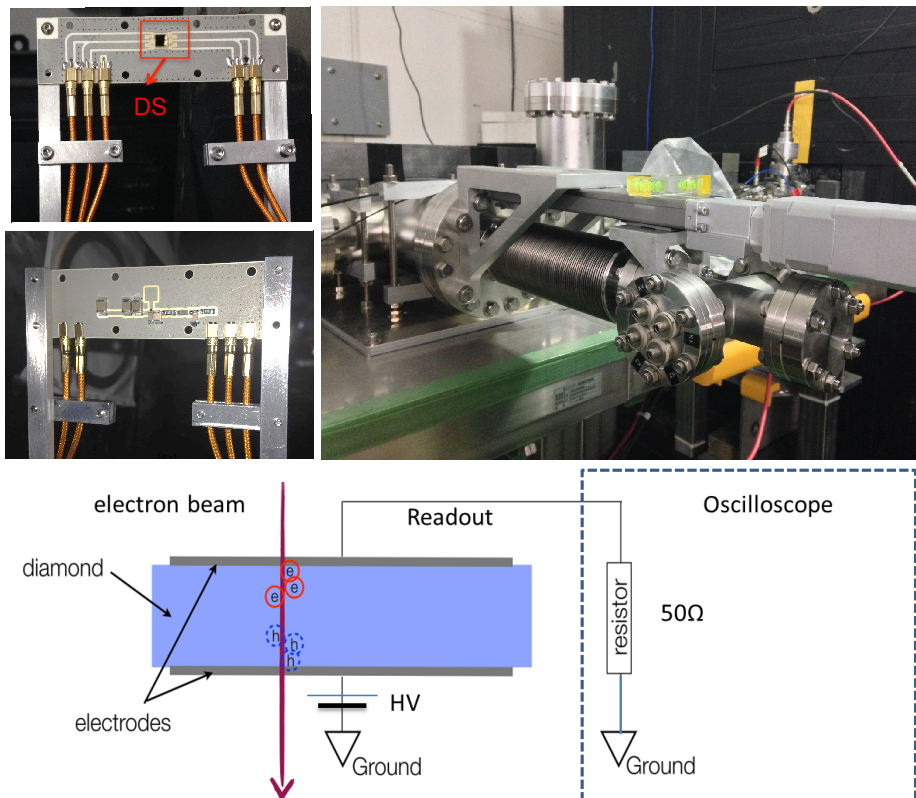
Figure 2.13: Horizontal DS installed in the Post-IP ATF2 beamline (top) and principle scheme (bottom).

YaG screen [75]

At the ATF2, a Cerium activated Yttrium Aluminium Garnet (YAG:Ce) screen was
installed at the exit of the DR, beginning of the EXT line, with the main objectives
of performing vertical beam size measurements. This monitor consists in a screen
formed by two slots separated by 1 *mm* as it is illustrated in Fig. 2.14. The screen
scan the beam and the photons generated due to the interaction of the screen with the
beam and a CCD collects the photons generated due to the interaction of the screen
with the beam. The image of the distribution is used to determine the beam size. The
screen has a 10 *mm* diameter and it is made of 50 *μm* thick single crystal. The dynamic
range archived with this device is about 10^{-3} with a measured resolution of 7 *μm*. This
monitor was used in the past to measure the beam size after being extracted from the
DR. Now it is being used to investigate the transverse beam halo distribution working
in cooperation with the DS team.
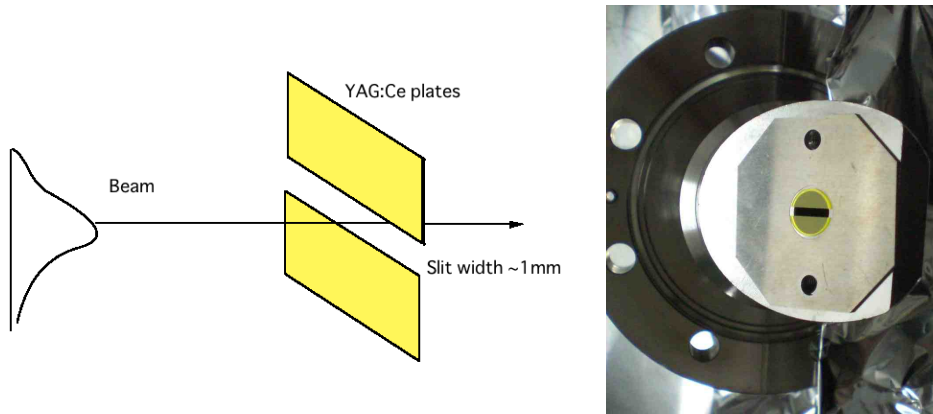
Figure 2.14: YAG:Ce screen scheme (left) and real slot (right).

ODR/OTR [58]

Recently, a new station for beam size measurements has been installed in the FFS of
the ATF2. The station is formed by a combined Optical Transition Radiation system
(OTR) and an Optical Diffraction Radiation system (ODR). This technique is non in-
vasive and the project has the main goals of developing a high-resolution measurement
system for LCs, pushing the limit of current OTRs resolution further down to 100 *nm*
and developing ODR technology to measure beam size at the *μm* scale. Notice here
the difference on the achievable resolution between this new unit and the previously
introduced multi-OTR system, which has a resolution about 2 *μm*. The monitor con-
sists in an Si target used to generate the radiation and an optical system to collect the
radiation emitted. A scheme of the system is depicted in Fig. 2.15.

2.3 Beam halo and background sources in the ATF2

The beam halo could be defined as the low-density beam particles distribution with
high-amplitude and/or high-energy deviation with respect to the nominal one in phase
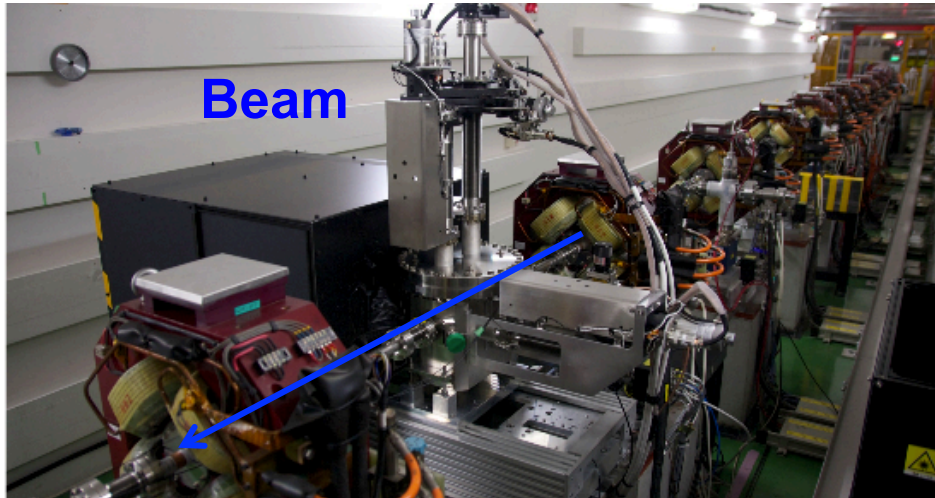
Figure 2.15: OTR/ODR system installed in the ATF2 FFS.

space surrounding the beam core. When the beam halo particles reach the vacuum chamber they start showering in the material and a large number of secondary particles are produced. Places where these tail particles most likely get intercepted are in the last focusing quadrupole magnets, just before the collision point. In FLCs, such particle losses will be unacceptable near the collision point, as the produced secondary particles would have devastating effects on the experiments. Therefore, the reduction and control of the beam halo is a crucial aspect for the FLCs and must be controlled to enable the most ambitious luminosity configuration on the order of $10^{34} - 10^{35}$cm^{-2} s^{-1}. In the ATF2 in order to investigate the transverse beam halo distribution different measurement campaigns have been carried out with wire scanners [9], the YaG screen located in the EXT line [76] and the recently installed DSs in the Post-IP region [74, 77]. The motivation for these measurements is to understand the beam halo formation in the ATF2 and its dependence on some beam and machine conditions, such as the beam intensity and DR vacuum pressure. In addition, these studies aim for a realistic beam halo parametrization in order to perform realistic tracking simulations. The main source of beam halo in the ATF2 has been demonstrated to be due to beam gas scattering in the DR. Some analytical calculations were performed and reported in [78] providing a reasonable estimate of vertical beam halo levels. Measurements are on-going to confirm these predictions by using the DSs. The measurements performed show that the beam halo is mainly formed in the DR and there is no significant enhancement of it when it is focused along the ATF2 beamline. The feasibility of developing a new YaG screen to be installed in the EXT line to complement the DSs measurements is in progress. The idea is to develop a new system with two YaG screens and one OTR screen for beam halo and beam core measurements in both planes in the same location. The current YaG screen only allows you to measure in one plane (the vertical one) and the dynamic range is limited to 10^3.

The beam halo formed in the ATF DR goes into the ATF2 beamline and hits some components producing undesired background photons. The most critical region is the IP and Post-IP where additional background photons may be mixed with the IPBSM

Compton photons and limit the precision of the IPBSM measurements. Experimentally, and by means of tracking simulations has been proven that the aperture of the last bending magnet (BDUMP) is the main source of background photons in the IP region. The BDUMP has an elliptical aperture with a vertical axis of 26 *mm* and a horizontal one of 56 *mm*. A scheme of this phenomenon is depicted in Fig. 2.16 and the mechanical drawing of the BDUMP is shown in the Annex 3.
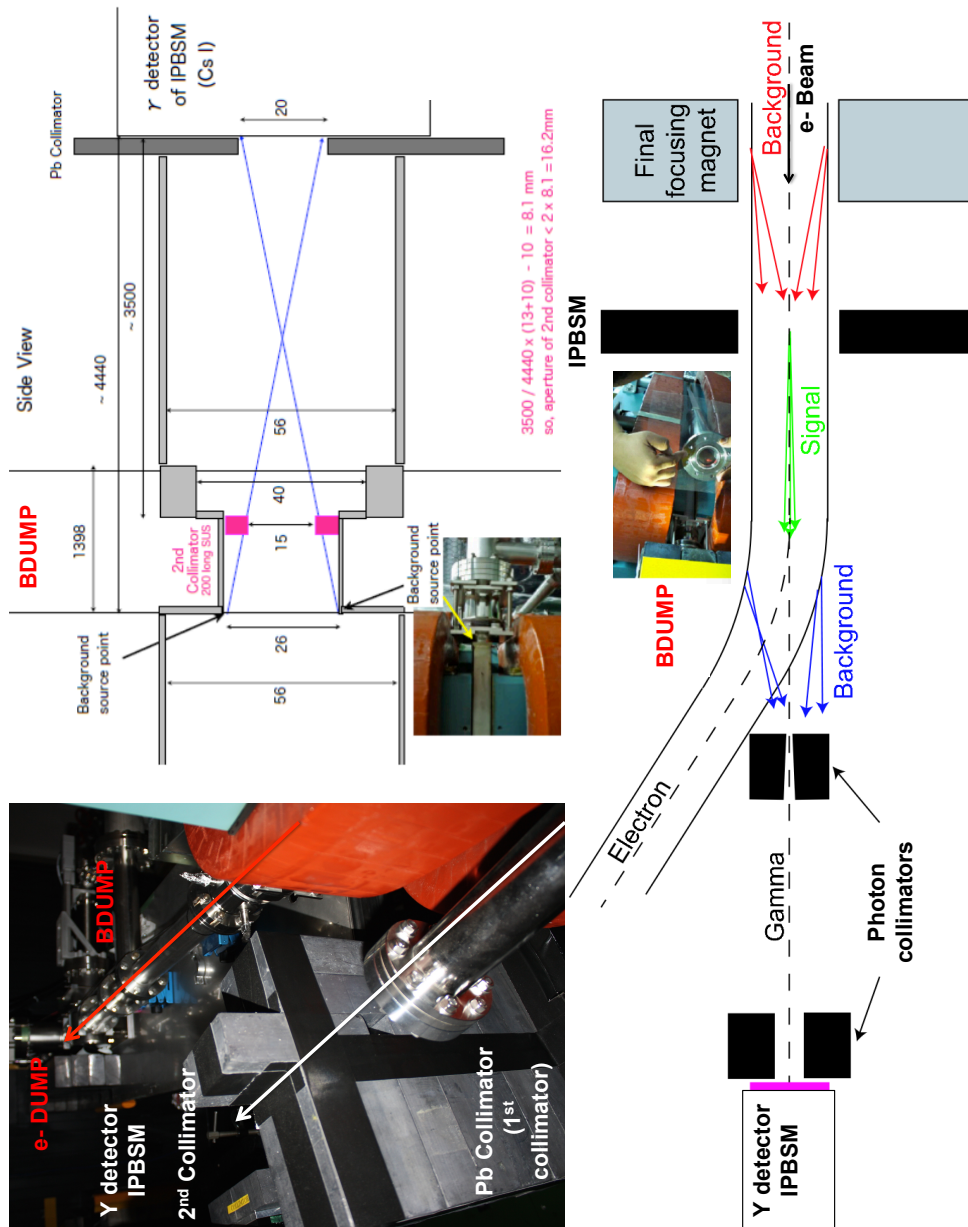
Figure 2.16: ATF2 IP and Post-IP background sources scheme and photon collimators layout between the BDUMP and the IPBSM gamma detectors.

The IPBSM measures the Compton photons produced in the IP due to the interaction

of the IPBSM laser and the electron beam. An example of the modulation measured is shown in Fig. 2.17. In ths plot, the average background was already subtracted. For doing this, the laser-off signal for every phase position is measured and then subtracted for the online plot during the scanning. **The background contribution can change shot to shot and this introduces an uncertainty and instability on the Compton photon measurements**. The total signal measured, A, will be the sum of the Comp-
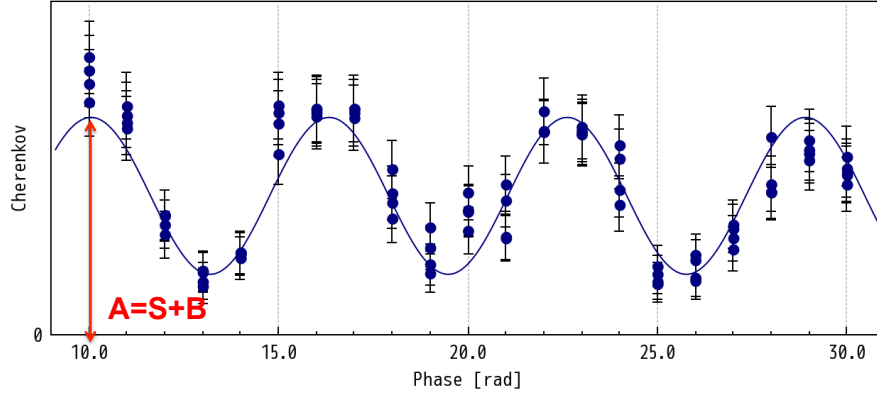
Figure 2.17: IPBSM Cherenkov monitor signal and modulation fitted.

ton photons, S, and the background photons B. The associated error to the Compton electron signal used to reconstruct the vertical beam size can be estimated in a first approximation as:

$$\Delta S = \sqrt{\Delta A^2 + \Delta B^2} \tag{2.4}$$

As can be deduced from Eq. (2.4) the precision of the IPBSM measurements will increase if the ratio A/B increases. In order to reduce the photons generated in the BDUMP first a Tapered Beam Pipe (TBP) made of Stainless Steal (SS) was installed between the quadrupoles $QD10BFF$ and $QD10AFF$ in the FFS. The details of the structure are depicted in Fig. 2.18. The TBP proved to reduce the the ratio A/B by a factor 4, improving the precision of the IPBSM measurements by a 25% [79]. Furthermore, two other collimators for background photons were installed (depicted in Fig. 2.16); one at the exit of the BDUMP window and the other one next to the the IPBSM detector, with a consequent reduction by a factor 10 on the signal to noise ratio, A/B. These solutions were adopted in order to reduce the background in the IP and post-IP region however no dedicated studies were performed to mitigate the origin of the background photons and the TBP which acts as a kind of collimation system with a fixed aperture.

Therefore, it is crucial to use a collimation system to confirm our understanding of the origin of the backgrounds in the Post-IP region of the ATF2 and reduce it a controlled way is crucial. Furthermore, the work in modeling the beam halo and understanding the background sources in the ATF2 provides invaluable knowledge for the FLCs.

A complete **collimation system study** has been performed by means of tracking simulations and loss map studies. Both **energy and betatron** collimation systems have been studied with the following **main goals**:
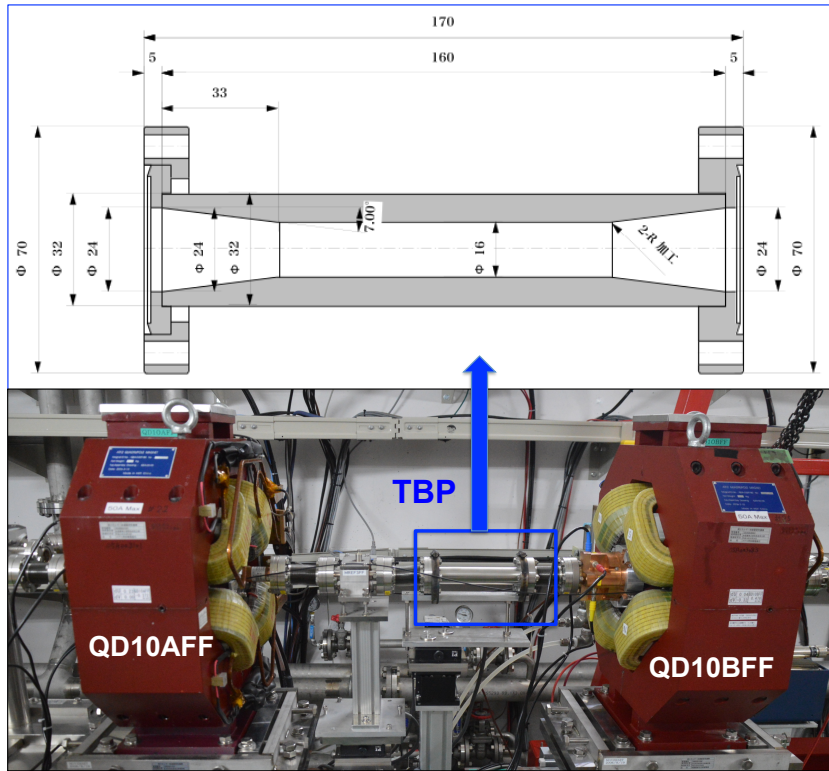
Figure 2.18: TBP mechanical drawing (top) and installed at ATF2 (bottom).

- Improve the IPBSM precision in a controlled way by **avoiding the beam halo
  losses in the Post-IP region**, specially in the BDUMP for any ATF2 operation
  mode (different intensities and optics).

- **Provide an experimental tool for the beam halo investigation with the DSs**:

  - To test the reliability of the beam halo measurements with the vertical DS
    by means of measuring the beam halo cut and comparing it with the ex-
    pected value from tracking simulations.

  - Collimate the horizontal beam halo distribution at the level of 8 σ_x in
    the context of IPBSM second-order Compton electron measurements with
    the horizontal DS. This study was one of the main objectives of the DSs
    project. The study to asses the efficiency of a collimation system in this
    context was performed before the installation of the DS and the results
    presented in this section. However, once the DS was installed and the
    beam halo was measured, it was observed that the pick up signal of the DS
    covers the expected second-order Compton signal as can be seen in Fig.
    2.19 [57]. Due to this fact the second-order Compton measurements can
    not be performed with the present performance of the DS.
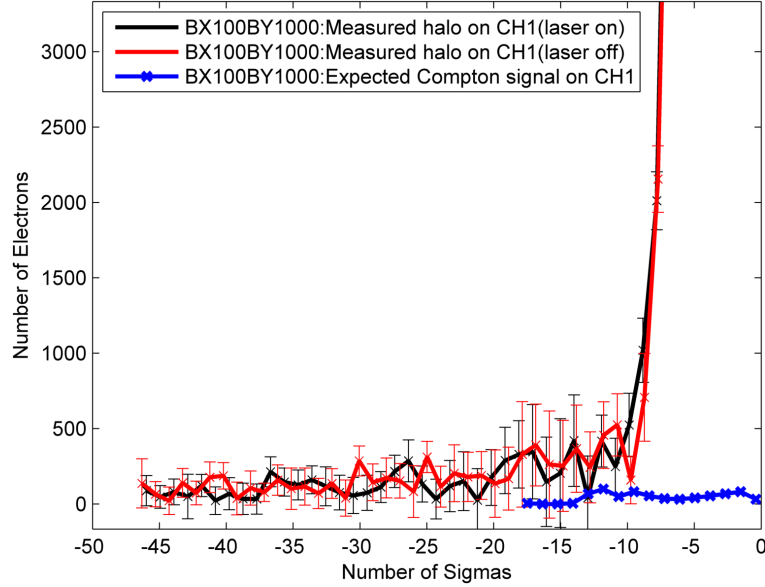
Figure 2.19: Measured horizontal beam halo distribution in 2015 with the horizontal DS (red and black points) compared with the expected second order Compton signal calculated from simulations (blue). In this figure, we can see that the pick up level of the DS is at the level of the expected second order Compton signal [57].

2.4 Beam halo tracking simulations

Tracking codes are used in accelerator physics to design the optics and to understand the beam dynamics of charged particles traveling in an accelerator. MAD-X [80] is a tracking code widely used for machine design. This code with the recent module added called PTC [81] allows you to perform single particle tracking. A map formalism is used by PTC. The aim of these studies is to find the required kind of collimation, the most efficient location from the optics point of view and the required aperture needed to fulfill the requirements specified in the previous section. For that purpose, the tracking code MADX-PTC has been used for a first qualitative study. In this first study, the interaction of the beam with the jaws and collective effects (such as, for example wakefields) have not been taken into account. In the next chapters other tracking codes, including beam halo regeneration and wakefields have been used. In the next subsections, the input parameters of those simulations are described and the results are presented and discussed.

2.4.1 Tracking simulation input parameters: beam halo models

The nominal intensity of the ATF2 beam is 10^{10} electrons and the beam halo population expected (from measurements) is about 10^7 electrons. However, for our studies we have generated a beam halo distribution with 10^4 electrons and we have performed relative studies in order to reduce the simulation time. A transverse beam halo distribution (horizontal and vertical) with 10^4 electrons of 1.3 GeV has been generated based on three different halo models: Gaussian, realistic based on measurements done in

2005 at the ATF2 [9] and uniform. In order to make the collimation system effect evident we have defined a factor n_X that multiplies the different distributions used. This factor has been used to make visible the Gaussian distribution visible and make evident the collimation effect. In a Gaussian distribution at 10 σ the number of particles expected is less than 0.000001 % of the total number of particles of the distribution. By multiplying the density functions by this factor we increase the number of particles in the beam halo region.

The associated **probability functions normalized by the total number of particle** of the distribution, N, are the following:

Gaussian :

$$\rho_{H,V}/N = n_X \frac{1}{\sigma_X \sqrt{2\pi}} e^{-\frac{X^2}{2}} \tag{2.5}$$

Realistic :

$$\rho_H/N = n_X \ X^{-3.5}$$
$$\rho_V/N = n_X \begin{cases} X^{-3.5} & with \quad 3 < X < 6 \\ 0.17 \ \ X^{-2.5} & with \quad \ \ X > 6 \end{cases} \tag{2.6}$$

Uniform :

$$\rho_{H,V}/N = \begin{cases} \frac{1}{-2n_X X} & -n_X X < X < n_X X \\ 0 & X < -n_X X, X > n_X X \end{cases} \tag{2.7}$$

where X is the number of sigmas in the horizontal and vertical plane respectively, σ_X is the transverse beam size.

In order **to generate the transverse beam halo distribution** we proceed as following:

- First, $x(s)$ and $y(s)$ are generated according to the Gaussian, realistic and uniform probability functions described by the Eq.(2.5, 2.6, 2.7) respectively as:

$$x(s) = [g1] \sqrt{\beta_x(s)\epsilon_x}$$
$$y(s) = [g3] \sqrt{\beta_y(s)\epsilon_y} \tag{2.8}$$

Where [g1] and [g3] are the variables generated with the Gaussian, realistic and uniform probability functions described by the Eq.(2.5, 2.6, 2.7). In order to generate comparable distributions for later comparison first we defined the n_X for the Gaussian beam halo distribution and accordingly we determine the values for the realistic one in order to have approximately the same beam halo distribution amplitude. In the case of the uniform distribution in order to make it comparable with the other two models we define the amplitude of the uniform distribution to be equivalent to the amplitude of the Gaussian distribution.

The Gaussian transverse beam halo distributions at the beginning of the EXT line has been generated with an n_X value of 5 in the horizontal plane and 10 in the vertical plane. For the realistic distribution n_X is set to 60 and 90 for the horizontal and vertical planes respectively. In the last case, for the uniform distribution, n_X is set to 20 and 30 for the horizontal and vertical planes respectively. The extension of the beam halo has been chosen bigger than the tightest

apertures on the EXT and FFS beamlines corresponding to the TBP installed in the FFS (named in this work as COLLB) with 8 mm half aperture in both planes ($28\ \sigma_x$ for the horizontal plane and $27\ \sigma_y$ for the vertical plane).

- The angular distributions $x'(s)$ and $y'(s)$ are generated using [71]:

$$x'(s) = [g2]\frac{\sqrt{\epsilon_x}}{\sqrt{\beta_x(s)}} - [g1]\alpha_x(s)\frac{\sqrt{\epsilon_x}}{\sqrt{\beta_x(s)}}$$
$$y'(s) = [g4]\frac{\sqrt{\epsilon_y}}{\sqrt{\beta_y(s)}} - [g3]\alpha_y(s)\frac{\sqrt{\epsilon_y}}{\sqrt{\beta_y(s)}} \qquad (2.9)$$

Where [g1], [g2], [g3] and [g4] are the variables generated with the Gaussian, realistic and uniform probability functions described by the Eq.(2.5, 2.6, 2.7). [g2] and [g4] have been generated with the same extension as [g1] and [g3] given by the n_X values defined before.

- As we are interested only in, the beam halo propagation and interaction with the ATF2 beamline apertures we select the particles of the beam halo as the particles with amplitude higher than:

$$\frac{x^2(s)}{\sigma_x} + \frac{y^2(s)}{\sigma_y} > 9 \qquad (2.10)$$

No coupling between x-y planes has been taken into account. The resulting xy phase space for each probability distribution used can be seen in Fig. 2.20, the xx' and yy' phase space in Fig. 2.21 and the corresponding x and y projections in Fig. 2.22. For the longitudinal distribution a Gaussian model was used with an energy spread of 0.08%. Multipoles have been taken into account but not misalignment errors.
For the nominal simulations the optic configuration used was 10 times the nominal β_x^* and the nominal β_y^* known as $(10\beta_x^* \times 1\beta_y^*)$ which corresponds to the usual operation mode of the ATF2 (V5.2 optics version). However, the performance of the collimation system has also been studied for other optic modes $(1\beta_x^* \times 1\beta_y^*)$ and $(10\beta_x^* \times 0.5\beta_y^*)$. In Fig. 2.23 the comparison of the betatron function, $\beta_{x,y}$, for each case studied is shown.

Furthermore, realistic apertures of the cavity BPMs, horizontal and vertical correctors, dipoles and quadrupoles have been introduced on the ATF2 lattice V5.2 shown in Fig. 2.24. The beam halo amplitude in the transverse plane (considering the Gaussian beam halo model with the amplitude described in this section) is also shown in this plot in order to illustrate the critical points regarding the beam halo losses. The critical regions where losses can occur are the high-β regions at the beginning of the EXT line due to the cavity BPMs and in the FFS, also due to the cavity BPMs and the TBP and in the Post-IP in the BDUMP.

2.5 Collimation system studies

In this section, a study to assess the feasibility and effectiveness of an energy and betatron beam halo collimation system for the ATF2 is presented. The first step in the
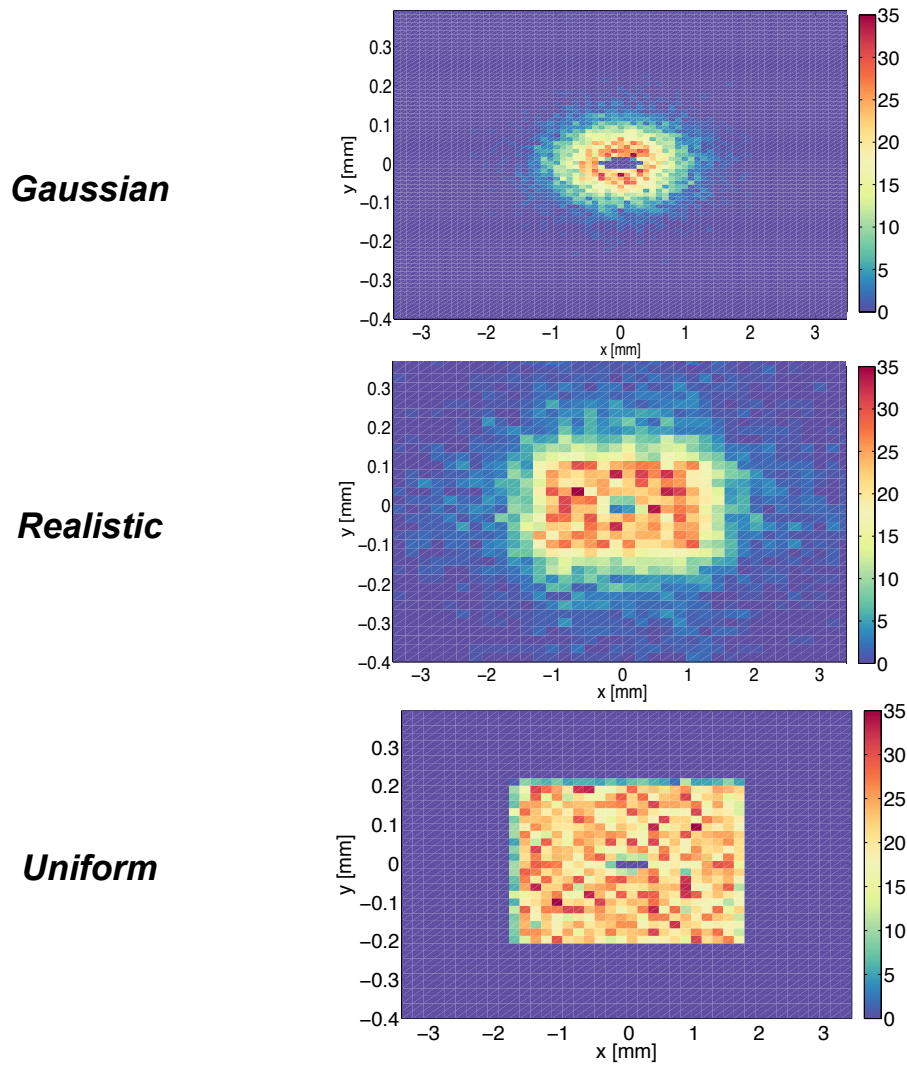
Figure 2.20: Gaussian (left), realistic (middle) and uniform (right) phase space.
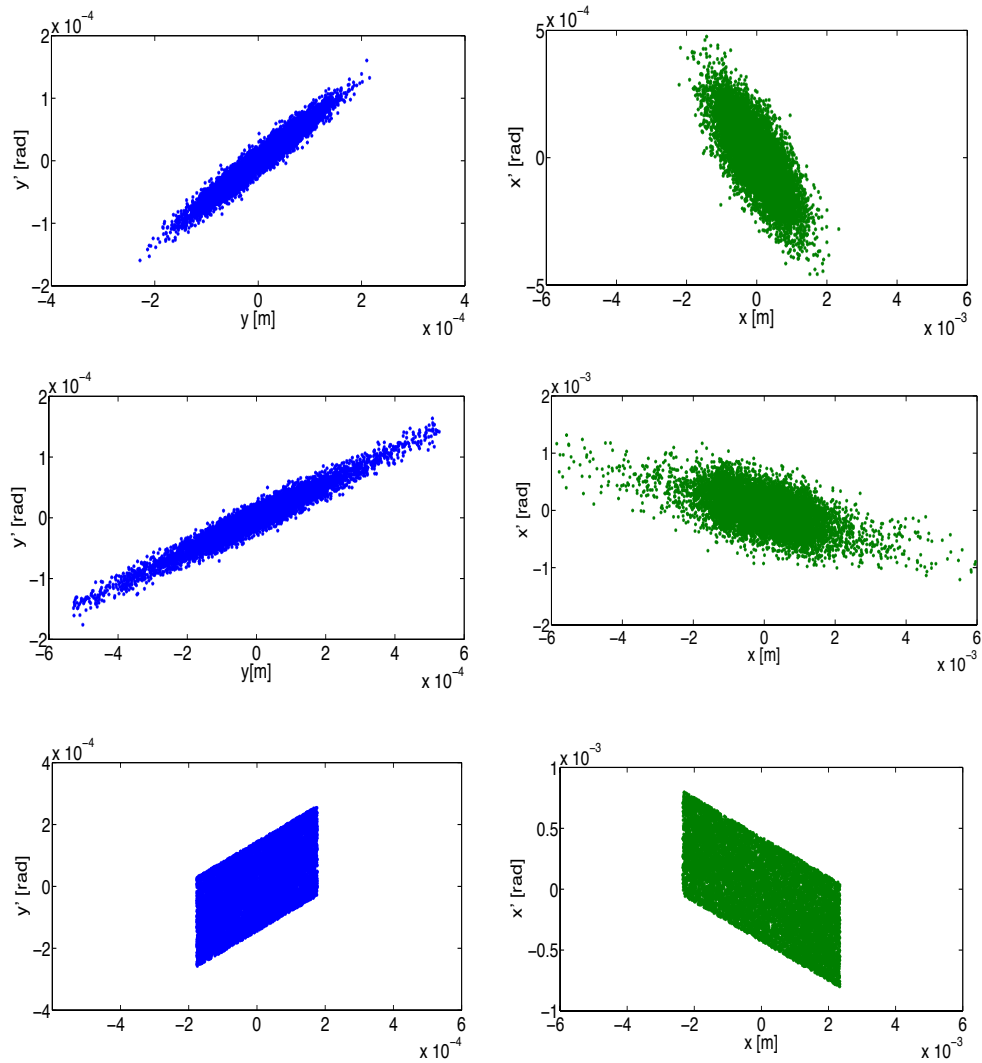
Figure 2.21: Gaussian (top), realistic (middle) and uniform (bottom), vertical (left) and horizontal (right) beam halo distributions yy' (left) and xx' (right). Notice the change in the vertical axis for the horizontal case.
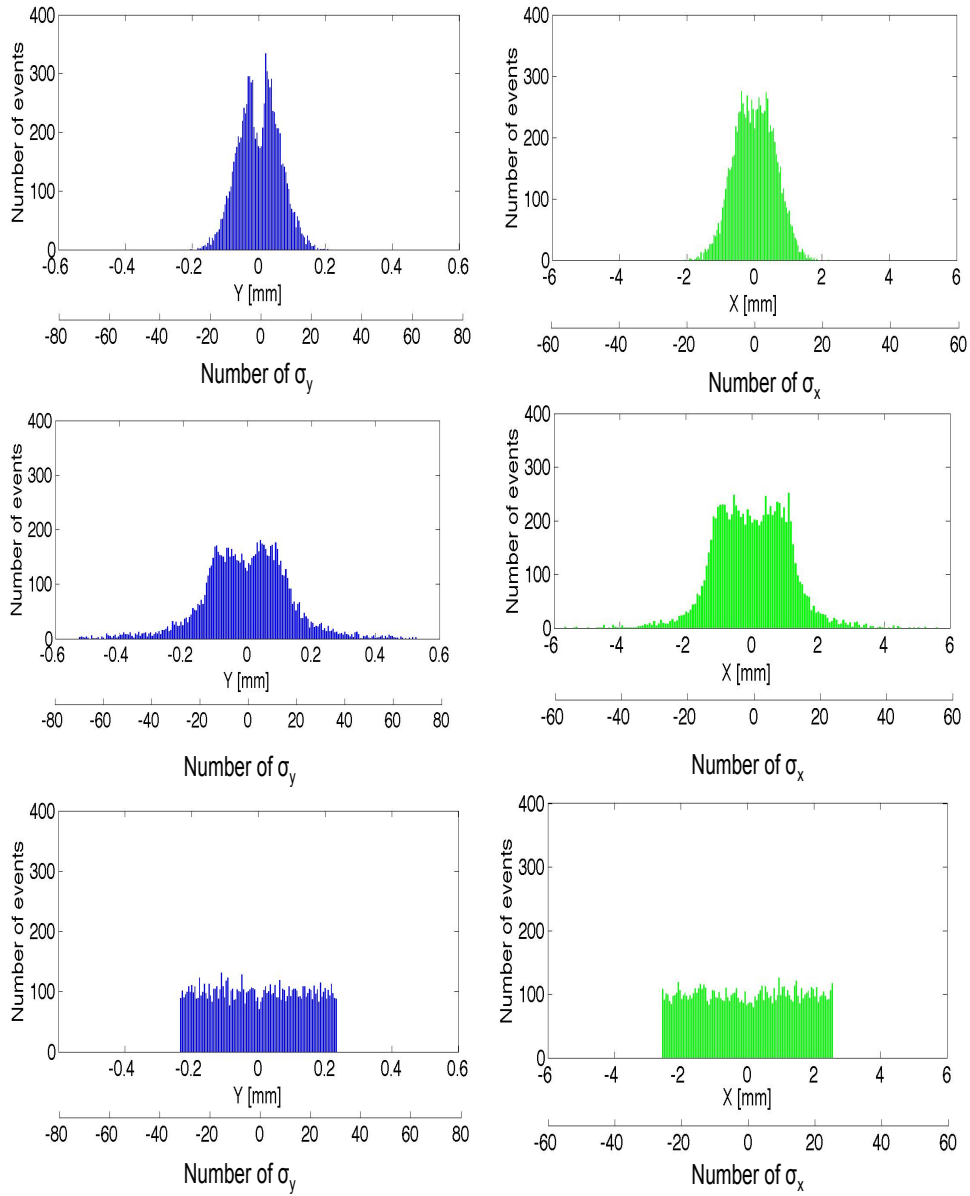
Figure 2.22: Gaussian (top), realistic (middle) and uniform (bottom), vertical (left) and horizontal (right) beam halo distributions used for the beam halo tracking studies. Notice that in the vertical and horizontal distribution particles occupying the $\pm 3\sigma$ region are coming from the generation of the distribution in the other transverse plane horizontal and vertical respectively.
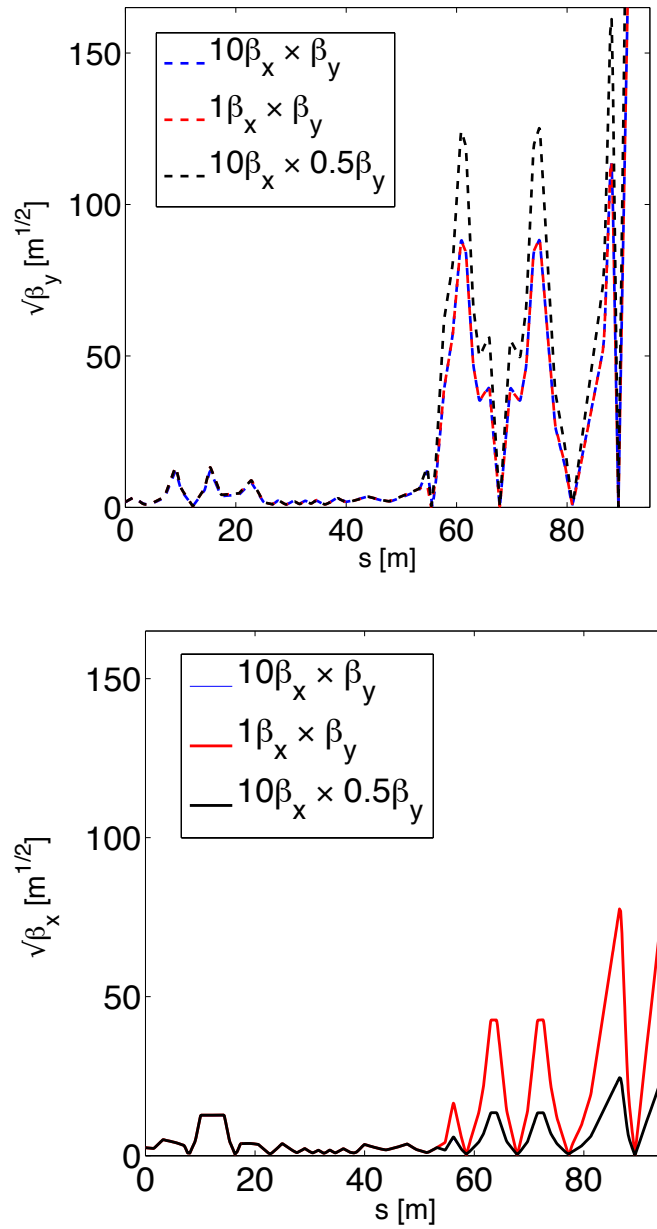
Figure 2.23: Comparison of the ATF2 $\beta_{x,y}$ function for different optics V5.2. Notice that for the vertical case the blue and red line overlap because they correspond to the same optics. The same happens in the horizontal case but with the blue and black lines.
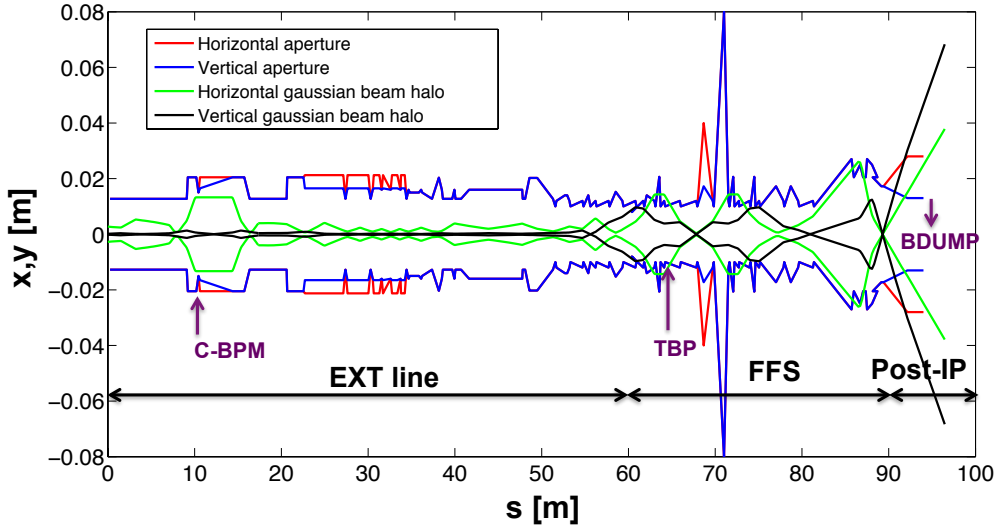
Figure 2.24: Geometric apertures along the ATF2 beamline considering the $(10\beta_x^* \times 1\beta_y^*)$ V5.2 optics.

study was to propose suitable locations from the optics point of view and available free
space for both kind of collimation systems. The second step consisted in performing
tracking simulations with the tracking code MADX-PTC with the input parameters de-
scribed in the section 2.3.1 **in order to study the efficiency and find out what is the
required collimation depth to avoid any loss at the BDUMP and cut the beam halo
in the horizontal plane at the horizontal DS location at the level of 8** σ_x (collima-
tion depth required from simulations in [57] in the context of second order Compton
electron studies).

Notice here, that in this first study performed using MADX-PTC, the ATF2 geometri-
cal apertures are treated as black absorbers and any particle with a betatron amplitude
higher than the geometric aperture of the different accelerator elements is completely
absorbed. In this first study, the emission of secondary particles and beam halo re-
generation is not taken into account. A more detailed study tacking into account the
emission and propagation of secondary particles generated at the collimation system
using the Beam Delivery Simulation (BDSIM) code [82] is presented in chapter 4.

In order to study the efficiency of the collimation system the losses along the ATF2
beamline have been studied. For different collimation system configurations, beam
and machine conditions the **relative loss map** has been constructed taking into ac-
count the remaining particles at different markers located at the end of some ATF2
components normalized to the total number of particles simulated. We put markers in:
the cavity BPMs, the energy collimation system when added (COLLEX), the vertical
and horizontal betatron collimation systems when added (COLLBY and COLLBX),
the TBP (COLLB), the IP, the BDUMP and the DS. The impact of the collimation
systems has also been studied by looking at the cut in the transverse phase space at the
collimation targets of the study.

2.5.1 Betatron collimation system

For a pure betatron collimation system to be efficient from the optics point of view, as explained in chapter 1, it is convenient to install the collimation system where the $\beta_{x,y}$ function is high and where the dispersion function, $D_{x,y}$, is close to zero. In addition, the phase advance between the collimation system and the collimation targets (BDUMP and DS) should be $n\pi$, where n is an integer.

For a **single collimation stage**, the collimation depth, $N_{x,y}$ determines how much we need to close the collimation system for a required beam halo cut at the collimation target. In the case of a **pure betatron collimation system** and for a given collimation system aperture, $a_{x,y}$, the collimation depth, $N_{x,y}$ is defined:

$$N_{x,y} = \frac{a_{x,y}}{\sigma_{x,y}} = \frac{a_{x,y}}{\sqrt{\beta_{x,y}\epsilon_{x,y}}} \tag{2.11}$$

where $\sigma_{x,y}$ is the beam size at the collimation system location.

Collimation system optics considerations for location optimization

Different locations have been studied for a single vertical and single horizontal beam halo collimation system different locations have been studied. The proposed locations are depicted in Fig. 2.25 for the $(10\beta_x \times 1\beta_y)$ optics V5.2. The corresponding phase advances between the collimation system locations studied and the BDUMP and the DSs (collimation targets) are summarized in Fig. 2.26.
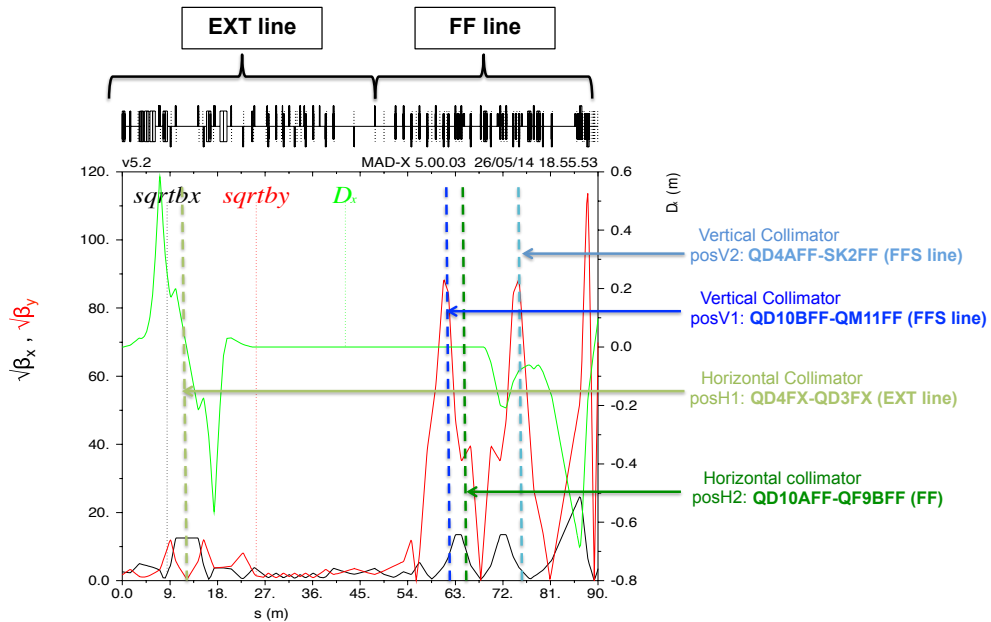
Figure 2.25: ATF2 beamline $(10\beta_x \times 1\beta_y)$ optics V5.2 with the vertical (blue) and horizontal (green) betatron beam halo collimation system locations studied.

Two possible locations have been studied for a single vertical collimation system and
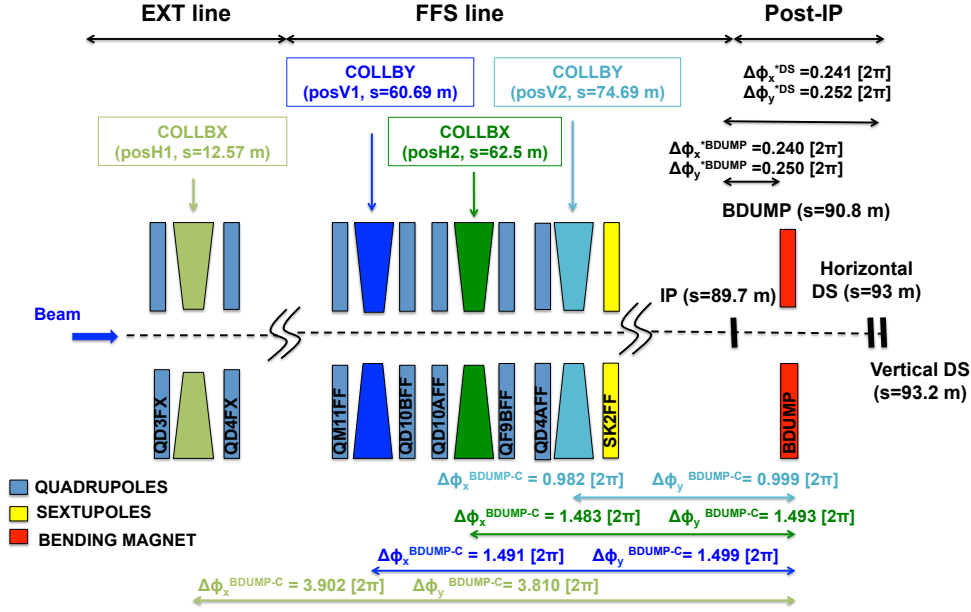
Figure 2.26: Phase advance difference between the collimation system (COLLBY and COLLBX), the BDUMP and the DSs. Notice that the locations are not "in scale".

other two for a single horizontal one. For the vertical collimation system the first location studied is between $QM10BFF$ and $QM11FF$ with 0.8 m of available free space ($posV1$). The second location proposed is between $QD4AFF$ and $SK2FF$ with 0.3 m of available free space ($posV2$). For the horizontal collimation system the locations studied are one in the EXT line between $QD4FX$ and $QD3FX$ with 2 m of available free space ($posH1$) and the other one in the FFS between $QD10AFF$ and $QF9BFF$ with 0.7 m of available free space ($posH2$).

Table 2.2 summarizes the Twiss function, beam sizes at the locations studied for the betatron beam halo collimation system and the phase advance difference between the beam halo collimation system and the IP, BDUMP and DS.

	Units	$PosV1$	$PosV2$	$PosH1$	$PosH2$
s	[m]	60.69	74.69	12.57	62.5
$\beta_{x,y}$	[m]	9.91/6415	15.50/7000	156.12/0.13	56.84/6572
$D_{x,y}$	[m]	0/0	0/0	0/0	0/0
$\sigma_{x,y}$	[mm]	0.14/0.28	0.17/0.29	0.55/0.001	0.33/0.28
$\Delta\phi_{x,y}^{*C}$	[2π]	1.256/1.250	0.7392/0.750	3.429/3.559	1.243/1.240
$\Delta\phi_{x,y}^{BDUMP-C}$	[2π]	1.491/1.499	0.982/0.999	3.902/3.810	1.483/1.493
$\Delta\phi_{x,y}^{DS-C}$	[2π]	1.493/1.499	0.983/1	3.903/3.810	1.484/1.495

Table 2.2: Twiss functions, beam sizes at the locations studied for a betatron collimation system and relative phase advance difference between the collimation system and the IP, BDUMP and DS for the ($10\beta_x \times 1\beta_y$) optics V5.2.

Tracking simulations and efficiency studies

In this section, we have studied separately the efficiency of a single vertical and a single horizontal collimation system. First, the results of the tracking studies when adding the single vertical collimation system are presented for both collimation targets (BDUMP and vertical DS) and after the results corresponding to the scenario when adding only the horizontal one are discussed. The efficiency has been studied as a function of the collimation system locations ($pos1V$ and $pos2V$ for the vertical case and $pos1H$ and $pos2H$ for the horizontal one) for different half apertures of the collimation system and different transverse beam halo models (Gaussian, realistic and uniform). In addition, the efficiency as a function of the ATF2 optics ($10\beta_x \times 1\beta_y$), ($1\beta_x \times 1\beta_y$) and ($10\beta_x \times 0.5\beta_y$) V5.2 has also been investigated.

Vertical beam halo collimation system

BDUMP collimation target

Location and aperture study for different beam halo models: Gaussian, realistic and uniform

First, the efficiency as a function of the half aperture of the vertical collimation system for the two proposed locations has been studied. In Fig. 2.27 the resulting loss map (taking into account the Gaussian (top), the realistic (middle) and the uniform (bottom) beam halo distribution) is shown. In these simulations, the horizontal half aperture of the collimation system has been fixed to 12 *mm* (standard beam pipe half aperture) while the vertical half aperture has been changed from 5 to 12 *mm*. The same study has been performed for the case of adding a vertical collimation system in $posV2$ and the results are shown again for the three different beam halo models studied in Fig. 2.28.

In Fig. 2.29 (top), the resulting loss map for the case of putting the vertical collimation system in $posV1$ and for the three different beam halo models is shown. The efficiency of the vertical collimation system in the reduction of losses in the last bending magnet is independent on the model used as can be seen in Fig. 2.29. The results for the different beam halo models are very similar. The losses observed in these studies along the beamline are consistent with the particle density of the beam halo tails according to the beam halo model. Then, in Fig. 2.30 the efficiency in reducing the losses in the BDUMP for the case of a Gaussian beam halo distribution is shown for the two proposed locations as a function of the vertical collimation system half aperture.

From these studies we conclude:

- In all the resulting loss maps the beam halo particles are lost in the EXT line between $MQF1X$ and $MQF7X$ where the β_x has a maximum and we have tight apertures corresponding to the corrector ZH1X (15 *mm* half aperture in both planes), to the quadrupole $QF3X$ (16 *mm* half aperture in both planes). The observed losses in the FFS are at some cavity BPMs: $MQM12FF$, $MQ11FF$, $MQF5BFF$, $MQF9BFF$ which have a half aperture of 10 *mm*, the TPB (8 *mm*) half aperture and the vertical collimation added (with variable half aperture). In
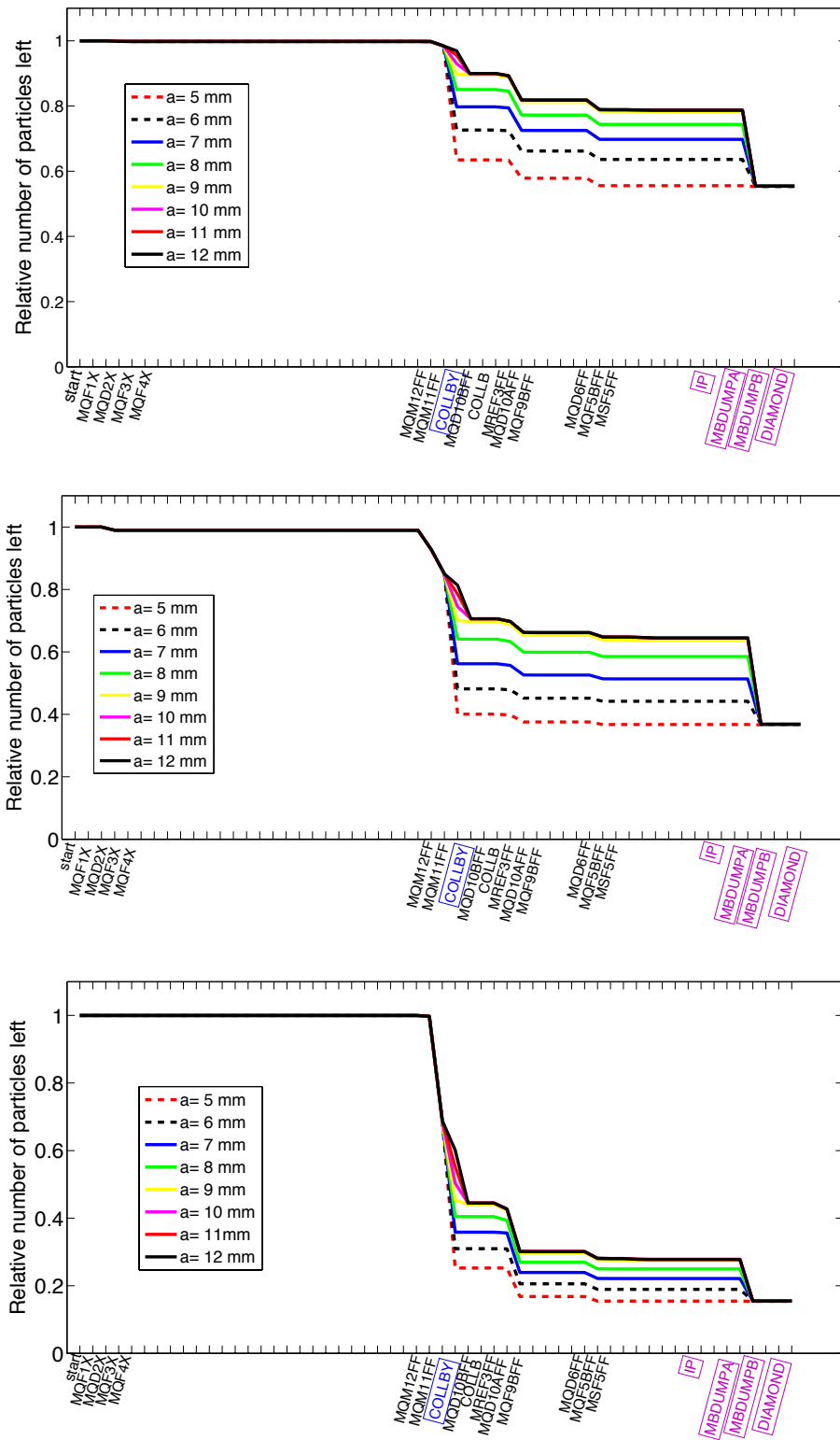
Figure 2.27: Relative loss map when adding **a single vertical collimation system** at
*posV*1 as a function of the collimation system half aperture for the Gaussian (top),
realistic (middle) and uniform (bottom) beam halo distributions.
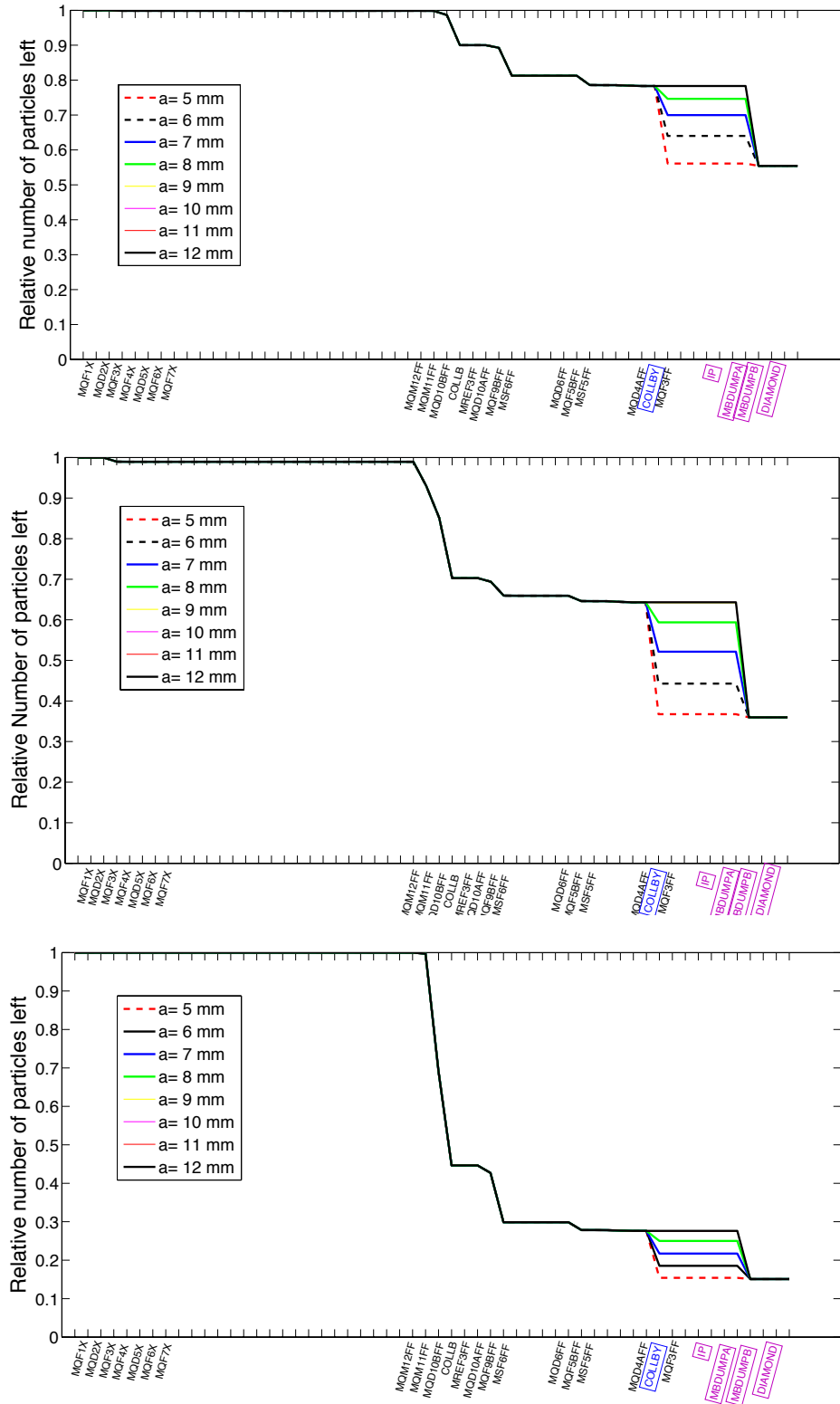
Figure 2.28: Relative loss map when adding **a single vertical collimation system** at *posV2* as a function of the collimation system half aperture for the Gaussian (top), realistic (middle) and uniform (bottom) beam halo distributions.
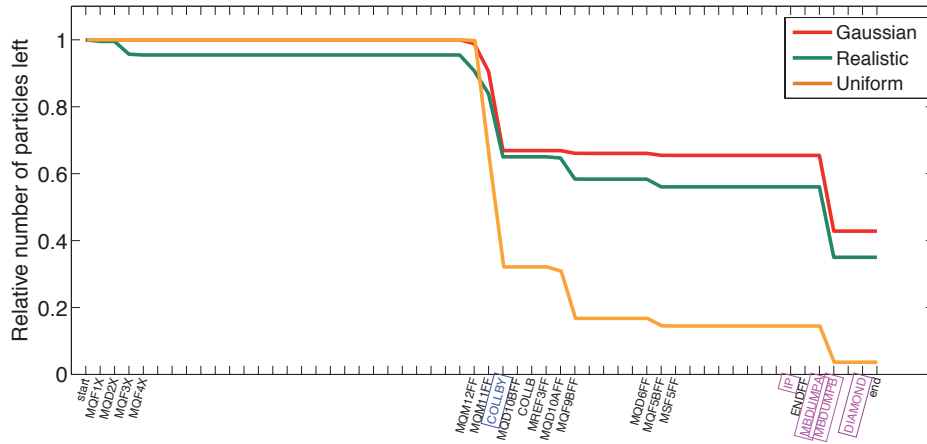
Figure 2.29: Relative loss map for the three different beam halo models when adding
the single vertical collimation system in *posV*1 with half aperture of 8 *mm*.
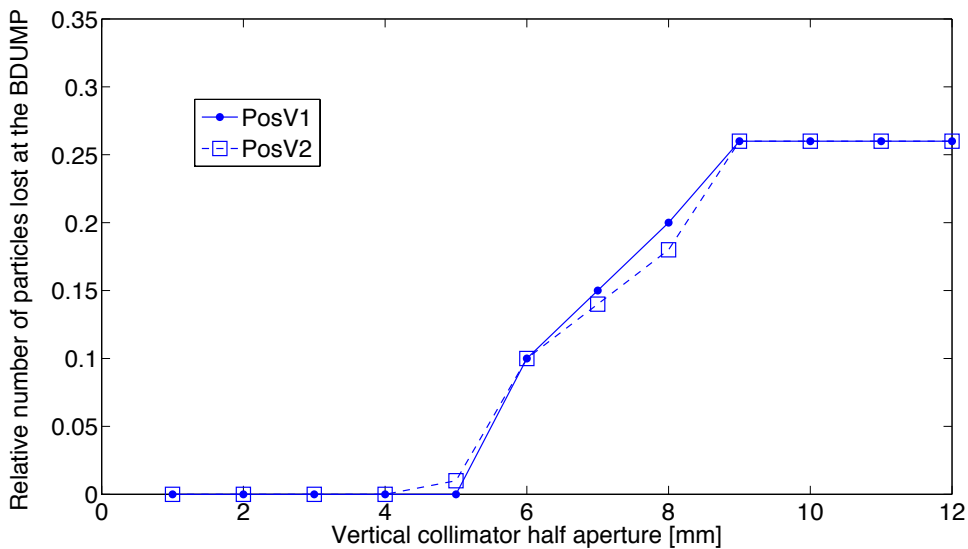
Figure 2.30: Relative number of particles lost at the BDUMP for the two proposed
location (*posV*1 and *posV*2) for **the single vertical collimation system** as a function
of the collimation system half aperture.

the Post-IP line we also observe losses in the last bending magnet (BDUMP).

- The **impact** of **a single vertical collimation system** is visible at the BDUMP
  when we close the collimation system to **8** *mm*, corresponding to 27 σ_y for both
  studied locations.

- **Collimating only in the vertical plane at 5** *mm* (corresponding to a collimation
  depth of 12 σ_y) **prevents losses at the BDUMP** beam pipe.

- **The relative collimation system efficiency is very similar for all beam halo**

models studied.

- The resulting efficiency in reducing the losses at the BDUMP is very similar for both possible locations proposed. But *posV*1 **is a better candidate** because there is more available free space at this location and it is further from the IP, decreasing the probability that the shower of particles generated at the collimation system reach the IP.

Collimation system efficiency studies for different ATF2 optics

The loss map has been studied for the ATF2 optic models $(10\beta_x \times 1\beta_y)$, $(1\beta_x \times 1\beta_y)$, $(10\beta_x \times 0.5\beta_y)$ V5.2. Given the fact that the relative efficiency does not depend on the beam halo model, the study has been performed only considering the Gaussian beam halo model. For all cases studied the vertical collimation system is efficient to avoid the losses in the BDUMP as can be seen in Fig. 2.31 when it is closed to a half aperture of 5 *mm* corresponding to a collimation depth of 12 σ_y.

Figure 2.31: Relative loss map for the three different optics $(10\beta_x \times 1\beta_y)$, $(1\beta_x \times 1\beta_y)$, $(10\beta_x \times 0.5\beta_y)$ V5.2 when adding **the single vertical collimation system** in *posV*1 with half aperture of 5 *mm*.

DS collimation target

The other collimation target in this study is the vertical DS. Two DSs were installed in 2015 and early 2016 in the Post-IP beamline to investigate the beam halo distribution. The vertical DS can be used to test the performance of the vertical collimation system therefore the collimation impact on the vertical DS has also been studied. In Fig. 2.32, you can see the horizontal (left) and vertical (right) beam halo particles' phase space with a vertical collimation system installed in *posV*1 for different vertical collimation system half apertures.

Figure 2.32: Horizontal (left) and vertical (right) beam halo particles phase space having **a single vertical collimation system** installed in *posV*1 for vertical half aperture *a* = 12, 5, 3 *mm*.

From these studies we could conclude:

- In order to see the **impact** of the vertical collimation system on the vertical **DS** we need to **close the collimation jaws more than 5** *mm*, due to the fact that the vertical DS is located after the BDUMP. The BDUMP vertical half aperture cuts the beam halo at the same level of sigmas as the vertical collimation system when it is closed to 5 *mm*.

- When we close the collimation system to 3 *mm* a reduction of beam halo particles is also observed in the horizontal plane; an effect that could be measured with the horizontal DS.

Horizontal beam halo collimation system

BDUMP collimation target

Location and aperture study for different beam halo models: Gaussian, realistic and uniform

In the same way, a similar study has been performed to study the efficiency of a single horizontal beam halo collimation system. In this case, only the Gaussian distribution has been used, as we already concluded from the previous studies that the three different beam halo models have a similar loss pattern. The results from the loss map studies as a function of the half aperture of the collimation system for the Gaussian beam halo model can be seen in Fig. 2.33 for the first (top) and second (bottom) proposed location, *posH*1 and *posH*2, respectively.
We could conclude from these studies:

- **Collimating only the horizontal plane is not efficient** in avoiding the losses in the **BDUMP**.

- The relative efficiency for the **two proposed locations is very similar**.
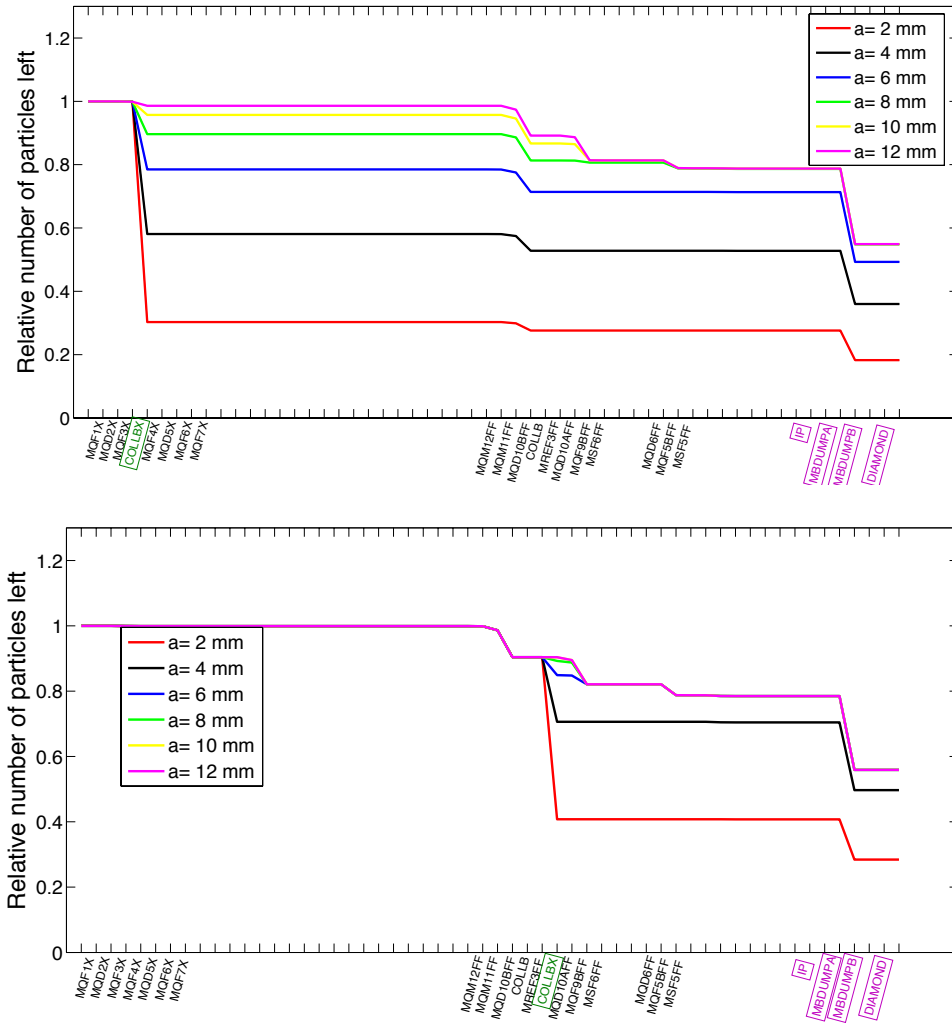
Figure 2.33: Relative loss map adding **a single horizontal collimation system** in *posH*1 (top) and *posH*2 (bottom) for different collimation system half apertures.

Collimation system efficiency studies for different ATF2 optics

To complete these studies, the loss maps have been studied for different optics ($10\beta_x \times 1\beta_y$), ($1\beta_x \times 1\beta_y$), ($10\beta_x \times 0.5\beta_y$) V5.2. In Fig. 2.34 the results of these simulations are shown adding the horizontal collimation system in *posH2*.
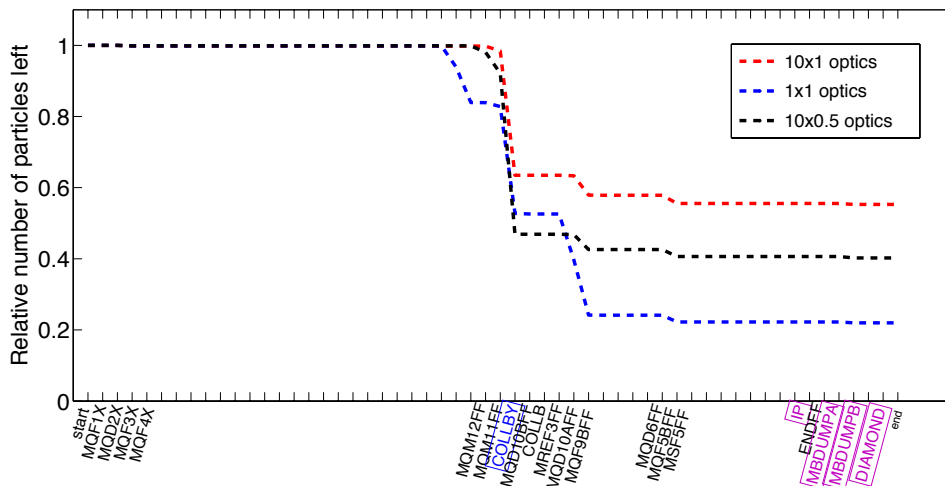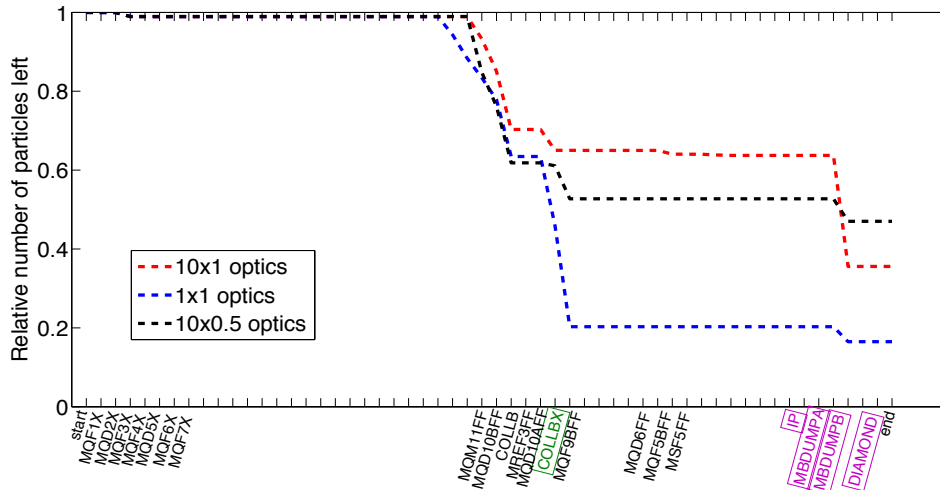

Figure 2.34: Relative loss map for the different optics ($10\beta_x \times 1\beta_y$), ($1\beta_x \times 1\beta_y$), ($10\beta_x \times 0.5\beta_y$) V5.2 for a fixed **single horizontal collimation system** half aperture of 8 *mm*.

We conclude from these studies that the relative efficiency in avoiding any loss at the BDUMP is the same for all the optics studied. However, different relative number of particles left can be observed depending on the optics. One can notice, that for the ATF2 design optics ($1\beta_x \times 1\beta_y$) the losses caused by the horizontal beam halo are absorbed by the horizontal collimation system due to the increase of horizontal β function at the collimation system location.

DS collimation target

The horizontal collimation study is mainly focused on the second collimation target of the study, the horizontal DS. The comparison of the efficiency in reducing the beam halo at the DS location for the two proposed locations is shown in Fig. 2.35 as a function of the collimation system half aperture. Then, in Fig. 2.36 the horizontal (left) and vertical (right) beam halo particles phase space having a single horizontal collimation system installed in *posH1* are shown at the DS for collimation systems half apertures of 12 and 6 *mm*.

In summary, from these simulations we could conclude that in order to achieve the required collimation depth of 8 σ_x at the horizontal DS we need to close the single horizontal collimation system to 6 *mm* if it is located a *posH1* while it has to be closed to 4.5 *mm* if we place it at *posH2*. However one has to notice that *posH1* has some disadvantages with respect to *posH2*. *PosH1* is located before the coupling correction section and if the coupling is not corrected the induced wakefields also have an impact
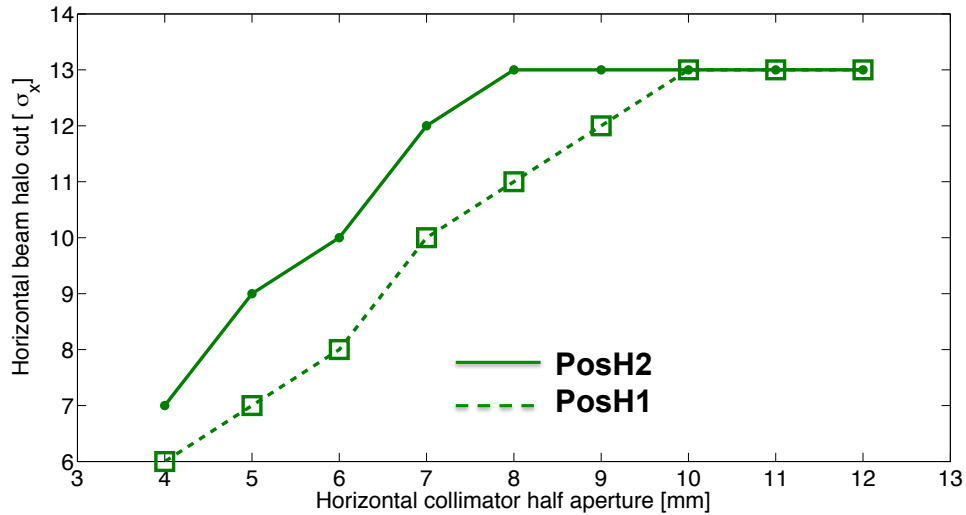
Figure 2.35: Comparison of the horizontal beam halo cut at the horizontal DS as a function of the half aperture of **a single horizontal collimation system** for the two proposed locations.
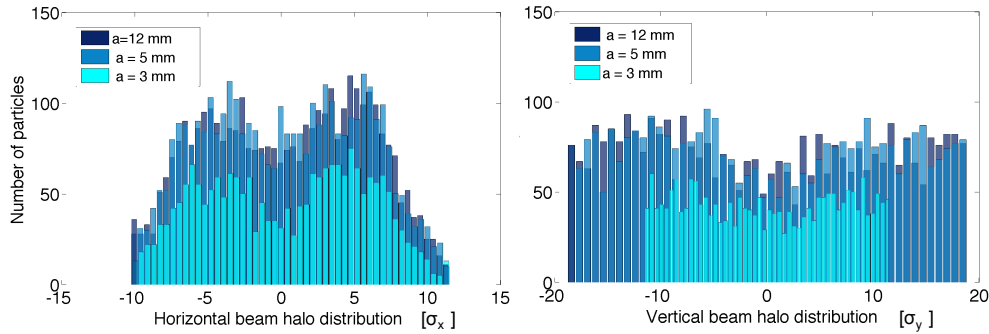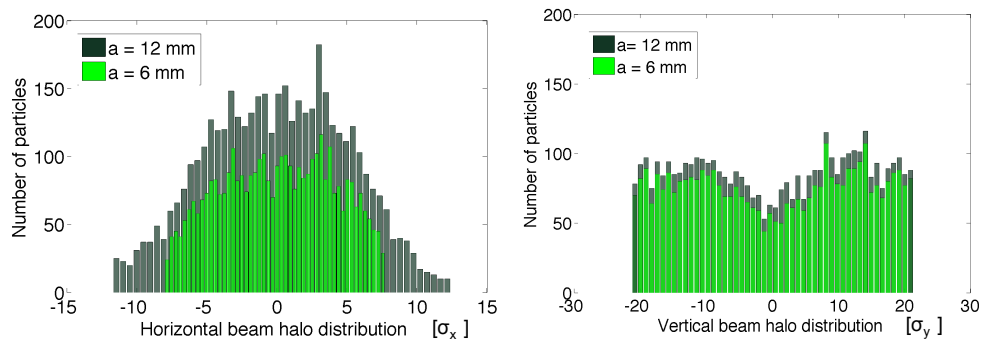

Figure 2.36: Horizontal (left) and vertical (right) beam halo particles phase space having **a single horizontal collimation system** installed in *posH*1 for collimation system half aperture of 12 and 6 *mm*.

on the vertical plane.

2.5.2   Energy collimation system

In order to perform efficient energy collimation from the optics point of view, we need to locate the collimation system in a region with high dispersion where particles with higher σ_E will have higher amplitude. The energy collimation system will be characterized by the collimation depth defined by the required energy spread to be collimated in order to fulfill the collimation goals described in this section. As explained in chapter 1, energy collimation is usually performed in the horizontal plane where the dispersion is orders of magnitude higher than in the vertical plane. In this case the collimation depth is defined as:

$$N_x = \frac{a_x}{\sqrt{\beta_x \epsilon_x + (D_x \sigma_E)^2}} \tag{2.12}$$

Collimation system optics considerations for location optimization

In the ATF2 beamline we find three different regions with high horizontal dispersion. Two are located at the beginning of the EXT line created by two dipoles for dispersion correction and the third one is located close to the IP region for chromaticity correction. The two possible locations studied are the ones at the beginning of the EXT line, in order to protect the IP region from possible backgrounds originated at the collimation system. The locations studied are depicted in Fig. 2.37 considering the $(10\beta_x \times 1\beta_y)$ optics V5.2. The corresponding phase advance between these locations and the BDUMP and DS (these locations being the collimation targets of this study) are illustrated in Fig. 2.38. Both locations under study are in phase with the collimation targets. The first option, $posE1$, is located between the quadrupoles $QF1X$ and $QD2X$ where we have about 0.2 m of available free space. The second option, $posE2$, between $QF6X$ and $QD7X$ has 0.6 m of available free space. In Table 2.3 Twiss functions and beam sizes at the locations studied are summarized.

	Units	$PosE1$	$PosE2$
s	[m]	8.49	18.44
$\beta_{x,y}$	[m]	5.25/90.14	14.22/14.98
$D_{x,y}$	[m]	0.25/0	-0.20/0
$\sigma_{x,y}$	[mm]	0.22/0.03	0.23/0.01
$\Delta\phi_{x,y}^{*C}$	[2π]	4.723/3.813	4.210/3.298
$\Delta\phi_{x,y}^{BDUMP-C}$	[2π]	4.963/4.053	4.451/3.548
$\Delta\phi_{x,y}^{DS-C}$	[2π]	4.964/4.054	4.452/3.549

Table 2.3: Twiss functions, beam sizes at the locations studied for an energy collimation system and relative phase advance difference between the collimation system and the IP, BDUMP and DS for the $(10\beta_x \times 1\beta_y)$ optics V5.2.
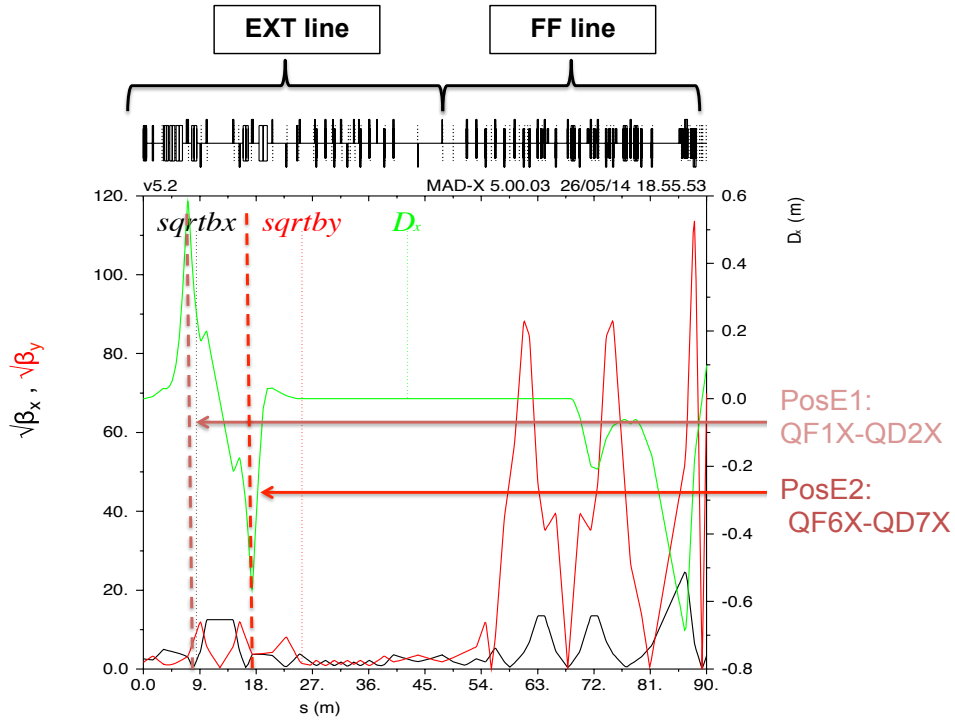
Figure 2.37: ATF2 ($10\beta_x \times 1\beta_y$) optics V5.2 with the possible energy collimation system locations depicted.
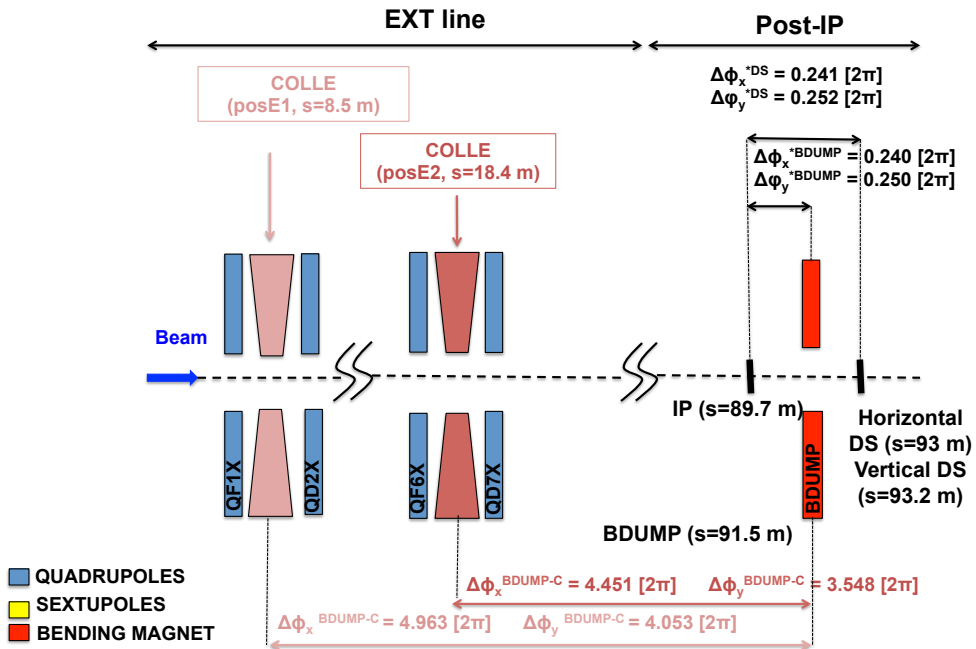
Figure 2.38: Phase advance difference between the energy collimation systems and the IP, BDUMP and DS for the two proposed locations (posE1 and posE2). Notice that the locations are not "in scale".

Tracking simulations and efficiency studies

Tracking studies have been performed in order to study the collimation system efficiency for the two proposed locations (*pos*1*E* and *pos*2*E*) by considering a single horizontal collimation system. These studies have been performed for different half apertures in the horizontal plane while the vertical half aperture of the collimation system has been fixed to 12 *mm* (standard beam pipe half aperture). Furthermore, the simulations have been performed for the three different beam halo models (Gaussian, realistic and uniform) and compared in order to investigate the beam halo distribution influence. This study has also been performed for different beam halo energy spreads. As for the betatron study, the results of these studies are divided into two parts corresponding to the two collimation targets: the BDUMP and the DS.

BDUMP collimation target

Location and aperture study for different beam halo models: Gaussian, Realistic and Uniform

The efficiency in reducing the losses in the BDUMP has been studied for different beam halo models and different apertures for the energy collimation system located in *pos*1*E*. The result of these tracking simulations can be seen in Fig. 2.39 for the Gaussian (top), realistic (middle) and uniform (bottom) beam halo distribution. In these simulations the horizontal collimation system half aperture has been changed from 1 to 4.5 *mm*. The results for the same kind of study but for the case of adding the energy collimation system in *pos*2*E* are shown in Fig. 2.40.
As a summary, the comparison of the loss maps when putting the energy collimation system in *posE*1 for the three different beam halo models is shown in Fig. 2.41.

From these studies we conclude:

- In all the resulting relative loss maps the **beam halo particles lost** are in agreement with the tracking simulation studies performed for the betatron collimation system.

- The pattern of the **loss map for the different beam halo models studied is similar**; losses are observed at the same locations as for the betatron case.

- The efficiency in reducing the losses in the BDUMP is similar for both proposed locations and no impact is observed when the horizontal half aperture is bigger than 3 *mm*.

- **This system is not efficient in avoiding the losses at the BDUMP**, even when closing the collimation system jaws to 1 *mm* half aperture.

Beam halo energy spread influence study

As we conclude from the location and aperture study that the loss pattern is similar for the three beam halo models, the following studies have been performed only considering the Gaussian beam halo distribution. The results for the same scenario
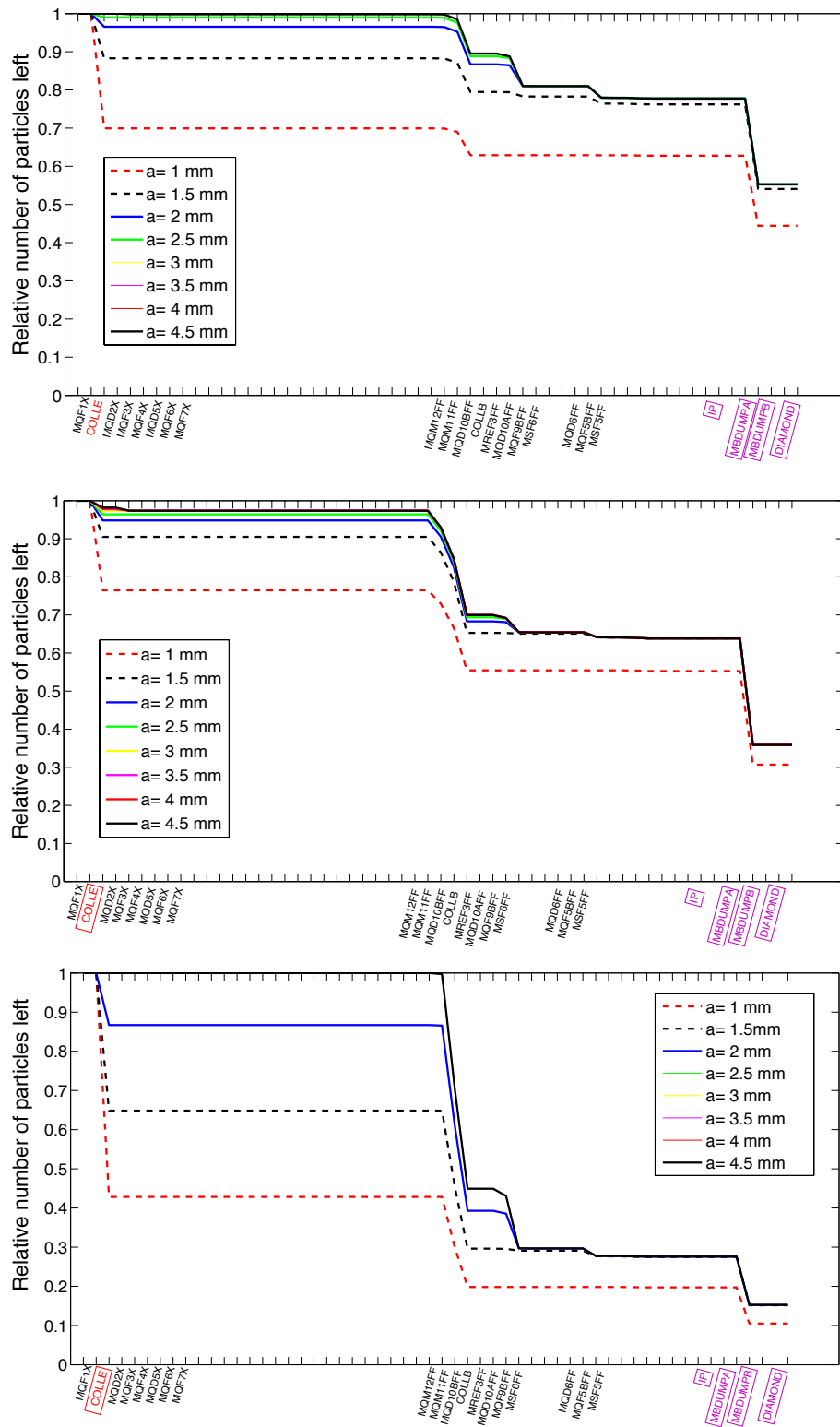
Figure 2.39: Relative loss map for an **energy collimation system** (*COLLE*) located in *posE*1 for horizontal half apertures of the collimation system from 0.5-4 *mm* considering the Gaussian (top), realistic (middle) and uniform (bottom) beam halo distribution. For apertures higher that 3 *mm* no impact is observed.
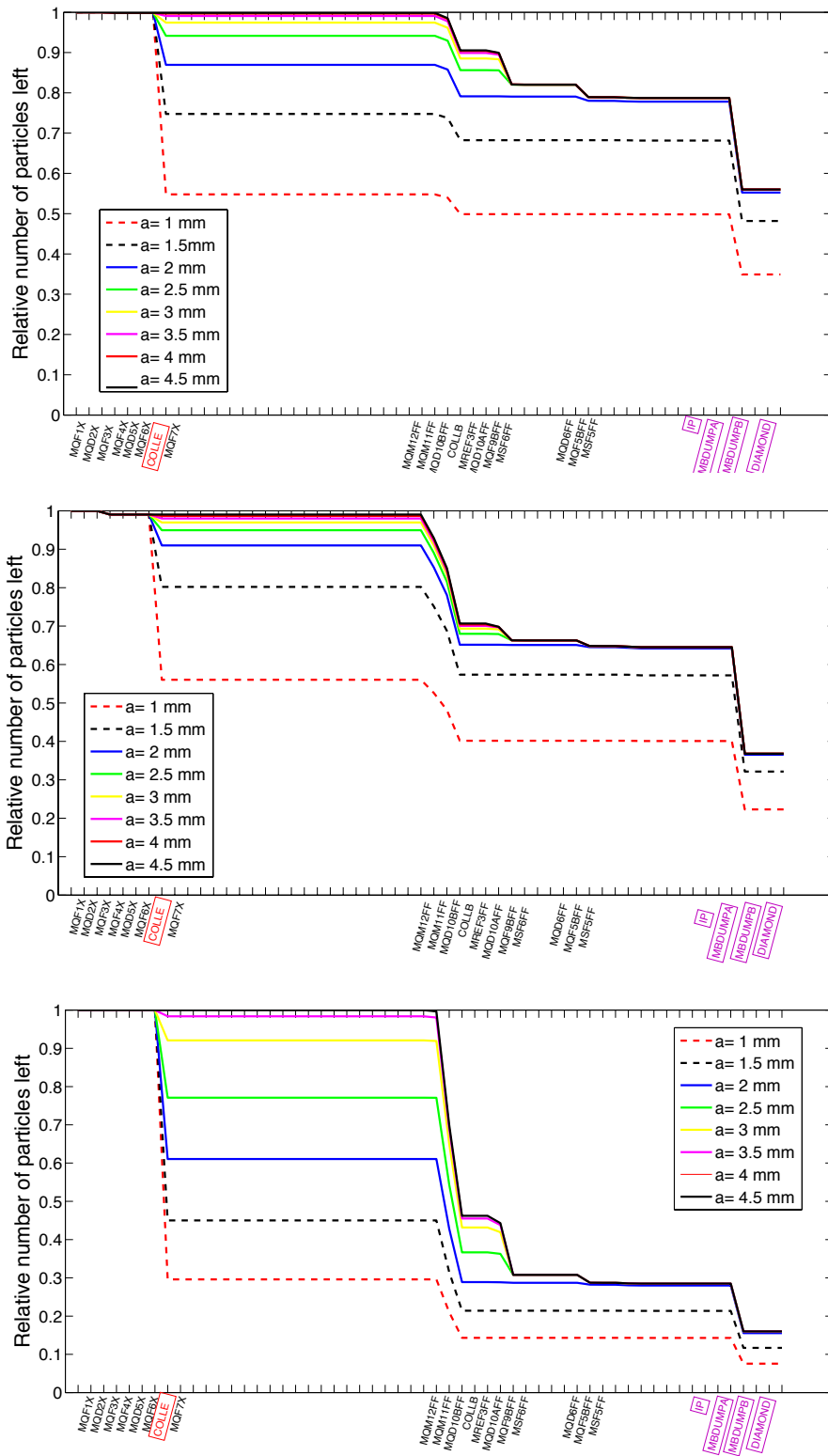
Figure 2.40: Relative loss map for an **energy collimation system** (*COLLE*) located in *posE*2 for horizontal half apertures of the energy collimation system from 0.5-4 *mm* considering the Gaussian (top), realistic (middle) and uniform (bottom) beam halo distribution. For apertures higher that 3 *mm* no impact is observed.
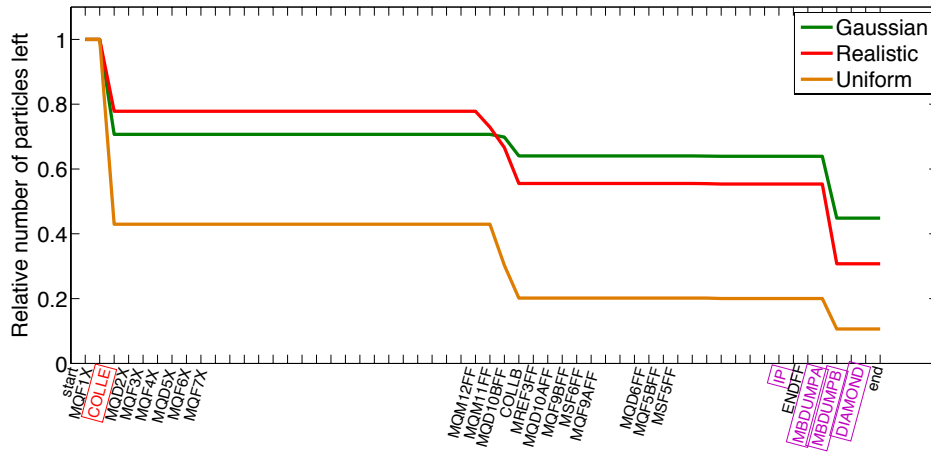
Figure 2.41: Relative loss map comparison for different beam halo models with **the energy collimation system** located in *posE*1 with a half aperture of 1 *mm* (top).

obtained but for the two additional energy spreads studied (where σ_E stands for 0.5 % and 1%) are depicted in Fig. 2.42 for a horizontal half aperture of 1 *mm*.
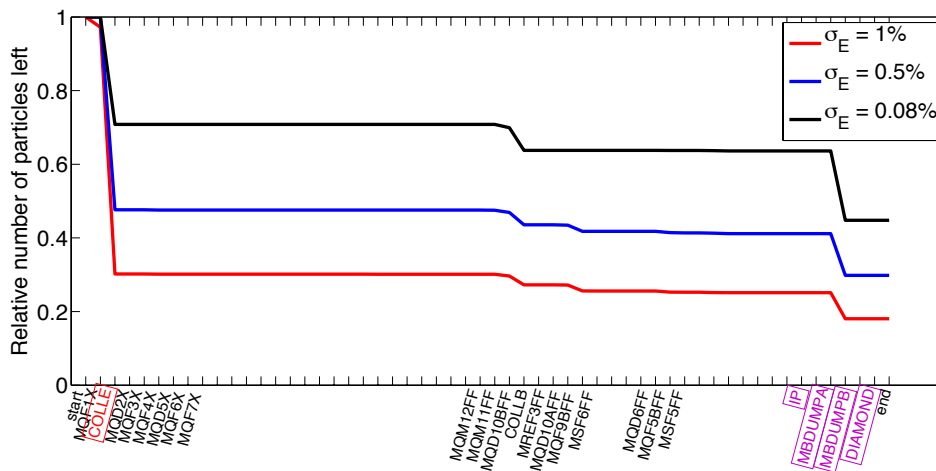
Figure 2.42: Relative loss map study for three different initial beam halo energy spreads with **the energy collimation system** located in *posE*1 with a half aperture of 1 *mm*.

From this study we could conclude that the efficiency in reducing the losses in the BDUMP does not depend on the energy spread defined for the initial beam halo distribution. Additional losses are only observed at the added energy collimation system with very tight half aperture. This study suggests that the energy beam halo distribution is not the main source of background in the BDUMP.

DS collimation target

The other collimation target of this study is the horizontal DS. The horizontal beam
halo amplitude cut has been studied as a function of the energy collimation system half
aperture for the two proposed locations. The comparison of the impact at the horizontal DS location is depicted in Fig. 2.43 considering a Gaussian beam halo distribution.
No impact is observed at the DS for an energy collimation system with a half aperture
bigger than 1.5 *mm*. In Fig. 2.44 the vertical (top) and horizontal (bottom) beam halo
distribution at the DS location are shown when the horizontal aperture of the energy
collimation system is 1 *mm* at both locations considering the Gaussian beam halo distribution. This study has been repeated for the three different beam halo models under
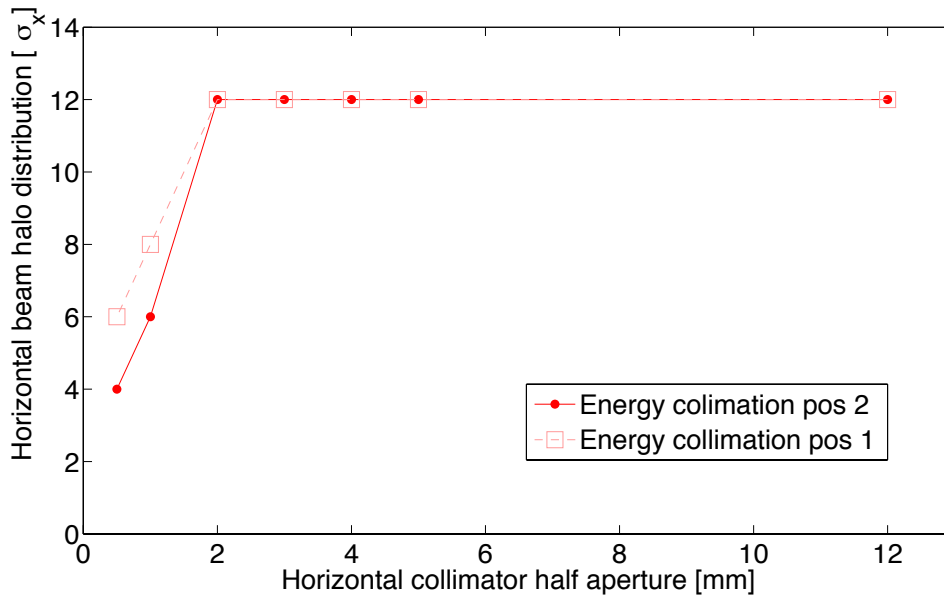
Figure 2.43: Expected horizontal beam halo amplitude cut for the two proposed locations for **the energy collimation system** as a function of the energy collimation system
half aperture.

study. A summary of the beam halo cuts in the horizontal plane at the horizontal DS
for the three different beam halo models can be seen in Table .2.4.

Halo model	$PosE1$ cut at DS [σ_x]	$PosE2$ cut at DS [σ_x]
Gaussian	8.2	5.8
Realistic	7.2	5.3
Uniform	7	4.5

Table 2.4: Horizontal beam halo amplitude cut at the horizontal DS for the two proposed locations and the three different beam halo models for 1 *mm* collimation system
half aperture.
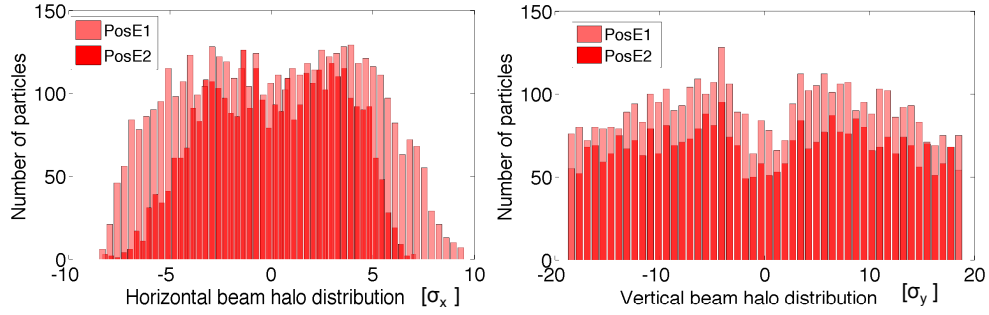
Figure 2.44: Horizontal (left) and vertical (right) beam halo distribution with and without **energy collimation system** located in *pos1E* and *pos2E* for half aperture of 1 *mm*.

From these studies we could conclude:

- Between the two positions studied the location *pos2E* **is more efficient** than *pos1E*. The required aperture to collimate the horizontal beam halo distribution at the level of 8 σ_x is about 1.5 *mm* for *posE2* and 1 *mm* for *posE1* considering the Gaussian beam halo distribution.

- **The results of the tracking for the different beam halo distributions studied are very similar** as all the studies have been performed in a relative way.

2.6   Summary and discussion

The efficiency of a betatron and energy collimation system has been studied in detail for different beam halo models, locations and optics. From these studies we could conclude:

- Different beam halo models (Gaussian, realistic and uniform) have been studied and the relative efficiency obtained is very similar in all the cases. In the following we decided to use the **Gaussian beam halo** distribution.

- Concerning the efficiency in reducing the **background** photons generated **in the BDUMP** in order to **improve the IPBSM** measurements **a single vertical collimation system** is required with a vertical half aperture of 5 *mm* corresponding to a collimation depth of 15 σ_y. In Fig. 7.1 the impact of reducing the beam halo losses in the BDUMP can be seen for the two systems studied (betatron and energy) as a function of the collimation system half aperture.

- Regarding the **best location** for the vertical collimation system *posV1* at s = 60.69 *m* between the quadrupoles *QD10BFF* and *QM11FF* where we have a maximum of $\beta_y = 7487.51$ *m* is more efficient. The phase advance difference between the vertical collimation system and the BDUMP are $\Delta\phi_x^{BDUMP-C} = 1.483$ [2π] and $\Delta\phi_y^{BDUMP-C} = 1.493$ [2π] and the available free space is about 0.8 *m*.

- Related to the **reduction of the horizontal beam halo** distribution, the **horizontal collimation system** has been proven to be more efficient than the energy collimation system. The **most efficient location** found for the horizontal collimation system is $posH2$ at s = 63.02 m between $QD10AFF$ and $QF9BFF$ with a maximum of β_x = 157.02 m. The phase advance difference between the horizontal collimation system and the DS are $\Delta\phi_x^{DS-C}$ = 1.493 $[2\pi]$ and $\Delta\phi_y^{DS-C}$ = 1.499 $[2\pi]$ and the available free space is 0.7 m. However, this system is **not useful for the present status of the DS** due to pick up effect.
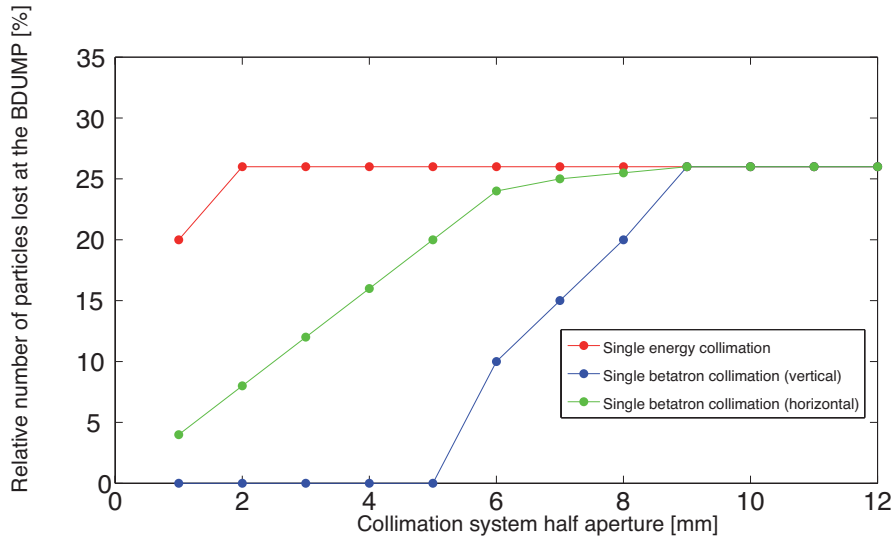
Figure 2.45: Relative number of particles lost at the BDUMP when we add a single vertical betatron collimation system (blue), a single horizontal betatron collimation system (green) and a single energy collimation system (red).

The vertical collimation system which has been proven to be efficient for the present ATF2 settings to control and reduce the losses in the IP and Post-IP region has been studied in detail for its implementation in the ATF2. The rest of this thesis focuses on the design, wakefield study, construction, installation, commissioning and first efficiency measurements of a single vertical beam halo collimation system.

Chapter 3

Wakefield studies and design implications for the ATF2 vertical collimation system

3.1 Introduction

In chapter 2, we demonstrated by means of tracking simulations with MADX-PTC the efficiency of the ATF2 vertical collimation system in order to control and reduce the losses in the IP and Post-IP region . As introduced in chapter 1, the wakefields induced by collimation systems, which have to be placed very closed to the beam, could have an impact on the beam dynamics and can compromise the beam stability and performance of the accelerator. Due to this fact, the efficiency of a collimation system is a trade off between the beam halo cleaning required by the machine and the wakefields induced. Therefore, a retractable system has been considered in order to be able to adjust the collimation depth required without introducing intolerable wakefields for different beam operation modes and experiments. In addition, the design of the system has been inspired on a preliminary design made for the ILC spoilers and all the learning in designing, wakefield characterization and operation will be crucial for the future ILC collimation system design. Furthermore, the studies being performed for ATF2 could be later scaled to the ILC scenario in order to understand the performance and wakefield implication of this kind of systems in the ILC case. Benchmarking studies between analytical models, numerical simulations and measurements of such effect are essential.

One of the main objectives of this thesis consisted in optimizing the geometry and material of the collimation system jaws in terms of wakefields, efficiency and survivability. This chapter is organized as following. First, the wakefield effect induced in rectangular tapered jaws has been studied in detail with two different approaches: using analytical models and performing numerical simulations. The analytical models used to calculate the transverse wakefield impact are introduced in order to understand the physics behind this effect and its relation with the collimation system geometry and material. Then, the settings required to perform reliable and accurate simulations with the CST PS EM solver are described. In the third section, the wakefields induced by

a rectangular tapered jaw are calculated for different geometries and materials. These calculations have been performed with the two different approaches and compared with other ATF2 elements with well studied wakefield impact. In the fourth section, two other studies are presented performed providing arguments for choosing the best material for the jaws. In order to ensure efficiency and minimize the beam halo regeneration the number of radiation lengths required to stop 1.3 GeV electrons and the EM shower produced for different materials has been calculated. Also the induced rise temperature by the beam passing through and hitting the jaws has been estimated because of survivability issues. Based on these studies at the end of this section the geometry and material choice of the collimation system jaws is discussed. Furthermore, for the final jaw parameters design the wakefield impact has been characterized in all planes and studied as a function of the vertical beam offset and the bunch length. In the last section, the impact on the beam dynamics has been studied using the tracking code PLACET and compared with the linear transport of the wakefield kick calculated with the EM solver CST PS [6, 41, 42] using the formulas introduced in chapter 1. We encounter some discrepancies between the results given by these two methods due to the difference on the definition of the analytical models regimes relevant for the ATF2 case used. The problem was solved and the program was modified accordingly in a new version of the tracking code PLACET [43].

3.2 Collimation system wakefield static calculations in the ATF2 case

For both, the analytical calculations and the numerical simulations a model based on two movable rectangular and vertical tapered jaws has been used. This model is shown in Fig. 3.1 with the main geometric parameters depicted. These jaws are tapered only in the vertical plane while the horizontal plane is described by a fixed half width h. Longitudinally, it is described by the tapered parts defined by the tapered angle α, and the half height $b(z)$ which changes between the maximum gap b and the minimum gap a, and a flat part with a length L_F. The tapered parts of the collimation system jaws induce geometric wakefields and both tapered and flat parts contribute to the resistive wall wakefields.
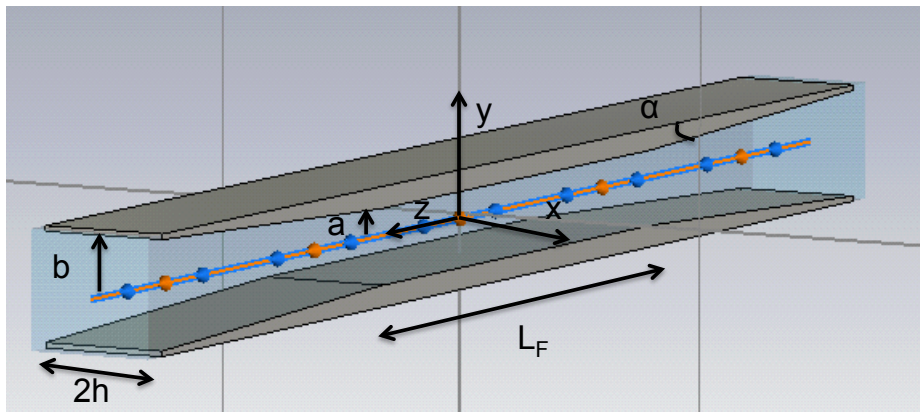
Figure 3.1: Collimation system jaws model with main geometric parameters depicted.

For the wakefield minimization studies only the vertical wakefield effect has been studied in detail because the strongest contribution to the wakefields will come from the vertical geometric change seen by the beam. Furthermore, from the beam dynamics point of view the most sensitive plane is also the vertical one with expected beam size at the IP one and six orders of magnitude smaller than the horizontal and longitudinal one, respectively. However, in the last section for the optimized jaws the wakefield effect has been calculated in all planes for completeness.

3.2.1 Analytical transverse wakefield kick for rectangular tapered jaws

The wakefield effects induced by rectangular tapered collimation system jaws have been extensively studied and different analytical approaches can be found in the literature [18, 20, 83–85, 87–90, 93, 102, 103]. These models describe the wakefield strength providing information about the impact of some specific geometry and beam parameters on the wakefields induced. A summary of the different formulas can be find for circular and rectangular tapered collimation system jaws in [94]. In our study we have used the analytical formulas in [84] developed by G. Stupakov.
As introduced in chapter 1, the wakefields are induced if there is a geometric change on the beam pipe and because the wall is not made by a perfectly conducting material. Two contributions can be distinguish: the **geometric** and the **resistive** one. In order to calculate the total kick factor, both contributions are added linearly. In the following, we describe the analytical models used in this work to calculate the wakefield kick for each case.

Geometric component

The EM fields resulting from the interaction of the field carried by the beam within the collimation system jaws depend on the geometry and on the beam parameters. G. Stupakov [84] used the image method in order to understand this EM problem and differentiate three different regimes depending on the jaw geometric parameters and on the bunch length. In each of these regimes, considering some approximations, he computed the impedance and the corresponding wakefield kick. In this model, when the beam is passing through the collimation system jaws an image current is induced on the walls. This image current will propagate in synchronism with the beam if the wall is considered to be made of a perfect conductor and there is no longitudinal geometric change of the beam pipe. In this case, the EM fields carried by the beam will not interact with the surrounding and no wakefields will be induced on trailing bunches. When the beam encounters a transition the image current induced that was travelling parallel to the beam will modify the path following the shape of the wall. In this case, the image current description will be modulated by a function of the transition geometry. The image current induced will be different in each point of the tapered and as a result the image current will be described by a spectrum of frequencies with different phase velocities. If the phase velocity of the image current becomes equal to the phase velocity of an eigenmode of the structure, the characteristic EM modes of the structure will be excited. These modes are called "trapped modes" and propagate in the structure. The frequency of the EM fields carried by the beam are related with the bunch

length, σ_z, as:

$$\omega \propto 1/\sigma_z \tag{3.1}$$

Depending on the **the geometry** of the transition and **the frequency associated to the beam** these "trapped modes" will be or not excited. The higher the number of modes excited the strongest the wakefields induced in the structure. A collimation system based on rectangular tapered jaws with big aspect ratio ($a << h$) (see Fig. 3.1) can be approximated by a rectangular waveguide. G. Stupakov relates the range of frequencies describing the image current with the cut-off frequency needed to excite the first mode in a rectangular waveguide. The relation that has to be satisfied between **the geometry of the jaws** and **the bunch length** to excite **the first eigenmode** is:

$$\alpha > \frac{\pi^2 a \sigma_z}{h^2} \tag{3.2}$$

When Eq. (3.2) is satisfied we are in the **diffractive** regime in which "trapped modes" are induced in the structure. If this condition is not satisfied the EM fields induced will not be "trapped" and the **inductive** regime is defined. In addition, G. Stupakov introduced an **intermediate** regime for rectangular tapered collimation systems because numerical simulations revel that there was a large range of frequencies not cover by the limiting models (inductive and diffractive). A first limit for this regime was defined by G. Stupakov when Eq. (3.2) is satisfied but the frequency is not high enough to excite all the EM "trapped modes" given by $\alpha << c/a\omega = \sigma_z/a$, where c is the velocity of the light in vacuum. In this case, in the calculation of the impedance only the Transverse Electric (TE) modes (modes that have no electric field in the longitudinal direction) are taken into account and not the Transverse Magnetic (TM) modes (modes that have no magnetic field in the longitudinal direction). However, a possible different limit definition for the intermediate regime was suggested in [20, 86] when the geometry and bunch length of the problem under study sits close to the hypothesis made to solve the EM problem performed by G. Stupakov. In the cases close to the limits, the benchmarking of the analytical models with numerical EM simulations and measurements is crucial.

The three different regimes defined by G. Stupakov depend on σ_z, α, a and h (parameters depicted in Fig. 3.1) and are valid in the near center region (smalls offset of the bunch), for jaws with a half width bigger that the smallest aperture ($h >> a$), short bunch scenarios ($\sigma_z << a$) in the case of the intermediate and diffractive models and ultrarelativistic beams. The numerical factors on the limits definition were found by setting the parameters at which the kick factor given by two adjacent regimes become equal. Special attention has to be paid in the scenarios close to the limits of the regimes where the accuracy may not be good. The resulting limits given by G. Stupakov are the following:

- **Inductive**, $\alpha < \frac{10a}{h^2}\sigma_z$

- **Intermediate**, $\frac{1}{10a}\sigma_z > \alpha > \frac{10a}{h^2}\sigma_z$

- **Diffractive**, $\alpha > \frac{1}{10a}\sigma_z$

In Fig. 3.2 the geometric regimes as a function of the tapered angle, α, and the minimum half aperture, a, of a rectangular collimation system jaws are shown for a fixed half width, h, of 12 mm and a bunch length, σ_z of 7 mm (parameters relevant for ATF2).
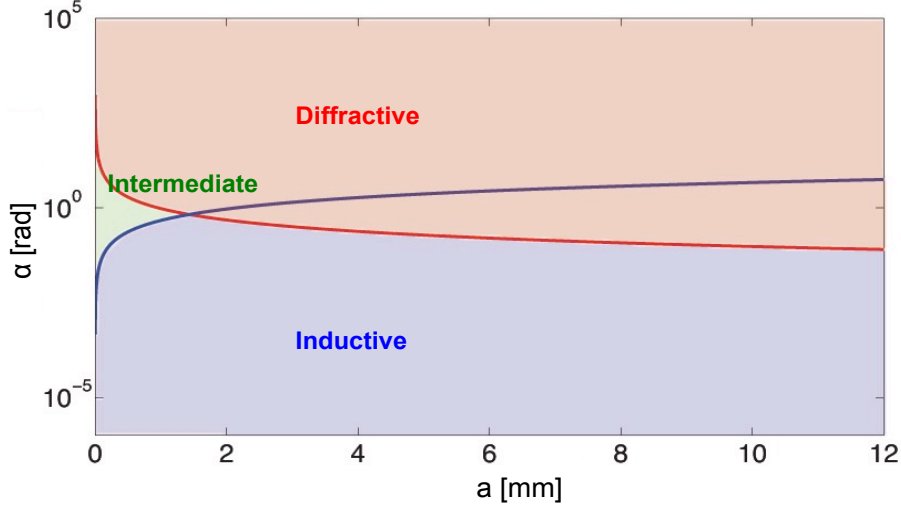
Figure 3.2: Regimes definition in [84] as a function of the tapered angle, α, and the minimum half aperture, a with $h = 12$ mm and $\sigma_z = 7$ mm (parameters relevant for ATF2).

In the following, we will introduce the analytical expressions calculated in [84] to quantify the strength of the wakefields induced by the collimation system. Furthermore, as we are studying a vertical collimation system only tapered in the vertical plane all the formulas are applied to the vertical case. The same description is applicable to the horizontal plane by replacing y by x. The geometric wakefield kick for each regime is summarized in the following.

- **Inductive**, $\alpha < \frac{10a}{h^2}\sigma_z$

    The **inductive regime** is defined when the frequency of the image current is lower than the cut off frequency to excite the first "trapped mode" in the rectangular structure. This regime corresponds to very smooth tapers and/or very long bunches. For this regime the impedance is calculated in the low frequency approximation ($\omega \to 0$) corresponding to long bunches as indicated by the Eq. (3.1). In this case, the real part of the impedance is zero and therefore the impedance is purely imaginary and does not depend on the frequency. The impedance for a rectangular tapered structure in the inductive regime is given by:

$$Z_y^g = -\frac{iZ_0}{4\pi}[(2\pi hI_2 - 2I_1)\Delta y + I_1 y] \tag{3.3}$$

$$I_1 = \int_0^\infty \frac{b'(s)^2}{b(s)^2}ds \tag{3.4}$$

$$I_2 = \int_0^\infty \frac{b'(s)^2}{b(s)^3} ds \tag{3.5}$$

Replacing the integration of Eq. (3.4) and Eq. (3.5) being $b(s) = \alpha s + a$ in Eq. (3.3) we have:

$$Z_y^g = -\frac{iZ_0}{4\pi} \left[\left(\pi h\alpha \left(\frac{1}{a^2} - \frac{1}{b^2} \right) - \frac{2(b-a)^2}{abL_T} \right) \Delta y + \frac{2(b-a)^2}{abL_T} y \right] \tag{3.6}$$

The resulting geometric kick factor considering a Gaussian beam distribution as the impedance does not depend on the frequency is obtained by replacing Eq. (1.34) into Eq. (1.30):

$$\kappa_y^g = -\frac{c}{2\sqrt{\pi}\sigma_z} Im Z_y^g \tag{3.7}$$

The geometric kick factor can be expressed in practical units of mm^{-1} for a given vertical offset, Δy, and all the units length in mm putting the integration of Eq. (3.6) into Eq. (3.7) and multiplying by $4\pi/Z_0 c$ as:

$$\kappa_y^g[mm^{-1}] = \frac{1}{2\sqrt{\pi}\sigma_z} \left[\left(\pi h\alpha \left(\frac{1}{a^2} - \frac{1}{b^2} \right) - \frac{2(b-a)^2}{abL_T} \right) \Delta y + \frac{2(b-a)^2}{abL_T} y \right] \tag{3.8}$$

By using Eq. (1.36) and considering Eq. (3.8) we can write this kick in units of rad as:

$$\Delta y'[rad] = \frac{Nr_e}{\gamma} \frac{1}{2\sqrt{\pi}\sigma_z} \left[\left(\pi h\alpha \left(\frac{1}{a^2} - \frac{1}{b^2} \right) - \frac{2(b-a)^2}{abL_T} \right) \Delta y + \frac{2(b-a)^2}{abL_T} y \right] \tag{3.9}$$

When the kick is applied to the centroid of the bunch (dipolar kick component), the geometrical kick factor is given by the Eq. (3.8) but substituting $\Delta y = y$.

- **Intermediate**, $\frac{\sigma_z}{10a} > \alpha > \frac{10a}{h^2}\sigma_z$

  The **intermediate regime** impedance was calculated in [84] only for the dipolar component, if one wants to take into account both, dipolar and quadrupolar components, Yokoya's coefficients can be used $(0.85\Delta y + 0.43y)$ [83] which are valid for ultrarelativistic particles and good conductors. Considering the impedance symmetry properties respect to the frequency and the causality principle one can calculate the wake functions only knowing the real part of the impedance [88]. The real part of the impedance in this regime is given by:

  $$ReZ_y^g(\omega) = \frac{8\sqrt{\pi}\sqrt{\alpha}}{3\sqrt{\omega/c}\sqrt{a^3 c}} (0.85\Delta y + 0.43y) \tag{3.10}$$

  Considering a Gaussian bunch and the impedance of Eq. (3.10) the wake function can be calculated. Then replacing the resulting wake function in Eq. (1.28) and Eq. (1.30) the resulting geometric kick factor in the intermediate regime in units of mm^{-1} for a given vertical offset, Δy, and all the units length in mm is:

  $$\kappa_y^g[mm^{-1}] = 2.7 \sqrt{\frac{\alpha}{\sigma_z a^3}} (0.85\Delta y + 0.43y) \tag{3.11}$$

By using Eq. (1.36) and considering Eq. (3.11) we can write the wakefield impact in units of *rad* as:

$$\Delta y'[rad] = \frac{Nr_e}{\gamma}2.7\sqrt{\frac{\alpha}{\sigma_z a^3}}(0.85\Delta y + 0.43y) \tag{3.12}$$

As fo the inductive case, by replacing $(0.85\Delta y + 0.43y)$ by Δy in Eq. (3.11) the dipolar component can be calculated.

- **Diffractive**, $\alpha > \frac{\sigma_z}{10a}$

Finally, the **diffractive regime** corresponds to abrupt transitions and /or very short bunches. In this case, the same relation used to calculate the transverse kick in the intermediate regime can be used but the real part of the impedance for a rectangular jaw taking into account Yokoya's coefficients is given by [84]:

$$ReZ_y^g(\omega) = \frac{4(1 - a^4/b^4)}{\omega a^2}(0.85\Delta y + 0.43y) \tag{3.13}$$

Replacing the resulting wake function calculated using Eq. (3.13) in Eq. (1.28) and Eq. (1.30) the kick factor obtained in units of mm^{-1} for a given vertical offset and all the units length in *mm* is:

$$\kappa_y^g[mm^{-1}] = \left(\frac{1}{a^2} - \frac{1}{b^2}\right)(0.85\Delta y + 0.43y) \tag{3.14}$$

By using Eq. (1.36) and considering Eq. (3.14) we can write the impact in units of *rad* as:

$$\Delta y'[rad] = \frac{Nr_e}{\gamma}\left(\frac{1}{a^2} - \frac{1}{b^2}\right)(0.85\Delta y + 0.43y) \tag{3.15}$$

And as for the two previous cases, the dipolar component of the kick is given by changing $(0.85\Delta y + 0.43y)$ by Δy in Eq. (3.15).

Resistive component

As introduced in chapter 1, we can distinguish two different components to the total wakefield kick. In the following we will describe the **resistive component** due to the finite conductivity of the materials of the collimation system jaws.
In order to calculate the wakefields due to the resistive conductivity of the surrounding beam walls the perturbation method was used in [87] to solve the Maxwell's equations. The resulting electric field in the longitudinal plane obtained was:

$$E_z = -\frac{Z_0 c}{4\pi}\frac{16q}{b(s)^2}\left[\frac{1}{3}e^{-\frac{z'}{s_0}}\cos\frac{\sqrt{3}z'}{s_0} - \frac{\sqrt{2}}{\pi}\int_0^\infty \frac{m^2 e^{-\frac{m^2 z'}{s_0}}}{m^6 + 8}dm\right] \tag{3.16}$$

where the characteristic length, s_0, was defined as:

$$s_0 = (2a^2/Z_0\sigma)^{1/3} \tag{3.17}$$

where a is the half aperture of the beam pipe, Z_0, is the impedance in the vacuum and σ is the conductivity of the walls material. Then, in order to compute the wakefields in

the transverse plane the Panozsky-Wenzel theorem is used and the integration of Eq. (3.16) is performed for axisymmetric parts of the collimation system. The total kick is the sum of the different parts as:

$$\kappa_y^r = 2\kappa_{y,taper}^r + \kappa_{y,flat}^r \tag{3.18}$$

There are two terms in Eq. (3.16). The first term is defined as a resonant term that goes with $(\cos \sqrt{3}s'/s_0)$ and the second one is a non-resonant one. Two regimes are defined depending on the relation between the bunch length with its associated frequency and the conductivity. When $\sigma_z \gg s_0$, the case for long bunches and/or high conductivity materials, the second term of Eq. (3.16) dominates and the first term can be neglected, this is known as the **long range regime**. In the opposite case $\sigma_z \ll s_0$, the case of short bunches and/or bad material conductivity, both terms are important and have to be taken into account, this constitutes the so called **short range regime**. As a summary the resistive regimes are defined as following:

- **Long range regime**, $s_0 \ll \sigma_z \ll (2a^2 Z_0 \sigma)$

- **Short range regime**, $\sigma_z < s_0$

For small offsets of the beam the approximated formulas to compute the induced wakefields of the collimation jaws valid if the penetration skin depth of the material is smaller than the half gap, a, in the two regimes are the following [89, 90]:

- **Long range regime**, $s_0 \ll \sigma_z \ll (2a^2 Z_0 \sigma)$:

$$\kappa_y^r[mm^{-1}] = \frac{\pi}{8a^2}\Gamma(\frac{1}{4}) \sqrt{\frac{2}{\sigma_z \sigma Z_0}}(\frac{L_F}{a} + \frac{1}{\alpha})(0.85\Delta y + 0.43 y) \tag{3.19}$$

  with all lengths in *mm* and where $\Gamma(1/4) = 3.6256$. By using Eq. (1.36) we can write Eq. (3.19) in units of *rad* as:

$$\Delta y'[rad] = \frac{Nr_e}{\gamma} \frac{\pi}{8a^2}\Gamma(\frac{1}{4}) \sqrt{\frac{2}{\sigma_z \sigma Z_0}}(\frac{L_F}{a} + \frac{1}{\alpha})(0.85\Delta y + 0.43 y) \tag{3.20}$$

  This expression is already the result of the sum of the tapered and flat part of the collimation system.

- **Short range regime**, $\sigma_z < s_0$:

$$\begin{aligned}\kappa_y^r =& \frac{2}{q\Delta y} \int_{-\infty}^{+\infty} \rho(z)dz \int_{-\infty}^{z} \int_{0}^{L_{tapered}} E_z(x, \Delta x, y, \Delta y, z - z', s)dz'ds+ \\ &+ \frac{1}{q\Delta y} \int_{-\infty}^{+\infty} \rho(z)dz \int_{-\infty}^{z} \int_{0}^{L_{flat}} E_z(x, \Delta x, y, \Delta y, z - z', s)dz'ds'\end{aligned} \tag{3.21}$$

where E_z is the electric field described in Eq. (3.16). As in previous cases by using Eq. (1.36) we can write the impact in units of *rad* as:

$$\Delta y'[rad] = \frac{Nr_e}{\gamma}\kappa_y^r(0.85\Delta y + 0.43 y) \tag{3.22}$$

In addition, the short regime can be calculated for AC and DC conductivity if the dependence of the conductivity on the frequency wants to be taken into account or not, respectively.

3.2.2 Calculation of the wakefield impact using 3D EM solvers

The 3D EM solver CST PS has been used to compute in time domain the EM fields resulting from a passing charged particle through a 3D collimation system. This software includes a wakefield solver to calculate the fields in time domain and compute the resulting wake potential by integrating these fields over the charged particle distribution. The Finite Integration Technique (FIT) is used in order to solve the Maxwell's equations. In order to perform realistic and accurate simulations different settings have to be studied and determined carefully. In the following we will describe briefly the basic steps to compute the wake potential of a 3D structure (more detail explanation of all different setting can be found in [15]):

- **3D model design**. The first step consist in designing the 3D model of the structure to simulate. This can be done using the CST PS graphic interface where basic geometries can be drawn easily and assembled. Another option is to import the model from a commercial graphic software (CATIA [95]...). When the model is built one must verify that it has no mechanical and EM leaks using the function "model intersection check" to avoid non physical solutions, and if so, one has to make the appropriate changes until there are no leaks. The material of the different components of the model can also be defined allowing to simulate both geometric and resistive contributions to the wake potential.

- **Mesh definition**. This step is the most critical one in order to perform accurate simulations without increasing dramatically the computation time. The model is divided in cuboids where the EM fields are calculated. These cuboids are called mesh cells. In CST PS a hexahedral mesh is implemented. The mesh can be controlled with the "global mesh properties" where the lines per wavelength (related with the bunch length), the "lower mesh limit" and "the mesh line ratio limit" can be modified. Also it is possible to adjust the mesh locally for some components of the model which need more detailed simulation of the field gradient with the "local mesh panel". More mesh cells more accurate the field gradient will be computed. However, this can be critical regarding the simulation time. A convergence study prior to the simulations has to be performed to fix the spatial discretization of the model and keep the computational time acceptable.

- **EM source definition**. The EM source has to be defined. The particle beam is defined by a charge distribution, the bunch length and the relativistic factor, β. It is possible to offset the trajectory of the beam and the integration path. By adding and offset to the beam and integrating in the beam path the dipole component of the wake potential is computed. By moving the integration path to the location of the test particle where $x, y \neq 0$ one can compute the quadrupolar component of the wake potential as illustrated in Fig. 3.3. The bunch length will define the maximum relevant frequency of the fields to compute. This frequency value is calculated by the CST PS software and output when defining the beam but has to be set by the user before starting the simulations. The mesh lines are related with the wavelength associated to the bunch length therefore one has to notice that increasing unnecessary the frequency will lead to a very small mesh discretization without contributing to the increase of accuracy.
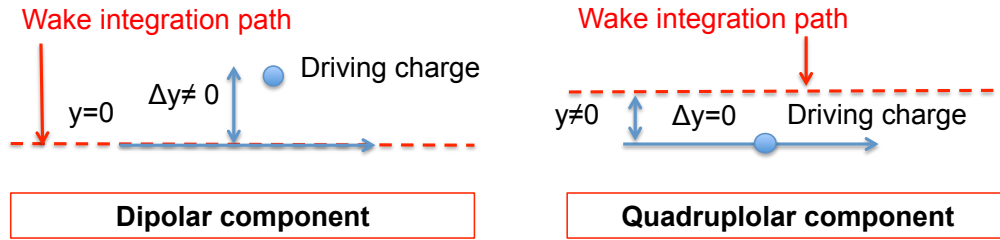
Figure 3.3: Dipolar and quadrupolar scheme computation in CST PS.

- **Boundary and background condition**. The boundary conditions of the problem have to be defined from the EM point of view in each plane. Furthermore, the background material surrounding the model, has to be defined as: normal (same material as the 3D component) or Perfect Conductor (PEC). Also ports at the entrance and exit of the structure can be added to absorb the fields and avoid reflections.

- **Wakefield calculation settings**. In order to calculate the wake potential the transient solver has to be chosen in order to compute the fields in time domain. Then, two different integration methods can be considered: direct (integration path is located in the beam path) or indirect (the integration path is located in the gaps of the structure). The second method, the indirect one, can be used to reduce the computational time but only with structure with symmetric entrance and exit (step structures). The second method is not valid for our model in which the transitions in which the EM fields are calculated are characterized by a smooth transition between a maximum aperture at the entrance and a minimum aperture at the center of the collimation system. The length over the wake potential is computed, has also to be defined in order to perform accurate impedance simulations.

In the following, I will describe the settings used in the simulations presented in this chapter. For this optimization study a simple model has been considered where the geometric parameters studied are depicted in Fig. 3.1. This simplified model consists in a rectangular chamber with two vertical rectangular independent movable jaws with tapered angle only in the vertical plane. The main volume of the model is set to vacuum and it is surrounded by PEC background material. The collimation system jaw materials studied are: Cu, Stainless Steel (SS) and Al. The entrance and exit of the beam pipe are matched with ports in order to completely absorb outgoing field that can affect the wakefield calculations. A beam charge distribution has been defined (Gaussian by default) with a bunch length of 7 *mm* and a bunch charge of 1 *pC* (notice that the resulting wake potential is charged normalized). For this bunch length the maximum relevant frequency computed by the CST PS software corresponds to 25 *GHz* related with the bunch length as $\omega \propto 1/\sigma_z$. Only the dipolar component has been computed by setting the integration path to the beam path ($y = 0$). The direct integration method has been used to compute the fields excited by the driving particle with 1 *mm* offset in the vertical plane over 600 *mm* (wakelenght). In order to optimize the number of mesh cells for the study **a convergence study** has been performed as a function of the num-

ber of lines per wavelength (parameter which increases the total of mesh cells). As a
figure of merit of this convergence study the wakefield kick, κ_y, has been computed as
a benchmark parameter. The κ_y as a function of the number of mesh cells can be seen
in Fig. 3.4. The wakefield kick has been calculated by integrating the automatically
stored wake potential in units of V/pC along the structure convoluted with a Gaussian
charge distribution normalized to the bunch charge and driving particle offset. From
this study we conclude that a good agreement is found with 3 millions of mesh cells
corresponding to 15 "lines per wavelength" (corresponding to a minimum mesh line
of 0.45 *mm*). However, in order to avoid non physical results (wake potential values
different from zero before the arrival of the bunch) the mesh in the beam propagation
plane, *z*, needed to be adjusted by using the "local mesh properties" defining a mesh
in this plane with a mesh line size of 0.3 *mm*.
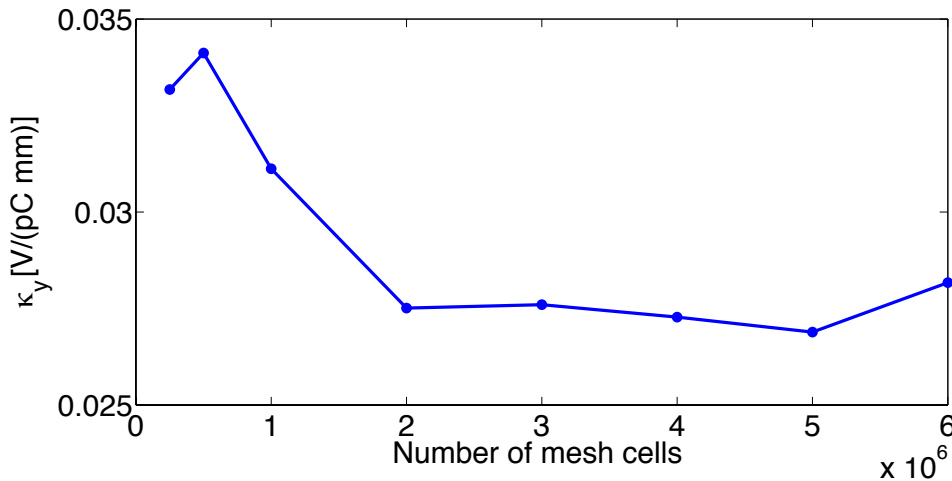
Figure 3.4: CST PS mesh cells optimization as a function of the wakefield kick, κ_y,
induced by the collimation system jaws.

Geometry wakefield study

The geometric parameters studied are the half aperture, *a*, the tapered angle, α, and
the flat length, L_F depicted in Fig. 3.1. The different geometric parameters have been
studied separately by changing their values while keeping the other geometric param-
eters fixed. For all the studies the beam has been offset 1 *mm* and the jaws have been
modeled with Cu. The aperture have been changed in the range of 2 to 8 *mm* while
the tapered angle, α, was fixed to 3° and the flat length, L_f, to 100 *mm*. The tapered
angle impact was studied for tapered angle values in the range of 3° to 90° while the
half aperture was fixed to 8 *mm* and the flat length to 100 *mm*. Last, the influence of
the flat length was studied by varying this parameter in the range of 50 to 300 *mm* with
a fix half aperture of 8 *mm* and a tapered angle of 3°. In Fig. 3.5 the vertical wake
potential obtained with CST PS for the different *a* (top), α (middle) and L_F (bottom)
are shown. Then, in Fig. 3.6 the calculated wakefield kick for all cases studied using
the analytical models introduced in this chapter are compered with the ones calculated

using the CST PS wake potential form Fig. 3.5. The analytical wakefield kick has been calculated taking into account both contributions, the geometric and the resistive one.

From these studies we conclude (see Fig. 3.6):

- **The half aperture**, a, has a big impact on the wakefield effect and good agreement was found between CST PS simulations and analytical calculations.

- The influence of **the tapered angle**, α, is close to linear for angles down to $10°$ and good agreement has also been observed between simulations and analytical calculations for small angles (**inductive regime**) and angles bigger than $60°$ (**diffractive regime**). The combination of the geometric parameters studied and the ATF2 bunch length never determine to use the intermediate regime using the G. Stupakov limits however the diffractive model does not agree with the simulations preformed with CST PS in the range of tapered angles between $10°$ and $50°$. A small tapered angle, as much as the manufacture constraints allow, is required to minimize the wakefield effect.

- The influence of **the flat part**, L_F, in the case of considering Cu as the material for the rectangular jaws is very small compared with the effect of a and α (note the scale difference) in Fig.3.6.

In order to illustrate graphically the influence of the geometry on the resulting EM fields induced by the beam and the jaws an electric field monitor has been implemented on the CST PS simulations to record the electric field evolution in time. In Fig. 3.7 and Fig. 3.8 the vertical electric field for three different time steps is illustrated when the beam is entering the structure (top) in the middle (middle) and at the exit of the structure (bottom) for two different geometries. In Fig. 3.7 the parameters of the jaw made of Cu are the following: $a = 2$ mm, $\alpha = 45°$ (corresponding to the **diffractive** model regime) and $L_f = 2$ mm. While for the second case in Fig. 3.8, the geometric parameters are the following: $a = 4$ mm, $\alpha = 3°$ and $L_f = 10$ mm (corresponding to the **inductive** model regime). For the first case corresponding to a more abrupt transition, the asymmetry on the resulting electric fields up and down in the vertical plane is stronger and will result in a higher kick induced to the beam.

Material wakefield study

The influence of the material of the collimation system jaws on the wakefield kick has been studied. Three different materials have been considered: Cu, SS and Al. The results for the case of considering a jaw with a=5 mm, α=3° and L_f=100 mm are summarized in Table 3.1 for the three different materials with the corresponding conductivity, σ.

The difference observed between the impact of Cu, Al and SS is small compared with the impact of the geometric parameters, however SS shows to be the worst candidate. Higher conductivity less wakefield impact observed with both, analytical models and CST PS simulations. Cu and Al show a similar wakefield impact while the calculated wakefield strength for SS is a 20% higher than for the other two materials.
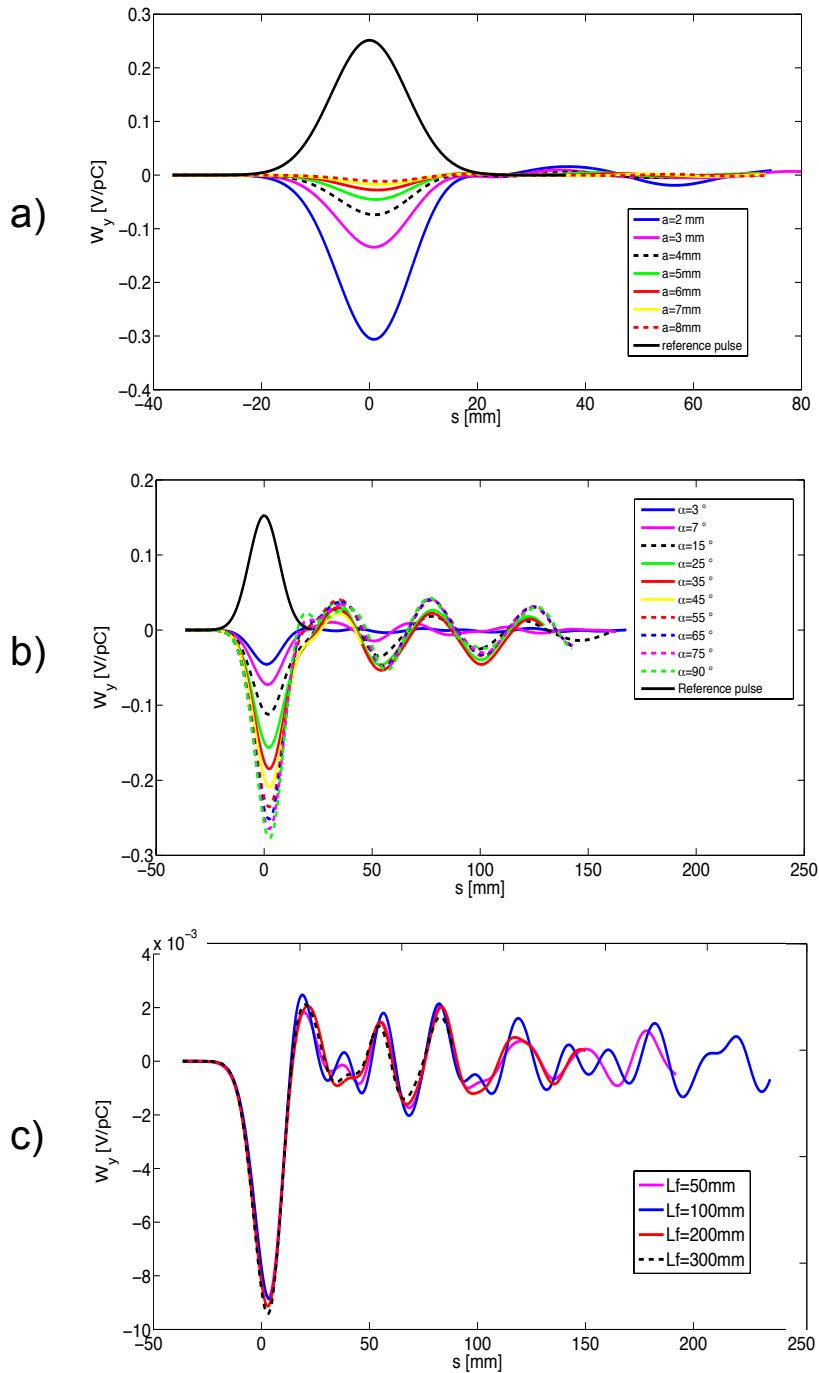
Figure 3.5: Vertical wake potential calculated with CST PS for: a) half apertures varying from 2 to 8 *mm* with a tapered angle of 3° and a flat length of 100 *mm*. b) tapered angle varying from 3 to 90° with a half aperture fixed to 5 *mm* and the flat length to 100 *mm*. c) flat lengths varying from 50 to 300 *mm* with a fix half aperture of 8 *mm* and a tapered angle of 3°.
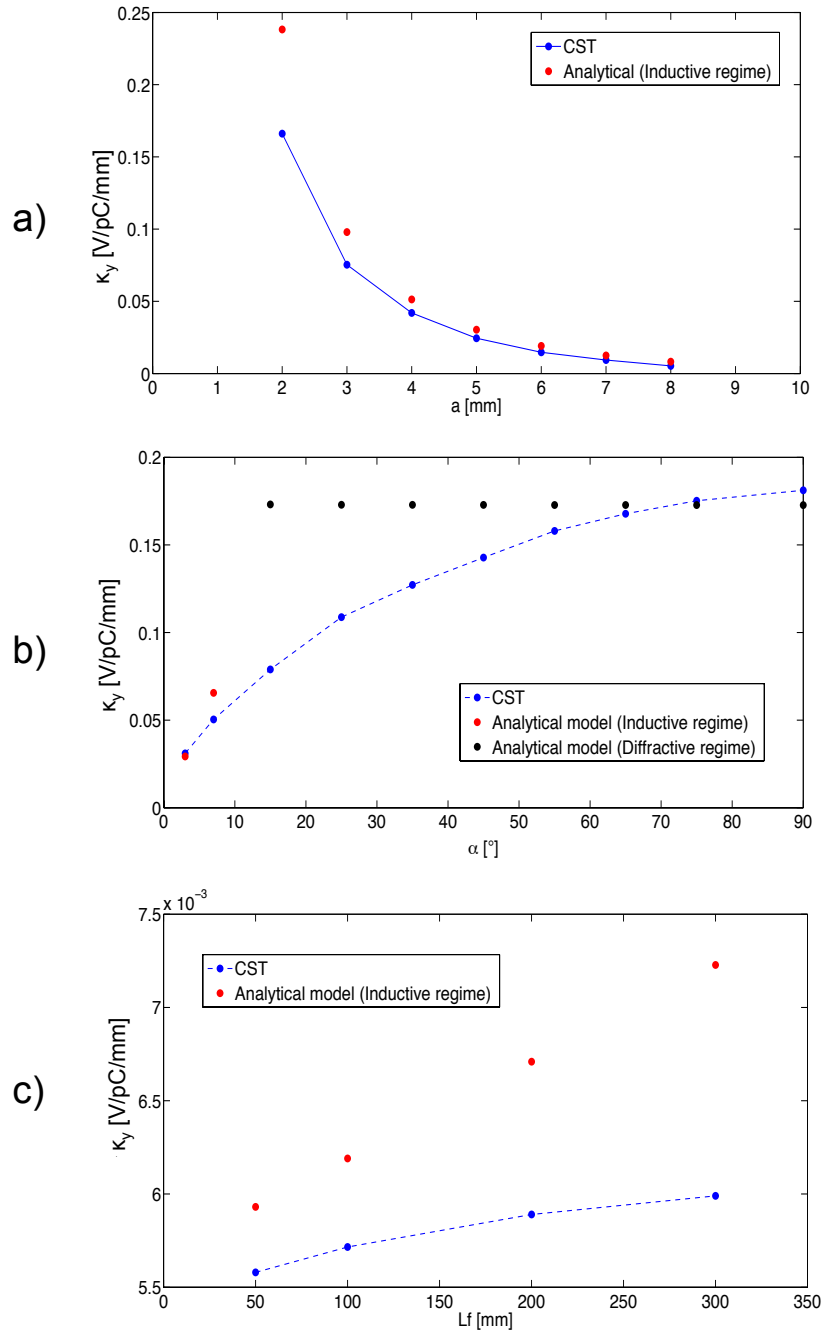
Figure 3.6: CST PS and analytical wakefield kick for: a) half apertures varying from 2 to 8 *mm* with a tapered angle of 3° and a flat length of 100 *mm*. b) tapered angle varying from 3 to 90° with a half aperture fixed to 5 *mm* and the flat length to 100 *mm*. c) flat lengths varying from 50 to 300 *mm* with a fix half aperture of 8*mm* and a tapered angle of 3°.
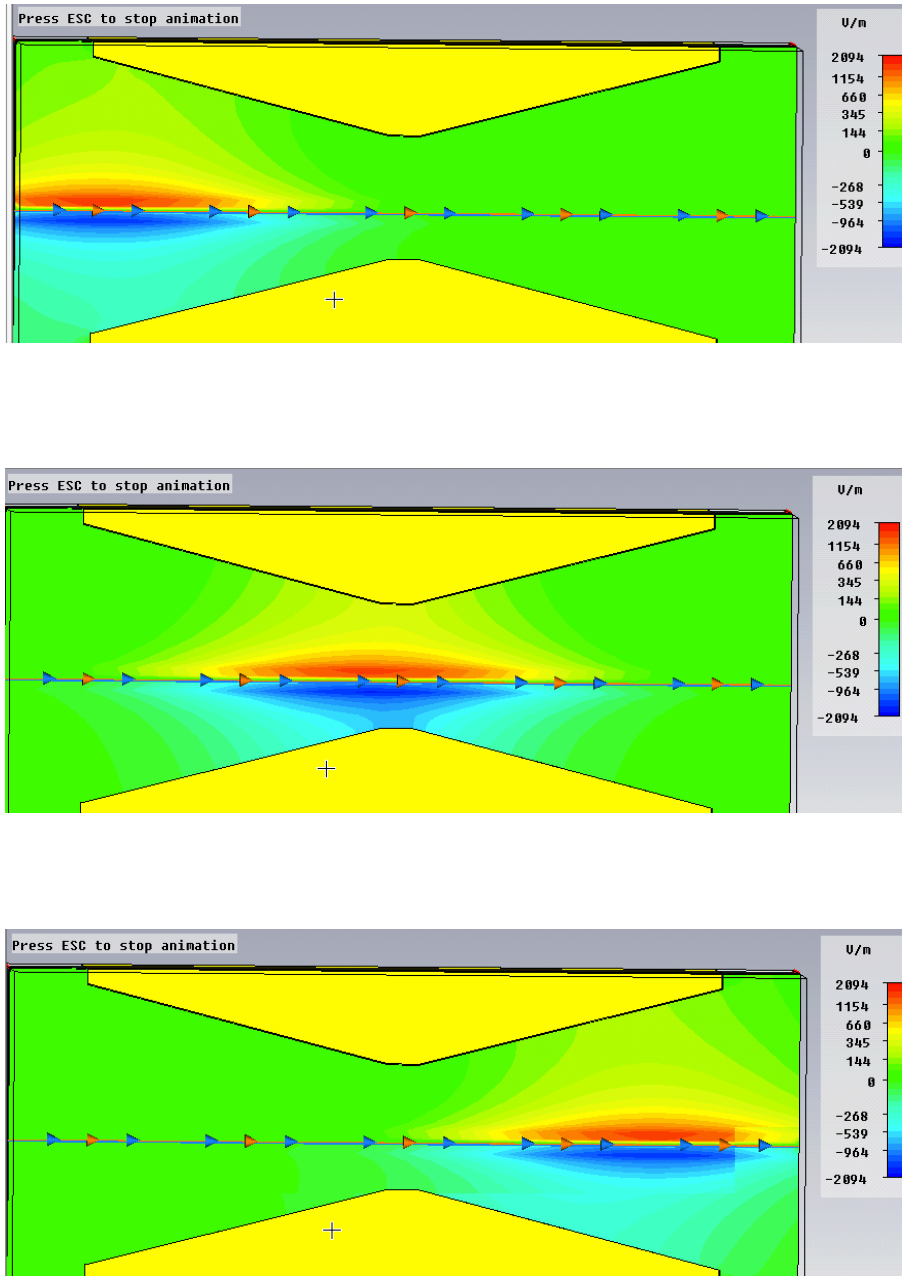
Figure 3.7: CST PS vertical electric field evolution for $a=2$ mm, $\alpha = 45°$ and $L_f = 2$ mm and Cu jaws. For this abrupt transition geometry ($\alpha >>$) and the ATF2 bunch length of 7 mm (long bunches) the geometric regime corresponds to the **diffractive**.
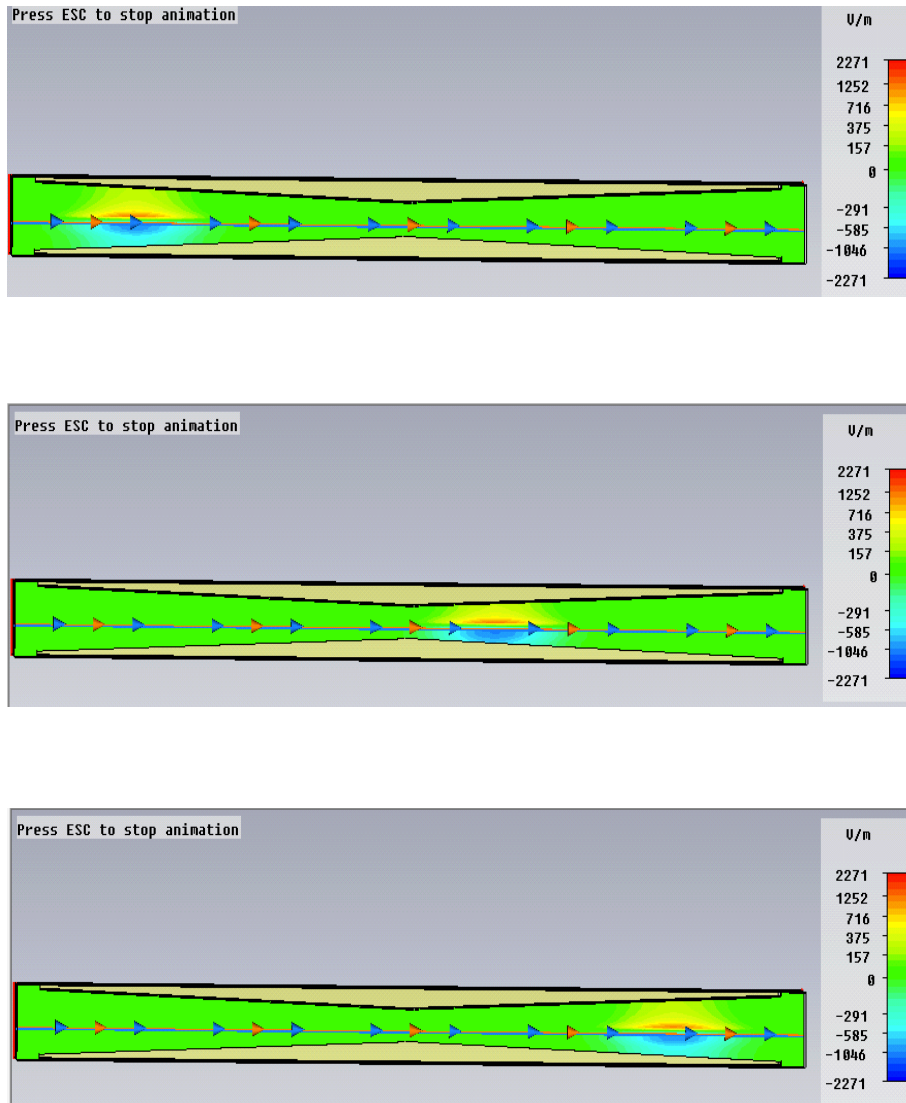
Figure 3.8: CST PS vertical electric field evolution for $a = 4$ mm, $\alpha = 3°$ and L_f = 10 mm and Cu jaw. For this smooth tapered transition geometry ($\alpha \ll$) and the ATF2 bunch length of 7 mm (long bunches) the geometric regime corresponds to the **inductive** one.

Material	$\kappa_y^{Analytic}[V/pC/mm]$	$\kappa_y^{CST\ PS}[V/pC/mm]$	$\sigma[S/m]$
Cu	0.024	0.025	5.9×10^7
Al	0.025	0.025	3.7×10^7
SS	0.030	0.032	1.3×10^6

Table 3.1: Materials studied with the corresponding analytical, $\kappa_y^{Analytic}$, and numerical, $\kappa_y^{CST\ PS}$, wakefield kick calculated and the corresponding material electric conductivity [96].

3.2.3 Other design studies

Flat length considerations

The collimation system has to be able to stop 1.3 GeV electrons and the EM cascade produced. By using the simple model introduced in chapter 1 one can calculate which is the required length of the jaws depending on the material. The calculation has been performed for 3 different materials: Cu, Al, SS and it is summarized in Table 3.2.

Material	Z	ρ [g/cm^3]	E_C[MeV]	X_0[cm]	n	z_{max}[cm]
Cu	29	8.96	20.17	1.44	6	8.6
Al	13	2.70	42.84	8.90	5	44.48
SS	26	7.86	22.39	2.26	6	13.24

Table 3.2: Materials studied, with the corresponding atomic number, Z, the density, ρ, the critical energy, E_C, the radiation length, X_0, the required number of radiation lengths, n, and the corresponding length, z_{max} for the number of radiation lengths calculated.

From the calculations summarized in Tabe 3.2 we conclude that to stop the EM cascade gnerated by 1. 3 GeV electron with Cu we need about a flat length of 8.6 cm. The length of material needed using Al is 4.5 times more while in the case of using SS it is about 1.5 times more.

Power loss calculation

In order to estimate if cooling of the jaws is needed, the temperature rise due to the power dissipated by the beam in case of the impact of a full bunch has been estimated. The wakefields induced could rise the temperature of the jaws by power dissipation. The power dissipated by the beam can be calculated using the kick loss factor, κ_{loss}, calculated with CST PS using the following relation:

$$P_{lost} = \kappa_{Loss}q^2N_bf_{rep} \tag{3.23}$$

where q is the charge of the beam, N_b the number of bunches and f_{rep} the repetition frequency. In Fig. 3.23 the resulting κ_{Loss} as a function of the half aperture of the collimation system can be seen in blue and the corresponding associated power loss in green calculated using Eq. (3.9). Where for the calculation of the power loss the ATF2 nominal beam parameters have been used being $q = 1.6\ nC$, $N_b = 1$ and $f = 3\ Hz$.
The jaws will be installed in a vacuum chamber as the ATF2 beamline operates at ultra low vacuum. For these reason, the heating dissipation could be assumed to be only due to radiation which allows us to neglect the heating by convection and conduction. In this case, the net power loss by radiation is given by the Stefan-Boltzmann equation:

$$P = e\sigma\frac{A}{f}(T^4 - T_c^4) \tag{3.24}$$

where e is the emissivity of the material, σ is the Stefan-Boltzmann constant, A is the area of the jaw seen by the beam, f is the view factor, T is the temperature of the jaw,
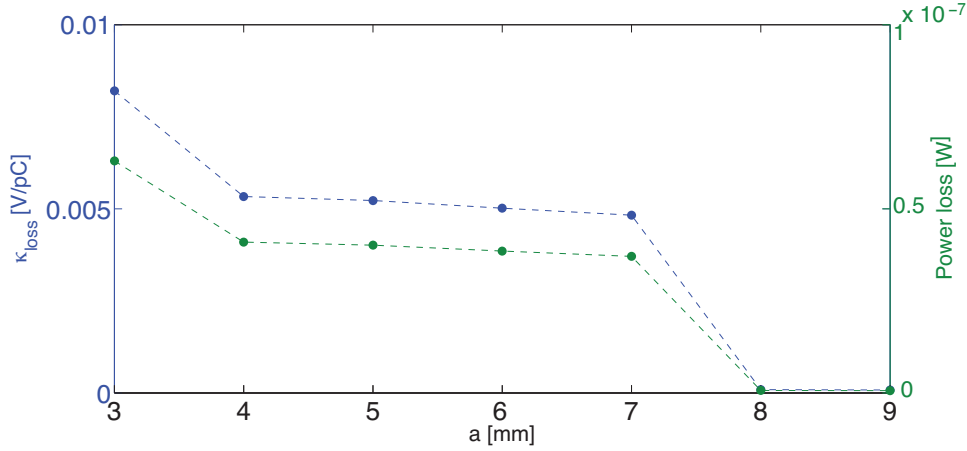
Figure 3.9: Wakefield kick loss (blue) and power loss due to wakefields (green) for different collimation system jaws half apertures.

and T_c is the temperature of the beam pipe. Using the Eq. (3.24) we can estimate the rise temperature of the jaws due to the power dissipated by the a bunch of particles. For this calculation we considered the worst case corresponding to the case when the collimation system is closed to a half aperture of 3 mm. For this aperture the power dissipated shown in Fig. 3.9 stands for 0.06 μW. The emissivity of the Cu is 0.015, the Stefan-Boltzmann constant stands for 5.672×10^{-8} W/m^2 K^4 and the room temperature has been considered to be 298 K. The dimensions considered for these calculations are 250 mm in the longitudinal axis and 24 mm for both the horizontal and vertical axis. With this dimension the surface of the jaws that will be absorbing radiation facing the beam stands for 0.005 m^2. The view factor is calculated estimating the angle occupied by the jaws with respect the 2π angle of a cylinder covering the beam pipe where the beam power is being dissipated uniformly in all directions. For our case, the view factor has been estimated to be 0.1667. With all this defined parameters and using Eq. (3.24) the temperature rise of the jaws due to the radiation absorbed by the jaws due to the wakefileds induced by the beam is about 0.02 mK.

Another mechanism which can lead to temperature rise of the jaws to be considered here is the direct interaction of the electrons of the beam with the jaws. In order to get an order of magnitude of the jaws rise temperature due to this phenomenon and determine if further simulation studies are required a first calculation can be done using the following equation:

$$U = c_p m \Delta T \tag{3.25}$$

where U is the energy deposited, c_p is the specific heat, m the mass of the object and ΔT the temperature change. If we consider that a full bunch of particles with the nominal ATF2 beam intensity and energy deposit all the energy in a uniform way on the Cu jaw the resulting variation of temperature is about 5 mK per bunch. In this calculation the specific heat of Cu used is 390 $J/kg/K$ (at 283 K), the total energy deposited by a full bunch of particles considering the ATF2 nominal beam parameters is about 2 J and the total mass of the Cu jaw has been considered to be 1 kg.

From these calculations we could conclude that the temperature rise of the Cu jaw is negligible from the mechanical point of view even if a full bunch impact into the jaw. As a consequence we consider unnecessary to perform more accurate simulations regarding this issue for the collimation system design and no cooling system is required.

3.2.4 Discussion and choice of the jaws geometry

The design of the collimation system jaws has to be done in terms of wakefield minimization, efficiency considering that only a single jaw will be installed and survivability. In order to determine the geometry and material of the jaws the following issues have been taken into account:

- **The flat part of the jaws** has to be able to absorb the EM shower produced by 1.3 *GeV* electrons to be efficient minimizing the emission of secondary particles and beam halo generation. Regarding the material, **Cu** shows to be the **best candidate** requiring a shorter flat length in order to absorb the 1.3 *GeV* electrons and produced EM shower. This is also valuable concerning that the available space to install the collimation system is limited. At the same time contributes in minimizing the wakefields due to its high conductivity.

- The available free space is about 600 *mm*. From this space only about 300 *mm* can be used for the jaws because space is also needed for the flexible transition part which will connect the jaws with the beam pipe. This **transition part** has to be **smooth** ($\alpha <<$) in order to not add additional wakefields.

- From the survivability point of view the **rise temperature** due to the beam power lost and impact of a full bunch has been estimated. The rise temperature calculated is **negligible** and therefore no restriction in this aspect is introduced to chose of the material and no cooling for the jaws will be needed.

- Concerning the **wakefield impact** induced by the **collimation system jaws** other two structures installed in the ATF2 with well known wakefield impact have been simulated with CST PS for the sake of **comparison**. Several **reference cavities** are installed in the ATF2 beamline in order to calibrate the C-BPMs system. The wakefield impact of one of these systems installed in the past between the QM10AFF and QM10BFF magnets was studied in detailed by means of numerical simulations using Gdfidl [97] and measurements [98]. This structure was removed and changed by the currently installed **TBP** because of the high vertical wakefield impact induced observed. The reference cavity has a circular geometry with a half aperture transition from 8 to 19 *mm* without taper (90° transition) (see Fig. 3.10 (left)) while the TBP has a circular geometry with a fixed half aperture of 8 *mm* and a tapered angle of 7° (see Fig. 3.10 (right)). The simulations performed of the reference cavity were compared with the previous studies performed with Gdfidl to benchmark the CST PS numerical simulation performed in this work. Using CST PS and the settings presented on this chapter, the wake potential for these two structures has been computed and compared with the one obtained for the vertical jaws with different geometries. The resulting wake potential for 1 *mm* beam offset is depicted in Fig. 3.11

for the reference cavity and the TBP. The wakekield kick for the reference cavity considering a beam offset of 1 mm is $\kappa_y^{CST\ PS}$=0.079 $V/pC/mm$ while for the TBP is $\kappa_y^{CST\ PS}$=0.005 $V/pC/mm$, one order of magnitude difference is observed between the wakefield strength of these two structures.
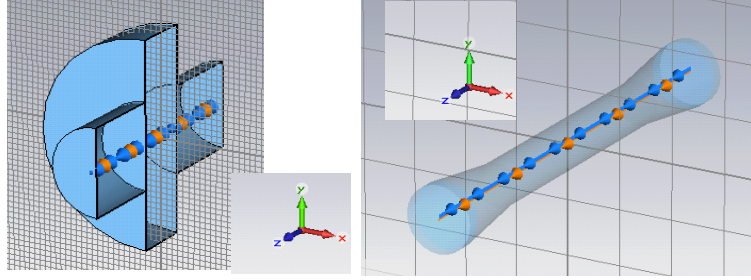
Figure 3.10: Reference cavity CST PS model (left) and TBP model (right).
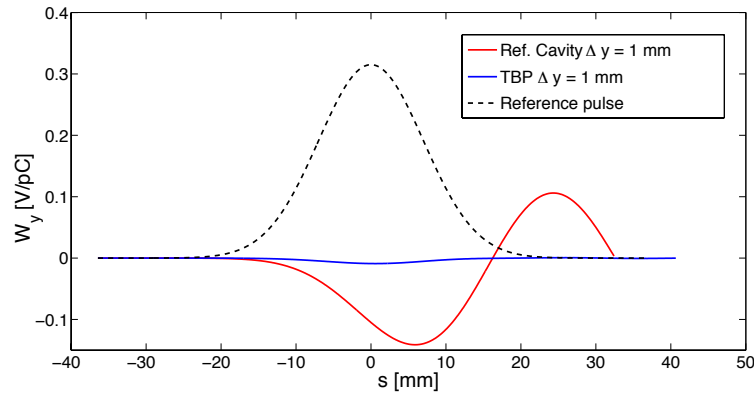
Figure 3.11: Wake potential for the reference cavity and TBP considering a bunch length of 7 mm and a beam offset of 1 mm (parameters relevant for the ATF2).

In order **to reduce the wakefield impact** a small tapered angle as the available free space and mechanical constraints allow us is needed. Considering a **flat part of the jaw of 100** mm **of Cu**, the available space and the mechanical constraints lead to a minimum **tapered angle of 3°**. With these parameters the wakefield kick for different apertures have been calculated and compared with the reference cavity and the TBP calculation for 1 mm vertical offset, Δy, in Table 3.3. For these specifications the wakefield impact of the jaws when closing the collimation system to 8 mm is $\kappa_T^{CST\ PS}$ = 0.006 V/pC/mm, value which is comparable with the impact of the TBP. With the described rectangular collimation system we need to consider a half aperture of 3 mm to have the same order of magnitude wakefield impact than the reference cavity.

- The **collimation system aperture** chosen allowing to work with different half apertures in different operation modes to cover different experiments is **between 3 and 12** mm.

Structure	a [mm]	$\kappa_y^{CST\ PS}\,[V/PC/mm]$
Ref. Cavity	19	0.079
TBP	8	0.008
COLLBY	3	0.075
COLLBY	8	0.006
COLLBY	12	0

Table 3.3: Reference cavity, TBP and different collimation system jaws half apertures
wakefield kick. Notice that the standard ATF2 half aperture corresponds to 12 *mm*.
Calculations performed for 7 *mm* bunch length.

The chosen **geometry and material for the collimation system jaws is summarized**
in Table 3.4.

	Material	a [mm]	$\alpha[\circ]$	$L_F[mm]$
COLLBY	Cu	3-12	3	100

Table 3.4: Final geometry and material specifications for the vertical collimation sys-
tem.

The wake potential for Cu jaws with $\alpha = 3°$, $L_f = 100$ *mm* and considering a half aper-
ture of 5 *mm* for the transverse and longitudinal planes is depicted in Fig. 3.12 due to a
vertical beam offset, Δy, of 1 *mm*. The black curve corresponds to the reference pulse
indicating the bunch length duration. The red curve corresponds to the wakefields ex-
ited in the horizontal plane, W_x, which are zero if the beam is only offset in the vertical
plane. In green we have the induced wake potential in the longitudinal plane, W_z, and
in blue the strongest contribution corresponding to the vertical wake potential, W_y. The
average of the transverse wake potential will lead to a displacement of the bunch of
particles while the longitudinal will lead to a variation of the energy of the bunch. By
integrating the wake potential of Fig. 3.12 the transverse and longitudinal wakefield
kick factors can be calculated.
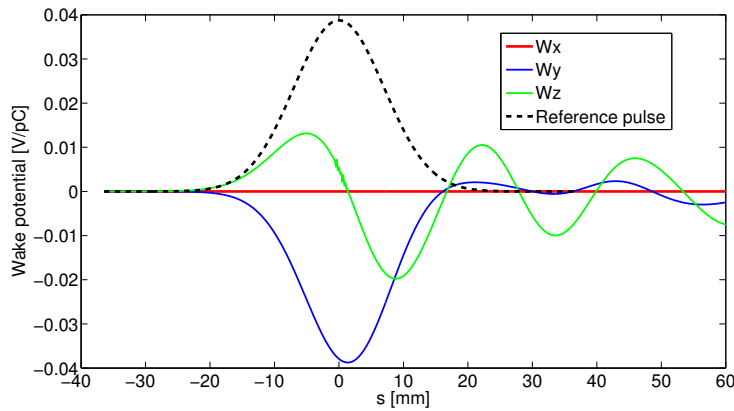
Figure 3.12: Wake potential calculated with CST PS for the optimized jaws parameters
(Cu, α=3°, L_f=100 mm and a=5 *mm*).

The longitudinal wake potential induces and energy variation quantified by the loss kick factor, κ_{loss} as:

$$\delta E = \kappa_{loss} Q \qquad (3.26)$$

where δE is the bunch energy loss due to the longitudinal wake potential induced by the vertical collimation system, κ_{loss} is the loss kick factor computed with CST PS and Q is the total charge of the bunch.

A summary of the wakefield impact for different collimation system jaw half apertures is shown in Table 3.5. In these calculations the ATF2 design beam parameters have been considered being the beam intensity 1600 pC (10^{10} electrons) and the beam energy 1.3 GeV. The wakefield kick is expressed in units of $V/pC/mm$ and physical units of rad for the vertical case and in units of V/pC and eV for the longitudinal case.

a [mm]	$\kappa_y^{CST\ PS}$ [V/pC/mm]	$\kappa_y^{CST\ PS}$ [$\times 10^9$ rad]	$\kappa_{loss}^{CST\ PS}$ [V/pC]	$\kappa_{loss}^{CST\ PS}$ [eV]
3	0.075	58	0.008	13
4	0.042	32	0.005	8
5	0.024	19	0.005	8
8	0.005	4	0.0001	0.2
12	0	0	0	0

Table 3.5: Wakefield kick factor summary for the optimized jaws geometry in units of $V/pC/mm$ and physical units of rad for the vertical case and in units of V/pC and eV for the longitudinal case.

The impact of an additional offset in the horizontal plane has also been investigated. In Fig. 3.13 the comparison of the horizontal and vertical wake potential for horizontal and vertical beam offsets from 1 to 3 mm are shown. As the collimation system is only tapered in the vertical plane and the horizontal aperture is as big as the beam pipe, the resulting wake potential in the horizontal plane is one order of magnitude smaller than in the vertical plane for the same beam offset in the corresponding plane. For 1 mm horizontal offset the resulting wake potential is one order of magnitude lower than the one of the TBP.

Furthermore, the dependence of some beam parameters (as the beam offset and the bunch length) on the wakefields induced has also been studied for a better understanding of the impact that this structure may have when being installed in the ATF2 beamline for different operation modes. In Fig. 3.14 the vertical wake potential (top) and vertical kick (bottom) for different **vertical beam offsets** is shown for the vertical collimation system optimized parameters. **A linear dependence can be observed** in agreement with expected.

The dependence on **the bunch length**, σ_z, has also been investigated for possible future scaling to other scenarios as the FLC. In Fig. 3.15 the vertical wake potential (top) and vertical kick compared to the analytical calculations (bottom) (inductive regime) are shown. **Good agreement is observed between the analytical dependence and the numerical one** for the bunch length range studied.
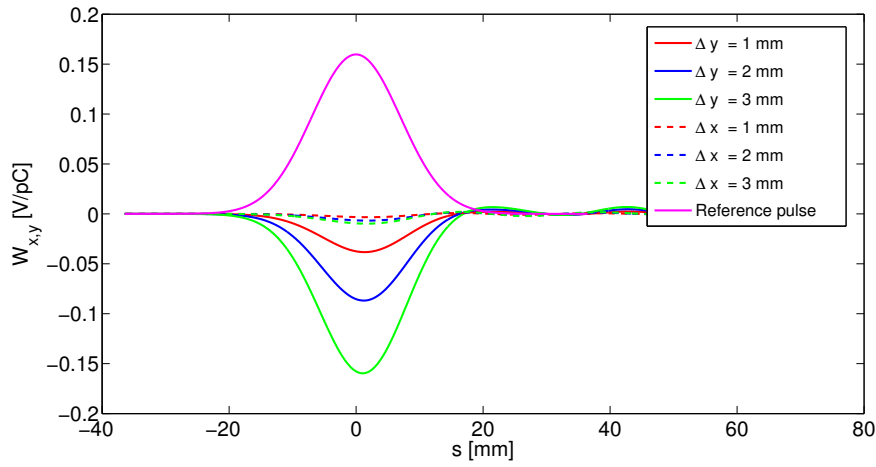
Figure 3.13: Comparison of the horizontal and vertical wake potential for horizontal and vertical beam offsets respectively from 1 to 3 *mm*.
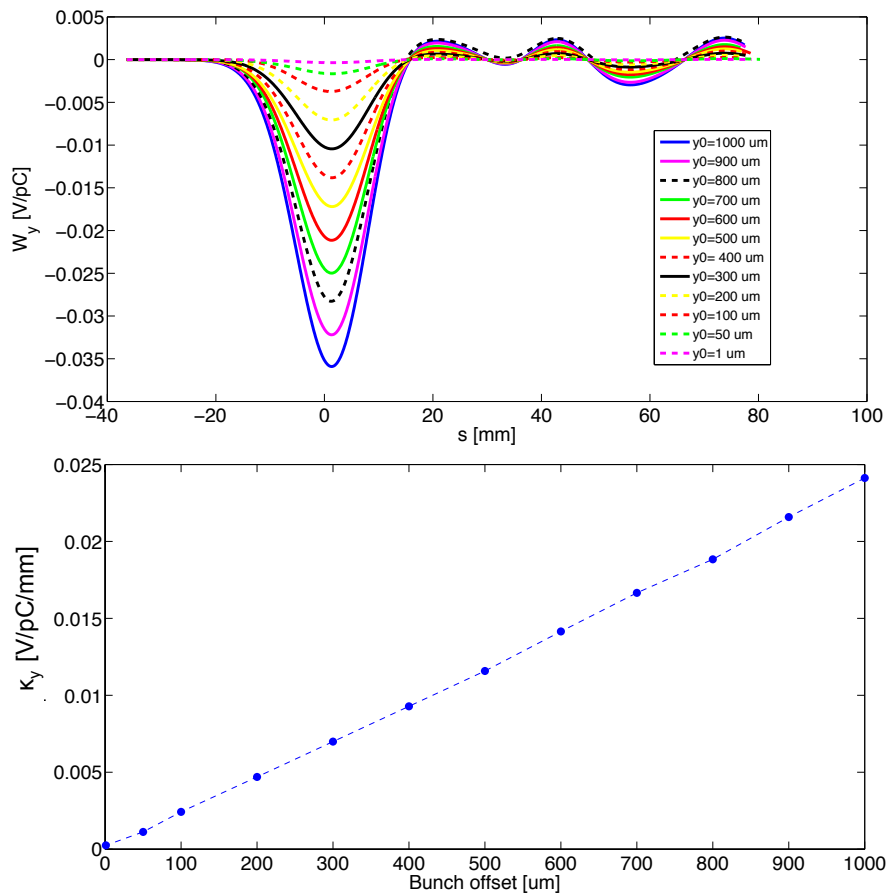
Figure 3.14: Vertical wake potential (top) and vertical wakefield kick (bottom) calculated with CTS PS for different vertical beam offsets for a bunch length of 7 *mm* (ATF2 bunch length) and 5 *mm* vertical collimation system half aperture.
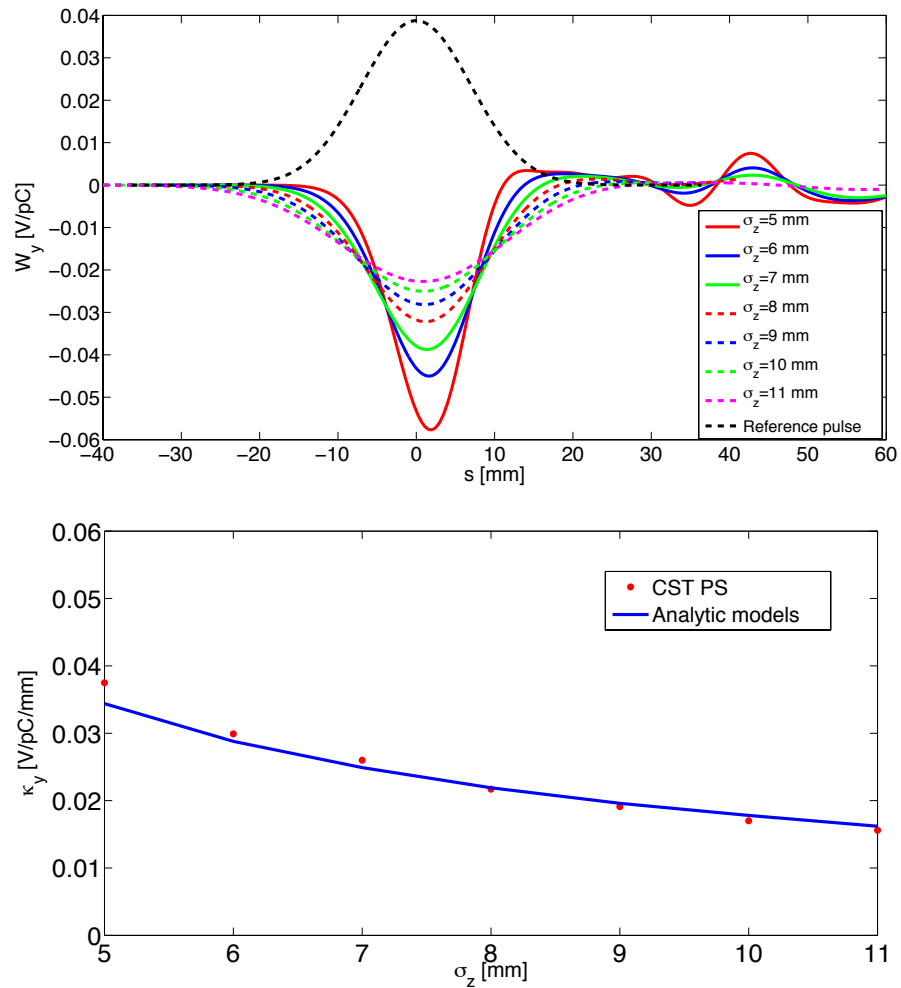
Figure 3.15: Vertical wake potential (top) and vertical wakefield kick compared with the analytical estimations (bottom) calculated using CST PS for different bunch lengths, 1 *mm* vertical beam offset and 5 *mm* vertical collimation system half aperture.

3.3 Collimation system induced wakefields beam dynamic studies in the ATF2 case

The very small vertical beam size at the IP in ATF2 and the IPBSM measurements determine very tight tolerances in the FFS. Small perturbation on the orbit of each individual particle and the bunch due to static and dynamic imperfections yield to an increase of the beam size at the IP. The implications of the wakefields induced by the vertical collimation system on the beam dynamics have to be evaluated to determine if the induced changes on the beam dynamics are acceptable or not.

One of the tracking codes that can be used to evaluate some collective effects, as the wakefields, is the tracking code PLACET [99]. We were specially interested in the tracking code PLACET because it has a module to compute the wakefields of rectangular collimation systems based on the analytical models used on this work introduced at the beginning of this chapter.

The thick lens tracking code PLACET is a code written in C++ fully programmable and modular that simulates the beam transport and correction of the orbit in linear machines. The tracking studies are performed in 4D and 6D using two possible beam models: single particle or sliced beam. The code implements several collective effects like synchrotron light emission, long and short resistive range wakefields (for AC and DC conductivity) and geometric collimation system wakefields.

A set of library functions compose the code and the user writes his own simulation program using the functions provided by the simulation system. It is easy to access to the different functions to check or understand what it is implemented. Furthermore, regarding the wakefield effects it is possible to implement the CST PS numerical wake potential for a fixed offset of the structure. A text file has to be added and the code has a function to interpolate the wake potential and apply it to the sliced beam in order to transport a more accurate calculation of the wakefields induced by arbitrary geometries.

In this section, we present first a benchmarking study performed to test the results of the tracking code PLACET. This study has been performed comparing the results from the tracking code PLACET with the linear propagation of the calculated wakefield kick using CST PS. In the second part of this section the wakefield impact of the vertical collimation system on the beam orbit and beam size, as well as its intensity dependence, have been studied.

3.3.1 Tracking code PLACET (v1.0.0) benchmarking and upgrade

In order to benchmark the results from the tracking code PLACET, the resulting beam orbit and beam size growth have been compared with the linear propagation of the calculated wakefield kick from CST PS. However, when comparing the results some discrepancies were found between the results obtained with PLACET (v1.0.0) and the linear propagation of the wakefield kick calculated with CST PS by one order of magnitude. A detailed study was performed and the source of the discrepancies was found to be on the definition of the limits of the analytical calculation relevant for the ATF2 case. The problem was solved and the program has been modified accordingly in a new version of the tracking code PLACET (v1.0.1) [43]. Then, the new version of the tracking code PLACET (v1.0.1) was used to study the wakefield effect induced

on the ATF2 orbit and beam size at the IP. The results of these studies are presented at the end of this section.

The collimation system transverse wakefield module in PLACET (v1.0.0)

The geometric and resistive wakefield components implemented in the tracking code are based on the models described in this chapter but for the resistive case the calculations were expanded for AC-conductivity and an additional intermediate regime was defined by G. Rumolo [103]. Both dipolar and quadrupolar contributions are taken into account in the linear regime, where the particles are close to the machines axes with respect to the collimation system half aperture. For beam halo particles, nonlinear components may become important and in that case the wake function is scaled as described in [101]. In this section, we will describe the formulas implemented in the tracking code PLACET (v1.0.0) for the vertical plane, y, because the collimation system under study is only tapered in the vertical plane but the same formulas apply for the horizontal case by just replacing y by x.

Geometric component

First, we will describe the **geometric kick factor**. The classification implemented in PLACET (v1.0.0) for the geometric wakefield kick is the following:

- **Inductive**, $\alpha < \frac{a}{10h^2}\sigma_z$

- **Intermediate**, $\frac{a}{10h^2}\sigma_z > \alpha > 10\frac{a}{h^2}\sigma_z$

- **Diffractive**, $\alpha > 10\frac{1}{h^2}\sigma_z a$

In Fig. 3.16, the geometric limits implemented in PLACET (v1.0.0) (bottom) as a function of the tapered angle, α, and the minimum half aperture, a, for a vertical collimation system with $h = 12$ mm and $\sigma_z = 7mm$ (relevant for ATF2) are shown in comparison with the regimes defined by G. Stupakov [84] (top). As can be seen in this figure for the ATF2 collimation system case (indicated with a black line) in PLACET (v1.0.0) the intermediate regime is considered while following the prescription from G. Stupakov the inductive regime should be used. **The applicability of the analytical models has to be carefully assessed since they are developed under some concrete approximations and can only describe specific cases which satisfy all these approximations. Numerical simulations and measurements are essential for benchmarking.**
The geometric transverse kick in units of rad is implemented in PLACET for each particle or macroparticle at a longitudinal position, z, assuming that each electron slice in the bunch acts only on itself as following:

$$\Delta y'(z)[rad] = \frac{Nr_e}{\gamma}\rho(z)\tilde{\kappa}_y[A\Delta y + By] \tag{3.27}$$

where $\rho(z)$ is the bunch distribution, $\tilde{\kappa}_y$ is the wakefield kick and $[A\Delta y + By]$ corresponds to the dipolar and quadrupolar components. A and B are given by the calculation done by G. Stupakov in the case of the inductive regime and by Yokoya's coefficients in the
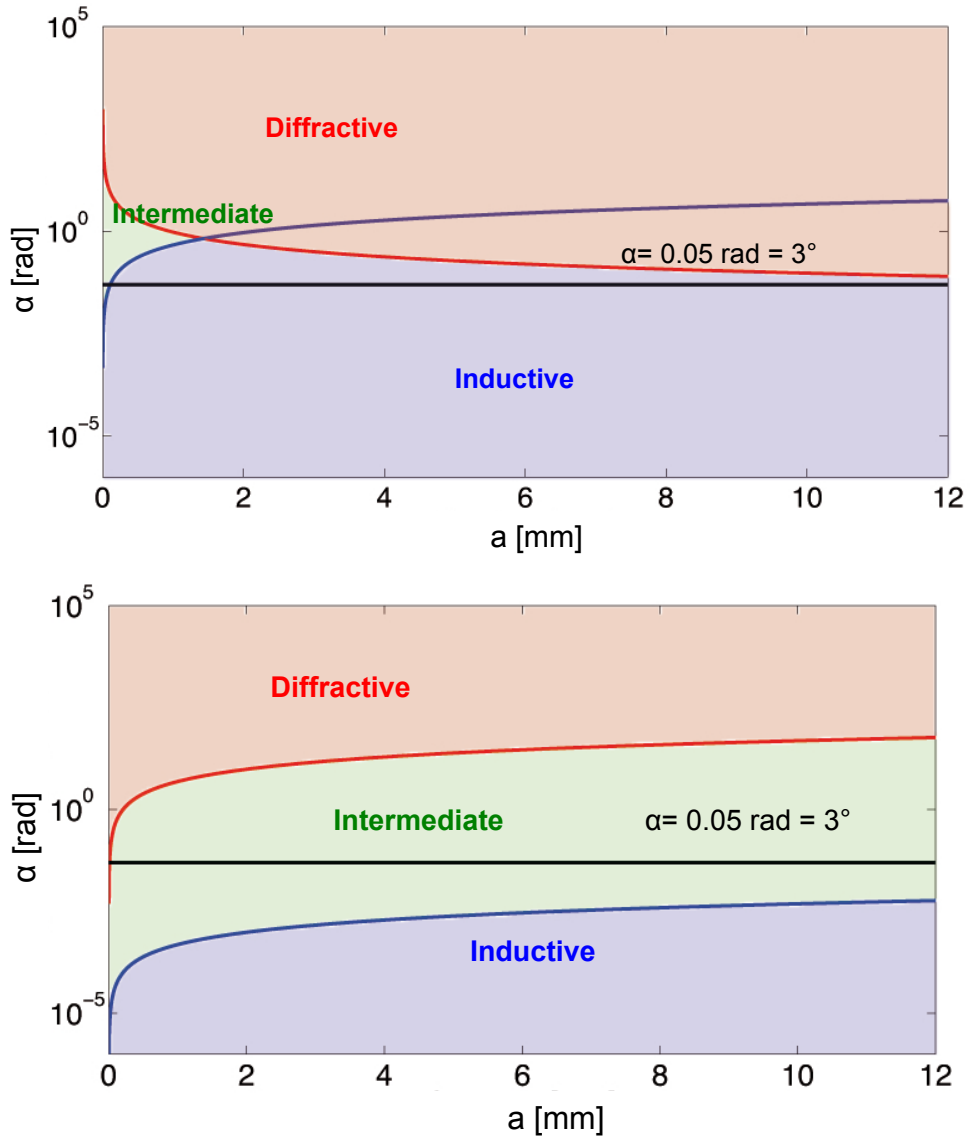
Figure 3.16: Regimes definition in [84] (top) and implemented in PLACET (bottom)
as a function of the tapered angle, α, and the minimum half aperture, a. The black line
indicates the ATF2 collimation system case.

case of the intermediate and diffractive regime. This gives a kick that varies according
to the position in the bunch depending on the particles in each slice. The kick factor,
$\tilde{\kappa}_y$, is implemented in the code such as the average of $\Delta y'(z)$ gives the analytical κ_y
presented in section 1.2.

The geometric kick for each particular regime in units of rad and all lengths in mm is
given by:

- **Inductive**, $\alpha < \frac{a}{10h^2}\sigma_z$ to be compared with Eq. (3.9),

$$\Delta y'(z)[rad] = \frac{Nr_e}{\gamma}\frac{1}{\sqrt{2\pi}\sigma_z}exp\left(-\frac{z^2}{2\sigma_z^2}\right)\left[\left(\pi h\alpha\left(\frac{1}{a^2}-\frac{1}{b^2}\right)-\frac{2(b-a)^2}{abL_T}\right)\Delta y+\frac{2(b-a)^2}{abL_T}y\right]$$
(3.28)

- **Intermediate**, $\frac{a}{10h^2}\sigma_z > \alpha > 10\frac{a}{h^2}\sigma_z$ to be compared with Eq. (3.12),

$$\Delta y'(z)[rad] = \frac{Nr_e}{\gamma}\frac{1}{\sqrt{2\pi}\sigma_z}exp\left(-\frac{z^2}{2\sigma_z^2}\right)2\frac{8\sqrt{\pi}\sqrt{\alpha}\sqrt{\sigma_z}}{3\sqrt{a^3}}(0.85\Delta y+0.43y)$$
(3.29)

- **Diffractive**, $10\frac{a}{h^2}\sigma_z < \alpha$ to be compared with Eq. (3.15),

$$\Delta y'(z)[rad] = \frac{Nr_e}{\gamma}\frac{1}{\sqrt{2\pi}\sigma_z}exp\left(-\frac{z^2}{2\sigma_z^2}\right)\frac{2\sqrt{\pi}\sqrt{2}\sigma_z(1-a^4/b^4)}{a^2}(0.85\Delta y+0.43y)$$
(3.30)

Resistive component

In the following, we will describe how the **resistive kick factor** is implemented on the code. The implementation of the **resistive wakefield** contribution in the tracking code PLACET (v1.0.0) is described in [103] based on [89, 90, 100]. The regimes were reviewed and expanded by G. Rumolo. The resulting classification is the following:

- **Long range regime**, $10s_0 < \sigma_z$

- **Intermediate range regime**, $10s_0 > \sigma_z > 0.1s_0$

- **Short range regime**, $\sigma_z < 0.1s_0$

In this case, the wake function is integrated over all possible longitudinal distances between the particles, z', as:

$$\Delta y'(z,s) = \frac{Nr_e}{\gamma}\int_{-\infty}^{z}\rho(z)w_y(z-z',s)dz'[A\Delta y+By]$$
(3.31)

And as explained in chapter 1, the Panofsky-Wenzel theorem is used to compute the transverse wake function, w_y, in the three regimes by integrating the longitudinal wake function, w_L. In the case of a rectangular collimation system, the total resistive contribution, $\Delta y'(z)$, has to be calculated for the tapered and flat parts (see Fig. 3.17) and added up as:

$$\Delta y'(z) = 2\int^{L_{tapered}}\Delta y'(z,s)ds+\int^{L_{flat}}\Delta y'(z,s)ds$$
(3.32)

where the variation in the longitudinal axis of the tapered part is described by $b(s) = a + z(b-a)/L_T$ and for the flat part by $b(s) = a$. The **resistive wakefield kick** in units of *rad* for the three different regimes implemented in the tracking code PLACET (v1.0.0) are the following in units of *rad* and all lengths in *mm*:
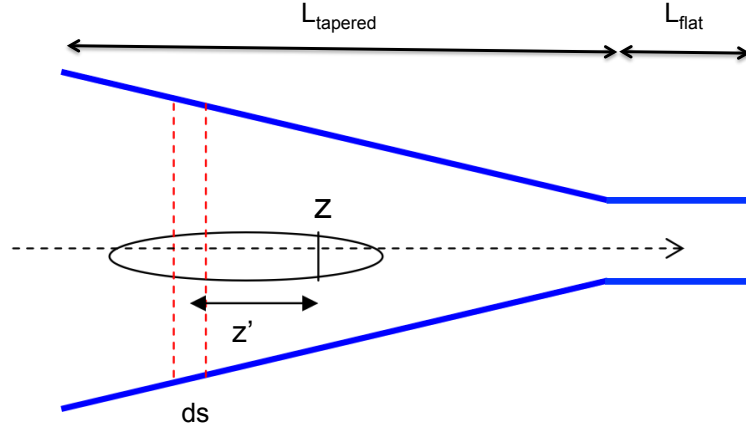
Figure 3.17: Scheme of the integration parameters for the resistive kick calculation.

- **Long range regime**, $10s_0 < \sigma_z$ to be compared with Eq. (3.19):

$$\Delta y'(z,s)[rad] = \frac{Nr_e}{\gamma} \frac{1}{\sqrt{2\pi}\sigma_z} \frac{4\sqrt{\lambda}}{b^3(s)} \int_{-\infty}^{z} \frac{1}{\sqrt{z'}} exp\left(-\frac{(z+z')^2}{2\sigma_z^2}\right) dz' \ (0.85\Delta y + 0.43y) \quad (3.33)$$

  where $\lambda = (c\sigma\mu_0)^{-1}$ and the other factors are described in previous sections.

- **Intermediate range regime**, $10s_0 > \sigma_z > 0.1s_0$:

$$\Delta y'(z,s)[rad] = \frac{Nr_e}{\gamma} \frac{1}{\sqrt{2\pi}\sigma_z} \int_{-\infty}^{z} w_y(z',s) exp\left(-\frac{(z+z')^2}{2\sigma_z^2}\right) dz' \ (0.85\Delta y + 0.43y) \quad (3.34)$$

$$w_y(z',s) = -\frac{cZ_0}{\pi b^3(s)} \left[\frac{s_0 e^{(-\alpha_t z'/s_0)}}{3(\alpha_t^2 + k_t^2)} \left(\alpha_t \cos(\frac{k_t z'}{s_0}) + k_t \sin(\frac{k_t z'}{s_0}) - \alpha_t\right) - \frac{\sqrt{2}}{\pi} \int_0^\infty \frac{m^2 e^{-\frac{m^2 z'}{s_0}}}{m^6 + 8} dm \right] \quad (3.35)$$

- **Short range regime**, $\sigma_z < 0.1s_0$, to be compared with Eq. (3.21):

$$\Delta y'(z,s)[rad] = \frac{Nr_e}{\gamma} \frac{1}{\sqrt{2\pi}\sigma_z} \int_{-\infty}^{z} w_y(z',s) exp\left(-\frac{(z+z')^2}{2\sigma_z^2}\right) dz'(0.85\Delta y + 0.43y) \quad (3.36)$$

$$w_y(z',s) = \frac{cZ_0}{\pi b^3(s)} \left[\frac{s_0 e^{(-\alpha_t z'/s_0)}}{3(\alpha_t^2 + k_t^2)} \left(\alpha_t \cos(k_t z'/s_0)\right) - \frac{\sqrt{2}}{\pi} \int_0^\infty \frac{m^2 e^{-\frac{m^2 z'}{s_0}}}{m^6 + 8} dm \right] \quad (3.37)$$

where α_t, k_t are functions of the relaxation factor, $\Gamma = c\tau/s_0$ characteristic of each material. The intermediate and short regimes are implemented for DC-conductivity (constant conductivity) and AC-conductivity (conductivity that depends on the frequency). For DC conductivity the material characteristic function are $\alpha_t = 1$ and $k_t = 1.7$ and for AC-conductivity α_t and k_t are functions of the frequency.

Analytic models, CST PS numerical simulations and PLACET comparison

Following the analytical models described in [84] **the collimation system under study belongs to the inductive regime** while in the PLACET (v1.0.0) tracking code the analytical formula corresponding to the intermediate regime is used. In Fig. 3.16 the **discrepancies between the limits described in [84] (top) and the limits implemented on the tracking code PLACET (v1.0.0)** (bottom) are shown. The top plot corresponds to the classification described in [84] and the bottom plot to the classification implemented on PLACET (v1.0.0), the black line indicates the ATF2 collimation taper angle. Therefore for the PLACET calculations we have used the current version of the program where the intermediate geometrical regime is used and using a modified version of PLACET (v1.0.1) changing in the code the limits to the ones described in [84]. The corresponding values for the wakefield kick, κ_y, for 1 mm beam offset can be seen in Table 3.6 for a half aperture of the collimation system of 5 and 8 mm. Good agree-

	Analytic	**PLACET(v1.0.0)**		**PLACET(v1.0.1)**		**CST PS**
a	$\kappa_y^{g,ind.}$	κ_y^r	$\kappa_y^{g,interm.}$	$\kappa_y^{g,ind.}$	κ_y^r	$\kappa_y^{CST\ PS}$
[mm]	[$V/pC/mm$]	[$V/pC/mm$]	[$V/pC/mm$]	[$V/pC/mm$]	[$V/pC/mm$]	[$V/pC/mm$]
8	0.006	0.0004	0.101	0.006	0.0002	0.006
5	0.022	0.002	0.191	0.019	0.006	0.024

Table 3.6: Analytical, PLACET calculation and CST PS simulations of the total kick factor for 1 mm offset of the source particle and a beam intensity of $N = 6 \times 10^9$.

ment is found between analytical calculations, numerical simulations and PLACET simulations when considering the inductive regime in the PLACET tracking code corresponding to the modified version (v1.0.1) as can be seen in Fig. 6.21.

Also the shape of the wake potential given by PLACET can be compared with the one computed with CST PS. In the PLACET tracking code the transverse wakefield kick is computed in units of rad for different longitudinal positions defined by the number of slices selected. From this calculation we can reconstruct the wake potential. To compute the kick given by PLACET in units of V/pC we need to multiply the kick applied to each macroparticle in units of rad by the energy of the beam corresponding to $E = 1.3\ GeV$ and divide it by the total charge of the bunch corresponding to $q = 1\ nC$. Then, we plot these values as a function of s, the longitudinal position of each slice. The results of the comparison for a half aperture of the collimation system of 5 mm can be seen in Fig. 3.19. With PLACET the wake potential was computed taking into account the inductive regime (purple) and the intermediate regime (red). The level of the wakefield impact implemented at each slice in PLACET is at the order of magnitude as the result given by CST PS when the inductive regime is used.

From these studies we could conclude that the discrepancies were due to **the difference on the limits definition** between the regimes defined by G. Stupakov and the limits implemented in the tracking code PLACET (v1.0.0). The analytical and linear calculations considering the G. Stupakov limits are in agreement with CST PS simulations and PLACET (v1.0.1) results, where the G. Stupakov limits have been implemented. The regimes definitions have been modified in a **new version of the tracking code**
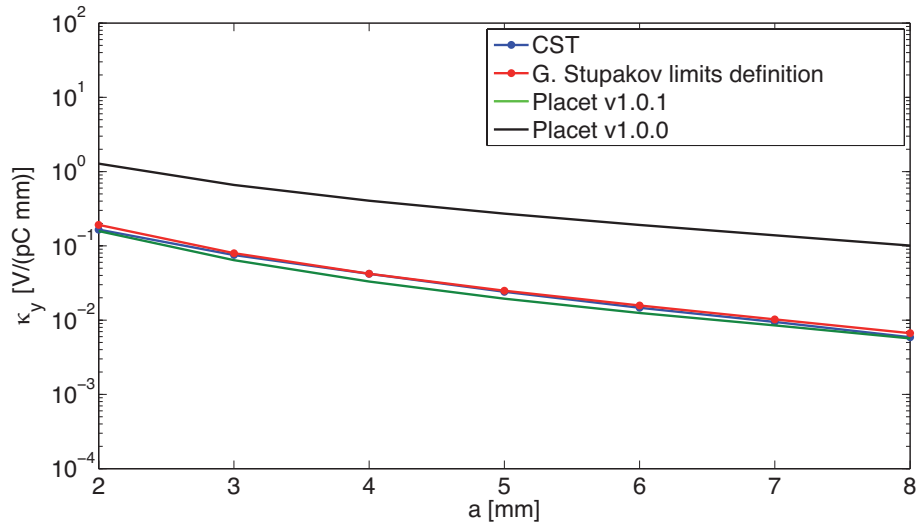
Figure 3.18:   Analytical wakefield kick compared with CST PS simulations and
PLACET calculations as a function of the half aperture of the collimation system with
α=3° and L_f=100 mm (parameters of interest for the ATF2 case). In these calcula-
tions, both contributions, the geometric and the resistive one, have been taken into
account.
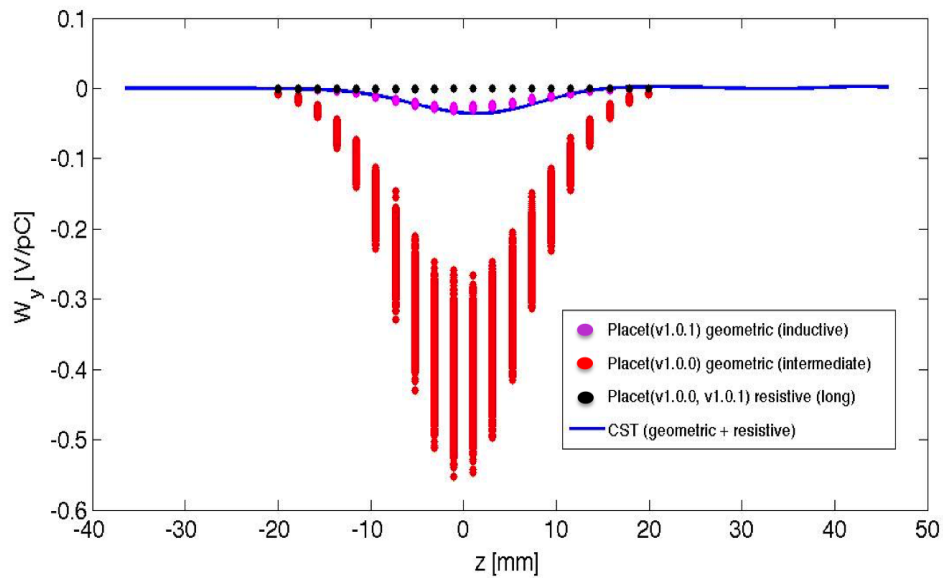
Figure 3.19: CST PS geometric and resistive wake potential (in blue), geometric wake
potential using PLACET (v1.0.0) in which the intermediate is considered (in red), ge-
ometric wake potential using PLACET (v1.0.1) in which the inductive regime is con-
sidered (in purple) and resistive wake potential in PLACET (the same in both versions)
(in orange) for a half aperture of 5 *mm*.

PLACET v(1.0.1) to be in agreement to the ones described in [84].

3.3.2   Wakefield impact on the orbit and beam size

The modified version of the tracking code PLACET (v1.0.1) has been used to perform tracking simulations and study the collimation system wakefield impact on the orbit and beam size at the ATF2 IP. In order to benchmark the results from the PLACET tracking simulations these studies have been compared with the linear transport of the wakefield kick calculated using the CST PS wake potential. Notice here that we expect some differences as with CST PS only the dipolar component has been calculated while in the analytical module in PLACET both contributions are taken into account weighted by Yokoya's coefficients. These studies have been focused on the vertical plane because the effect on the vertical plane, as shown in the first section of this chapter, is higher than the impact of the horizontal one. In addition, the vertical beam size at the IP is one order of magnitude smaller than the horizontal one making this magnitude more sensitive to the wakefield effect induced by the collimation system.

Tracking input parameters

For the tracking simulations a Gaussian electron beam with 6×10^9 particles was generated with an energy of 1.3 *GeV* and energy spread of 0.08%. The beam is divided in 20 slices in the longitudinal plane with 5000 macroparticles in each slice. No coupling between x-y planes has been taken into account. Multipoles have been added to the simulations but not misalignments. The collimation system description used for these studies corresponds to the optimized geometry and material presented in this chapter.

Wakefield impact on the orbit

In Fig .3.20, the orbit displacement at the IP induced by the collimation system wakefields as a function of the half aperture (top) and beam offset (bottom) is shown. The calculations have been performed using the two approaches introduced in this chapter. The linear transport of the wakefield kick and the PLACET (v1.0.1) simulations results are compatibles. From the PLACET (v1.0.1) simulation results we observed that:

- For a vertical collimation system half aperture of 5 *mm* the bunch is displaced at the virtual IP by around 30% of the IP vertical beam size corresponding to 37 *nm*.

- For a vertical collimation system half aperture of 8 *mm* the impact is about a 10%.

- **The orbit displacement has a linear dependence with the beam offset** both in the linear approximation and in the PLACET (v1.0.1) simulations results, as expected.

- For 5 *mm* half aperture of the vertical collimation system and a beam offset of 0.5 *mm* the impact on the orbit 13% of the IP vertical beam size. If we consider a smaller beam offset of 0.1 *mm* the impact on the orbit is reduced to a 3%.

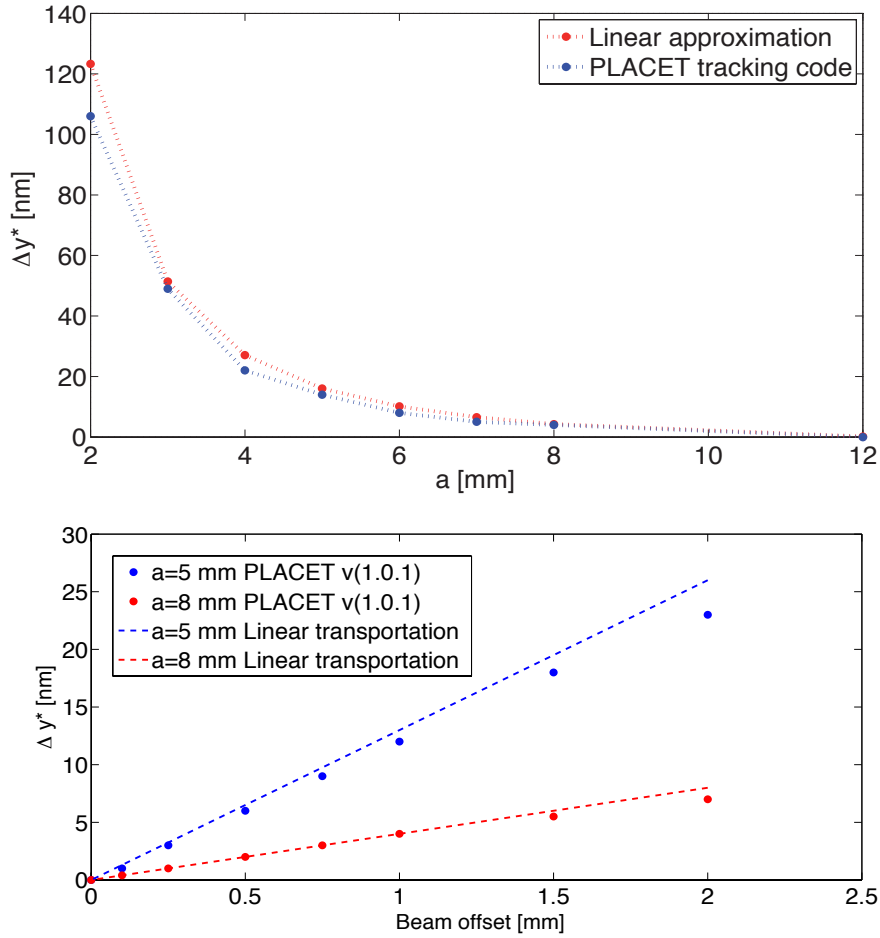Figure 3.20: Linear approximation and PLACET (v1.0.1) tracking simulations of the orbit displacement at the IP as a function of the vertical collimation system half aperture, a, (top) and the vertical beam offset (bottom). In these simulations and calculations the ATF2 bunch length of 7 mm, 1 mm vertical beam offset and a beam intensity of 0.6×10^{10} electrons have been considered.

Beam size growth wakefield impact

In Fig. 3.21, the linear calculation and the PLACET (v1.0.1) simulations of the beam size growth induced by the vertical collimation system wakefields as a function of the collimation system half aperture (top) and beam offset (bottom) are shown.
From these simulations we could conclude that:

- Concerning the dependence on the collimation system half aperture good agreement is found between the two approaches.

- For a vertical collimation system half aperture of 5 *mm* the beam size growth at the IP is about a 16% of the IP vertical beam size while for a half aperture of 8 *mm* it is about a 1%.

- **A non linear dependence can be seen of the beam size growth with the beam offset** simulated with PLACET (v1.0.1) while the linear transport predicts a linear dependence. This is due to the quadrupolar contribution which is also implemented in the tracking code PLACET (v1.0.1). The quadrupolar contribution is important in our calculations due to the fact that the vertical collimation system is located at high β_y location where the vertical and horizontal beam sizes are σ_y= 0.3 *mm* and σ_x= 0.5 *mm* respectively. **From these studies we could conclude that in order to perform a more accurate calculation of the wakefield impact on the beam size growth the tracking code PLACET (v1.0.1) has to be used**.

- From the PLACET (v1.0.1) simulation we observed that for 5 *mm* half aperture of the vertical collimation system and a beam offset of 0.5 *mm* the impact on the vertical beam size at the IP is about 10% of the IP vertical beam size. If we consider a smaller beam offset of 0.1 *mm*, we have obtained almost the same value for the beam size growth at the IP corresponding to 9%. **Alignment of about a few hundreds of μm is desirable in order to minimize the wakefield impact.**

The IP **beam size intensity dependence** problem due to wakefields has been addressed all along the ATF2 operation during the last years. Hardware modifications in the OTR chamber, the introduction of bellow electromagnetic shielding, a reduction of aperture steps and several other ideas have been realized to mitigate this persistent problem. A particular effort has been made in 2016 in order to solve this problem, and a dedicated "wakefield measurement campaign" has been made during the November-December 2016 operation. The vertical beam halo collimation system has been designed in terms of wakefield minimization. However, for completeness and to identify if the system can have an impact on these intensity dependence studies, the beam size growth with the beam intensity has been studied for different collimation system half apertures. The results of these studies can be seen in Fig. 3.22. For a half aperture of 4 *mm* the beam size growth is below 10 *nm* for the design ATF2 beam intensity which stands for 10^{10} electrons. In order to have a significant impact of the beam size growth induced by the vertical collimation system (higher than 25% of the beam size at the IP), the system has to be closed by more than 3 *mm*.
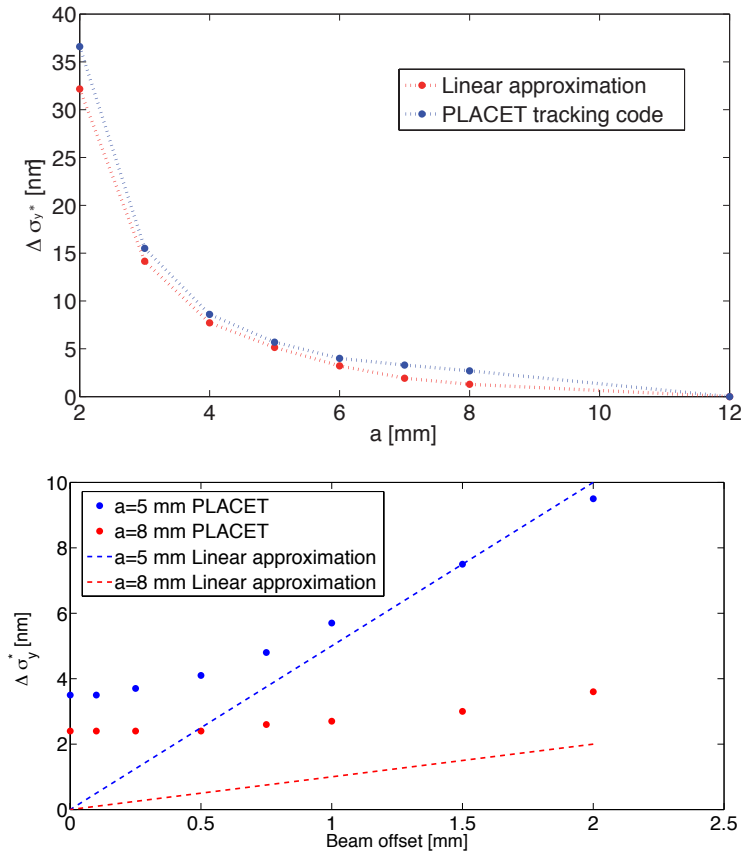
Figure 3.21: Linear approximation and PLACET (v1.0.1) simulations of the beam size
growth as a function of the vertical collimation system half aperture, a, (top) and the
vertical beam offset (bottom). In these simulations and calculations the ATF2 bunch
length of 7 *mm* and a beam intensity of 0.6×10^{10} electrons have been considered.
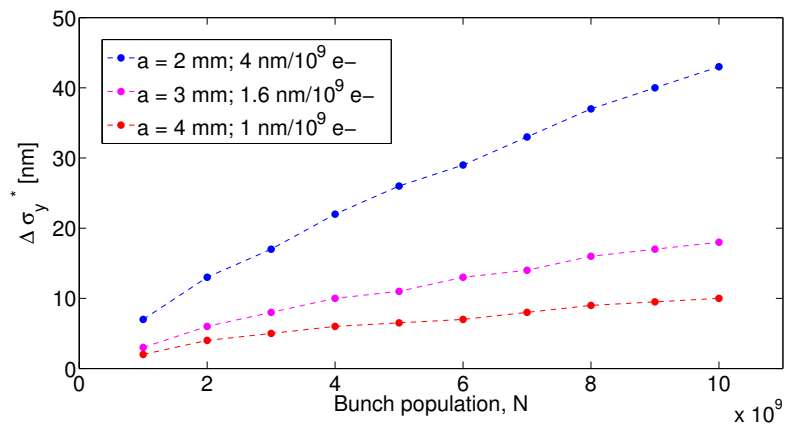
Figure 3.22: Beam size growth intensity dependence calculated with PLACET (v1.0.1)
for the AFT2 bunch length of 7 *mm*.

ATF2 vertical collimation system realistic efficiency studies using BDSIM

4.1 Introduction

In order to study the efficiency of a collimation system in a more realistic way, the background produced by the collimation system has to be considered. Tracking simulations of the particles of the beam halo through the accelerator lattice as well as simulating their interaction with the accelerator components are required. BDSIM is a code that allows us to perform these two features in one integrated simulation. This particle tracking code uses Geant4 [104], ROOT [105] and CLHEP [106] and it is a C++ based software. The beam is tracked and when the particles hit a geometrical aperture Geant4 is used. Monte Carlo radiation transport is used to propagate the distribution of particles simulating their full interaction with the accelerator components. When Geant4 is used the typical $4th$ order Runga Kutta magnetic field steppers are used. For in vacuum, thick lens, 6D transport matrix tracking routines are used in order to increase the speed of the simulation.

The validation of the significant recent developments on the BDSIM code [107] motivated the update of the ATF2 model and the experiments performed in 2015 using two Cherenkov based detectors installed in the ATF2 FFS. The detectors were used to perform relative background measurements since they are not absolutely calibrated. Correctors close to the detectors were used to scan the beam to create varying patterns in both detectors. In addition, background measurements were taken inserting the OTR screen of each station of the ATF2 multi-OTR system. These experiments were carried out by the Royal Holloway group [108] developers of the tracking code BDSIM. The analysis of the measurements and simulations benchmarking is on going. The optics of the ATF2 model have also been calculated with the MADX-PTC tracking code for benchmarking. The comparison of the optics V5.2 along the ATF2 beamline are shown in Fig. 4.1.

The efficiency of the vertical collimation system for the ATF2 has been studied with the tracking code BDSIM and the output of those simulations have been compared

149
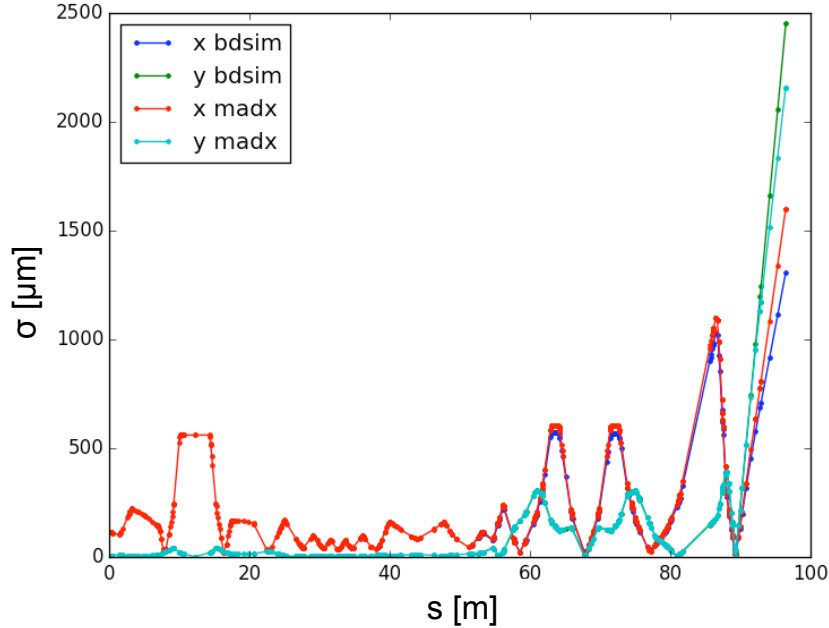
Figure 4.1: BDSIM V0.91 and MADX $(10\beta_x \times 1\beta_y)$ optics V5.2 comparison [108].

with the MADX-PTC tracking results. Furthermore, a more detailed analysis has been performed of the interaction of the beam halo particles with the BDUMP because it has been demonstrated to be the main source of background photons at the ATF2 in the Post-IP region. In addition, a detailed simulation study of the background generated by the collimation system is being made [109] for benchmarking with measurements.

4.2   BDSIM tracking efficiency studies

The main goals of this study are:

- **To verify** that the EM shower produced by **the collimation system does not generate additional background photons in the IP region**.

- **To quantify the efficiency** of the collimation system in the reduction of photons that can reach the gamma detector of the IPBSM located after the BDUMP window.

Simulations have been performed with BDSIM V0.91 of the ATF2 FFS considering the $(10\beta_x^* \times \beta_y^*)$ optics V5.2. A Gaussian transverse beam halo distribution (x, x', y, y') with 10^6 electrons of 1.3 GeV has been generated from $\pm 3\sigma_{x,y}^{core}$ (only the beam halo tails are considered in these studies) with $\sigma_x^{halo} = 5\sigma_x^{core}$ and $\sigma_y^{halo} = 10\sigma_y^{core}$. No coupling between x-y planes has been taken into account. For the longitudinal distribution a Gaussian model has also been used with an energy spread of 0.08%. Regarding the static errors no multipoles and misalignments have been taken into account. In these

simulations only EM processes as ionization, bremsstrahlung, Cherenkov, and multiple scattering have been considered. An scheme of the ATF2 FFS beam line model is shown in Fig. 4.2 where the shower of particles produced due to the interaction of one beam halo electron in the high-β region of the FFS with the beam pipe of one C-BPM is illustrated. Each color line correspond to a type of particles. The green lines correspond to photons, the blue ones to electrons and the red ones to positrons.
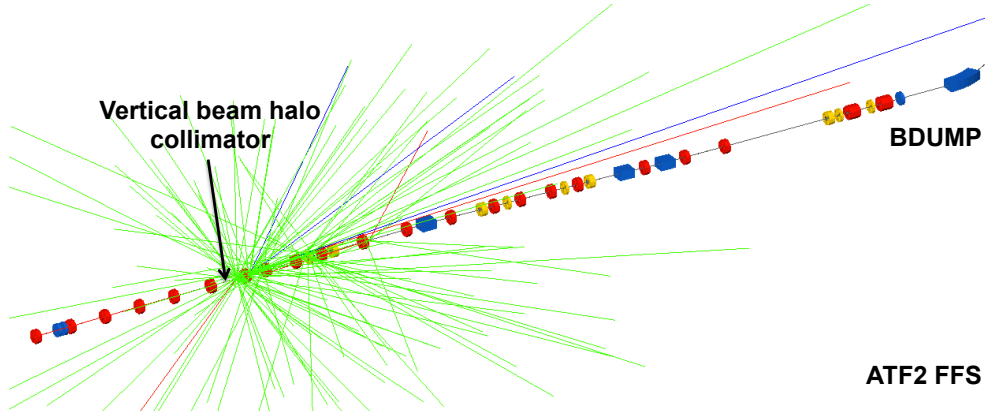
Figure 4.2: BDSIM ATF2 FFS model and EM shower produced by an electron hitting a C-BPM in the high-β region at the beginning of the FFS.

Furthermore, the geometric apertures of the different ATF2 components have been added to the lattice. Some markers have been implemented to study the distribution of primary beam halo electrons and secondary particles at these locations for different collimation system half apertures. The corresponding vertical and horizontal beam sizes at these locations are summarized in Table 4.1.

	Exit Coll	IP	Entrance BDUMP	WINDOW	Exit BDUMP
σ_x [mm]	0.163	0.009	0.348	0.497	0.640
σ_y [mm]	0.284	0.000035	0.522	0.7433	0.964

Table 4.1: Vertical and Horizontal beam sizes calculated with BDSIM at the exit of the vertical collimation system, at the IP, at the entrance of the BDUMP, at the WINDOW and at the exit of the BDUMP. Calculations performed for the $(10\beta_x^* \times \beta_y^*)$ optics V5.2.

In Fig. 4.3, the primary (top) and the secondary (bottom) particles in the horizontal (left) and vertical (right) planes **at the exit of the collimation system** are shown. In the distribution of the primary electrons we can observe the cut in the vertical plane (top right) corresponding to the collimation system aperture and some scattered electrons in the horizontal plane (top left) as we close the vertical collimation system. The distribution of secondary particles (including photons, electrons and positrons) increases as we decrease the aperture of the collimation system in both planes (bottom plots) and in the vertical distribution the edges of the collimation system can be distinguished (bottom right).

In Fig. 4.4, the primary (top) and the secondary (bottom) particles in the horizontal (left) and vertical (right) planes **at the IP** are shown. In this case, the same distribution of primaries is observed for the different half apertures of the vertical collimation
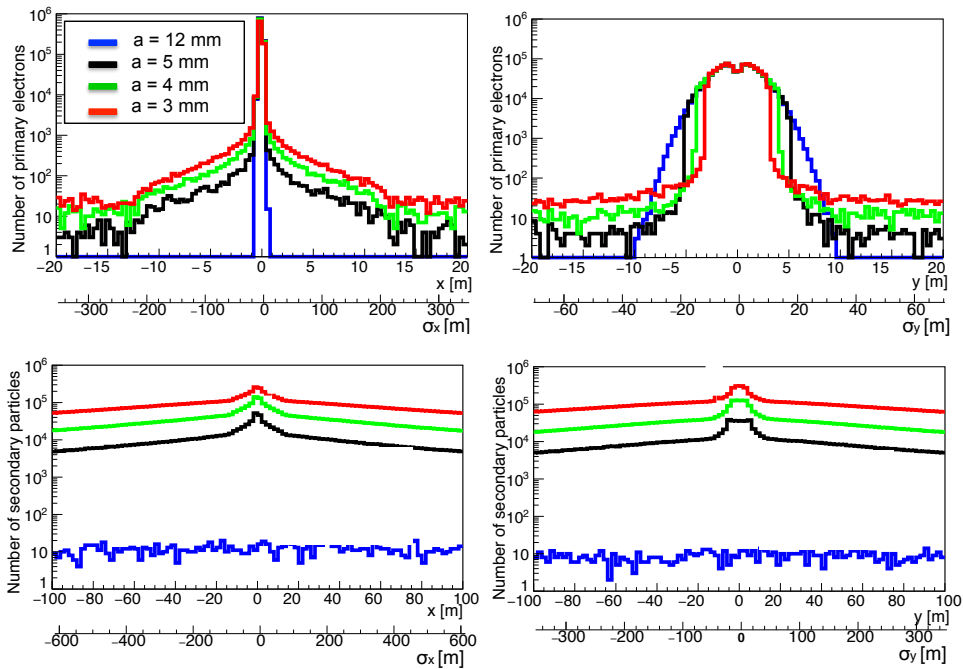
Figure 4.3: Primary (top) and secondary (bottom) particles **at the exit of the collimation system**.

system studied (top plots). Concerning the distribution of secondary particles (bottom plots), no additional particles at the IP are observed when we close the vertical collimation system.

In Fig. 4.5, the primary (top) and the secondary (bottom) particles in the horizontal (left) and vertical (right) planes **at the entrance of the BDUMP** are shown. The cut on the vertical beam halo distribution is observed for a collimation system half aperture of 5 *mm* (top right). Concerning the distribution of secondaries, no particles are created at the BDUMP entrance when the collimation system is closed to 5 *mm* half aperture (two bottom plots). The edges of the BDUMP beam pipe can be observed on the vertical distribution of secondary particles when the collimation system is opened (bottom left).

In Fig. 4.6, the primary (top) and the secondary (bottom) particles in the horizontal (left) and vertical (right) planes **at the window for photons** (located around 0.8 m from the entrance of the BDUMP) are shown. In this case, the cut on the vertical beam halo distribution is observed for a collimation system half aperture smaller than 5 *mm*. Notice that the vertical beam halo distribution cut by the vertical collimation system closed to 5 *mm* overlaps with the expected cut of the BDUMP beam pipe (top right). In the horizontal distribution of primary particles an asymmetric distribution is observed due to the effect of the BDUMP (top left). Concerning the distribution of secondaries the edges of the BDUMP aperture can be discern (bottom right) and no secondaries are created when the vertical collimation system is closed to 4 *mm* half aperture (two bottom plots). In Fig. 4.7 the primary (top) and the secondary (bottom) particles in the horizontal (left) and vertical (right) planes **at the end of the BDUMP** are shown.
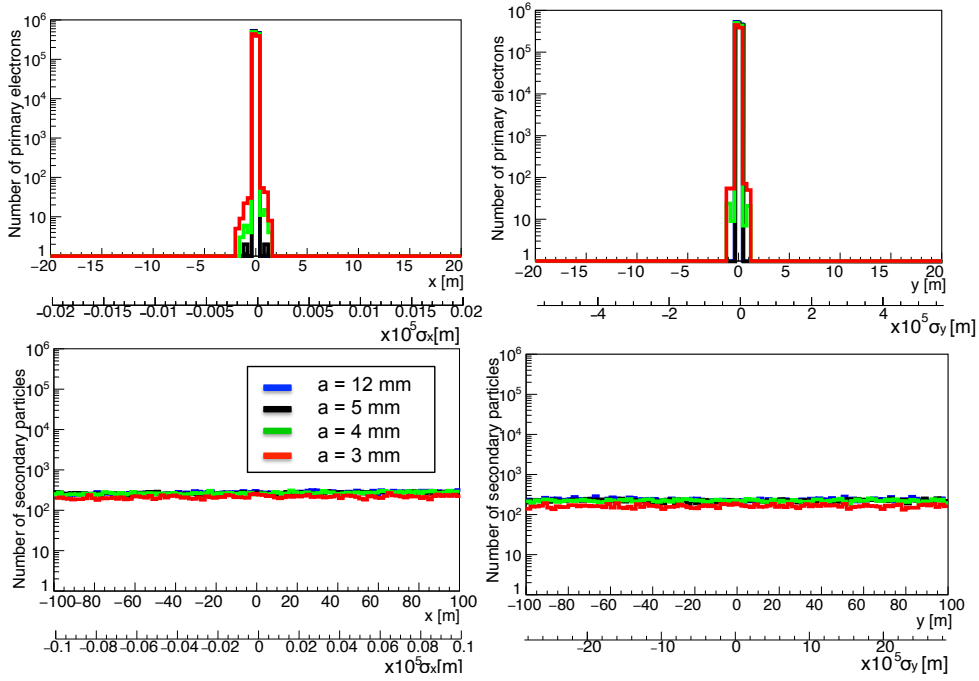
Figure 4.4: Primary (top) and secondary (bottom) particles **at the IP**.
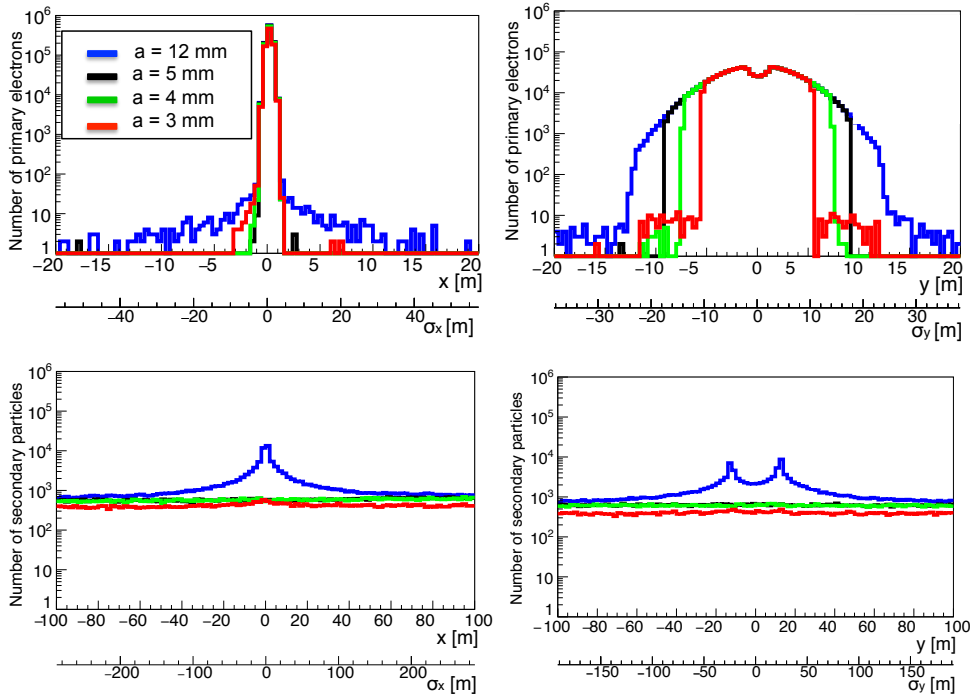
Figure 4.5: Distribution of primary (top) and secondary (bottom) particles **at the entrance of the BDUMP**.
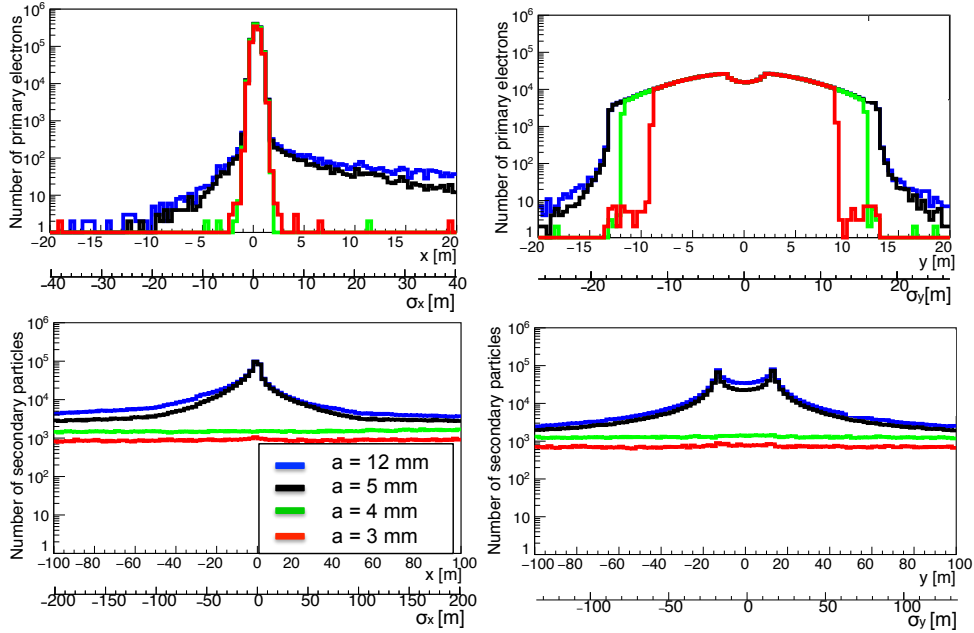
Figure 4.6: Primary (top) and secondary (bottom) particles **at the window for photons** (located about 0.8 *m* from the BDUMP entrance).

In this case, in the vertical plane (top right), the cut of the vertical collimation system at 4 *mm* at this location overlaps with the cut of the BDUMP and as a consequence secondaries are produced in the last section of the BDUMP. In the horizontal plane (top left), additional particles populate the tails of the distribution due to the bending magnet field which will deflect particles with different energies. Concerning the secondaries we can observed that in order to avoid completely the losses up to this location the vertical collimation system has to be closed to 3 *mm* (two bottom plots).

Secondary particles transport study

Some of the secondary particles produced at the collimation system propagate inside the beam pipe and can be lost in other locations along the beamline. In order to investigate where these particles are absorbed and if they can cause some additional background in the IP, other markers have been added on the simulations at: the closest bending magnet to the collimation system $BF5FF$, before the FD, at the IP, at the Post-IP WS, at the entrance of the BDUMP, at the window for photons, at the exit of the BDUMP and at the DS. The number of secondary particles at the enumerate markers can be seen in Fig. 4.8 for different vertical collimation system half apertures. From these simulations we could observe:

- An increase of secondaries at $BF5FF$ (8 *m* downstream the collimation system) as we decrease the vertical collimation system half aperture.

- No increase of secondary particles is observed before the FD (26 *m* downstream the collimation system) and at the IP (30 *m* downstream the collimation system)
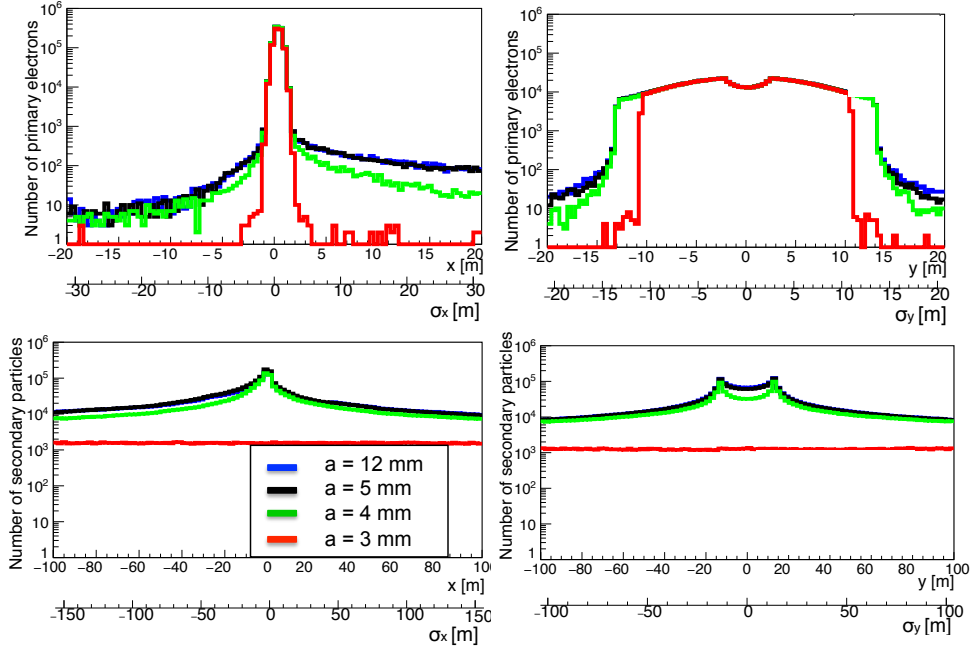
Figure 4.7: Primary (top) and secondary (bottom) particles **at the end of the BDUMP**.

even for a very small collimation system half aperture of 3 *mm*.

- In the last markers, after the IP, the number of secondary particles is reduced as we close the collimation system.

Efficiency studies

The efficiency of the vertical collimation system in reducing the beam halo losses and generation of background photons in the Post-IP has been studied in the detail. In Fig. 4.9 a scheme of the Post-IP is shown where the window sampler is indicated as well as the location of the IPBSM gamma detectors.

The efficiency of the vertical collimation system has been quantified in a relative way studying the reduction of primary electrons which interact with the BDUMP beam pipe at the entrance. The impact regarding the number of primary electrons has been defined as **Primary Collimation Efficiency (PCE)** and calculated in a relative way with respect to the case of not having a collimation system as:

$$PCE = 100 \left(1 - \frac{P^{BDUMP}_{w\ coll}}{P^{BDUMP}_{w/o\ coll}} \right) \tag{4.1}$$

where $P^{BDUMP}_{w\ coll}$ corresponds to the total number of primary particles lost at the entrance of the BDUMP for different collimation system half apertures and $P^{BDUMP}_{w/o\ coll}$ corresponds to the total number of primary particles lost in the BDUMP without vertical collimation system. In Table 4.2 a summary of the percentage of PCE obtained for different collimation system half apertures is shown.

In addition, in order to quantify the reduction of secondary particles produced in the
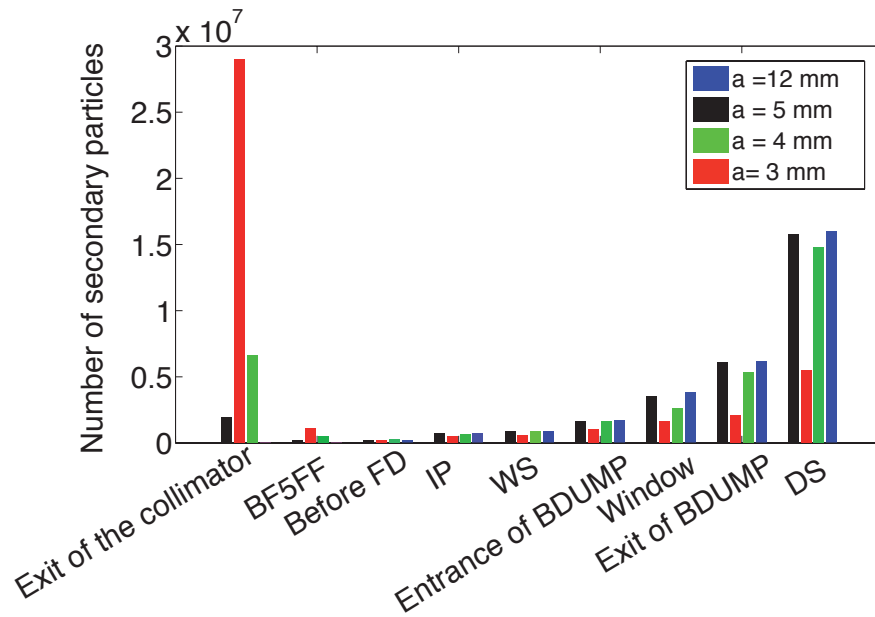
Figure 4.8: Number of secondary particles calculated using BDSIM V0.91 at different markers in the ATF2 beamline for different collimation system half apertures.
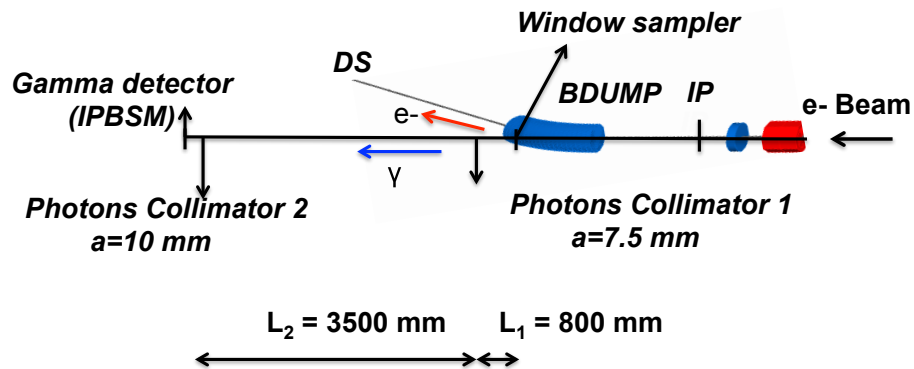
Figure 4.9: Post-IP scheme with the window sampler indicated as well as the location of the IPBSM gamma detectors.

a	[mm]	12	6	5	4
PCE	[%]	0	40	78	95

Table 4.2: Efficiency in reducing the number of primary particles stopped (PCE) at the entrance of the BDUMP.

BDUMP due to the collimation system, the amount of secondary photons produced on the BDUMP has been estimated by subtracting the number of photons at the window sampler the number of photons at the entrance of the BDUMP for different collimation system half apertures. This calculation has been defined as **Relative Photon Collimation Efficiency ($\Delta\gamma$CE)** as:

$$\Delta\gamma CE = 100 \left(1 - \frac{\Delta\gamma_{w\ coll}^{BDUMP-WINDOW}}{\Delta\gamma_{w/o\ coll}^{BDUMP-WINDOW}} \right) \tag{4.2}$$

where $\Delta\gamma_{w\ coll}^{BDUMP-WINDOW}$ are the photons generated between the BDUMP entrance and the window with collimation system and $\Delta\gamma_{w/o\ coll}^{BDUMP-WINDOW}$ without collimation system.

In Fig. 4.10 $\Delta\gamma$ (right) and $\Delta\gamma CE$ (left) as a function of the vertical collimation system half aperture are shown. The efficiency of the vertical collimation system for a half aperture of 3 *mm* is about 80 %. Notice here that we are only collimating in the vertical plane and only with one collimation system device. Some horizontal beam halo particles could also generate some background as can be seen in Fig. 4.6 as well as some particles that will interact with the collimation system jaws surface losing some energy but without being stoped.
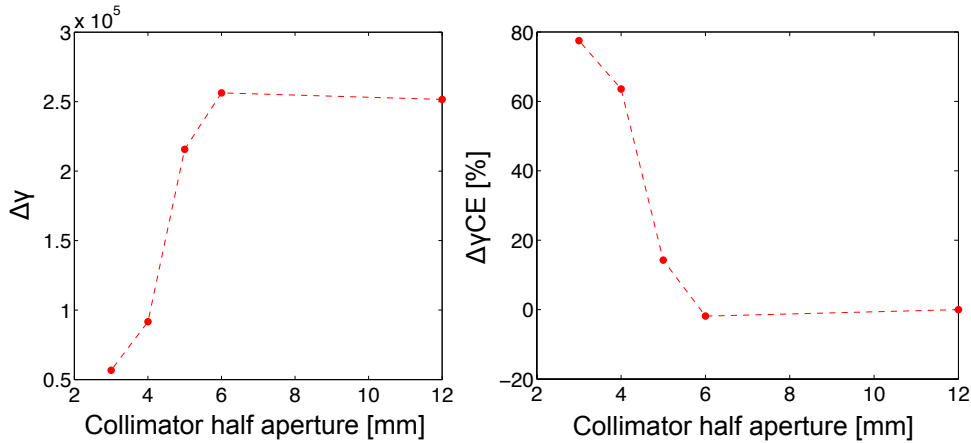
Figure 4.10: Number of background photons (left) and relative background photons reduction (right) at the window location for different collimation system half apertures.

Power loss discussion

Furthermore, in these tracking simulations the energy deposited is also calculated and we have estimated the amount of power lost in the collimation system when it is closed to 5 *mm*. The maximum number of losses have to be kept below 0.4% of the nominal beam intensity determined by the ATF2 radiation protection security. If we consider the nominal beam intensity to be 10^{10} electrons the ATF2 security limit is of the order of *mW*. In order to investigate this issue the energy deposited along the ATF2 beamline is depicted in Fig. 4.11. For 5 *mm* half aperture the losses at the collimation system are below 0.001% of the nominal ATF2 beam intensity and the power lost is of the order of μW.
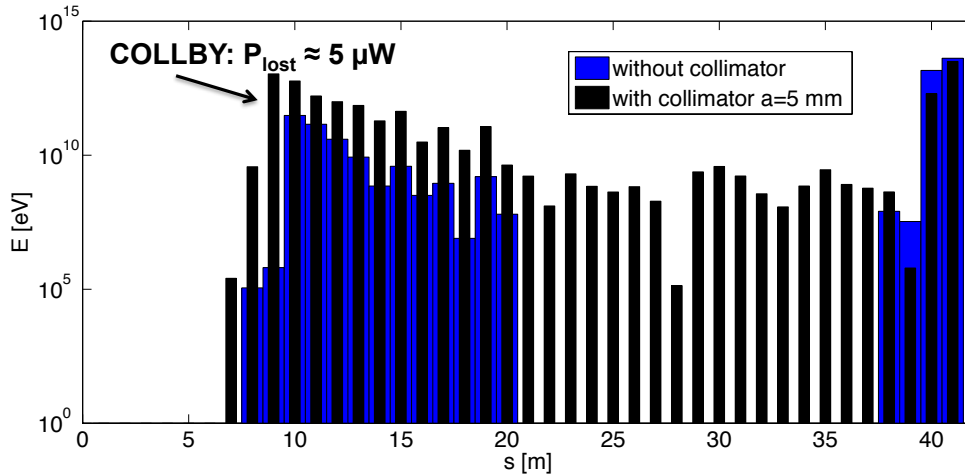
Figure 4.11: Energy deposited calculated with BDSIM V0.91 along the ATF2 beam-line without collimation system (blue) and with collimation system closed to 5 *mm* half aperture (black).

4.3 BDSIM and MADX-PTC tracking results discussion

BDSIM allows us to perform more **realistic tracking simulations** to study the **efficiency of the collimation system** taking into account the scattered **beam halo** and EM shower generated at the collimation system. In Fig. 4.12, the comparison of the relative reduction of primary electrons lost at the BDUMP is shown for the two tracking codes used to study the efficiency of the vertical collimation system (MADX-PTC and BDSIM). While from **MADX-PTC** simulations we could conclude that half aperture of **5** *mm* was enough to avoid losses in the entrance of the BDUMP, **BDSIM** shows that a **4** *mm* half aperture is required.

In BDSIM, the length of the BDUMP is considered. The fact that the beam size will change in the BDUMP as well as the fact that particles will be affected by the magnetic field of the BDUMP will modify the efficiency of the collimation system. Fig. 4.13 shows the amount of primary particles absorbed (top), primary particles hits (middle) and the energy deposited (bottom) along the BDUMP (with a total length of 1.2 *m*) for three different cases: without collimation system, with vertical collimation system closed to a 5 *mm* half aperture and with vertical collimation system closed to a 4 *mm* half aperture (black, red and blue respectively). We can observe that even for a 4 *mm* half aperture some losses are expected at the end of the BDUMP. From these studies we could conclude that simulations taking into account the **interaction of the particles with the jaws** is essential to study the performance of the collimation system and to defined a **more realistic collimation depth**.
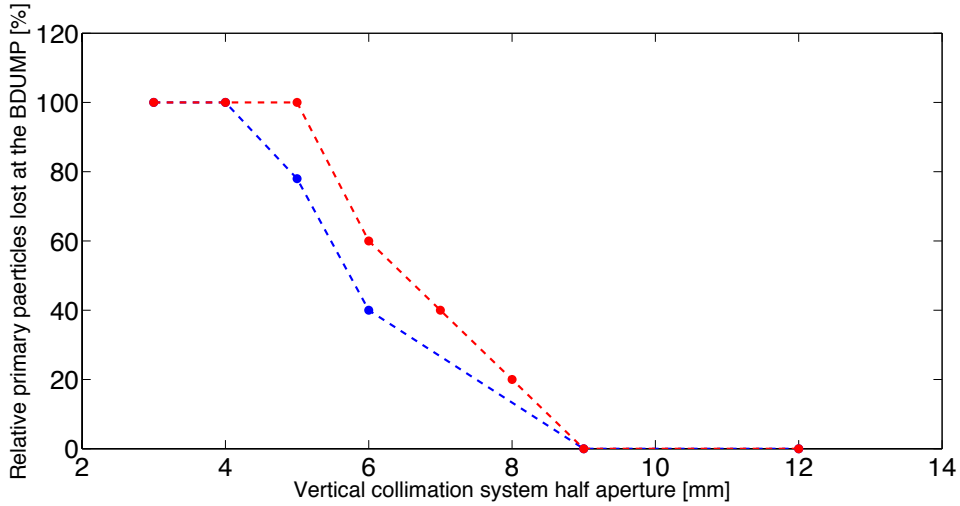
Figure 4.12:   Comparison of the relative reduction of primary electrons lost at the entrance of the BDUMP calculated with MADX-PTC (red) and BDSIM (blue).
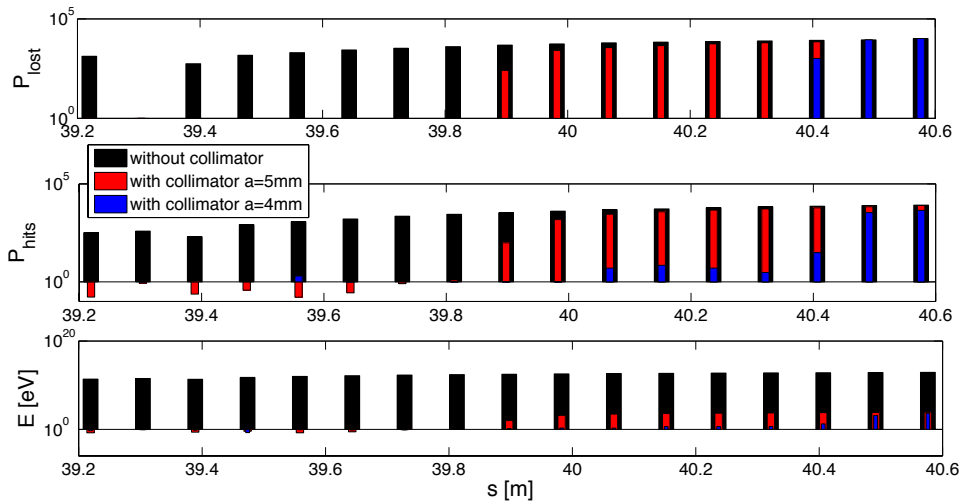
Figure 4.13:   Primary particles absorbed (top), primary particle hits (middle) and energy deposited (bottom) along the BDUMP (with a total length of 1.4 m) for three different cases: without the vertical collimation system (black) and with the vertical collimation system closed to 5 (red) and 4 mm (blue) half aperture.

Chapter 5

Design, construction, installation and commissioning of the ATF2 vertical collimation system

5.1 Introduction

Once the location, efficiency and wakefield impact were determined, the next step on the vertical collimation system design consisted in performing the 3D mechanical design. This work was performed by S. Wallon working in the accelerator department of the Depacc at LAL. The optimized parameters of the jaws described in chapter 3 (Cu with $\alpha = 3°$ and $L_F = 100$ *mm*) were given as input parameters to S. Wallon in order to perform the realist mechanical design. Furthermore, its design was inspired in previous experiences [110] and in a preliminary design made for the ILC spoilers [40]. In this chapter, we present the final 3D mechanical design and related 3D EM calculations performed to refine the material choice of the transition foil. Furthermore, the wake potential of the final 3D design has been performed in order to investigate the accuracy in evaluating the wakefield impact of the vertical collimation system taking into account only the jaws with respect to the case of considering the complete device. When the design was completed, the different components were purchased, cleaned and assembled at LAL, where in addition, alignment and vacuum tests were performed in the laboratory by S. Wallon. In March 2016, the vertical collimation system was installed in the ATF2 and first functionality and calibration tests were performed during the 2016 spring run. These first tests are presented and discussed in the last section of this chapter.

5.2 3D mechanical design and related 3D EM calculations

The 3D mechanical design is depicted in Fig. 5.1 (courtesy of S. Wallon). The vertical collimation system consists in a rectangular vacuum chamber with a single movable cover to check and adjust the collimation system jaws with respect to external references. This rectangular vacuum chamber is connected to the beam pipe by a transition

pipe with a rectangular part of 24×26 *mm*, in horizontal and vertical respectively, in one stream and the round beam pipe (12 *mm* standard half aperture). In the inside part of the vacuum chamber we have the two vertical collimation system jaws (indicated in Fig. 5.1 in orange). These two rectangular jaws are connected to the transition pipe by two metal transition foils (indicated in Fig. 5.1 in blue) of 0.1 *mm* thickness. The material of the transition part was studied by means of wakefield minimization and the comparison of the impact for different materials is presented in this section as well as the final choice discussion. The vacuum chamber is made of Al and the rest of the components are made of SS. Then, an adjustable bottom wall (indicated in Fig. 5.1 in yellow) was put to reduce the horizontal width seen by the beam and for pumping capacity. The total length of the jaws is 238 *mm* and we considered that only one motor was needed to move each vertical collimation system jaw. Two step by step EMMS-ST [111] motors were chosen to move independently the two vertical collimation system jaws with an expected precision of $\pm 10 \mu m$.
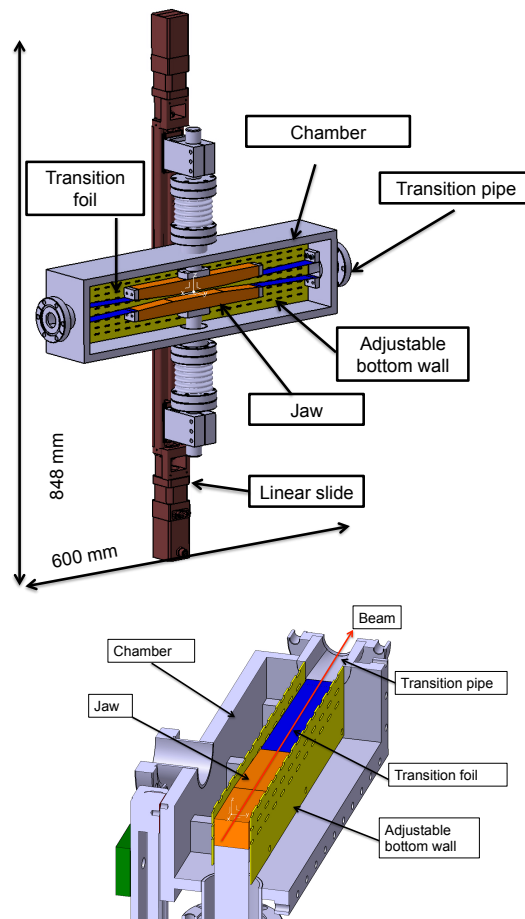
Figure 5.1: 3D vertical collimation system mechanical design with the different components indicated in different colors (top) and detailed view of the collimation system transition part in the longitudinal plane for half of the system (bottom).

Transition foil material study

In chapter 3, all the wakefield studies have been performed only for the vertical col-
limation system jaws, which constitute the part of the collimation system that will be
closer to the beam. However, the transition foil between the vertical collimation sys-
tem jaws and the beam pipe could introduce additional wakefields and needs to be
studied. The smoothness of the transition foil is constrained by the available space in
the ATF2 beamline and the length of the optimized vertical collimation system jaws.
Therefore, in this context, 3D EM simulations with CST PS were performed in order
to choose the best material for the transition foil. The simplified model shown in Fig.
5.2 based on the 3D mechanical design of Fig. 5.1 including the vertical collimation
system jaws and the transition foil has been used for these studies. Three different ma-
terials were studied for the transition foil: Cu, Al and SS. The vertical wake potential
calculated with CST PS is shown in Fig. 5.3 for the three materials studied. In Table.
5.1 the CST PS calculated vertical wakefield kicks, $\kappa_{y,transition}^{CSTPS}$, are summarized.
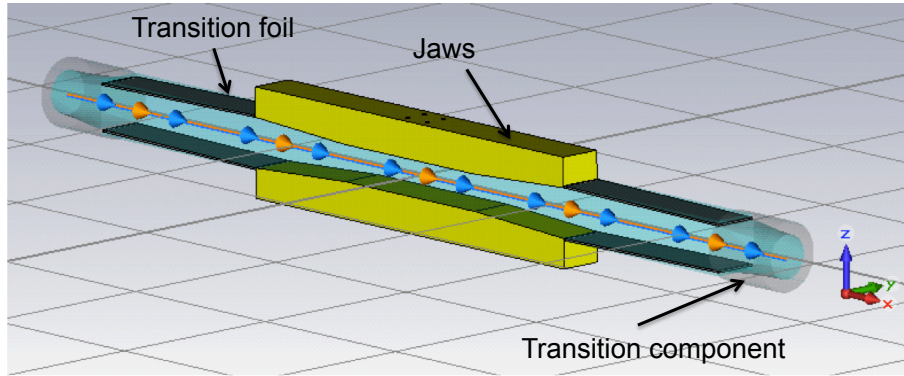
Figure 5.2: 3D CST PS model of the vertical collimation system including the jaws,
the transition foil and the transition part to the beam pipe component.

Material	$\sigma[S/m]$	$\kappa_{y,transition}^{CSTPS}[V/pC/mm]$
Cu	5.9×10^7	0.025
Al	3.7×10^7	0.025
SS	1.5×10^6	0.028

Table 5.1: Calculated wakefield kick with CST PS, $\kappa_{y,transition}^{CSTPS}$ for three different tran-
sition foil materials and the corresponding electric conductivity, σ, [96].

An increase of about 12% on the vertical collimation system induced wakefield kick,
$\kappa_{y,transition}^{CSTPS}$, is observed when considering the transition foil made by SS instead of Cu
or Al. The best candidates are Cu and Al. Since the vacuum chamber is made of Al
we decided to made the transition foil also of Al.
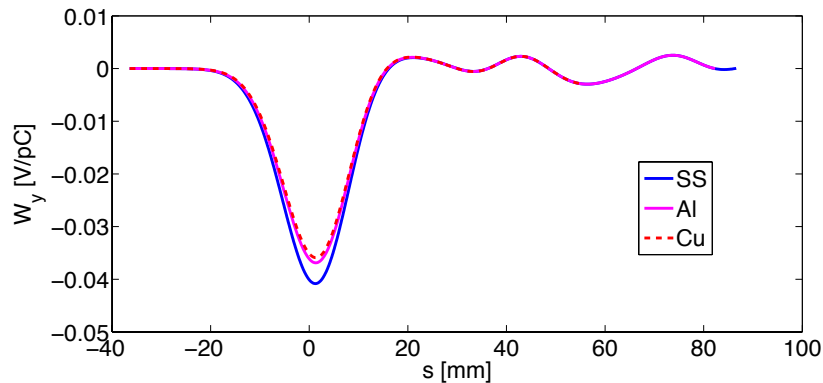
Figure 5.3: Vertical wake potential calculated with CST PS of the vertical collimation system model in Fig. 5.2 for three different transition foil materials.

Wakefield characterization of the 3D realistic mechanical design

Once the 3D mechanical design and the material choice was performed a realistic 3D EM calculation needed to be performed to characterize the impact of the complete vertical collimation system. These calculations were compared with the estimations performed in chapter 3 considering only the vertical collimation system jaws. In Fig. 5.4 the complete model of the vertical collimation system in CST PS exported from CATIA is shown. However, for the simulations only the relevant components from the wakefield point of view have been considered (jaws, transition foil, transition part and the adjustable wall). Otherwise the number of mesh cells of the complete volume was to high increasing the simulation time without contributing on the results. The main volume of the model is set to vacuum and it is surrounded by perfectly conducting material.
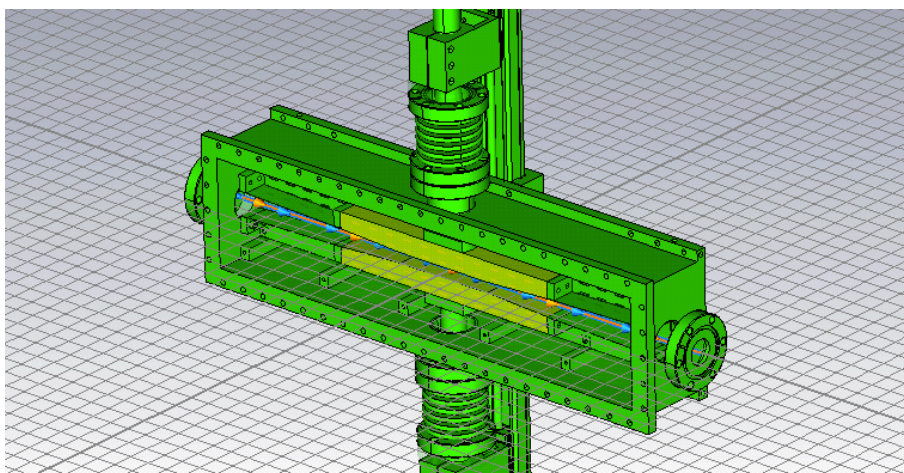
Figure 5.4: CST PS **realistic** model of the vertical collimation system.

The vertical wake potential (top) and vertical wakefield kick (bottom) as a function of the vertical collimation system half aperture are depicted in Fig. 5.5 for the 7 *mm* ATF2 bunch length. In Table 5.2 the comparison of the vertical wakefield kick calculated from the CST PS of only the vertical collimation system jaws, $\kappa_{y,jaws}^{CSTPS}$, and the realistic 3D mechanical design, $\kappa_{y,realistic}^{CSTPS}$ are shown. The observed increase in the impact of the full collimation system respect to the impact of only the collimation jaws is between 15-30 %.
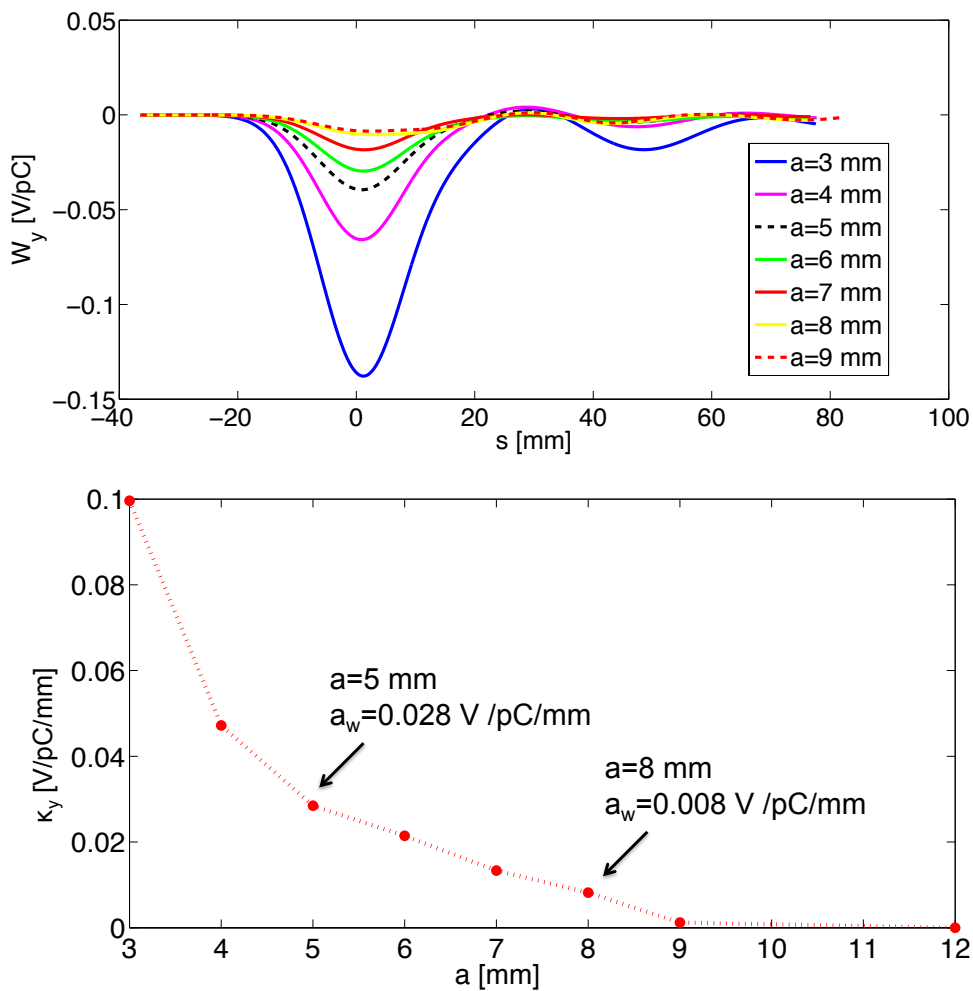
Figure 5.5: Vertical wake potential (top) and vertical wakefield kick (bottom) for different vertical collimation system half apertures and 1 *mm* vertical beam offset. The calculations have been performed using CST PS for the realistic model in Fig. 5.4 but without the vacuum chamber, the motors and the slide system.

a	$\kappa_{y,jaws}^{CSTPS}$	$\kappa_{y,realistic}^{CSTPS}$	$\Delta\kappa_{y,realistic-jaws}^{CSTPS}/\kappa_{y,realistic}^{CSTPS}$
[mm]	[$V/pC/mm$]	[$V/pC/mm$]	[%]
3	0.072	0.10	30
5	0.024	0.028	15
8	0.006	0.008	30

Table 5.2: Comparison of the realistic, $\kappa_{y,realistic}^{CSTPS}$, and jaws, $\kappa_{y,jaws}^{CSTPS}$, wakefield kick calculated with CST PS for the ATF2 bunch length of 7 mm.

5.3 Collimation system construction and laboratory calibration at LAL

When the 3D mechanical design was completed the different components were manufactured at LAL by S. Wallon, who cleaned and assembled the vertical collimation system. In Fig. 5.6 some of the components before being assembled (top) and the complete vertical collimation system (bottom) are shown. The different components were cleaned with an acid in order to erase imperfection, no polishing or sand blasting was carried out. Regarding the assembly, the seal of the rectangular chamber was made with indium wires and for the DN40CF flanges, Cu seals were used. Before closing the vacuum chamber with indium seels the alignment of the vertical collimation system jaws with a 3D machine and the response of the motors were measured. The vertical collimation system jaws were aligned with respect to external references (as external references to determine a 3D axis, the flanges and back planes depicted in Fig .5.9 were used) with a Mitutoyo CMM coordinate measuring machine with a rated accuracy of ± 4 μm. The resulting measured position as a function of the reading of the controllers is plotted in Fig. 5.7.

A linear fit was applied to the data in Fig. 5.7 for the upper and lower vertical collimation system jaws, respectively, given by the following equations:

$$y_{readout}^{upper} = (-0.9964 \pm 0.0002)y_{measured}^{upper} + 12.394$$
$$y_{readout}^{lower} = (-0.9807 \pm 0.0012)y_{measured}^{lower} + 12.548$$

(5.1)

where $y_{readout}$ is the value given by the controller and $y_{measured}$ is the position of the jaws measured with the 3D machine in the laboratory.

Notice that the maximum half aperture of the system is 12.394 mm for the upper jaw and 12.548 mm for the lower one. This difference of the maximum aperture could be due to machining tolerances and small deviations with expected position when the assembly was performed. The minimum half aperture is fixed by a mechanical stop located at 2.431 mm for the upper jaw and at 2.741 mm for the lower jaw. The upper jaw shows a more linear response than the lower one. In Fig. 5.8 the difference between the reading output from the controllers and the measured real displacement of the jaws in all the movement range is depicted. From these measurements we could conclude that the precision on the position achievable concerning the upper jaw is about 10-20 μm which accomplishes the specifications while the precision for the bottom jaw is about 200 μm. One possible explanation to this behavior could be the fact that the screw has a flaw, which means that the pitch is not constant. There was no time to replace it because of the shipping and installation schedule. We considered that we could tolerate
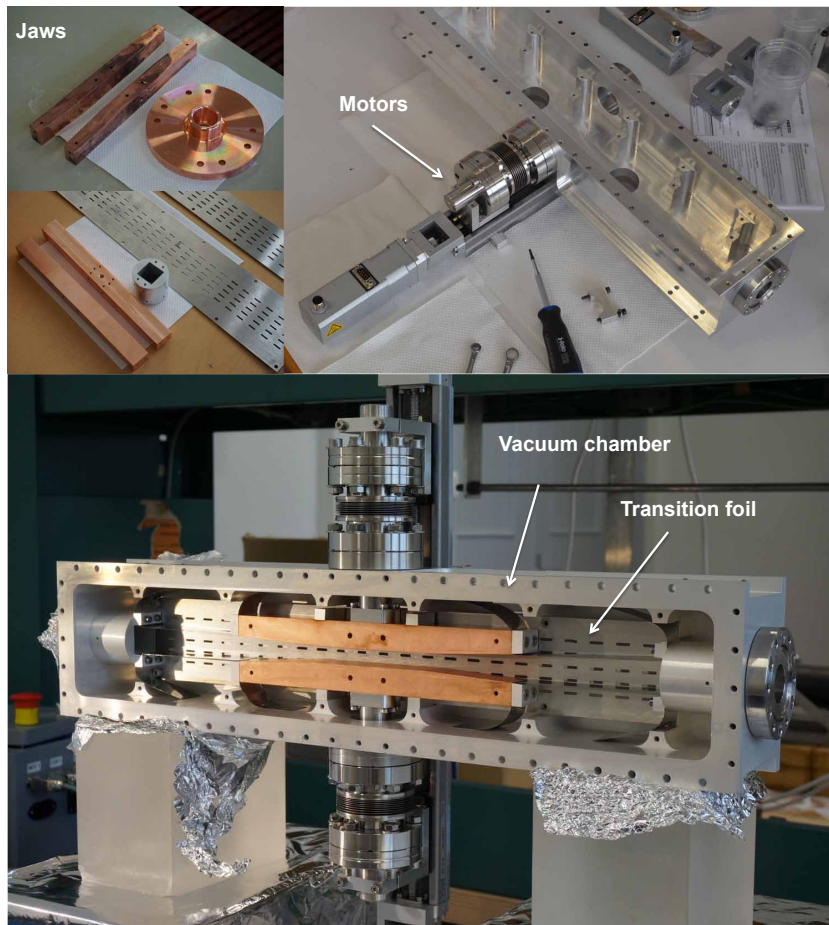
Figure 5.6: Jaws, transition components, motors and vacuum chamber before been assembled (top) and vertical collimation system mounted at LAL ready to be sent to KEK.
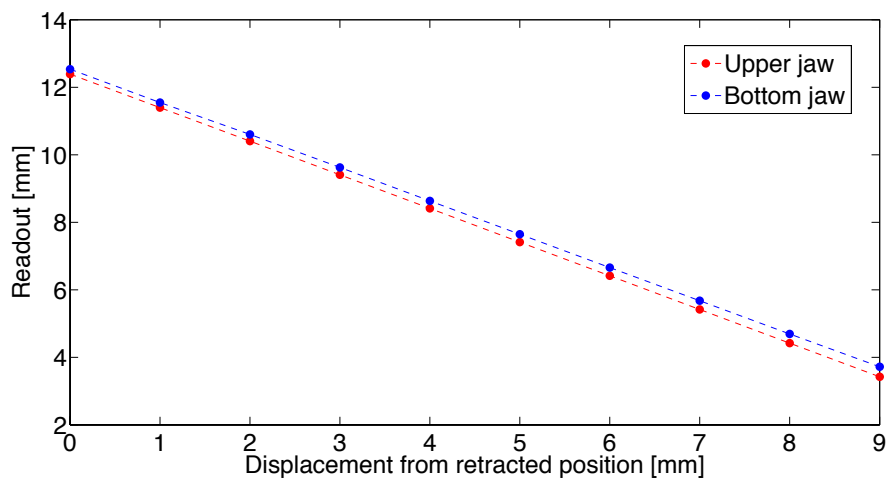
Figure 5.7: Upper and lower jaw position measurements performed at LAL with a Mitutoyo CMM 3D coordinate measuring machine.

this error on the position of one of the jaws for the experimental measurements. The calibration function in Eq. 5.1 can be used to determine the position the jaws position with a better resolution.
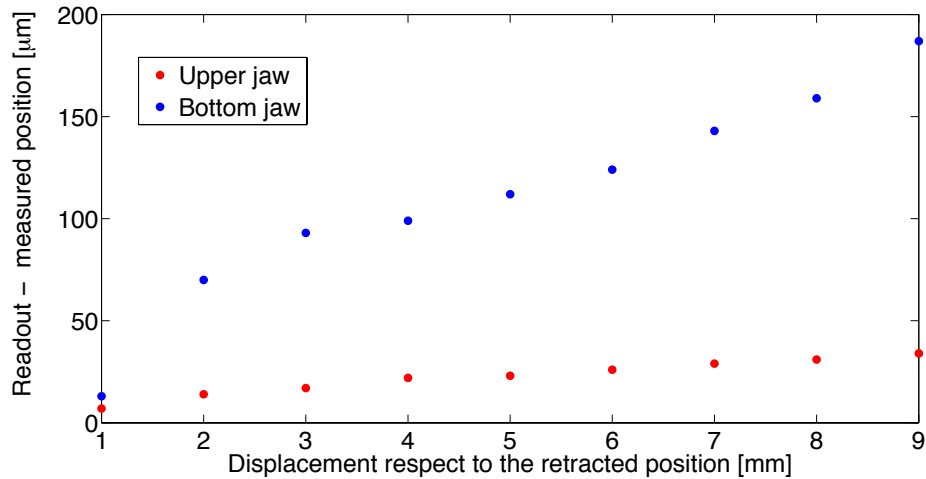
Figure 5.8: Difference between the reading output from the controllers and the measured displacement of the upper and lower jaws in all the movement range.

Furthermore, a vacuum test at the level of 10^{-8} Pa (ATF2 requirements) was performed successfully to verify possible mechanical leaks. First a pumping process was done showing that there was not out-gassing and then a helium leak test was performed.
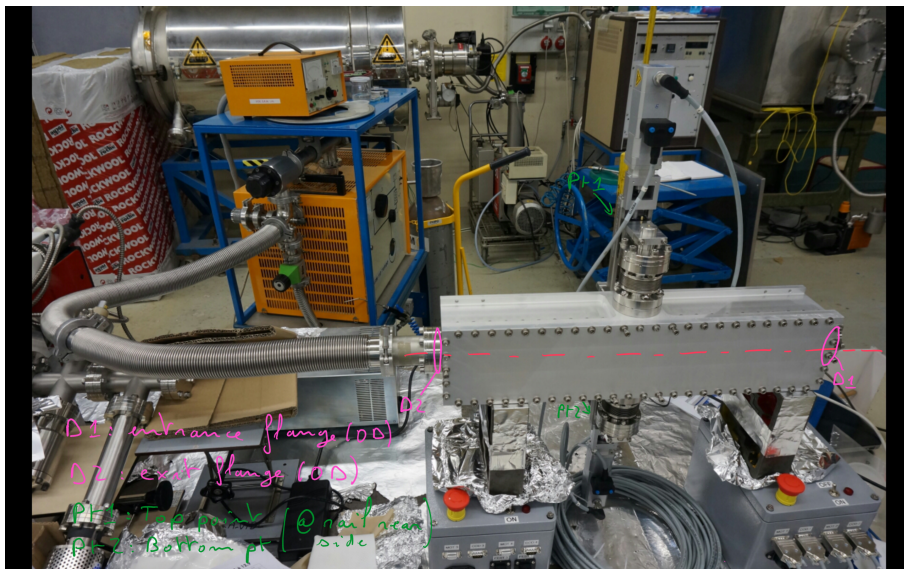
Figure 5.9: Vacuum test set up at LAL with the alignment external reference used in the 3D coordinate measurements depicted.

5.4 Installation and calibration with beam in ATF2

The vertical collimation system was installed in ATF2 the first week of March 2016
(from the 29/02/2016 to the 04/03/2016). In order to install the collimation system a
chassis was build to fix the collimation system in the beamline (see Fig. 5.10 (top)).
Then, a laser tracker was used to align the vertical collimation system external refer-
ences with respect to the magnets with a precision of 0.5 mm (see Fig. 5.10 (middle)).
In addition, a 10^{-8} Pa vacuum level test was performed. In a first test a leakage in the
flange of one of the exits was found, in order to solve the problem the indium seal was
crushed more by retightening the screws and a second vacuum test was perform suc-
cessfully. The displacement of the jaws was checked by using the commercial FESTO
software [112]. The motors were tested in case of a shut down occur and we observed
that the jaws keep the position without falling into the beam when this happens.

5.4.1 Software commissioning

The ATF2 lower level control system are the Input-Output Controllers (IOCs) that read
and write data from the beamline hardware systems. The first ATF IOC systems are
based on the V-SYSTEM control architecture. However, the new hardware systems are
based on EPICS. EPICS consists in a set of open source software tools, libraries and
applications to create soft real-time control systems for scientific instruments. Then,
additional EPICS IOC were written to generate EPICS Process Variables (PV's) syn-
chronized to the control variables in V-SYSTEM.

The FESTO [112] motors were provided by the company with a software to drive them,
however, this software is only supported by Windows. This software has also a web
interface which allows us to perform some simple actions as read the position, move
the jaws and put them in the retracted position. By using this web interface we wrote a
MATLAB [113] script in order to perform these actions from any other machine with
any other support system. The IP addresses to communicate with the two controllers
located in the collimation system control box (see Fig. 5.11) are 20.10.69.150 for the
upper jaw and 20.10.64.151 for the bottom one.

Furthermore, this script was translated by the KEK team into EPICS [114] in order to
implement the control of the collimation system in the ATF2 control room. The PV's
defined in EPICS to control the vertical collimation system are:

- **Collimator1:Gap** to read the position of the upper jaw.

- **Collimator2:Gap** to read the position of the lower jaw.

- **Collimator1:GoHome** to move the upper jaw to its retracted position.

- **Collimator2:GoHome** to move the lower jaw to its retracted position.

- **Collimator1:SetAperture** to set the upper jaw to a given aperture.

- **Collimator2:SetAperture** to set the lower jaw to a given aperture.

One can use these EPICS commands to record the vertical collimation system data
while taking other beam data. Furthermore, from the control panel in the ATF2 control
room it is also possible to control the vertical collimation system opening the **"ATF2**

Figure 5.10: Mechanical support fabricated at KEK for the installation of the vertical collimation system into the ATF2 beamline (top). Vertical collimation system installation and alignment procedure (middle). Vertical collimation system after installation in the ATF2 beamline (bottom).
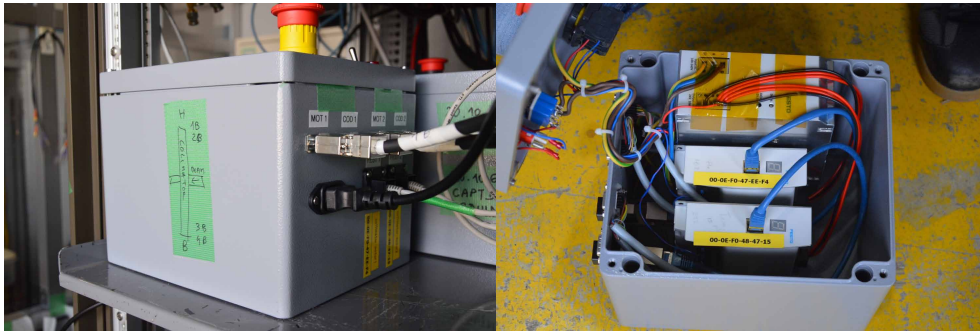
Figure 5.11: Control box located in the ATF2 with the two controllers for the upper and lower vertical collimation system jaws.

Collimator controller" shown in Fig. 5.12 (right). The current half aperture of the vertical collimation system is visualized in one of the windows in the ATF2 control room shown in Fig. 5.12 (left).
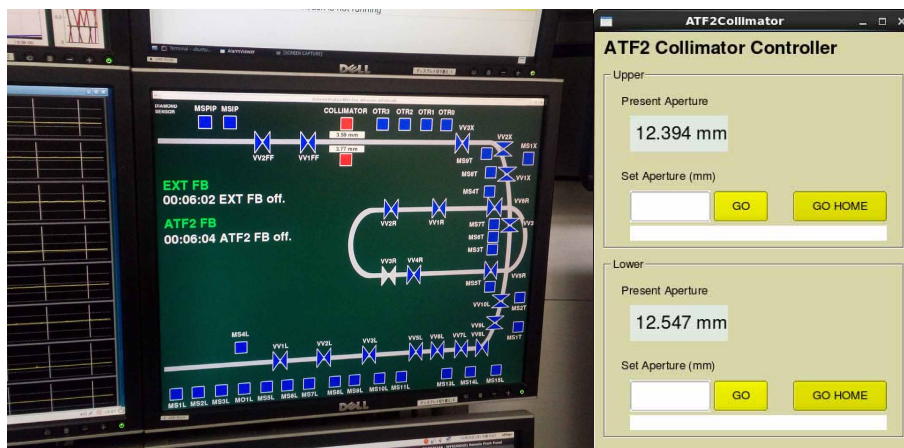
Figure 5.12: ATF2 control room window where the vertical collimation system aperture is visualized (left) and vertical collimation system control panel (right).

5.4.2 Hardware commissioning

In March 2016, four shifts were dedicated to check the functionality and final hardware to control the vertical collimation system. The main objectives of this test were:

- Verify and calibrate the control system.

- Measure the jaws-beam alignment.

During these shifts in order to test the control of the collimation system and measure the beam-jaws alignment the background monitor, the Post-IP WS, the vertical and horizontal DSs and the TBP were used. In addition, the FFS Beam Loss Monitor fiber (BLM fiber) installed along the FF line was used to monitor and control the relative increase of losses in the FFS when closing the vertical collimation system. The BLM

fiber is connected to a PMT at the beginning of the FFS and it is synchronized with the beam. The different diagnostic devices used are indicated in Fig. 5.13:
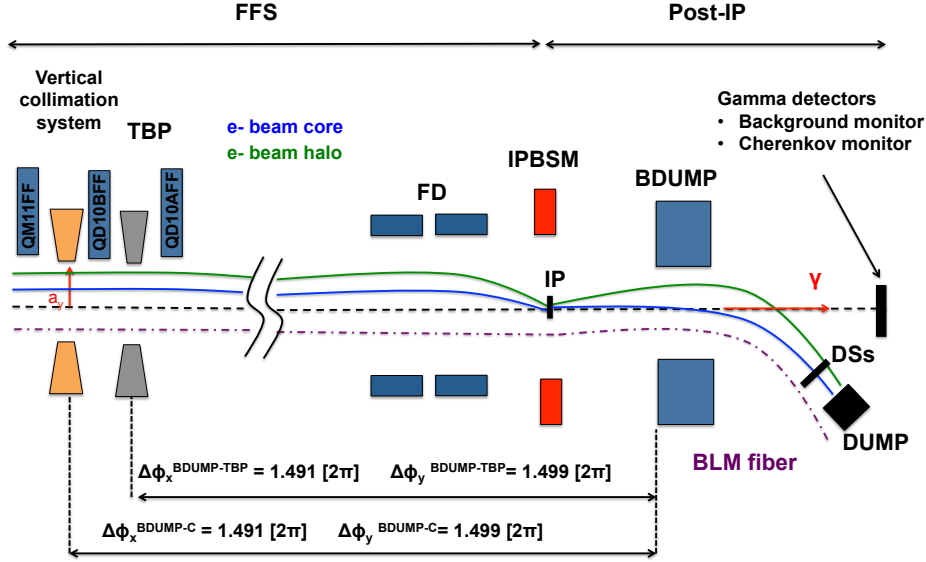
Figure 5.13: Experimental set up with the different diagnostic devices used to check the vertical collimation system functionality in March 2016.

In ATF2, the beam time is divided in three shifts named as **DAY** (between 9.00 am and 15.00 pm), **SWING** (between 17.00 pm and 1.00 am) and **OWL** (between 1.00 am to 9.00 am). In Table. 5.3 the time and kind of shifts dedicated for the vertical collimation system commissioning are summarized. In the following we will present the measurements performed in each of these shifts.

E = 1.3 GeV and $(10\beta_x \times 1\beta_y)$ optics V5.2			
Date	**Shift**	**Beam time**	**Test performed**
9/3/16	DAY	4h	Verify and calibrate the control system
11/3/16	OWL	8h	Jaws control and alignment measurements
11/3/16	DAY	4h	Alignment measurement with the DS team
16/3/16	OWL	8h	Jaws control and alignment measurements
18/3/16	DAY	8h	Jaws control and alignment measurements

Table 5.3: Date, kind of shift, time and main objective of the vertical collimation system dedicated shifts taken in March 2016.

Measurements on the 9th of March 2016

In this first dedicated half shift, the control system was tested and the movement of the vertical collimation system observed using **the background monitor and the BLM fiber**. During this shift the beam energy was 1.3 GeV, the intensity between 0.4 and 0.6 $\times 10^{10}$ electrons per bunch, and the optics configuration used was $(10\beta_x^* \times \beta_y^*)$. The shift was taken after the beam tuning was performed. In addition to the data of the Post-IP

background monitor and the BLM fiber, we also recorded the charge and position. To save the data we used the following EPICS commands:

- **BIM:EXT:nparticles**, beam charge measurements with the Integrator Current Transformer (ICT).

- **REFC1:amp**, beam charge measurements with a reference C-BPM.

- **atf2:xpos**, all horizontal beam position monitors measurements.

- **atf2:ypos**, all vertical beam position monitors measurements.

- **IPBSM:BGMonitor:Signal**, background monitor measurements.

- **slacvme1:sdigi1:WAV**, BLM fiber measurements.

First, the background photons were measured with **the background monitor** with a PMT voltage of 1300 *V* for different vertical collimation system half apertures. In Fig. 5.14 the background reduction as a function of the vertical collimation system half aperture from 3 to 12 *mm* is shown for two different beam intensities. In each position the background was measured for 100 pulses and averaged. The associated error corresponds to the standard statistical mean error. The beam offset in the vertical plane was estimated from the measurements of the two BPMs installed before and after the collimation system using a ballistic transport of the position. During this shift the offset was about -0.3 *mm* (about 1 σ_y). In Fig. 5.14 we can observe an increase of the background level for the higher intensity case. The effect of the vertical collimation system is visible when it is closed to a half aperture of 6-5 *mm*.

Figure 5.14: Post-IP background reduction as a function of the vertical collimation system half aperture for two different beam intensities and PMT voltage of 1300 *V*.

Furthermore, the losses were measured with **the BLM fiber** and an increase of the losses is observed when the vertical collimation system is closed to more than 6 *mm* as

can be sen in Fig. 5.15. This peak correspond to the losses in the high-β region. The second peak is identified as the DUMP region.
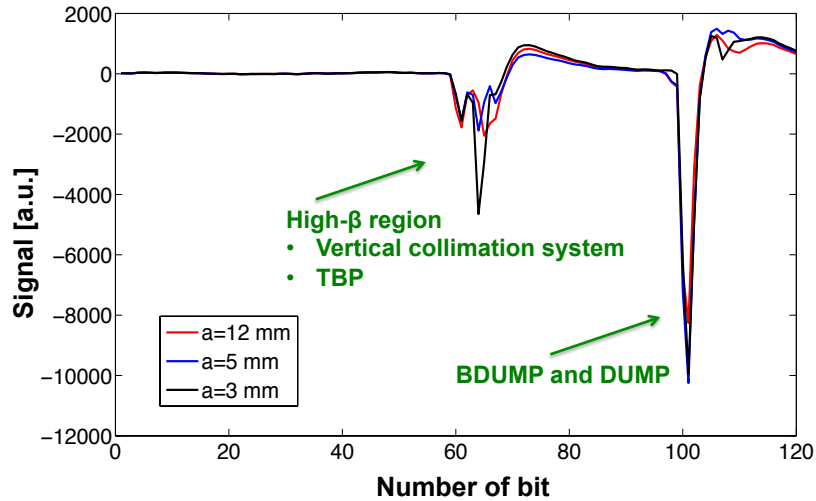
Figure 5.15: FFS beam BLM fiber signal for different vertical collimation system half apertures.

Measurements on the 11th of March 2016

In this second shift, the functionality of the system was tested using **the background monitor and the TBP**. Also the jaws-beam alignment was measured using the Post-IP WS. During this shift the beam energy was 1.3 GeV, the intensity 0.6×10^{10} electrons per bunch, and the optics configuration used was ($10\beta_x^* \times \beta_y^*$). The shift was taken after the beam tuning was performed.

As in the first shift, first **the background monitor** was used. For each aperture of the vertical collimation system the background was measured for 100 pulses. The beam offset in the vertical plane was estimated from the measurements of the two BPMs installed before and after the collimation system. The offset was about -0.3 *mm* (about 1 σ_y). In addition, the position of the TBP was changed from the optimized position (-0.465 *mm* offset) to another position (-2 *mm*). An increase of background is observed when the TBP is moved from -0.465 *mm* to -2 *mm* which corresponds to moving the TBP from a position for which the beam is passing through the center (the measured beam offset at the TBP position is about -0.5 *mm*) to a position in which the beam is not passing through the center as illustrated in Fig. 5.16.

The impact of closing the collimation system is observed in the reduction of photons detected by the background monitor. Notice here that when the TBP is centered the cut at its half aperture of 8 *mm* corresponds to 18 σ_y about the same cut when the vertical collimation system is closed to 5 *mm*. To reduce the background at the same level as the TBP the vertical collimation system has to be closed to 5 *mm*. When the TBP is not centered we are collimating only one side of the vertical beam halo.

In the second part of the shift in order to measure the **beam-jaws alignment**, the beam halo cut of the vertical collimation system was measured with **the Post-IP WS**. The
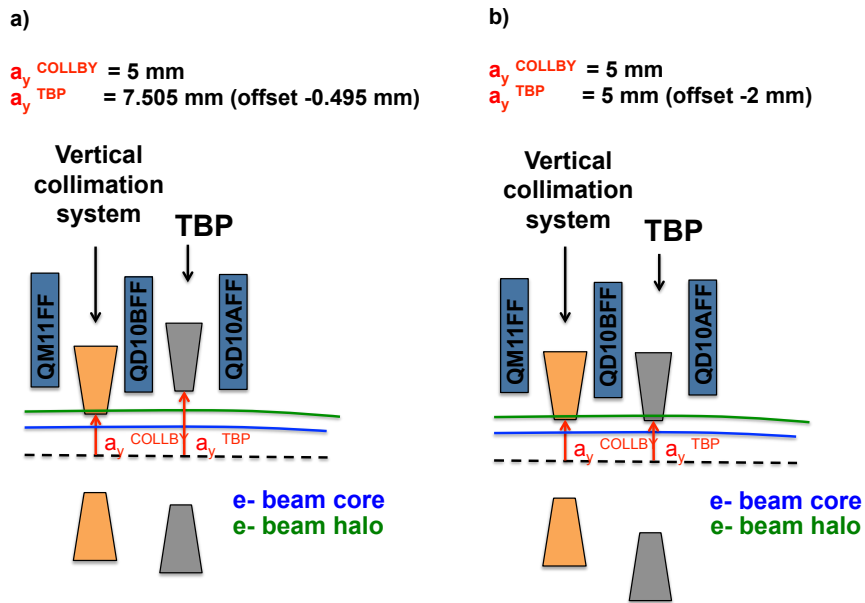
Figure 5.16: Vertical collimation system and TBP position for the two scenarios in which measurements have been taken: a) where the TBP has an offset of -0.495 *mm*. b) where the TBP has an offset -2 *mm* .
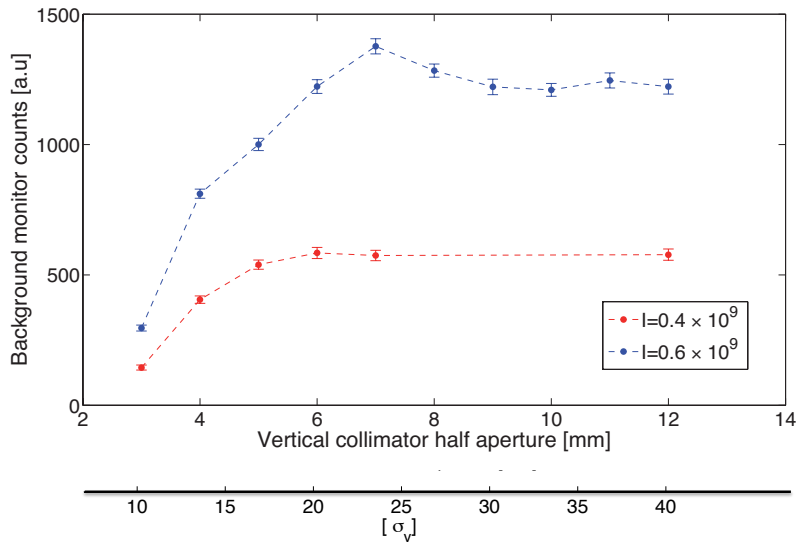

Figure 5.17: Post-IP background reduction as a function of the vertical collimation system half aperture for two different TBP positions and background monitor PMT voltage of 1300 *V*.

WS control panel was used to perform the measurements and save the data. The beam halo is scanned with different PMT voltages in order to increase the dynamic range for beam halo measurements. The data taken at higher voltages is normalized according to the overlap region with the data taken at lower voltages. The normalization procedure is explained in more detail in [9]. 500 *V* PMT voltage was used to measure the beam core while for beam halo the voltage was set to 900 and 1300 *V*. In these measurements, the carbon wire with 7 *μm* diameter was used. Then, following the procedure in [9] the beam halo distribution has been reconstructed. In Fig. 5.18 the vertical beam halo distribution measured when the vertical collimation system is closed to a half apertures of 3 *mm* is shown. The scanning range in *mm* has been normalized to the beam size measured using the Post-IP WS, being $\sigma_y = 0.270 \pm 0.007$ *mm*.

Figure 5.18: Post-IP WS vertical beam halo distribution measured when the vertical collimation system was closed to 3 *mm* half aperture.

The vertical beam size expected for the $(10\beta_y \times 1\beta_x)$ is about 0.230 *mm*. The beam halo cut observed in these measurements is on the left side about 10 σ_y and on the right side about 8 *sigma*$_y$. However, due to the beam orbit at the vertical collimation system the error associated to the beam halo cut observed is about one σ_y making within the associated error the beam halo cuts on the left and right side compatible.

In collaboration with the DS team, the beam halo distribution was also measured with **the DS** to investigate the beam-jaws alignment and **benchmark** the measurements with the **Post-IP WS measurements**. In order to observe the vertical collimation system cut in the DS as was shown in the tracking simulations presented in chapter 2, the vertical collimation system has to be closed to 3 *mm*. In Fig. 5.19 the horizontal (top) and vertical (bottom) beam halo distributions measured with the DSs are shown for the vertical collimation system opened and closed to 3 *mm*. In the vertical distribution a beam halo cut is observed when the vertical collimation system is closed to 3 *mm* at the level of 10 ±, on the left side, and 9 ±, on the right side. These measurements are in agreement with the associated errors with the Post-IP WS observations. The difference observed between the left and right side are compatible in both measurements and can be explained by the offset of the beam passing through the the vertical collimation system about one σ_y.
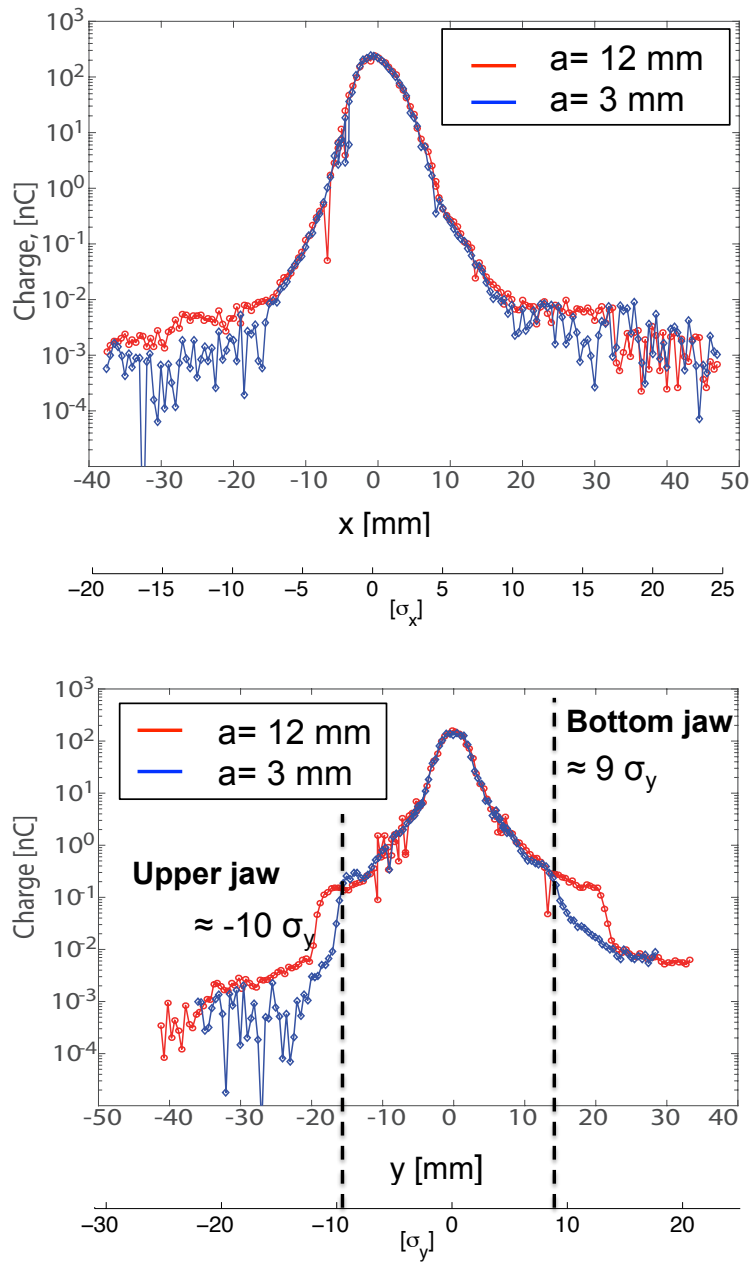
Figure 5.19: Horizontal (top) and vertical (bottom) beam halo distribution measured with the DSs for the vertical collimation system opened and close to 3 *mm* half aperture.

Measurements on the 16th of March 2016

In this shift, we repeated some of the tests performed in the first two shifts in order to confirm the observations. The Post-IP background monitor and the BLM fiber were used. The beam energy was 1.3 GeV. Part of the shift was dedicated to tune the beam to a high intensity in order to study the increase of background in the beamline as a function of the beam intensity. During the experiments the intensity was ranging from 0.2-1 $\times 10^{10}$ electrons per bunch, and the optics configuration used was ($10\beta_x^* \times \beta_y^*$). The vertical beam offset estimated from the measurements of the two BPMs installed before and after the collimation system during this shift was about -0.2 *mm*.

First using **the BLM fiber**, the total losses were measured as a function of the beam intensity. In Fig. 5.20 the beam losses along the ATF2 beamline (left) and the total losses (right) are shown. A linear increase of losses as a function of the intensity is observed. Then, following the same procedure as in previous shifts the background as a function of the vertical collimation system half aperture was measured for two different beam intensities using **the background monitor**. The results are shown in Fig. 5.21.
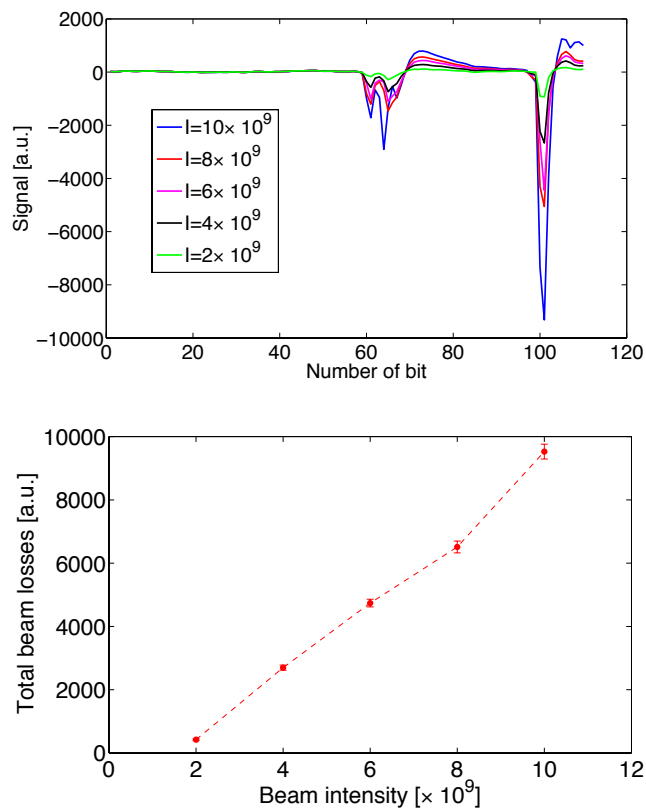
Figure 5.20: Beam losses along the FFS (top) and total losses measured with the BLM fiber in the FFS as a function of different beam intensities.
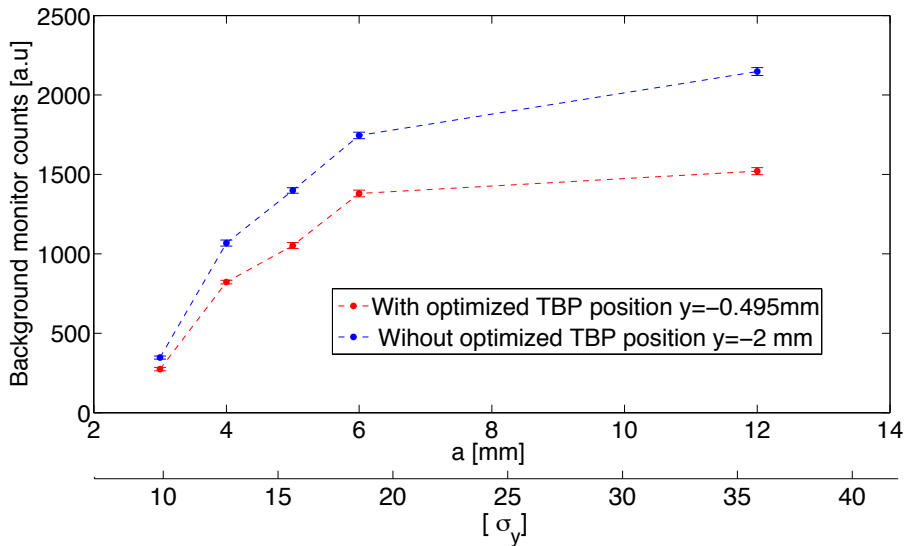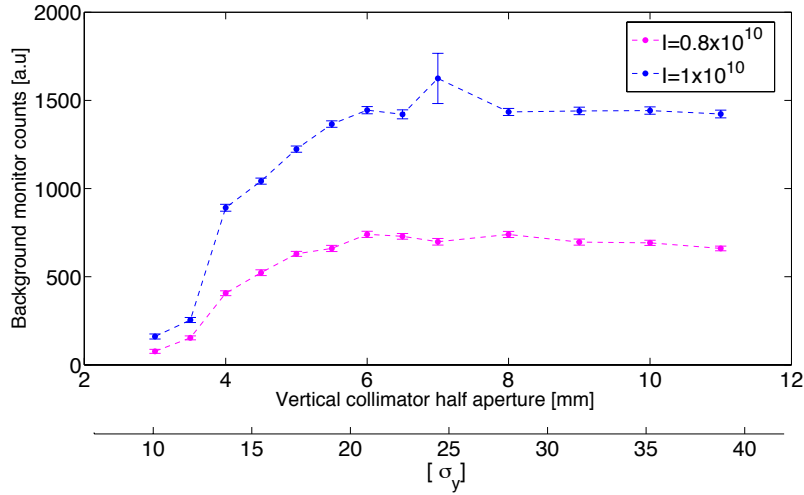
Figure 5.21: Post-IP background reduction as a function of the vertical collimation system half aperture for two different beam intensities and a background monitor PMT voltage of 1300 *V*.

Measurements on the 18th of March 2016

In order to have **more statistics** the Post-IP background measurements were taken **for a different beam intensity** and the Post-IP WS measurements were repeated for different vertical collimation system half apertures. During this shift the beam energy was 1.3 GeV, the intensity 0.7×10^{10} electrons per bunch, and the optics configuration used was $(10\beta_x^* \times \beta_y^*)$.

In Fig. 5.22, the signal of **the background monitor** is depicted as a function of the collimation system half aperture. A reduction of the background has been measured at the post-IP region for half apertures of the collimation system smaller than 6 *mm* in agreement with the measurements performed on the 11th and 16th of March 2016. The vertical beam offset estimated at the vertical collimation system was about -0.2 *mm*.

In Fig. 5.23, the vertical beam halo distribution measured with **the Post-IP WS** for the vertical collimation system half apertures of 3, 3.25 and 3.5 *mm* is shown. The same voltage configuration was used as in the 11th of March 2016 shift. 500 *V* PMT voltage was used to measure the beam core while for beam halo tails the voltage was set to 900 and 1300 *V*. In these measurements, the Tungsten wire with 7 *μm* diameter was also used. Then, following the procedure in [9] the beam halo distribution has been reconstructed. The scanning range in *mm* has been normalized to the beam size measured using the P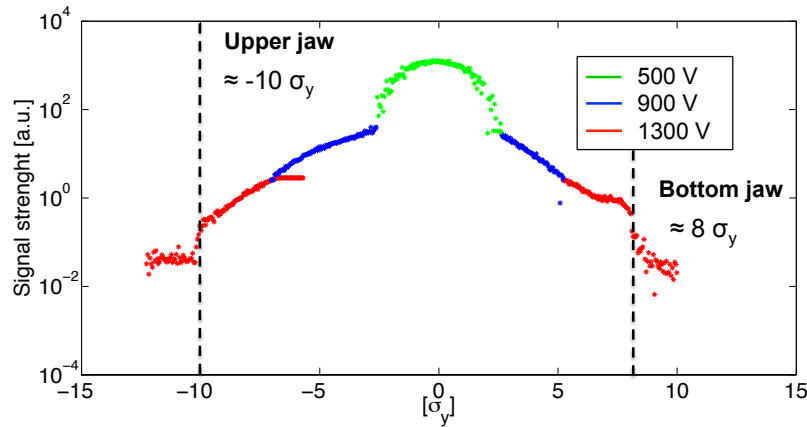ost-IP WS, being in this case σ_y = 0.274±0.007 *mm*. The vertical beam size expected for the $(10\beta_y \times 1\beta_x)$ is about 0.230 *mm*. The vertical beam halo cut observed on the left side is 8 and on the right side is 8. However, due to the beam orbit at the vertical collimation system the error associated to the beam halo cut observed is about one σ_y making the beam halo cut on the left and right side compatible.
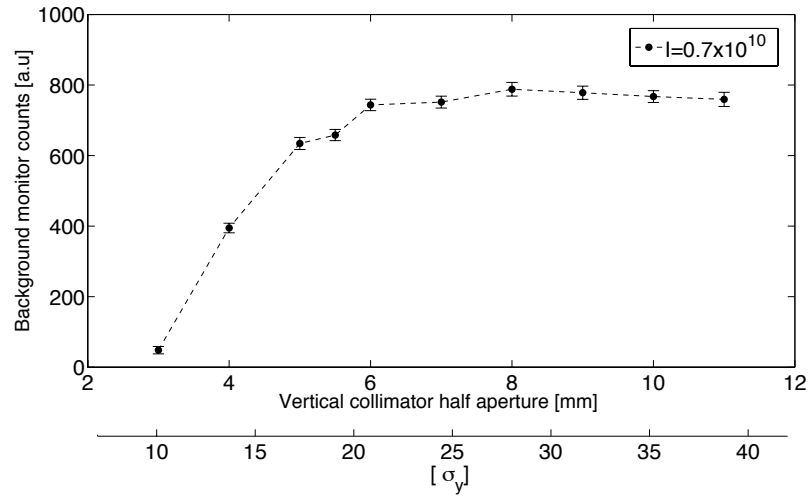
Figure 5.22: Post-IP background reduction as a function of the vertical collimation system half aperture and a background monitor PMT voltage of 1300 *V*.
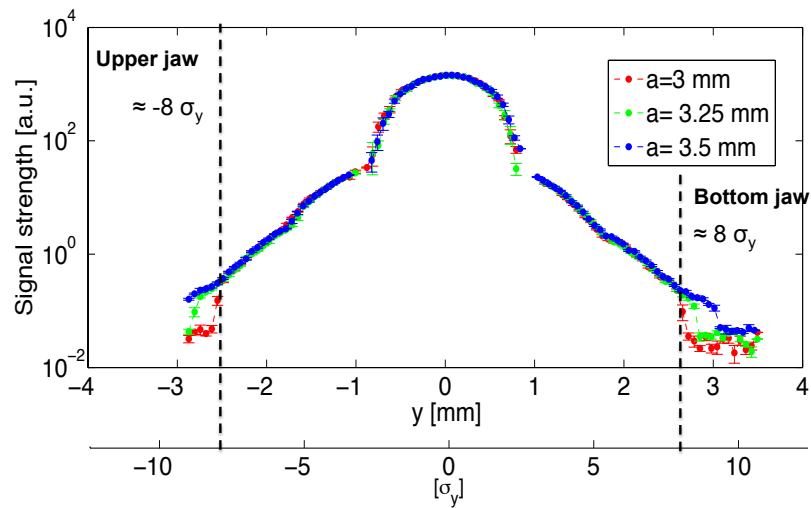
Figure 5.23: Vertical beam halo distribution measured with the Post-IP WS for 3, 3.25 and 3.5 *mm* vertical collimation system half apertures.

Summary of the measurements taken in March 2016

From these studies we could conclude:

- **The functionality and control** of the vertical collimation system have been **tested successfully**. The **background photons are reduced** as the vertical collimation system half aperture is closed more than **6** *mm***, in agreement** with the BDSIM **simulations**.

- The measured **beam halo cut for 3** *mm* **vertical collimation system half aperture with the Post-IP WS and the DS** is **compatible** with the associated errors. The measured cut on the vertical beam halo is comparable with the value of about $11\sigma_y$ observed on the MADX-PTC **simulations**.

6 Chapter

Experimental studies with the vertical collimation system in ATF2

6.1 2016 vertical collimation system experimental program summary

An experimental program has been carried out during 2016 in order to demonstrate the efficiency of the vertical collimation system in reducing the background photons in the Post-IP and measure the wakefields induced by such a system. Regarding the wakefields, only the impact on the orbit has been measured. The impact on the beam size growth could also be investigated by using the IPBSM monitor but because of time issues we could not perform this experiment.

The **optimum operation mode** of the vertical collimation system installed in the ATF2 has to be investigated in terms of efficiency and **acceptable wakefield impact**. Because of that, in the first part of the chapter, we present in detail the wakefield experiment. These studies are crucial for future design of the FLC collimation systems because **discrepancies exist in the wakefield kick described in different analytical models**, in the models implemented **in the tracking codes** and **between simulations and measurements** as reported in previous experiments (ESA (SLAC) 2001-2007 [36]). Furthermore, depending on the geometry of the jaws and beam parameters there are **different analytical models** to describe the geometrical component of the wakefield impact (inductive, intermediate, diffractive) and when the parameters of the problem sit **close to the limits of the models the estimations are not accurate**.

In our studies, we performed a systematic benchmark of the wakefield kick including CST PS numerical simulations and measurements contributing to the validation and understanding of the applicability of these models. Furthermore, the analytical models **only describe the jaws** of the collimation system and in our work we have studied the impact of a complete realistic collimation system including numerical simulations and measurements.

In the second part of this chapter, the measurements of the vertical collimation system efficiency are presented for different run periods, under different beam and machine conditions and compared with the BDSIM simulations. Furthermore, the efficiency

has been investigated in comparison to the TBP and on the IPBSM measurements. A summary of the shifts taken in the May, October, November and December 2016 runs is shown in Table. 6.1.

Vertical collimation system 2016 runs			
Date	Shift	Beam time	Test performed
17/05/16	SWING	4h	Cavity BPMs calibration
17/05/16	OWL	8h	Efficiency measurements
20/05/16	DAY	4h	Wakefield/Bunch length measurements
24/05/16	SWING	8h	Wakefield measurements
27/05/16	OWL	8h	Wakefield/ Efficiency measurements
19/10/16	SWING	8h	Wakefield/ Efficiency measurements
30/11/16	OWL	8h	Bunch length/IPBSM measurements
01/12/16	OWL	2h	Wakefield measurements

Table 6.1: Summary of dedicated shifts for the vertical collimation system in 2016.

6.2   Collimation system wakefield measurements

In this section, we present the measurements of the wakefield impact induced by the vertical collimation system on the orbit and all related studies performed to study the feasibility and accuracy of the experiment. In a first part, the experiment scheme is described and a feasibility study to determine if the wakefield impact on the orbit is measurable or not, and under which conditions, is presented. After, the raw BPM orbit data analysis, the BPMs calibration procedure and the resolution measurements are reported. In addition, in order to perform a systematic benchmarking study with previous calculations presented in chapter 3, the bunch length has been measured and the results are shown also in this section. Furthermore, in order to validate the analysis the experiment has been simulated using the tracking code PLACET (v1.0.1). In the final part of this section, the results of the experiment are presented as well as a **benchmarking study of theoretical models, numerical simulations and measurements**.

6.2.1   Experimental description

In this experiment, we only measured the **wakefield impact** induced by the vertical collimation system **on the orbit**. As introduced in chapter 1, the wakefields are induced when the beam is passing through an accelerator component with an offset, Δy^c. In our experiment, in order to simulate this condition we move the vertical collimation system around the beam in a symmetric way keeping constant the half aperture (a) of the system but changing the collimator-center-beam offset and we measure the induced orbit changed in the downstream BPMs. This could be done because the collimation system jaws can be moved independently. From Eq. (1.36) introduced in chapter 1, the orbit variation at a downstream BPM, Δy^{BPM}, is related with the offset at the collimation system, Δy^c as:

$$\Delta y^{BPM} = R_{34}\frac{eq}{E}\kappa_y \Delta y^c \qquad (6.1)$$
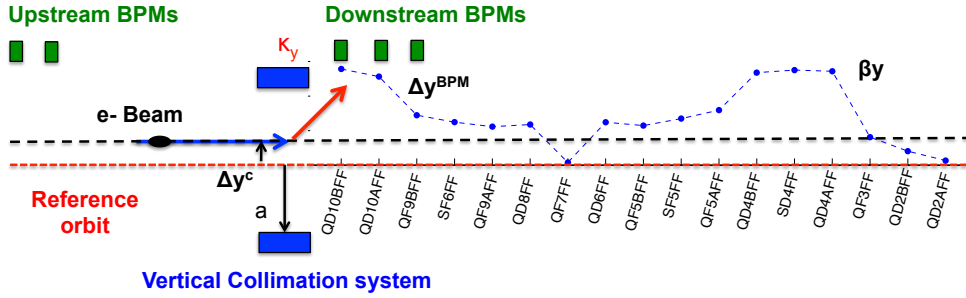
Figure 6.1: Vertical collimation system wakefield measurements set up description.

where R_{34} is the optics transfer matrix element, E is the nominal ATF2 beam energy and eq is the measured charge of the beam. Using the definition of the transfer matrix element R_{34}, from Annex 1, we can calculate the wakefield kick in practical units from Eq. (6.1) as:

$$\kappa_y[\frac{V}{pCmm}] = \frac{1}{\sqrt{\beta^{BPM}[mm]\beta^c[mm]}\sin\Delta\phi^{BPM-C}} \frac{E[eV]}{eq[pC]} \left(\frac{\Delta y^{BPM}}{\Delta y^c}\right) \qquad (6.2)$$

where β_y^c is the vertical β function at the vertical collimation system location, β_y^{BPM} is the vertical β function at the BPM location and $\Delta\phi^{BPM-C}$ is the phase advance difference between the vertical collimation system and the BPM.

From Eq. (6.1) we can already deduce which are the important **key parameters of the experiment** that will impact the accuracy of the measurements. These parameters are the optics, the beam intensity and the beam energy.

Prior to the realization of the experiment, **a feasibility study** was performed to asses if the vertical collimation system wakefield impact is measurable in the ATF2 or not. For this, we needed to identify which are the most sensitive BPMs and best beam and machine conditions.

In Fig. 6.2, the transfer matrix element R_{34} and $(\beta_y)^{1/2}$ for the $(10\beta_x \times 1\beta_y)$ optics V5.2 are shown for the seventeen C-BPMs located upstream the vertical collimation system.

From Eq. (6.1) we can deduce that the most sensitive C-BPMs are the ones located at a high R_{34} value. In Fig. 6.2 the best C-BPMs candidates are indicated in red. In addition, the $(\beta_y)^{1/2}$ function has been plotted in Fig. 6.2 to study which are the locations more sensitive to orbit beam jitter. The higher the β_y function, the higher the vertical beam size and the higher will be the orbit beam jitter. In the ATF2 a beam orbit jitter about 20-30 % of the transverse beam size has been measured. The argument of orbit jitter amplification with the beam size and therefore with the β function is the same as in Eq.(1.40) introduced in chapter 1.

The expected Δy^{BPM} has been calculated using Eq. (6.1) in order to asses an order of magnitude of the expected orbit variation at the downstream C-BPMs. These values have been compared with the C-BPMs resolution. In Fig. 6.3 the expected vertical collimation system wakefield impact at all downstream C-BPMs is calculated for the nominal beam intensity of 1×10^{10} and $(10\beta_x \times 1\beta_y)$ optics version V5.2. For these calculations we have used the vertical collimation system wakefield kick calculated with CST PS for 5, 4 and 3 mm half apertures, 9 mm bunch length and 1 mm vertical
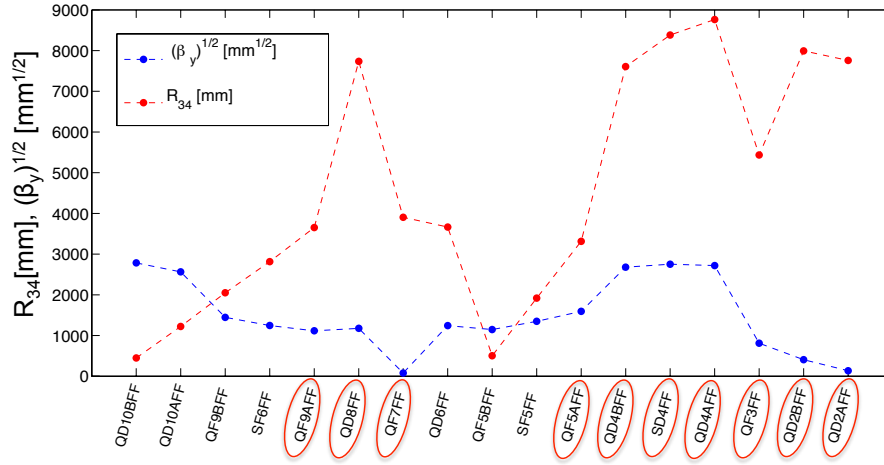
Figure 6.2: Vertical collimation system downstream C-BPMs R_{34} and $(\beta_y)^{1/2}$ function values for the $(10\beta_x \times 1\beta_y)$ optics V5.2. The best C-BPMs candidates are indicated in red.

beam offset. The reason why we have used for this calculation a bunch length of 9 *mm* instead of 7 *mm* as used in chapter 3 is because during these experiments we measured the bunch length and we obtained a longer bunch for high intensities. This is due to Intra-Beam Scattering (IBS) in the DR [116]. The bunch length measurements performed during our experiments and related studies are presented later in this section. In Fig. 6.3 the expected C-BPMs resolution is indicated and the C-BPMs at which the expected orbit variation, Δy^{BPM}, is higher than the expected C-BPMs resolution for all the vertical collimation system half apertures studied has been indicated in red. In blue, some additional candidates for the case of measuring the impact for 4 and 3 *mm* half aperture are also marked. However, different error sources could jeopardize the detection of the collimation wakefield impact in the different C-BPMs.

In the ATF2, the beam is operated at different intensities ranging from 0.1-1 $\times10^{10}$. The impact of the vertical collimation system wakefield kick increases linearly with the intensity as can be seen in Eq. (6.1). In order to investigate the impact of the beam intensity in our experiment the calculations presented in Fig. 6.3 have been repeated as a function of the beam intensity for the case of closing the vertical collimation system to half aperture of 4 and 3 *mm* (Fig. 6.4 top and bottom respectively). This calculation has been performed at three C-BPMs ($QF7FF$, $QD2AFF$ and $SD4FF$). In these plots the resolution measured in March 2016 of the three C-BPMs studied is indicated with dash lines with a different color for each C-BPM.

We could conclude from this first study that there are some C-BPMs where the vertical collimation system wakefield kick can be measured (indicated in red in Fig. 6.3) but the beam intensity should be higher than 0.8×10^{10} electrons for 4 *mm* vertical collimation system half aperture and higher than 0.4×10^{10} for 3 *mm* vertical collimation system half aperture.
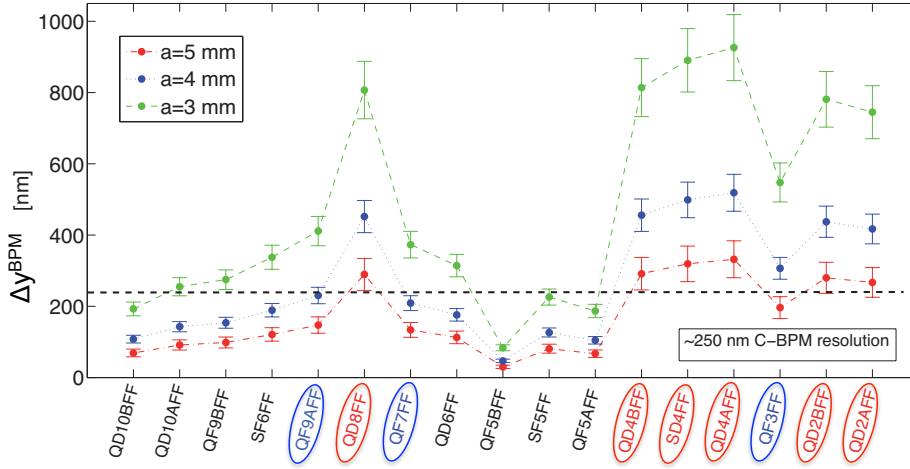
Figure 6.3: Estimated, Δy^{BPM}, considering the wakefield kick calculated with CST PS for 9 *mm* bunch length, a beam intensity of 1×10^{10} and 1 *mm* vertical beam offset. The design C-BPMs resolution is about 250 *nm* [63] indicated in the figure with a black dash line.

6.2.2 BPMs raw data analysis and BPM resolution measurements

The BPMs orbit data has to be carefully analyzed. One important point is the fact that the expected orbit variation is at the level of the expected orbit jitter. Therefore, a method to subtract this jitter effect has to be used. The method used is based on measuring the correlation between the upstream and downstream vertical collimation system C-BPMs. This correlation is then used to predict the orbit at a given vertical collimation system downstream C-BPM. The difference between the measured and predicted orbit is used to estimate the wakefield impact of the vertical collimation system. The orbit data is saved in two orbit matrices: A, for the upstream BPMs with dimension $P \times M_{up}$ and B, for the downstream BPMs with dimension $P \times M_{down}$. Where P is the number of pulses and M_{up} and M_{down} the corresponding number of upstream and downstream BPMs, respectively. The corresponding matrices are described as:

$$A = \begin{pmatrix} BPM_1^1 & BPM_2^1 & ... & BPM_{M_{up}}^1 \\ BPM_1^2 & ... & ... & ... \\ ... & ... & ... & .... \\ BPM_1^P & ... & ... & ... \end{pmatrix} B = \begin{pmatrix} BPM_1^1 & BPM_2^1 & ... & BPM_{M_{down}}^1 \\ BPM_1^2 & ... & ... & ... \\ ... & ... & ... & .... \\ BPM_1^P & ... & ... & ... \end{pmatrix} \quad (6.3)$$

In the following, we describe in detail the different steps performed in the analysis of the raw BPM data and the procedure to calculate from the measurements the vertical collimation system wakefield kick, κ_y:

1. **Data filtering and normalization**: the zeros in charge are removed as well as the pulses with a position and charge value higher 5σ of the corresponding distribution. In addition, we subtract the averaged orbit to all data in order to remove possible systematic offsets and we normalize the data to the charge.
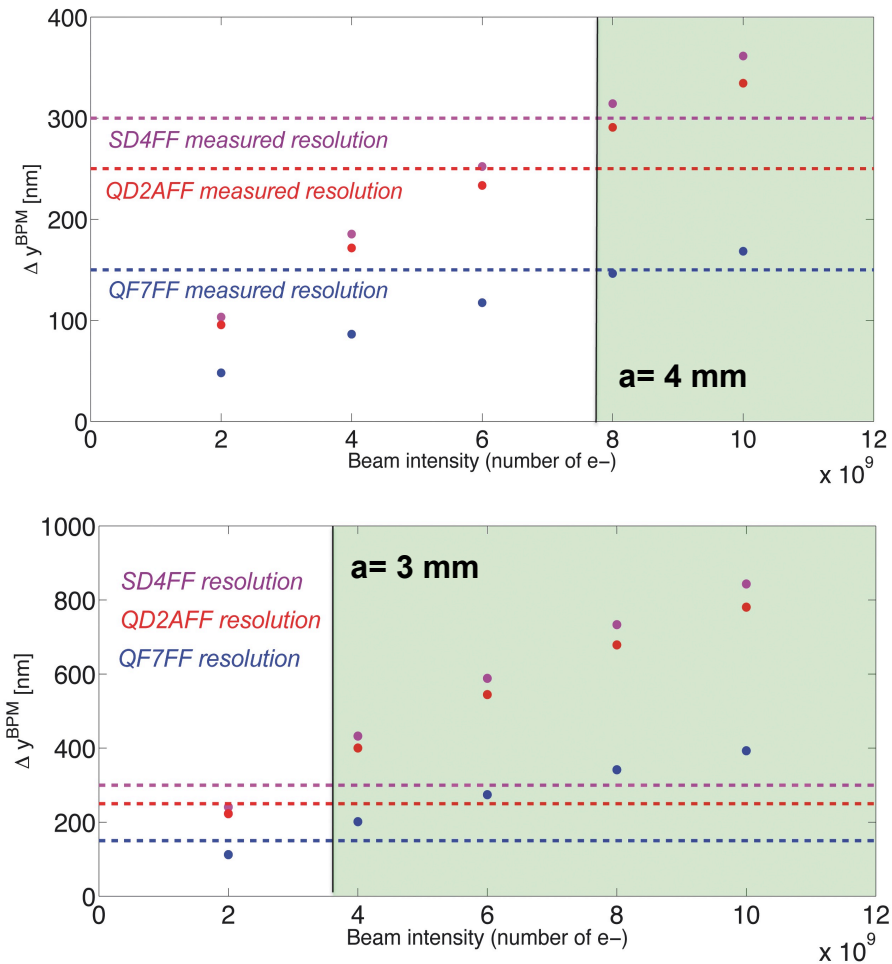
Figure 6.4: Calculated, Δy^{BPM}, at three C-BPMs ($QF7FF$, $QD2AFF$ and $SD4FF$) as a function of the beam intensity, considering the wakefield kick calculated with CST PS for a bunch length of 9 *mm* and 1 *mm* vertical beam offset. The study has been done for a vertical collimation system half aperture of 4 *mm* and 3 *mm* (top and bottom respectively). The resolution measured in March 2016 at the three C-BPMs studied has also been indicated with dash lines with a different color for each C-BPM. The region colored in green indicated the intensities for which the expected Δy^{BPM} is measurable given the C-BPM resolution.

2. **Orbit jitter subtraction**: In order to perform this we calculate the **correlation matrix, X**. The correlation matrix correlates the orbit at the vertical collimation system upstream BPMs, A, with the orbit at the downstream ones, B, as:

$$AX = B \qquad (6.4)$$

The orbit matrices A and B are measured and the correlation matrix, X, calculated as:

$$X = A^{-1}B \qquad (6.5)$$

For the calculation of the X matrix we use all orbit data taken during the scan for the different vertical collimation system positions with $(M_{up} \times P)$ dimension. In order to reduce systematic errors in our measurements we have analyzed the orbit at the upstream C-BPMs for the different vertical collimation system offsets. In some cases, we observed a correlation between the upstream vertical collimation system C-BPMs and the orbit. We do not consider the orbit of those C-BPMs in the analysis. This could be caused by misfunctioning of these C-BPMs or vibrations due to the movement of the collimation system for those C-BPMs close to the collimation system.

In order to invert the orbit matrix, A, containing the orbit data of the upstream C-BPMs the Singular Value Decomposition (SVD) method is used. The matrix A can be decomposed using the SVD method as:

$$A = USV^T \qquad (6.6)$$

Using the SVD method the inverse matrix of A can be calculated as:

$$A^{-1} = VS^{-1}U^T \qquad (6.7)$$

being S^{-1}, the inverse of a diagonal matrix (easy to calculate). Here, we apply a cut on the singular values lower than 10^{-4} to reduce the noise of the orbit signal. Using this result and substituting in Eq. (6.5) the matrix X is calculated.

Then, we average for all pulses. In that case, the correlation matrix is denoted as $\bar{X}$ with dimension $(M_{up} \times 1)$ and the orbit matrices as $\bar{A}$ and $\bar{B}$, with dimensions of $(1 \times M_{up})$ and $(1 \times M_{down})$, respectively.

In a second step, we calculate what we called the **residual** for a given downstream C-BPM, i, for each collimator-beam offset, R^i using the average correlation orbit matrix. We select a given downstream C-BPM, $\bar{B}^{i'}$, where we want to measure the wakefield kick impact and we calculate the residual for a given collimator-beam offset as:

$$R^i = \bar{A}\bar{X} - \bar{B}^i \qquad (6.8)$$

These residuals are equivalent to the Δy^{BPM} in Eq. (6.1) after subtracting the orbit jitter. From the correlation of these measured residuals, R^i, and the collimator-center-beam offset, Δy^c, the vertical collimation system wakefield kick can be estimated.

3. **Wakefield kick calculation**. The wakefield kick is calculated by fitting our residuals plot to a function of the form of Eq. (6.1):

$$\Delta y^{BPM} = R_{34} \frac{eq}{E} \kappa_y \Delta y^c \qquad (6.9)$$

where in our experiment the Δy^{BPM} corresponds to R^i. By comparing Eq. (6.9) with the equation of a first order polynomial fit and by using the R_{34} value from Annex 1, the wakefield kick is given by:

$$\kappa_y[\frac{V}{pCmm}] = \frac{1}{\sqrt{\beta^{BPM}[mm]\beta^c[mm]}\sin \Delta\phi^{BPM-C}}\frac{E[eV]}{eq[pC]}b \qquad (6.10)$$

where b is the coefficient of the linear term of the fit of the residuals plot. Notice that for this calculation other experimental parameters are needed as the beam intensity, the beam energy and the optics.

The resolution of the C-BPMs is also a key parameter of the experiment, The expected wakefield kick from the ATF2 vertical collimation system is of the order of 200-400 nm for 1 mm offset. In order to increase the statistics of the experiment we want to measure the impact at the maximum number of C-BPMs. In order to achieve the best C-BPMs resolution the C-BPMs are calibrated in each of the experimental runs. The C-BPMs system has been calibrated using the software developed by the RHUL team implemented on the ATF2 control room. In the following we briefly enumerate the calibration steps, more details can be found in [117]. From the ATF2 control room C-BPMs calibration panel we have to perform the following two steps:

1. **Digital Down Converter (DDC) frequency tune**. The output signal of the cavities is digitalized using a Digital Down Converter (DDC) which converts a digitized, band limited signal to a lower frequency signal at a lower sampling rate. The signal processing was designed in a way that the DDC frequency, ω^{DDC}, has to be optimized for both the dipole and reference cavities such as the amplitude and phase are sampled at a single point yielding to amplitude and phase. The value of this frequency is determined by minimizing the gradient of the phase of the DDC signal.

2. **Calibration scaling factors**. In a second step, the calibration constants which relates the signal with the beam position and angle of the beam passing through are measured by either moving the quadrupole which holds the BPM or by performing a 4-magnet closed orbit bump for those cavities not located inside quadrupoles on movers.

When performing this calibration, it is important to verify that the signal is not saturating the Analogical Digital Converter (ADC) which has a dynamic range of 14 bits (ADC range signal 16000 counts).

Once the C-BPMs have been calibrated, the resolution is calculated for each set of measurements, to check the performance of the C-BPMs and verify that the observations are reasonable.

Ideally, for each BPM, only random noise exists, and the standard deviation of the noise gives the resolution of the BPM. However, certain systematic noise often exists affecting the beam centroid motion as: beam injection position and phase jitter, beam energy jitter, beam intensity jitter.... The SVD analysis can be used to separate the coherent systematic noise from the random noise. In the following, we will enumerate the different steps involved on the resolution calculation:

1. **Orbit matrix measurement**. First, we measure the orbit matrix, O, with dimensions of $(P \times M_{all})$ of the form of:

$$O = \begin{pmatrix} BPM_1^1 & BPM_2^1 & ... & BPM_{M_{all}}^1 \\ BPM_1^2 & ... & ... & ... \\ ... & ... & ... & .... \\ BPM_1^P & ... & ... & ... \end{pmatrix} \tag{6.11}$$

where P is the number of pulses and M_{all} the total number of BPMs in the system.

2. **SVD decomposition and noise floor identifications**. The SVD decomposition is applied to the orbit matrix as $O = USV^T$. The diagonal elements of the singular matrix S (see Annex 4) give the correlation modes and the strength of them. The number of modes is equal to the number of BPMs in the system. An example of the diagonal elements of the matrix S for the 27th of May are shown in Fig. 6.5. In order to calculate the resolution of the BPMs one has to identify the noise floor modes corresponding to the diagonal elements of the matrix with lower values following a linear distribution (see zoom of Fig. 6.5). A zoom of the noise floor of the orbit data from the 27th of May is also indicated in Fig. 6.5. From this analysis one can also identify if there are some BPMs not
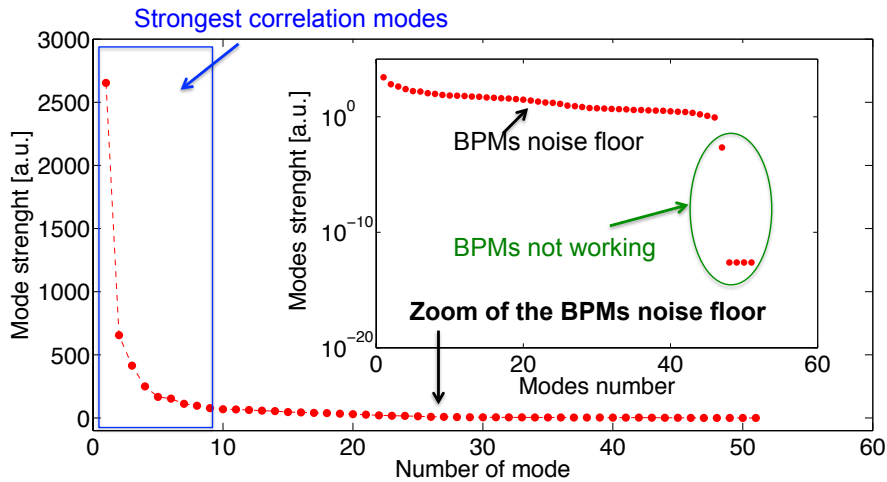
Figure 6.5: Example of the mode strength corresponding to the diagonal elements of the S matrix given by the SVD decomposition of the orbit matrix, O, calculated for an orbit data set from the 27th of May 2016.

working properly given by the number of modes with strength much smaller than the identified noise floor. In our example there are five modes satisfying this condition corresponding to five C-BPMs which are not currently working but still exist in the C-BPMs acquisition software named as $IP1$, $IP2$, $IP3$, $IP4$ and $FB2FF$.

3. **BPM resolution calculation**. Once the noise floor has been identified we recalculate the matrix O by zeroing the elements in S out of the identified noise

floor. The resolution of a given BPM is calculated as the standard deviation of the BPMs readings of the new orbit matrix without the coherent noise.

The BPMs were calibrated only in May, October and November 2016 runs. In Fig. 6.6 the resolution calculated for one shift of each run is shown. The resolution measured in March 2016 is slightly worst than in the other run periods but this difference could be significant for our experiment. For these calculations the first 10 higher modes were rejected.
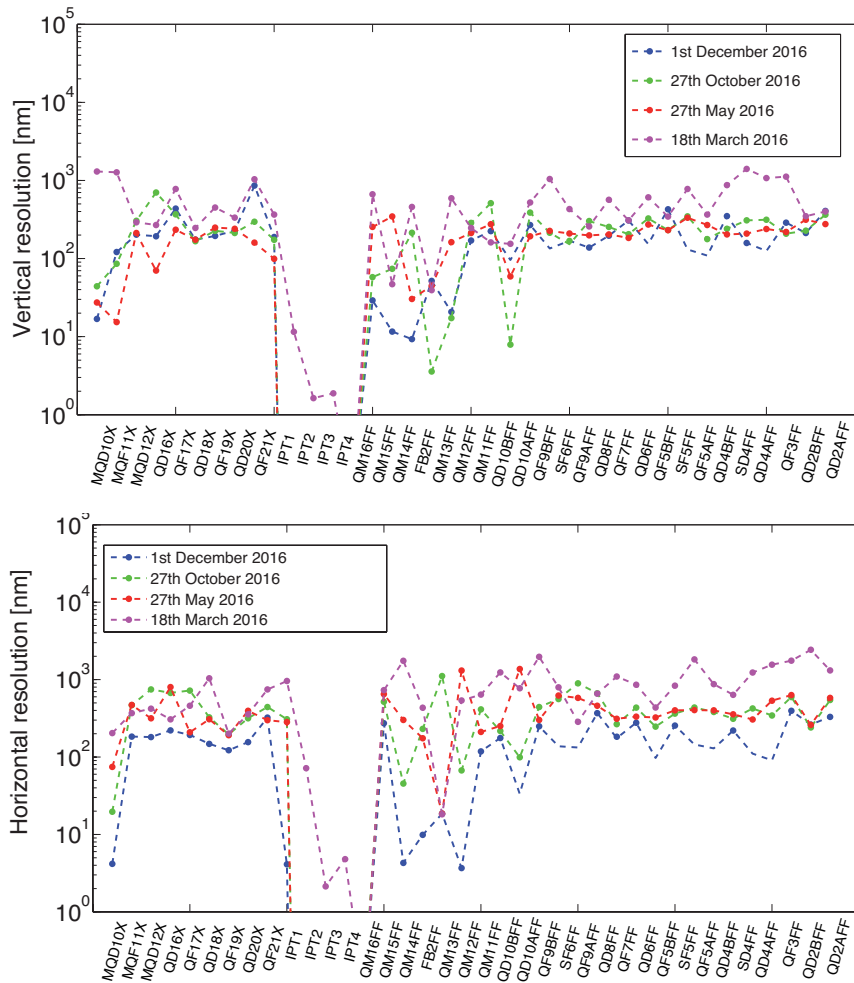
Figure 6.6: Vertical (top) and horizontal (bottom) C-BPMs resolution calculated for the March, May, October and November 2016 runs. Notice that the missing points in the November run correspond to the C-BPMs that were removed in this run period in order to perform a dedicated wakefield study.

6.2.3 Bunch length measurements

The accuracy in the benchmarking of the wakefield kick measurements with the simulations and analytical models will be limited by the bunch length uncertainty. In the

ATF2, the design value for the bunch length is 7 *mm* and most of the studies presented in chapter 3 were performed for 7 *mm* bunch length. However, due to the Intra-Beam Scattering (IBS) in the DR the bunch length increases from the design value as the beam intensity is increased [116]. The Streak camera [115] installed in the DR is used to measure the bunch length. This monitor is based on the measurement of the SR light emitted by the beam in the DR and has a resolution of 1.2 *ps* corresponding to about 0.04 *mm*. Bunch length measurements were performed in November 2016 as a function of the intensity and the results are shown in Fig. 6.7 (left). The measurements performed with the Streak camera are affected by a systematic error due to space charge effect for high intensities because of that an experiment was performed in order to estimate the accuracy of these measurements. This experiment consisted in measuring the bunch length for a given beam intensity of 0.8×10^{10} inserting filters in front of the Streak camera to change the intensity of the SR light arriving to the monitor with different absorption coefficients. The results of these measurements are shown in Fig. 6.7 (right). An 8% difference is observed between the bunch length measurements when all the SR light is arriving to the monitor and when the light is reduced to 10%. No change is observed when reducing the SR light arriving to the monitor an additional 40%. From these measurements we conclude that the error associated to the bunch length measurements at high intensity beam charge due to the space charge effect is about an 8 %.
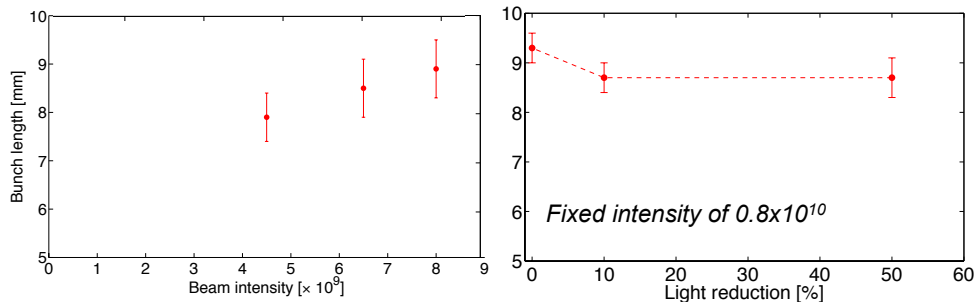
Figure 6.7: Bunch length measured in the DR with the Streak camera for different beam intensities (left) and Streak camera measurements for different filters absorption coefficient (right) for a fixed beam intensity of 0.8×10^{10}.

Due to the fact that to measure the wakefield kick of the vertical collimation system high intensity beams are required and measurements of the bunch length shows to depend on the intensity the wakefield kick has been calculated with both, CST PS and analytical models, as a function of the bunch length to complement the studies presented in chapter 3 and chapter 5. For these calculations a collimation system half aperture of 4 *mm*, a vertical beam offset of 1 *mm*, a beam intensity of 1×10^{10} and the ($10\beta_x \times 1\beta_y$) optics V5.2 have been considered. The results are shown in Fig. 6.8.

As a conclusion from all previous studies presented, the vertical collimation system wakefield kick is measurable at some C-BPMs only **for 4 and 3 *mm* vertical collimation system half aperture and high intensities**. The range of the scan of the experiment is also limited by the minimum half aperture of the vertical collimation
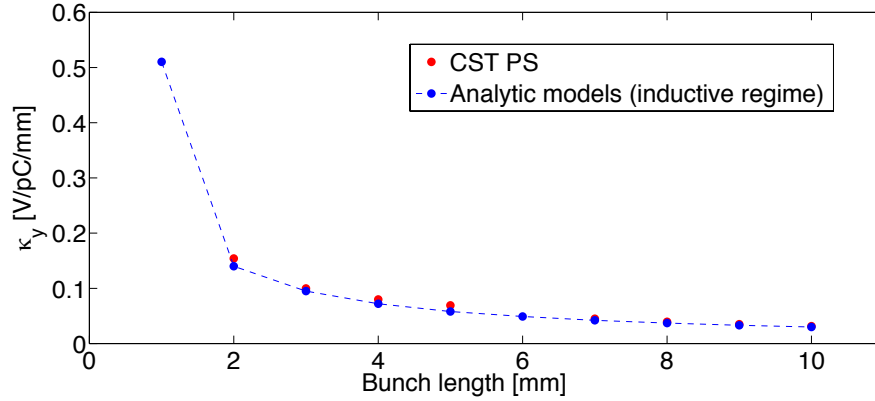
Figure 6.8: CST PS κ_y^{CSTSP} calculated for different σ_z in comparison to the analytical calculation (dash lines) ranging from 2 to 10 *mm*.

system which is fixed to 3 *mm* by a mechanical stop. In order to increase the wakefield impact in the experiments we follow two different strategies on the different runs, one consisted in increasing the intensity and the other in increasing the range of the scans by removing the mechanical stop. In May the strategy followed consisted in tuning the beam to high intensities. The intensity achieved was ranging from 0.9 to 1.1 $\times 10^{10}$. In October, we increase the range of the scans by removing the mechanical stop fixing the minimum half aperture of the vertical collimation system to 3 *mm* (installed for security reasons) from -2 to 2 *mm*. In December, both strategies were applied but the intensity was no high enough to perform the experiment for the vertical collimation system half aperture of 4 *mm*, therefore the experiment was performed only for a vertical collimation system half aperture of 3 *mm*.

6.2.4 Experiment simulations using PLACET (v1.0.1)

The PLACET (v1.0.1) tracking code has been used to simulate the experiment and test the analysis of the BPMs data described in this section in detailed. The orbit data has been recorded at each C-BPM for different vertical collimation system offsets. Then, the analysis method described in the previous section has been applied. The kick calculated from the simulated data has been compared with the calculated analytical value which is implemented in PLACET (v1.0.1) as described in chapter 3. The settings of the simulations are described in the following. A Gaussian beam distribution has been generated with 100 bunches with 50000 particles with the ATF2 energy of 1.3 *GeV* and a horizontal and vertical emittances of 2×10^{-9} *m.rad* and 1.18×10^{-11} *m.rad* respectively. The intensity of the beam was set to 6×10^9 electrons. The energy spread was set to the ATF2 nominal one being 0.08%. Furthermore, beam orbit jitter at the entrance of EXT line was generated following a Gaussian distribution with a standard deviation 20 % of the vertical beam size at the entrance of the EXT line. The nominal intensity and $(10\beta_x \times 1\beta_y)$ optics V5.2 have been used with multipoles included but no misalignment errors. The bunch length considered in these simulations was 9 *mm*. The experiment was simulated for a vertical collimation system half aperture of 4 *mm* and the system was offset from -1.5 to 1.5 *mm* with respect to the beam.

As an example of the results obtained from the simulations in Fig. 6.9 (top and middle) the residuals, R^i, are plotted as a function of the vertical collimation system offset with the linear fit depicted in red for two C-BPMs $QF7FF$ and $QD2AFF$. Using Eq. (6.2) the wakefield kick has been calculated at each C-BPM and the results are shown in Fig. 6.9 (bottom). The averaged value over all BPMs is indicated in red and corresponds to 0.033 $V/pC/mm$ which is in agreement with the expected value implemented on the PLACET (v1.0.1) collimator wakefield module based on analytical models. These simulations validated our data analysis and gave us an order of magnitude of the expected residuals at the different C-BPMs.
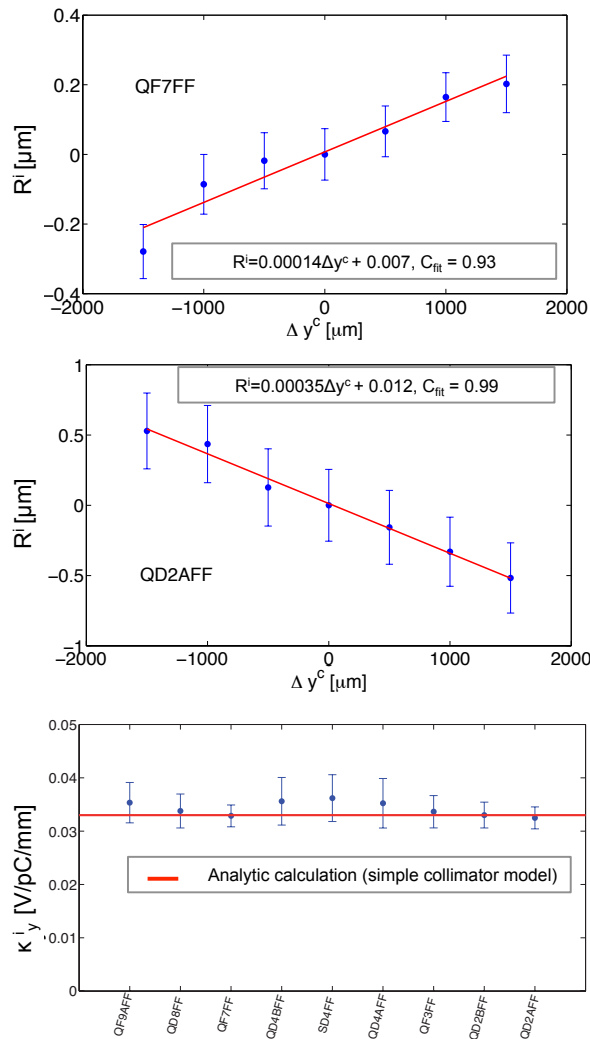
Figure 6.9: Residuals as a function of the Δy^c calculated from simulated orbit data generated with the PLACET (v1.0.1) tracking code at $QF7FF$ and $QD2AFF$ (top and middle) and κ_y^i calculated at the 9 C- BPMs downstream the vertical collimation system where the impact of the wakefield induced is expected to be measurable. The expected value calculated using the analytical models (in red) is indicated in the figure for comparison.

6.2.5   Wakefeld kick measurement

Based on the first studies presented in this section the experiment key parameters for each shift are summarized in Table. 6.2.

Vertical collimation system 2016 runs				
E = 1.3 *GeV* and ($10\beta_x \times 1\beta_y$) optics V5.2				
Date	a [*mm*]	BPMs calibration	σ_z[*mm*]	N[10^{10}]
20/05/16	4.00±0.01	No calibration	8.6±0.6	0.90±0.06
24/05/16	4.00±0.01	Only FFS BPMs	9.1±0.7	1.10±0.06
27/05/16	4.00±0.01	Complete	8.9±0.7	0.90±0.06
27/10/16	4.00±0.01	Complete	8.9±0.7	0.80±0.06
01/12/16	3.00±0.01	Complete	8.6±0.6	0.75±0.05

Table 6.2: Vertical collimation system 2016 wakefield kick measurements experimental set up summary.

In the following, we present in detail the results of the analysis of the vertical collimation system measurements taken in the 2016 runs. For each set of data, first the C-BPMs resolution has been measured and compared with the expected kick calculated for the shift parameters and 1 *mm* vertical collimator-beam offset. This first comparison gives us an indication to the C-BPMs which are more sensitive to the vertical collimation system wakefield impact. Notice here, that in some shifts the calibration of the C-BPMs system was not completed. The analysis has been applied to the data of all downstream C-BPMs.

20th of May 2016 run

In this shift, the calibration procedure **of the C-BPMs was not completed**. The measurements were performed for a fixed 4 *mm* vertical collimation system half aperture. The beam orbit was measured for different beam-collimation system offset ranging from -1 to 1 *mm* in steps of half a *mm*. For each vertical collimation system position 500 pulses were recorded. First, the C-BPMs resolution was measured and compared as an indicator with the expected orbit variation at the downstream C-BPMs as explained in detail in this section. This comparison is shown in Fig. 6.10 where the C-BPMs with resolution of the order or higher than the expected orbit variation, Δy^{BPM}, are indicated in red as possible candidates for the measurements. Δy^{BPM} has been calculated for 1 *mm* offset and the experiment parameters summarized in Table 6.2. Notice here, that the experiment has been performed for collimator-beam offset ranging from -1 to 1 *mm* in steps of half a *mm* and the calculation presented in Fig. 6.10 has been performed only for 1 *mm*.

Using the analysis procedure explained before, the C-BPMs raw data is cleaned and the residuals, R^i, calculated for each beam-collimation system offset and all C-BPMs. In Fig. 6.11 the residual plots measured at $QF7FF$ (top) and $QD2BFF$ (middle) are shown as an example. The wakefield kick calculated from the residual plot of those C-BPMs where a correlation has been observed is depicted in Fig. 6.11 (bottom). The expected value calculated from CST PS simulations (in green) and the analytic
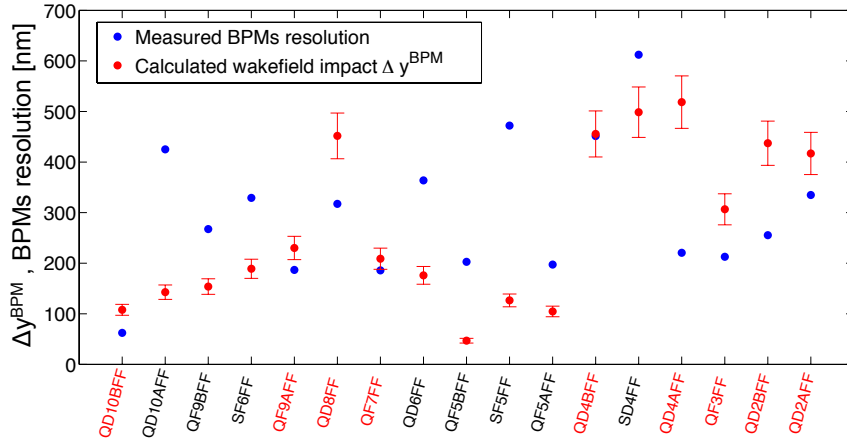
Figure 6.10: Comparison of the expected orbit variation, Δy^{BPM}, at the downstream C-BPMs with the measured C-BPMs resolution. Δy^{BPM} has been calculated for 1 *mm* offset and the experiment parameters summarized in Table 6.2. The BPMs with resolution of the order or higher than the expected variation are indicated in red for the 20th of May data set.

calculation (in red) are indicated in the figure for comparison. Measured fits with an associated error by one order of magnitude higher than the largest error depicted in Fig. 6.11 have not been considered when calculating the final average wakefield kick using Eq. 6.12 in order to reduce systematic errors, due to their negligible contribution. Possible reasons why some candidates C-BPMs were not sensitive to the measurements for this data set are a lack of precision in the analytic estimation of the expected wakefield kick, a bad performance of the C-BPMs as we are running at high intensity or a lack of accuracy on the reconstruction method due to large orbit shifts during the data taken process, or malfunctioning of a particular C-BPM.

We have calculated the average of the wakefield kicks depicted in Fig. 6.11 (bottom). For that, we have used the following equation where each measured wakefield kick calculated is weighted by its associated error:

$$\kappa_y^{average} = \frac{\sum_i \kappa_y^i / \sigma_{\kappa_y^i}^2}{\sum_i 1 / \sigma_{\kappa_y^i}^2} \tag{6.12}$$

The error of the average wakefield kick is given by:

$$\sigma_{\kappa_y^{average}} = \sqrt{\frac{1}{\sum_i \sigma_{\kappa_y^i}^{-2}}} \tag{6.13}$$

The error associated to each wakefield kick, κ_y^i, corresponds to the standard statistical error of Eq. (6.10) calculated as:

$$\sigma_{\kappa_y^i} = \left[\sigma_b^2 \left(\frac{\partial \kappa_y^i}{\partial b} \right)^2 + \sigma_N^2 \left(\frac{\partial \kappa_y^i}{\partial N} \right)^2 \right]^{1/2} \tag{6.14}$$

where the first contribution comes from the linear fit of the data and the second contribution corresponds to the beam intensity jitter. The design ATF2 values of the other factors involved in Eq. (6.10) have been used for the calculation. The main results of this shift are summarized in Table. 6.3.

a$[mm]$	Scan range $[mm]$	N $[x10^{10}]$	$\sigma_z[mm]$	$\kappa_y^{averaged}[V/pC/mm]$
4.00±0.01	±1.00 ± 0.01	0.90±0.06	8.6±0.6	0.047±0.006

Table 6.3: Measurements summary of the 20th of May 2016 run.

24th of May 2016 run

In this shift, only the calibration of the FFS C-BPMs was completed, however the C-BPMs upstream the collimation system already show a good resolution on the March data. The measurements were performed for a fixed 4 *mm* vertical collimation system half aperture. The beam orbit was measured for different beam-collimation system offsets ranging from -1 to 1 *mm* in steps of half a *mm*. For each vertical collimation system position 500 pulses were recorded. As for the previous shift the first step on the analysis consisted in comparing the expected orbit variation at the downstream C-BPMs with the measured C-BPMs resolution to determine the most sensitive C-BPMs for this set of data based on the analysis presented in detail in this section. This comparison is shown in Fig. 6.12 where the C-BPMs with resolution of the order or higher than the expected variation are indicated in red. Δy^{BPM} has been calculated for 1 *mm* offset and the experiment parameters summarized in Table 6.2.

Using the analysis procedure explained before, the C-BPMs raw data is cleaned and the residuals, R^i, calculated for each beam-collimation system offset and all C-BPMs. In Fig. 6.13 the residual plots measured at $QF7FF$ (top) and $QD2AFF$ (middle) are shown as an example. The wakefield kick calculated from the residual plot of those C-BPMs where a correlation has been observed is depicted in Fig. 6.13 (bottom). The expected value calculated from CST PS simulations (in green) and the analytical calculation (in red) are indicated in the figure for comparison. Notice again that not all C-BPMs candidates in Fig. 6.12 were sensitive to the measurements. The C-BPMs not shown in Fig. 6.13 have a measured fit value with an associated error by one order of magnitude higher than the largest error depicted in Fig. 6.13 as explained for the first measurements on the 20th of May. The main results of this shift are summarized in Table. 6.4.

a$[mm]$	Scan range $[mm]$	N $[x10^{10}]$	$\sigma_z[mm]$	$\kappa_y^{averaged}[V/pC/mm]$
4.00±0.01	±1.00 ± 0.01	1.10±0.06	9.1±0.7	0.037±0.003

Table 6.4: Measurements summary of the 24th of May 2016 run.

27th of May 2016 run

In this shift, the C-BPMs calibration was completed. The measurements were performed for a fixed 4 *mm* vertical collimation system half aperture. The beam orbit
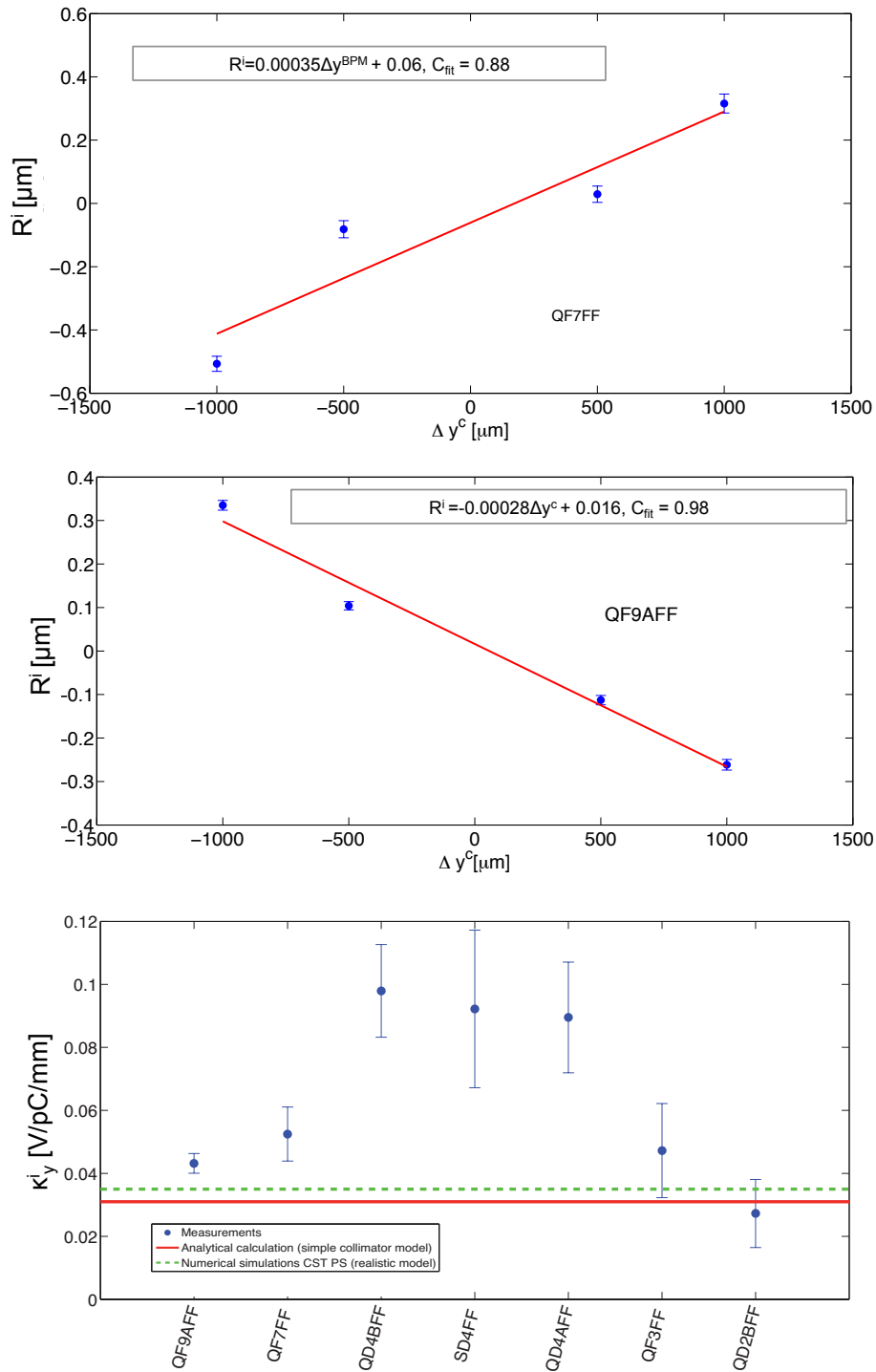
Figure 6.11: Residuals, R^i, as a function of collimator offset, Δy^c, at $QF7FF$ and $QD2AFF$ (top and middle) and κ_y^i measured at different C-BPMs. Measurements taken on the 20th of May. For completeness the green and red lines indicate the κ_y^{CSTPS} and $\kappa_y^{analytic}$ calculated for 9 mm bunch length.

Figure 6.12: Comparison of the expected orbit variation, Δy^{BPM}, at the downstream C-BPMs with the measured C-BPMs resolution. Δy^{BPM} has been calculated for 1 *mm* offset and the experiment parameters summarized in Table 6.2. The C-BPMs with resolution of the order or higher than the expected variation are indicated in red for the 24th of May data set.

was measured for different beam-collimation system offset ranging from -1 to 1 *mm* in steps of half a *mm*. For each vertical collimation system position 500 pulses were recorded. The expected orbit variation at the downstream C-BPMs with the measured C-BPMs resolution was compared to determine the most sensitive C-BPMs for this set of data based on the analysis presented in detail in this section. This comparison is shown in Fig. 6.14 where the BPMs with resolution in the order or higher than the expected variation are indicated in red. Δy^{BPM} has been calculated for 1 *mm* offset and the experiment parameters summarized in Table 6.2.

Using the analysis procedure explained before, the C-BPMs raw data is cleaned and the residuals, R^i, calculated for each beam-collimation system offset and all C-BPMs. In Fig. 6.15 the residual plots measured at $QF7FF$ (top) and $QD2AFF$ (middle) are shown as an example. The wakefield kick calculated from the residual plot of those C-BPMs where a correlation has been observed is depicted in Fig. 6.15 (bottom). The expected value calculated from CST PS simulations (in green) and the analytical calculation (in red) are indicated in the figure for comparison. The main results of this shift are summarized in Table. 6.5. Again not all C-BPMs candidates in Fig. 6.14 were sensitive to the measurements. The C-BPMs not shown in Fig. 6.15 have a measured fit value with an associated error by one order of magnitude higher than the largest error depicted in Fig. 6.15 as explained for the first measurements on the 20th of May. In this data set large errors were observed in almost all C-BPMs data fits with consequent reduction of the the statistics in our measurements for this data set.
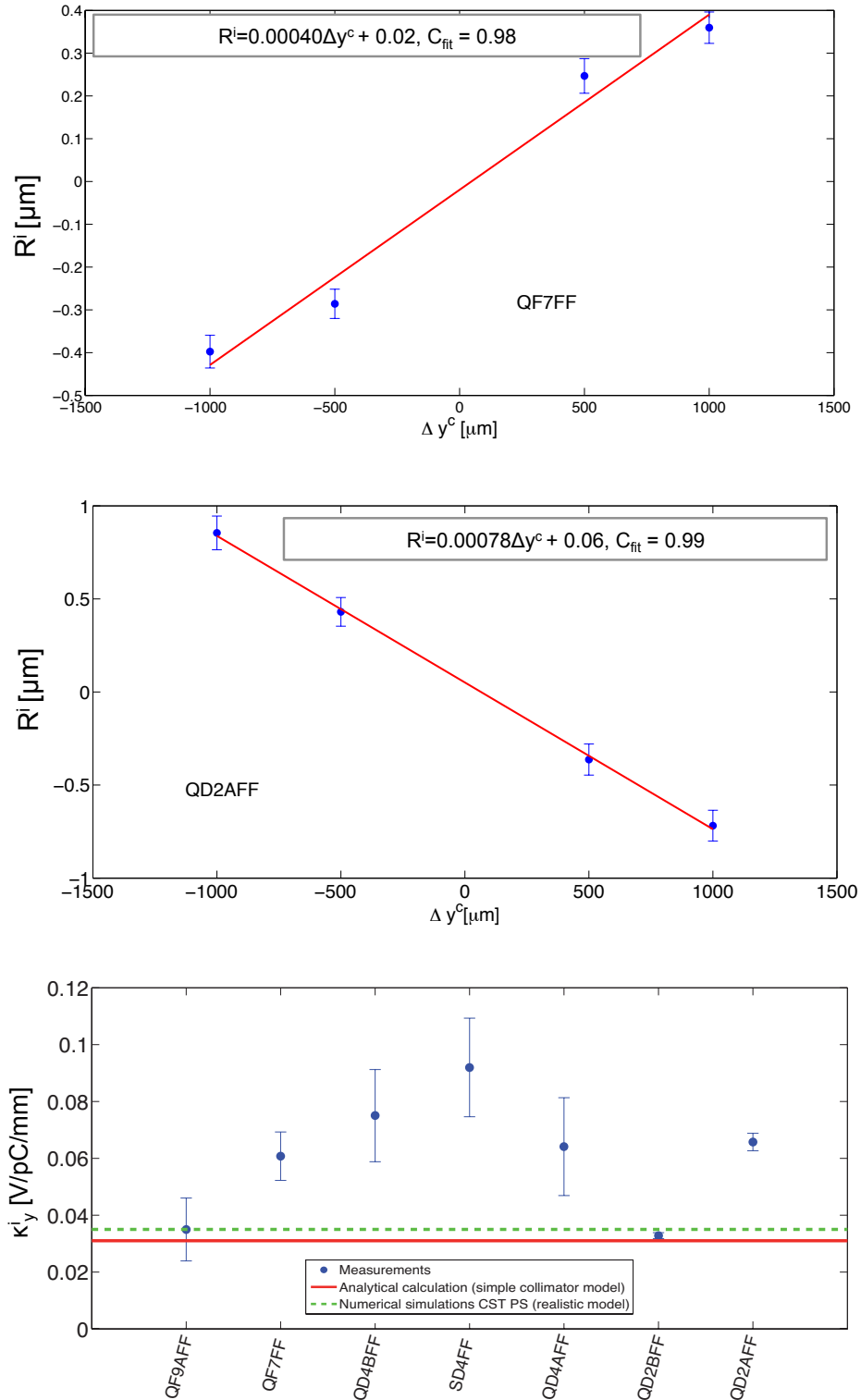
Figure 6.13: Residuals, R^i as a function of collimator offset, Δy^c, at $QF7FF$ and $QD2AFF$ (top and middle) and κ_y^i calculated at different C-BPMs. Measurements were taken on the 24th of May. For completeness the green and red lines indicate the κ_y^{CSTPS} and $\kappa_y^{analytic}$ calculated for 9 mm bunch length.
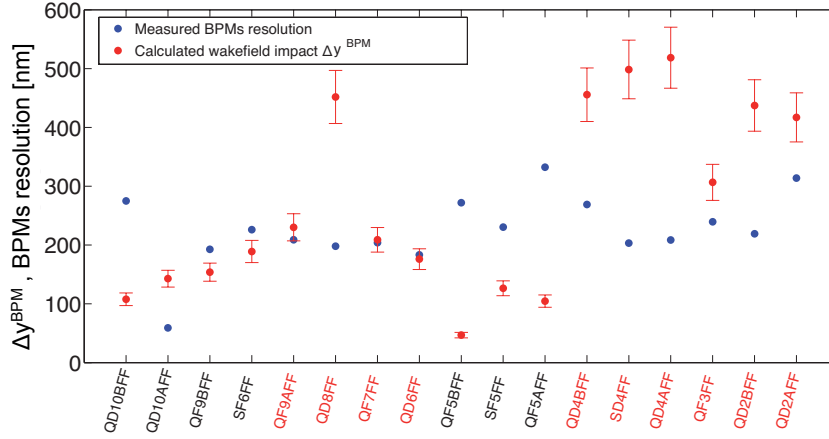
Figure 6.14: Expected orbit variation, Δy^{BPM}, at the downstream C-BPMs with the measured C-BPMs resolution. Δy^{BPM} has been calculated for 1 *mm* offset and the experiment parameters summarized in Table 6.2. The BPMs with resolution of the order or higher than the expected variation are indicated in red for the 27th of May data set.

a[mm]	Scan range [mm]	N [$x10^{10}$]	σ_z[mm]	$\kappa_y^{averaged}$[V/pC/mm]
4±0.01	±1.00 ± 0.01	0.90±0.06	8.9±0.7	0.041±0.002

Table 6.5: Measurements summary of the 27th of May 2016 run.

27th of October 2016 run

All C-BPMs system were calibrated at the beginning of the October run period. The measurements were performed for a fixed 4 *mm* vertical collimation system half aperture. The beam orbit was measured for different beam-collimation system offset ranging from -2 to 2 *mm* in steps of half a *mm*. For each vertical collimation system position 500 pulses were recorded. The expected orbit variation at the upstream BPMs with the measured BPMs resolution was compared as described in detail in this section to determine the most sensitive BPMs for this set of data. This comparison is shown in Fig. 6.16 where the BPMs with resolution in the order or higher than of the expected variation are indicated in red.

Using the analysis procedure explained before, the C-BPMs raw data is cleaned and the residuals, R^i, calculated for each beam-collimation system offset and all C-BPMs. In Fig. 6.17 the residual plots measured at $QF7FF$ (top) and $QD2AFF$ (middle) are shown as an example. The wakefield kick calculated from the residual plot of those C-BPMs where a correlation has been observed is depicted in Fig. 6.17 (bottom). The expected value calculated from CST PS simulations (in green) and the analytical calculation (in red) are indicated in the figure for comparison. The main results of this shift are summarized in Table. 6.6. Again not all C-BPMs candidates in Fig. 6.14 were sensitive to the measurements. The C-BPMs not shown in Fig. 6.17 have a measured fit value with an associated error by one order of magnitude higher than the largest error depicted in Fig. 6.17 as explained for the first measurements on the 20th of May.
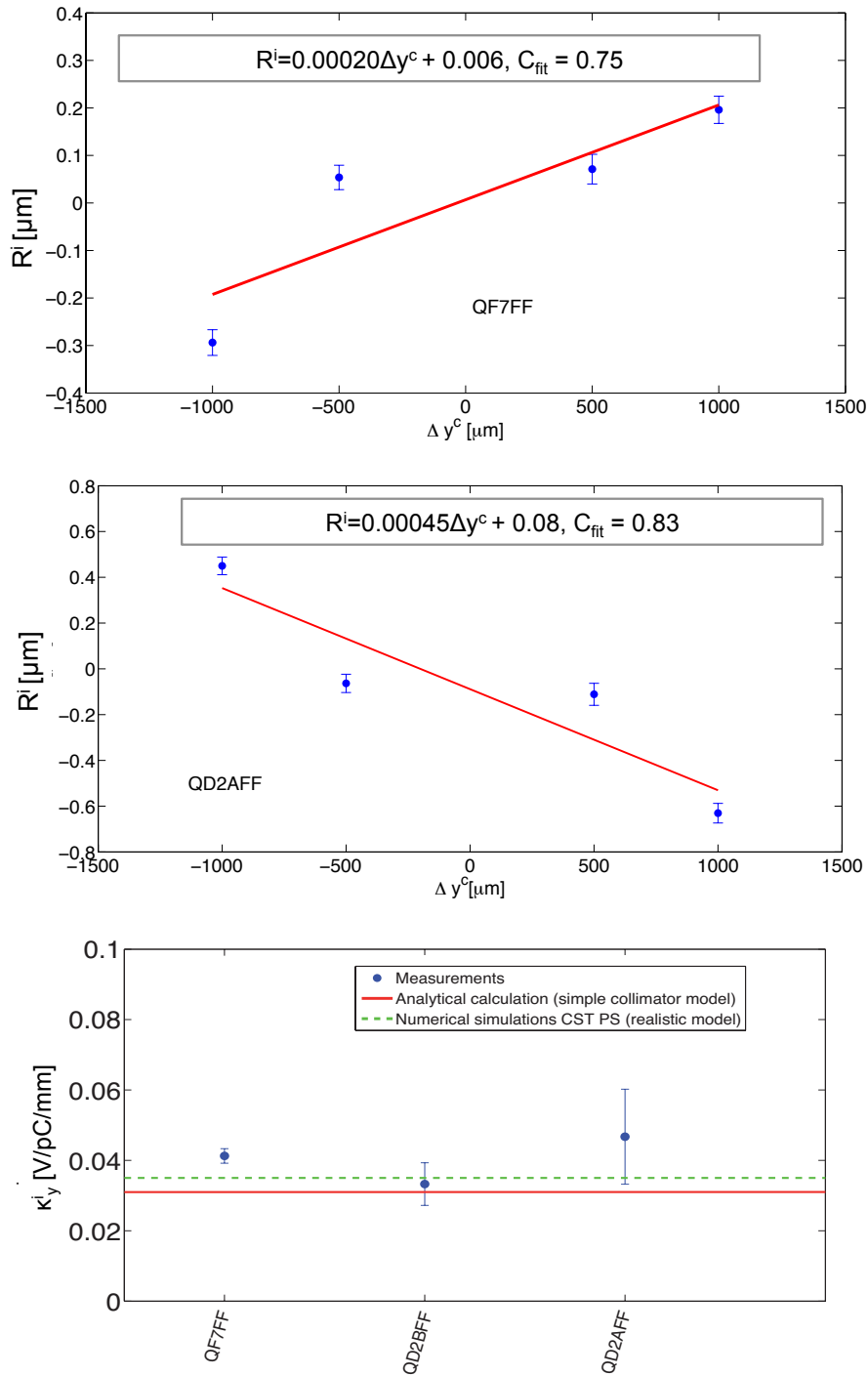
Figure 6.15: Residuals, R^i, as a function of collimator offset, Δy^c, at $QF7FF$ and $QD2AFF$ (top and middle) and κ_y^i calculated at different C-BPMs (bottom). Measurements were taken on the 27th of May. For completeness the green and red lines indicate the κ_y^{CSTPS} and $\kappa_y^{analytic}$ calculated for 9 mm bunch length.
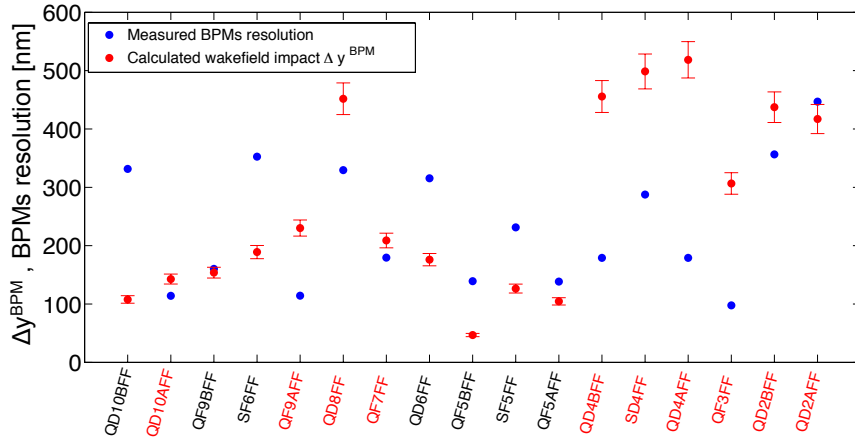
Figure 6.16: Comparison of the expected orbit variation, Δy^{BPM}, at the downstream C-BPMs with the measured C-BPMs resolution. The C-BPMs with resolution of the order or higher than the expected variation are indicated in red. Δy^{BPM} has been calculated for 1 *mm* offset and the experiment parameters summarized in Table 6.2. Measurements have been taken on the 27th of October.

In this particular set of data large errors were observed in almost all C-BPMs data fits with consequent reduction of the the statistics in our measurements for this data set.

a[*mm*]	Scan range [*mm*]	N [$x10^{10}$]	σ_z[*mm*]	$\kappa_y^{averaged}$[$V/pC/mm$]
4.00±0.01	±1.00 ± 0.01	0.80±0.06	8.9±0.7	0.040±0.006

Table 6.6: Measurements summary of the 27th of October 2016 run.

1th of December 2016 run

In this shift, the C-BPMs were also calibrated at the beginning of the November run period. The measurements were performed for a fixed 3 *mm* vertical collimation system half aperture. The beam orbit was measured for different beam-collimation system offset ranging from -1 to 1 *mm* in steps of half a *mm*. For each vertical collimation system position 500 pulses were recorded. In this case the constant vertical collimation system half aperture was fixed to 3 *mm* because the intensity was not high enough to measure the wakefield impact for 4 *mm* half aperture. The expected orbit variation at the upstream C-BPMs with the measured C-BPMs resolution has been compared to determine the most sensitive C-BPMs for this set of data as described in detail in this section. This comparison is shown in Fig. 6.18 where the BPMs with resolution of the order or higher than the expected variation are indicated in red. Δy^{BPM} has been calculated for 1 *mm* offset and the experiment parameters summarized in Table 6.2.

Using the analysis procedure explained before, the C-BPMs raw data is cleaned and the residuals, R^i, calculated for each beam-collimation system offset and all C-BPMs. In Fig. 6.19 the residual plots measured at $QF7FF$ (top) and $QD2AFF$ (middle) are
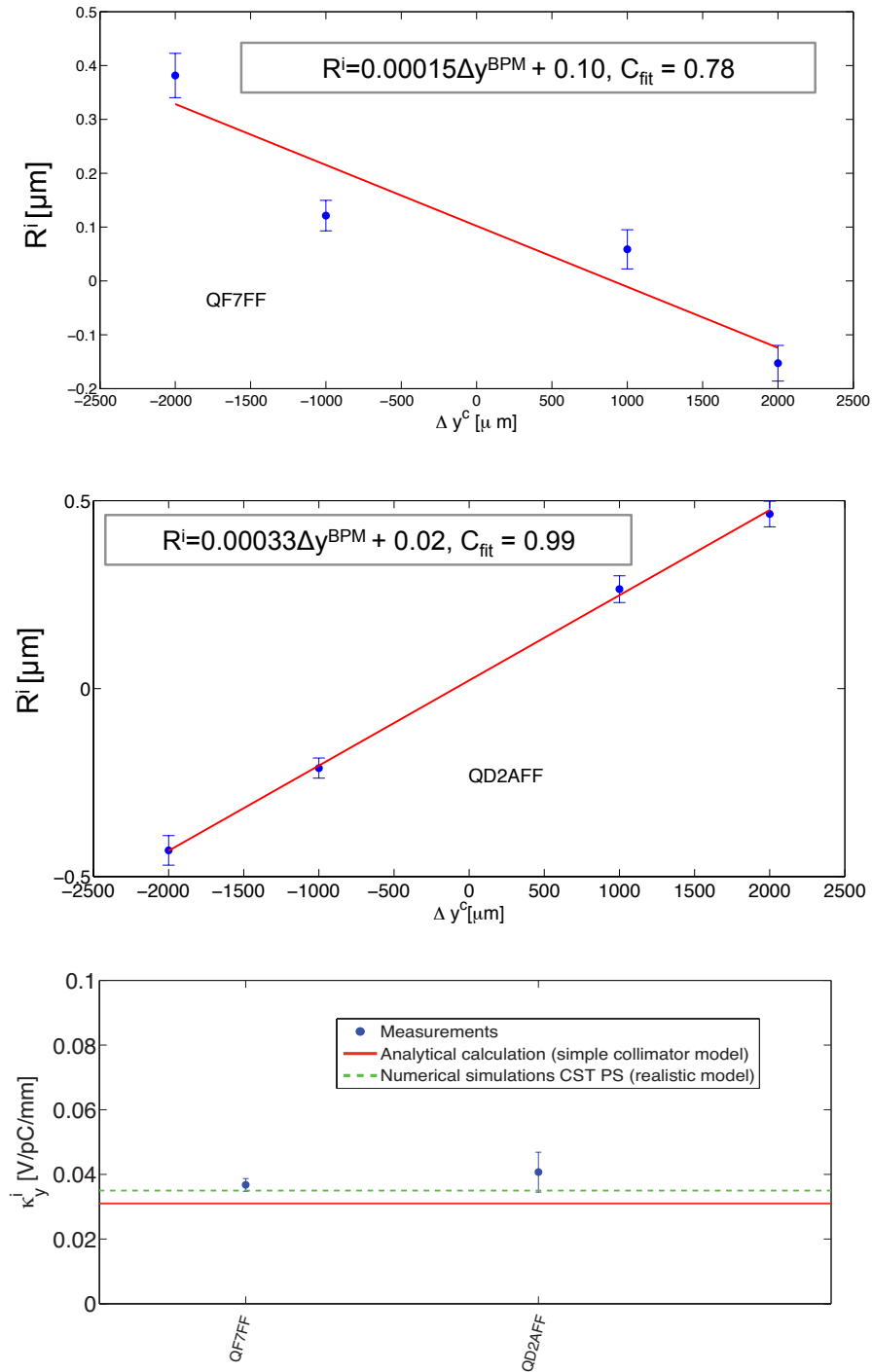
Figure 6.17: Residuals, R^i, as a function of collimator offset, Δy^c, at $QF7FF$ and $QD2AFF$ (top and middle) and κ_y^i calculated at different C-BPMs. Measurements have been taken on the 27th of October. For completeness the green and red lines indicate the κ_y^{CSTPS} and $\kappa_y^{analytic}$ calculated for 9 mm bunch length.
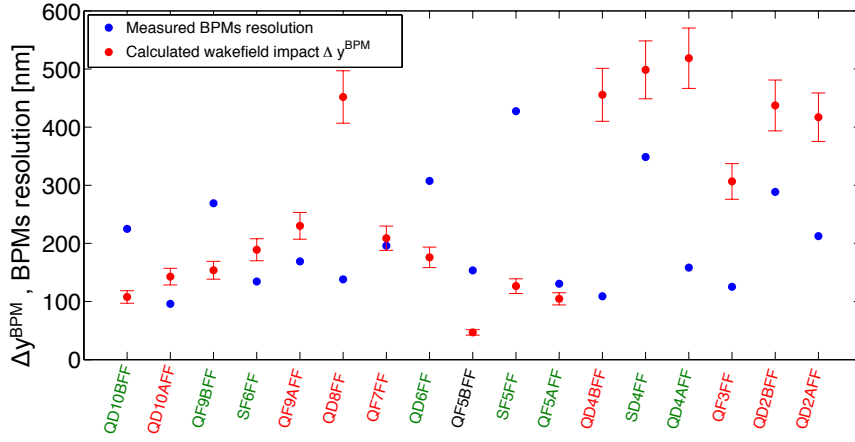
Figure 6.18: Comparison of the expected orbit variation, Δy^{BPM}, at the downstream C-BPMs with the measured C-BPMs resolution. The C-BPMs with resolution of the order of the expected variation or higher are indicated in red for the 1st of December data set. Δy^{BPM} has been calculated for 1 mm offset and the experiment parameters summarized in Table 6.2. The BPMs indicated in green were removed in this beam run period because the November/December run period was dedicated for wakefield measurements and the C-BPMs wakefield contribution was investigated.

shown as an example. The wakefield kick calculated from the residual plot of those C-BPMs where a correlation has been observed is depicted in Fig. 6.19 (bottom). The expected value calculated from CST PS simulations (in green) and the analytical calculation (in red) are indicated in the figure for comparison.The bunch length was also measured. The main results of this shift are summarized in Table. 6.7. Again not all C-BPMs candidates in Fig. 6.18 were sensitive to the measurements. The C-BPMs not shown in Fig. 6.19 have a measured fit value with an associated error by one order of magnitude higher than the largest error depicted in Fig. 6.19 as explained for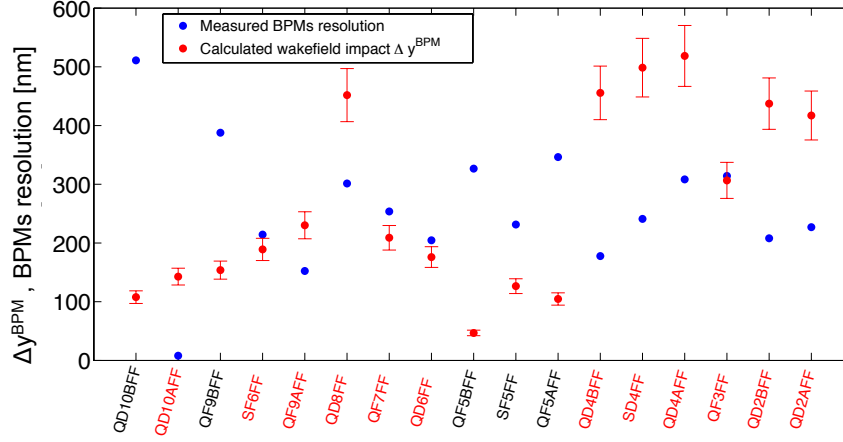 the first measurements on the 20th of May.In this data set large errors were observed in almost all C-BPMs data fits with consequent reduction of the the statistics in our measurements for this data set.

a[mm]	Scan range[mm]	N [$x10^{10}$]	σ_z[mm]	$\kappa_y^{averaged}$[$V/pC/mm$]
3.00±0.01	±1.00 ± 0.01	0.75±0.05	8.6±0.6	0.070±0.006

Table 6.7: Measurements summary of the 1st of December 2016 run.

6.2.6 Summary and first vertical collimation system wakefield kick conclusions

In Table 6.8 and Fig. 6.20 the measured averaged vertical collimation system wakefield kick values are compared with the analytical calculations and CST PS numerical simulations performed for the jaws and the realistic system for 4 and 3 mm half aperture.
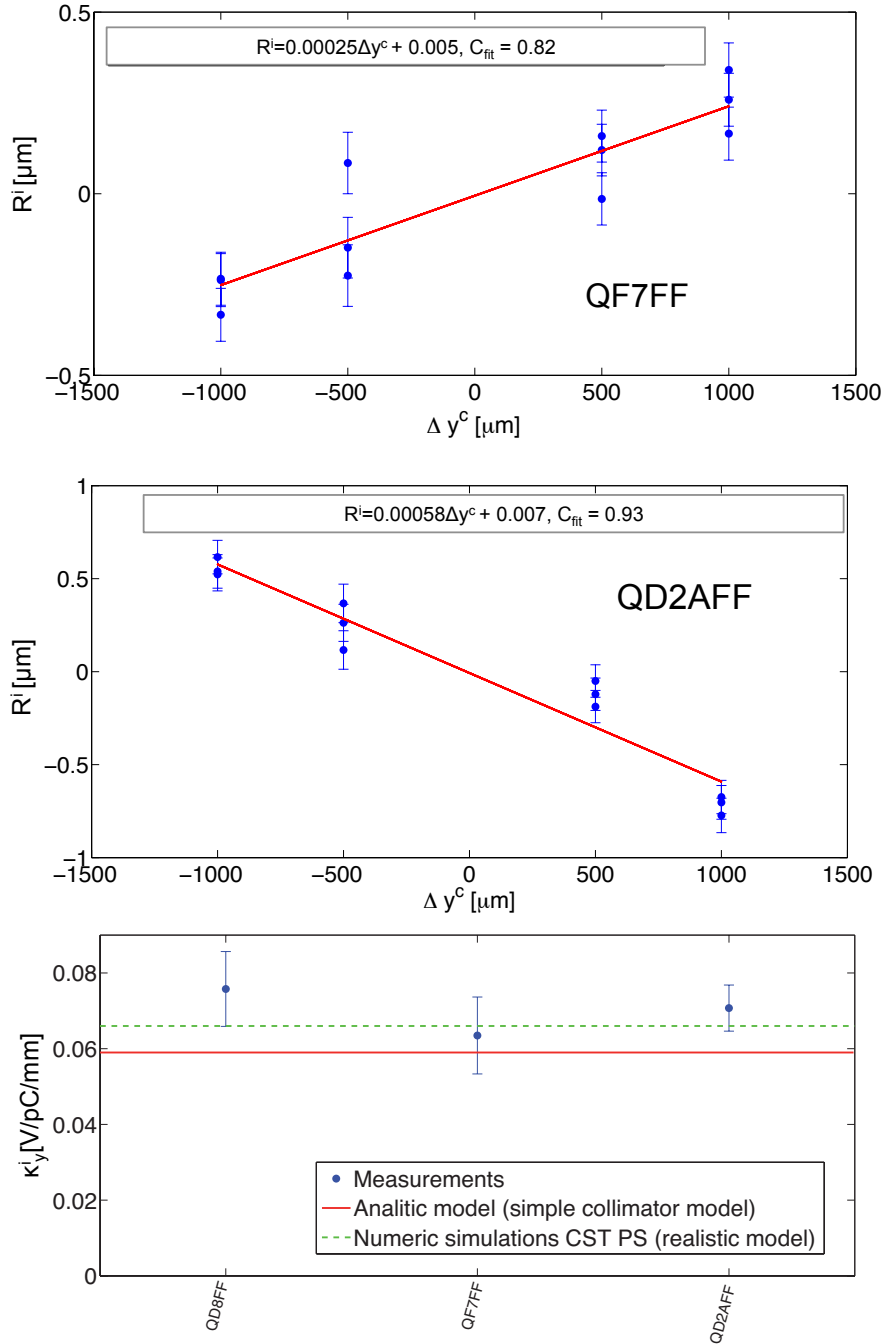
Figure 6.19: Residuals, R^i, as a of collimator offset, Δy^c, at $QF7FF$ and $QD2AFF$ (top and middle) and κ_y^i calculated at different C-BPMs. Measurements have been taken on the 1st of December. For completeness the green and red lines indicate the κ_y^{CSTPS} and $\kappa_y^{analytic}$ calculated for 9 mm bunch length.

Wakefield measurements summary 2016			
Parameter	Units	Values	
a	[*mm*]	4.00±0.01	3.00±0.01
Scan range	[*mm*]	±1.00 ± 0.01,±2.00 ± 0.03	±1.00 ± 0.01
N	[×10^{10}]	>0.80±0.06	0.75±0.05
σ_z	[*mm*]	8.6±0.6< σ_z <9.1±0.6	8.6±0.6
$\kappa_y^{analytic}$	[*V/pC/mm*]	0.033	0.059
$\kappa_{y,jaws}^{CSTPS}$	[*V/pC/mm*]	0.033	0.059
$\kappa_{y,transition}^{CSTPS}$	[*V/pC/mm*]	0.037	0.066
$\kappa_y^{averaged}$	[*V/pC/mm*]	0.040±0.004	0.070±0.006

Table 6.8: Summary of the 2016 vertical collimation system wakefield measurements.
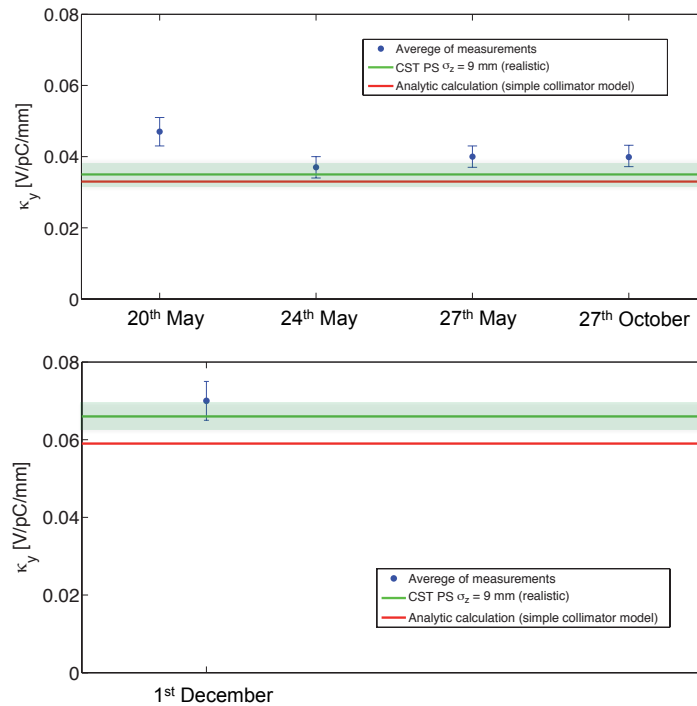
Figure 6.20: $\kappa_y^{averaged}$ measured for 4 and 3 *mm* (top and bottom respectively) vertical collimation system half aperture for each shift in comparison with the analytical and realistic CTP PS calculation for a bunch length of 9 *mm* (the green shadow band indicates the 8 % error associated to the bunch length measurements).

From these studies we could conclude:

- **Measurements of the wakefield kick** induced by the vertical collimation system are **in agreement within the associated error with the realistic numerical simulations** performed with CST PS.

- **The benchmarking accuracy is at the 10% level between measurements and numerical simulations**. Howevee, notice the lake of statistics in some of the data sets analyzed. The analysis of the cause this loss in statistics is out of the scope of this thesis.

- These wakefield measurements contribute to the **validation of CST PS as a wakefield simulation tool**.

- The difference observed within **measurements and analytical calculation of the jaws is about 20 %**.

6.3   Realistic collimation efficiency and related measurements

The vertical collimation system was designed with the main objective of reducing the background photons in the Post-IP region. The efficiency has been measured using the background monitor and the IPBSM Cherenkov monitor, both, located after the BDUMP. Furthermore, the efficiency has been studied in comparison with the TBP working as a kind of collimation system but with a fixed half aperture of 8 *mm* (for more details see chapter 2). Finally, a first attempt of measuring the impact on the IPBSM measurements was done as a function of the vertical collimation system half aperture.

6.3.1   Collimation system efficiency measurements and comparison with BDSIM

In order to investigate the vertical collimation efficiency in reducing the background photons in the Post-IP different measurements were performed with **the background monitor** in March, May and October 2016. A summary of the shifts dedicated to the efficiency studies with the corresponding beam and machine conditions is shown in Table 6.9. The offset at the vertical collimation system has been calculated using the averaged orbit measured at the two C- BPMs downstream and upstream the collimation system and considering a ballistic trajectory.

Vertical collimation system 2016 runs		
$E = 1.3$ *GeV* and $(10\beta_x \times 1\beta_y)$ optics V5.2		
Date	$N[10^{10}]$	$\Delta y^c [\mu m]$
18/03/16	0.70±0.06	300±20
17/05/16	0.80±0.06	-290±20
19/10/16	0.75±0.06	-110±10

Table 6.9: 2016 vertical collimation system efficiency studies beam and machine conditions summary.

In Fig. 6.21, the background reduction as a function of the vertical collimation system half aperture from 3 to 12 *mm* is shown. In each position, the background was measured for 100 pulses and averaged. The associated error corresponds to the standard mean statistical error. In the horizontal axis the error associated to the beam jaws position and beam orbit (see Δy^c in Table 6.9) has been taken into account. These measurements have been compared with the relative reduction of background photons generated in the BDUMP simulated with BDSIM. In chapter 3 we defined the **relative Photon Collimation Efficiency ($\Delta\gamma$CE)** as:

$$\Delta\gamma CE = 100\left(1 - \frac{\Delta\gamma_{w\ coll}^{BDUMP-WINDOW}}{\Delta\gamma_{w/o\ coll}^{BDUMP-WINDOW}}\right) \tag{6.15}$$

where $\Delta\gamma_{w\ coll}^{BDUMP-WINDOW}$ are the photons generated between the entrance of the BDUMP and the window with collimation system and $\Delta\gamma_{w/o\ coll}^{BDUMP-WINDOW}$ without collimation system.

These calculations are depicted in Fig. 6.21 in red and shows to be in relative good agreement with the measurements.
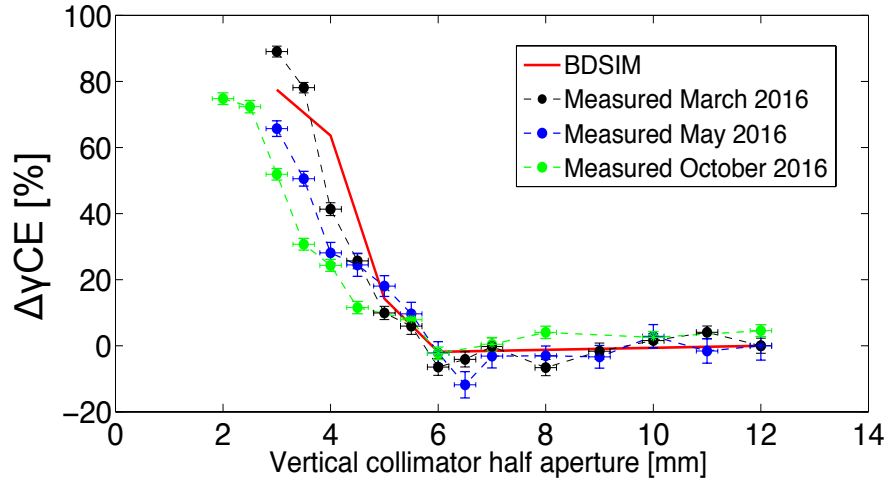
Figure 6.21: Comparison of the measured relative background photons reduction in the March, May and October 2016 runs in the Post-IP region with the BDSIM simulations.

6.3.2 Collimation efficiency measurements for different beam and machine conditions

The ATF2 studies require different beam and machine conditions. Because of that, the relative efficiency of the vertical collimation system has been studied for different beam intensities, DR vacuum pressures and ATF2 optics. **Measurements with the Post-IP background monitor** (CsI scintillator) and the **IPBSM Cherenkov monitor** (used by the IPBSM monitor for beam size measurements) have been taken for different vertical collimation system apertures. A summary of the beam and machine parameters in these shifts is shown in Table 6.10. In Fig. 6.22 the top plot shows the

efficiency for different beam intensities measured with the background monitor, the middle one shows the efficiency for the two DR vacuum pressures also measured with the background monitor and the bottom one corresponds to the efficiency measured for the two different optics studied measured with the IPBSM Cherenkov monitor. These plots characterize how the collimation depth needs to be adjusted for different beam and machine operation modes.

Vertical collimation system 2016 runs				
E = 1.3 GeV				
Date	N[10^{10}]	Δy^c[mm]	Optics	Vacuum pressure [Pa]
19/03/16	0.70-1.00±0.06	240±20	($10\beta_x^* \times 1\beta_y^*$)	$4.99 \times 10^{-7} Pa$
17/05/16	0.80±0.06	-290±20	($10\beta_x^* \times 1\beta_y^*$)	$4.99 \times 10^{-7} Pa$
				$1.06 \times 10^{-6} Pa$
27/10/16	0.60±0.06	-60±5	($10\beta_x^* \times 1\beta_y^*$)	$4.99 \times 10^{-7} Pa$
			($10\beta_x^* \times 0.5\beta_y^*$)	

Table 6.10: 2016 vertical collimation system beam and machine conditions efficiency studies summary.

6.3.3   TBP and collimation system efficiency comparison

On the 20th of May 2016 we dedicated one shift (8 hours) to measured and calibrate the effect of the vertical collimation system in comparison with the TBP used in ATF2 to control the background photons in the IPBSM (for more details see chapter 2). The TBP is efficient in reducing the background photons in the Post-IP region but it is limited to a maximum symmetric cut of 18 σ_y when the beam is passing through the center of the structure. Sometimes, in order to have an acceptable background level at the Post-IP the collimation depth has to be reduced. It is not possible to do it in a symmetric way with the TBP but in some cases it has been observed that by adjusting the TBP in a non symmetric way the background in the Post-IP can also be reduced. One possible explanation to this observations are the orbit at the TBP and the BDUMP locations.

The background photons were measured using the background monitor for a fixed vertical collimation system half aperture varying the TBP position. The measurements were repeated by using the Cherenkov monitor used in the IPBSM measurements. During this shift the beam energy was 1.3 GeV, the optics configuration used was ($10\beta_x^* \times \beta_y^*$) and the the intensity was 0.8 $\times 10^{10}$ electrons per bunch. In Fig. 6.24 these measurements are shown taken with the backgrounds monitor (left) and the IPBSM Cherenkov monitor (right).

From these measurements we could conclude that in order to achieve the same collimation depth as the one given by the TBP, the vertical collimation system has to be closed between 5- 6 mm corresponding to 15-18 σ_y. In February 2017 in order to perform new wakefield experiments a C-band cavity was placed at the location of the TBP and **the vertical collimation system is operated as the main collimation system**.
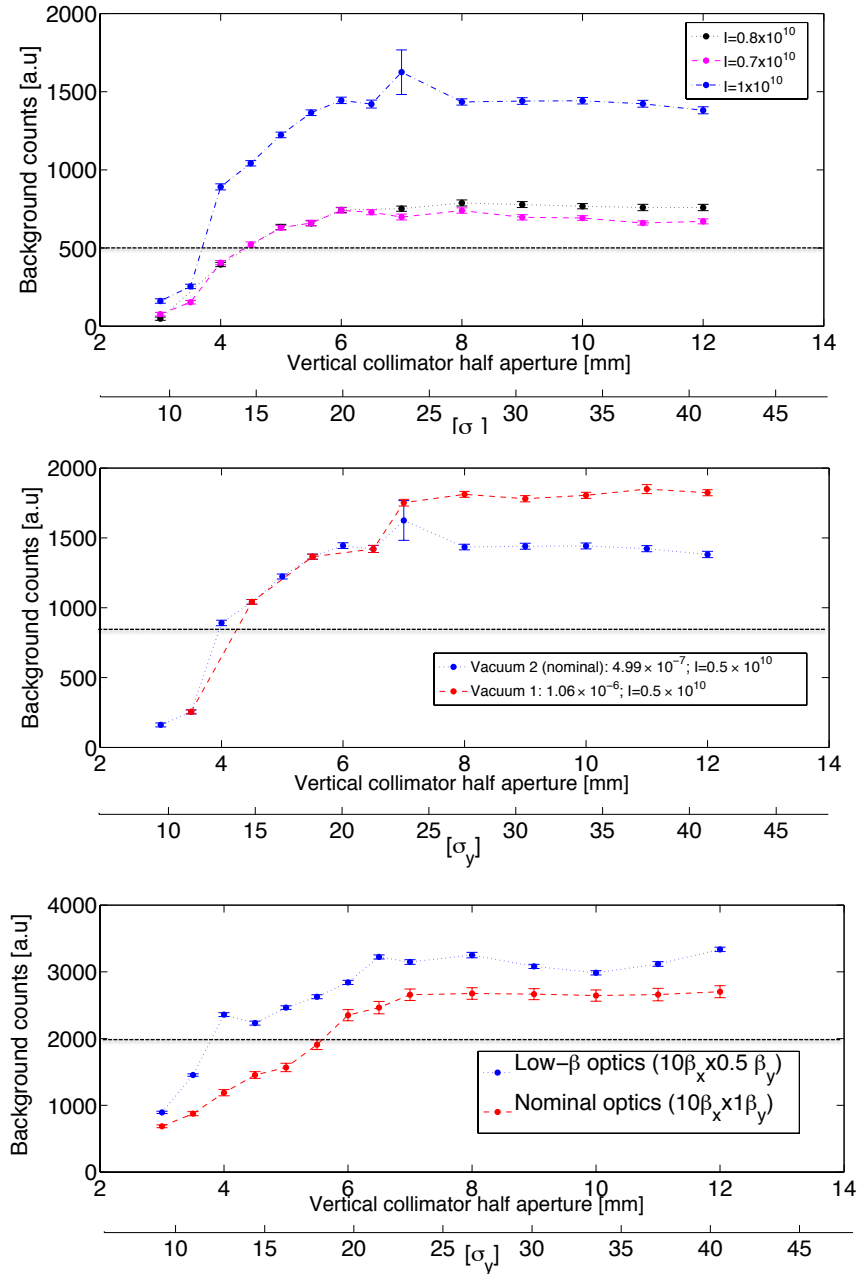
Figure 6.22: Relative reduction of background photons for different intensities (top), DR vacuum pressures (middle) and optics (bottom). One can see in these plots how the collimation depth has to be adjusted in order to achieve the same level of background photons for different beam and machine conditions. To illustrate this, a black dash line is indicated in each plot. Notice here that the last plot shows a different background level because the data was taken with the IPBSM Cherenkov monitor.
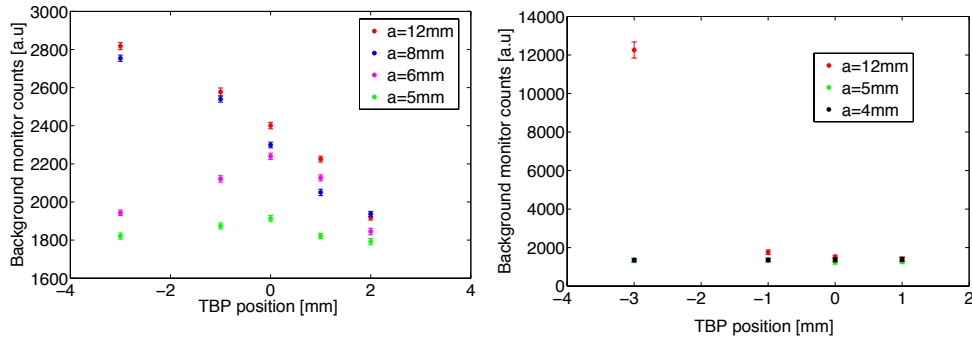
Figure 6.23: Post-IP background reduction measured with the background monitor as a function of the TBP position for different vertical collimation system half apertures using the background monitor (left) and the IPBSM Cherenkov monitor (right). Notice the difference on the background level measured with the different monitors due to their specifications.

6.3.4 Collimation system efficiency and IPBSM measurements

The 30th of November 2016 a full shift (8 hours) was dedicated to test the impact of the vertical collimation system on the IPBSM measurements. During this shift the beam energy was 1.3 GeV, the optics configuration used was ($10\beta_x^* \times \beta_y^*$) and the intensity was 0.7×10^{10} electrons per bunch. The background was measured with the background and IPBSM Cherenkov monitors with the IPBSM laser off and on. The reduction of background photons for both monitors is shown in Fig. 6.24, notice the different level of photons with the IPBSM laser on and off. In Fig. 6.25 the modulation directly related with the vertical beam size is shown as a function of the vertical collimation system half aperture. For these measurements the TBP was set at the optimized position and what was being measured is the effect of collimating more than 18 σ_y. Careful beam tuning is required to perform beam size measurements with the IPBSM at high intensities of linear and non linear knobs. Several shifts are required to prepare the beam for those measurements. Due to these difficulties and a lake of time only one set of measurements could be taken and no clear conclusion can be output from these measurements. More measurements will be required to understand better the direct impact of the vertical collimation system on the IPBSM measurements.
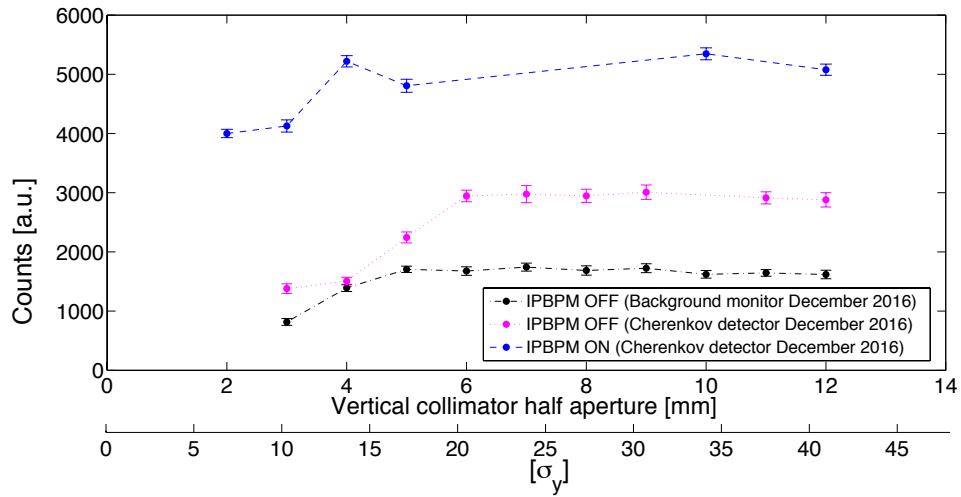
Figure 6.24: Post-IP background measurements performed on the 30th of November 2016 with the background and IPBSM Cherenkov monitor with the IPBSM on and off.
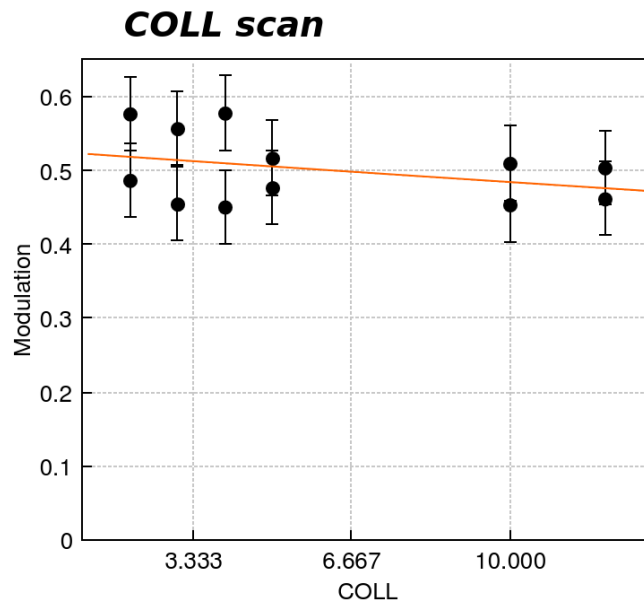
Figure 6.25: Vertical beam size measurements as a function of the vertical collimation system half aperture performed on the 30th of November.

6.3.5   Summary and first efficiency measurements conclusions

From these studies we could conclude:

- The **Post-IP background photons are reduced** when the vertical collimation system is closed more than **6** *mm* corresponding to a collimation depth of 15 σ_y.

- The relative background photons, ($\Delta\gamma CE$), is about 60-80 % for the vertical collimation system closed to 3 *mm* and **the measurements are consistent** over the three **different run periods**.

- The reduction of photons generated in the BDUMP was modeled using **BDSIM** as a function of the vertical collimation system half aperture showing **relative good consistency with measurements**.

- The background level increases for high intensity, high vacuum pressure and low$-\beta$ conditions. To achieve the same level of background level no change in the collimation depth is observed with different vacuum pressure but for **different intensities and for low$-\beta$ optics the collimation depth has to be adjusted**.

- The **TBP** has been used in the past as a kind of collimation system but limited to a maximum collimation depth of 18 σ_y for a beam passing through the center of the device. In order to achieve the same impact the vertical collimation system has to be closed between 5- 6 *mm* corresponding to 15-18 σ_y. **A symmetric collimation depth smaller than 18 σ_y is only possible with the vertical collimation system**. In February 2017, the TBP was removed to install an equipment for the newly planned wakefield study, the vertical collimation system started to play an important role successfully as the main collimation system for the ATF2 studies.

Chapter 7

Summary and conclusions

Undesired background due to the beam halo hitting the beam pipe of some machine components could limit the performance and experiments of the ATF2 and FLCs. In order to control and reduce the beam halo, **beam halo collimation systems** are necessary. The design of such a systems is a complex balance between the **efficiency** needed requiring very small apertures, and **the wakefields** induced, which can compromise the luminosity and beam stability. In this context, in the first part of this thesis we have performed a feasibility design study, construction, installation, commissioning and posterior experiments of a **single vertical collimation system for the ATF2** with the main objective of reducing the background photons in the Post-IP region. In the second part of the thesis, we have used the ATF2 vertical collimation system to perform a detailed study of the wakefields induced by such a system in the context of wakefield studies for the ATF2 and the FLCs. The wakefield impact is being studied deeply in the ATF2 in order to elucidate the impact on the beam sizes at high intensities. In this sense it was crucial to optimize the design of the collimation system in terms of wakefields. Furthermore, in order to define an optimum operation mode for the vertical collimation system in terms of efficiency and wakefields we have performed a **systematic benchmarking study** of the vertical collimation system **wakefield kick** in terms of **analytical calculations, numerical simulations and measurements**.

Concerning the **beam halo collimation topic**, in this thesis, we focus on linear collimation systems. We studied the efficiency of a betatron and energy collimation system for the ATF2. The studies were made for different beam halo models, locations and optics using the tracking code **MADX-PTC** in order to investigate the efficiency and required collimation depth for different ATF2 operation modes. From these studies we could conclude that the best candidate system to reduce the **background** photons generated in the Post-IP is a vertical collimation system with a vertical half aperture of **5** *mm* corresponding to a collimation depth of 15 σ_y. Because of that, the rest of this thesis focused only on a vertical collimation system. In order to make a more realistic study of the vertical collimation system efficiency taking into account the interaction of the beam halo particles with the accelerator components, the tracking code BDSIM has been used. These simulations show that a **4** *mm* half aperture is required corresponding to a collimation depth of 12 σ_y to avoid any beam halo loss before the

IPBSM window for photons in the BDUMP. In these simulations, we observed that even when collimating up to 3 *mm* we have some background photons generated in the BDUMP. One possible explanation for this, is the fact that we are using a single collimation system and we always have some particles scattered by the surface of the jaws, loosing some energy but without being stopped. Furthermore, with BDSIM we modeled the reduction of background photons in the Post-IP as a function of the vertical collimation system aperture for later comparison with measurements. The tracking code BDSIM has been improved and the ATF2 model updated by the RHUL team. The improvements include a more realistic magnet geometry and beamline apertures. In this context, our studies also contribute to the benchmarking campaign been carried out in the ATF2 in the last years in order to validate the recent BDSIM improvements. The benchmarking of this kind of tracking codes is of great importance towards the design of future machines, especially, high energy and intense beam machines and accelerators using photons based diagnostics, such as the Shintake monitor in the ATF2, where undesired losses could limit their performance.

The vertical collimation system was constructed and tested in the LAL laboratory and **installed in the ATF2 in 2016**. After some functionality and calibration tests performed in March 2016 an experimental program was carried out by the author of this thesis to measure the efficiency of such a system. The efficiency was demonstrated to be **about 35% for a 4** *mm* vertical collimation system half aperture. The efficiency measurements are in a reasonable agreement with the BDSIM simulations, taking into account that in our simulation with BDSIM we do not consider any orbit error source. However, in measurements the vertical collimation system has to be closed more than what is predicted in simulations. We could conclude that simulations taking into account the **interaction of the particles with the jaws** are essential to study the performance of the collimation system and to defined a **more realistic collimation depth**. The efficiency of the vertical collimation system has been compared with the effect of the TBP device that was used efficiently in the past as a kind of collimation system but limited to a maximum collimation depth of 18 σ_y for a beam passing through the center of this device. In order to achieve the same impact the vertical collimation system has to be closed between 5-6 *mm* corresponding to 15-18 σ_y. **A symmetric collimation depth smaller than 18 σ_y** is only possible with the **vertical collimation system**. In February 2017, the TBP was removed to install an equipment for the newly planned wakefield study, the vertical collimation system started to **play an important role as the main collimation system for the ATF2 studies successfully**.

The other main topic of this thesis is the **detailed study of the wakefields induced by the vertical collimation system**. The ATF2 vertical collimation system jaws were designed in terms of wakefield minimizations. In the design of such a system, the wakefield impact has been compared with the expected value of the reference cavity and the TBP corresponding to two ATF2 structures with well know wakefield impact. From all these studies we conclude that the best design parameters for the rectangular jaws of the vertical collimation system were: **a flat part of 100** *mm* **of Cu** and with a **tapered angle of 3°**. In addition, we considered that two movable jaws **with an aperture ranging between 3 and 12** *mm* is needed in order to cover different ATF2 operation modes. For these specifications, the vertical collimation system wakefield

impact is a factor 2 higher than the TBP and a factor 4 lower than the reference cavity one. These specifications were given to the engineer at LAL as a starting point to design the collimation system.

The vertical collimation system induced wakefields on the beam dynamics were also studied using the **tracking code PLACET**. Some discrepancies were found between the results obtained with PLACET (v1.0.0) and the linear propagation of the numerical wakefield kick calculated with CST PS by one order of magnitude. A detailed study was performed and the source of the discrepancies was found to be on the definition of the limits of the analytical calculation relevant for the ATF2 case. The program has been modified according to the results of our studies in a new version PLACET (v1.0.1) [43]. The main conclusions from these simulations are summarized in Table 7.1.

ATF2 vertical collimation system performance							
$I = 0.9 \times 10^{10}$, $\sigma_z = 9$ *mm*, $\Delta y^c = 0.5$ *mm* (PLACET) and $(10\beta_x \times 1\beta_y)$ optics V5.2							
BDSIM (V0.91) and PLACET (v1.0.1)							
[*mm*]	[%]		[*V/pC/mm*]			[*nm*]	
a	$\Delta\gamma PC^{BDSIM}$	$\Delta\gamma PC^{measured}$	$\kappa_y^{analytic}$	$\kappa_y^{CST\,PS}$	$\kappa_y^{measured}$	$\Delta\sigma_y^{*,PLACET}$	$\Delta y^{*,PLACET}$
5	15	15	0.015	0.017	—	4.5	6.5
4	60	35	0.033	0.037	0.040±0.004	6.2	11.1
3	78	70	0.059	0.066	0.070±0.006	9.9	21.6

Table 7.1: Vertical collimation system performance summary.

The analytical and numerical studies were completed by an experimental program carried out during 2016 with the main objective of measuring the vertical collimation system wakefield impact on the orbit. These measurements were done to investigate the **optimum operation mode** of the vertical collimation system installed in the ATF2 in terms of efficiency and **acceptable wakefield impact**. In addition, we performed a systematic **benchmarking study of theoretical models, numerical simulations and measurements**. These studies were motivated by **discrepancies in the wakefield kick described in different analytical models for the same regime**, in the models implemented **in the tracking codes**, and **between simulations and measurements** (ESA (SLAC) 2001-2007 [36]). In addition, there are **different analytical models** (inductive, intermediate, diffractive) depending on the geometry of the jaws and beam parameters and when the parameters of the problem sit **close to the limits the estimations are not accurate**. The study presented in this thesis applies for structures laying in **the inductive geometric wakefield regime and long range resistive one**. From the geometric point of view our collimation system is similar to some of the ILC spoilers and absorbers with the current design parameters (as illustrated in Annex 2). Therefore, the results of the studies presented in this thesis contribute to the understanding of the applicability of the tools used to simulate the wakefield impact, crucial for future design of FLC collimation system. The vertical collimation system wakefield impact was measured on the orbit. In these measurements, the contribution of the good performance of the C-BPMs system with resolutions of about to 250 *nm* and the ATF2 beam orbit stability were essential. The results of this benchmarking study shows that **measurements with the associated errors are in agreement**

with numerical simulations of the realistic vertical collimation system model. The **benchmarking accuracy is at the 10% level**. Howevere, notice the lake of statistics in some of the data sets analyzed. The analysis of the cause of this loss in statistics is out of the scope of this thesis. Based on the measurements presented in this thesis, the difference observed within measurements and analytical calculation of the jaws is about 20%. Notice here, that the analytical models **only describe the jaws** of the collimation system. The numerical simulations and measurements presented on this work have been performed for a complete structure including the transition to the beam pipe and the beam pipe itself. The impact of simulating the complete device and only the jaws was studied for different half apertures of the collimation system and the difference observed is about 15-30%. These numerical calculations with CST PS have been performed for the ATF2 bunch length. A proper scaling to the ILC scenario has to be done in order to perform realistic simulations of the wakefield impact in such a case.

The work performed and presented in this thesis contribute to the improvement of the simulation tools for the future design of the FLCs collimation systems including benchmarking with measurements. The vertical collimation system is successfully being used in ATF2 to mitigate and control in a stable way the Post-IP background. A summary of the ATF2 vertical collimation system performance from the efficiency and induced wakefields point of view is presented in Table. 7.1.

Bibliography

[1] N. Walker, "Physics and Technology of Linear Collider Facilities: Introduction and Overview", Notes for the US Particle Accelerator School (USPAS), 2003.

[2] The International Linear Collider: Technical Design report (TDR), www.linearcollider.org/ILC/Publications/Technical-Design-Report, 2013.

[3] CLIC Conceptual Design Report (CDR), Volume 1, www.project-clic-cdr.web.cern.ch/project-clic-cdr/CDR-Volume1.pdf, 2012.

[4] G. Minty, Frank Zimmermann, "Measurement and Control of Charged Particle Beams", Springer.

[5] H. Burkhardt, L. Neukermans, A. Latina, D. Schulte, I. agapov, G. A. Blair, F. Jackson, "Halo Estimates and Simulations for Linear Colliders", EUROTeV-Report-2007-064, CLIC-Note-714.

[6] N. Fuster- Martínez, A. Faus-Golfe, J. Resta- López, P. Bambade, R. Yang, S. Wallon. F. Toral, I. Podadera, K. Kubo, N. terunuma, T. Okugi, T. Tauchi. "Commissioning and first performance studies of a single vertical beam halo collimation system at ATF2", Proceedings IPAC16, Busan, South Korea.

[7] P.A.P. Nghiem, N. Chauvin, W. Simeoni, Jr. and D. Uriot, "Core-Halo Issues for a Very High Intensity Beams", Laser and Particle Beams, 32(1), pp. 109118. doi: 10.1017/S0263034613001055.

[8] M. Valette, "Etudes de dynamique faisceau pour les accélérateurs IFMIF", http://www.theses.fr/2015SACLS242.

[9] S. Liu, P. Bambade, N. Fuster-Martínez, A. Faus-Golfe, S. Bai, D. Wang, J. Gao,"Measurement of Beam Halo Transverse Distribution Using Wire Scanners at ATF2", ATF-14-09 report.

[10] ATF2 proposal, Volumes 1&2, ATF2 collaboration, SLAC-R771, 2005, http//www.slac.stanford.edu/cgi-wrap/getdoc/slac-r-771.pdf.

[11] J. B. Jeanneret, "Optics of a two-stage collimation system", Phys. Rev. ST Accel. Beams, 1-8-081001.

[12] J. Frish, E. Doyle, K. Sharpaas,"Advanced Collimator Engineering for the NLC", SLAC-PUB-9417, August 2002.

[13] L. Merminga, J. Irwin, R. Helm,R. D Ruth,"Optimizing a nonlinear collimation system for future linear colliders", SLAC-PUB-5507, C91-05-06".

[14] A. Faus-Golfe, F. Zimmermann, J.Resta-Lopez,"Non-Linear Collimation in Linear and Circular Colliders", WEXFI03 Proceedings of EPAC2006, Edinburgh, Scotland.

[15] https://www.cst.com/products/cst.

[16] A. Latina, Y. Levinsen, D. Schulte, J. Snuverink, "Evolution of the tracking code Placet", MOPWO053, Proc. IPAC13.

[17] http://svnweb.cern.ch/world/wsvn/clicsw/trunk/?#a0b40758157c8f16fa703ca3be466fa8a.

[18] B. W. Zotter, S. A. Kheifets, "Impedances and Wakes in High-Energy Particle Accelerators", World Scientific.

[19] S. Vaganian, H. Henke, "The Panafsky-Wenzel theorem and general relations for the wake potential", Particle Accelerator 1995Vol.48, pp239-242.

[20] B. Podobedov, S. Krinsky, "Transverse impedance of tapered transition with elliptical cross section", PRST AB, 10 074402 (2007).

[21] J. Resta-Lopez, "Single-bunch transverse emittance growth due to collimator wakefield effects", arXiv:1309.0480.

[22] NLC Post linac collimation task force, "New Postlinac Collimation System for Next Linear Collider", LCC-Note-0052, 21-Feb-2001.

[23] X.E. Lin and D. H. Whittum, Image Current Heating on Metal Surface Due to Charged Bunches, SLAC-PUB-8393 (2000).

[24] ATLAS collaboration, G. Aad et al., "Observation of a new particle in the search for the Standard Model Higgs boson with the ATLAS detector at the LHC", Phys.Lett.B716(2012)129, [1207.7214].

[25] CMS collaboration, S. Chatrchyan et al., "Observation of a new boson at a mass of 125GeV with the CMS experiment at the LHC,Phys.Lett.B716(2012)3061, [1207.7235].

[26] LHC Design Report, CERN-2004-003(2004); http:// www.cern.ch/lhc.

[27] http://cern.ch/fcc.

[28] http://cepc.ihep.ac.cn/preCDR/mainpreCDR.pdf.

[29] http://www.xfel.eu/en/.

[30] https://ilc.kek.jp/STF/.

[31] http://atf.kek.jp/twiki/bin/view/Main/ATFIntroduction.

[32] D. Rubin et al., CesrTA Layout and optics, PAC09, Vancouver, BC, Canada.

[33] http://agenda.linearcollider.org/event/6389/ contributions/30574/attachments/25255 /38888/gwhite_ilcbdsColl.pdf.

[34] P. Tenenbaum,"Collimator wakefield calculation for ILC-TDR Repor" ,LCC-NOTE-0101.

[35] A. Toader, R. J. Barlow, F. Jackson, D. Angal-Kalinin, "Effect of collimator wakefields in the beam delivery system of the International Linear Collider",WEPP167, Proceedings of EPAC08, Genoa, Italy.

[36] P. Tenenbaum, K. L. F. Bane, L. Eriksson, J. Irwin, R. K. Jobe, D. McCormick, C. K. Ng, T. O. Raubenheimer, M. C. Ross, G. Stupakov, D. Walz, D. Onoprienko, I. Zagorodnov, "Direct measurement of transverse wakefields of tapered collimators", Phys. Rev. ST-AB 10 (2007), 034401.

[37] S. Molloy, S. Seletskiy, M. Woods, J. David, A. Smith, C. D. Beard, J. L. Fernandez-Hernando, N. Watson, A. Bungau, A. Sopczak, "Measurements of the transverse wakefields due to varying collimator characteristics", Proceedings of PAC07, Albuquerque, New Mexico, USA, FRPMS074.

[38] J. L. Fernandez-Hernando, , S. Molloy, J.D.A. Smith, N. K. Watson, "Measurements of collimator wakefields at End Station A", Proceedings of EPAC08, Geonoa, Italy, WEPP163.

[39] R. Erickson, T. Fieguth, C. Hast, J. Jaros, D. MacFarlane, T. Maruyama, Y. Nosochkov, T. Raubenheimer, J. Sheppard, D.Walz, and M. Woods, "ESTB End Station Test Beam. A proposal to provide test beams in SLAC's End Station A", July 31,2009.

[40] J. D. A. Smith, "Full Structure Simulations of ILC collimators", FR5RFP041

[41] N. Fuster-Martinez, A. Faus-Golfe, J. Resta-Lpez, P. Bambade, S. Liu, S. Wallon, F. Toral, I. Podadera, K. Kubo, N. Terenuma, T. Okugi, T. Tauchi. Design study and feasibility study of a transverse beam halo collimation system for ATF2. Proceedings IPAC2014, Dresden, Germany, 2014.

[42] N. Fuster- Martnez, A. Faus-Golfe, J. Resta- Lpez, P. Bambade, S. Liu, S. Wallon. F. Toral, I. Podadera, K. Kubo, N. terunuma, T. Okugi, T. Tauchi. Design and construction study of a transverse beam halo collimation system for ATF2. Proceedings IPAC15, Richmond, EEUU.

[43] N. Fuster- Martnez, A. Faus-Golfe, A. Latina, J. Snuverink Geometrical wakefield study of a rectangular collimator for ATF2. ATF2-01-16 report and to be published as a CLIC note 1069.

[44] W. Farabolini et al., CTF3 probe beam linac comissioning and operation, Proceedings of LINAC10 Tsukuha, Japan.

[45] N. Catalan-Lasheras, A. Degiovanni, S. Doebert, W. Farabolini, J. Kovermann, G. McMonagle, B. Woolley, S. Rey, I. Syratchev, L. Timeo, W. Wuensch, J. Tagg, "Experience operating an X-BAND high power test stand at CERN", WEPME016, IPAC2014, Dresden, Germany.

[46] J. Resta Lopez, Ph.D thesis, "Design Performance Evaluation of Nonlinear Collimation System for CLIC and LHC".

[47] J. Resta-Lopez, C. I. Clarke, A. Faus-Golfe, N. Fuster-Martinez, C. Hast, R. M. Jones, A. Latina, M. Pivi, G. Rumolo, D. Schulte, J. Smith, R. Tomas," Proposal for Single-Bunch Collimator Wakefield Measurements at SLAC ESTB", rXiv: 1212.6023 [physics.acc-ph]. 2012-12.

[48] M. Modena, "Update on 2 Octupoles Procurement for ATF2 Final Focus Systems, 18th ATF2 Project meeting 2015.

[49] P. Tenenbaum, "The Final Focus Test beam", http://www.slac.stanford.edu/ pubs/beamline/25/ 1/25-1-tenenbaum.pdf.

[50] P. Tenenbaum, T. Shintake, "Measurements of small electron beam spots", SLAC-PUB-8057, February, 1999.

[51] ATF2 Collaboration (White, G.R. et al.), "Experimental Validation of a Novel Compact Focusing Scheme for Future Energy-Frontier Linear Lepton Colliders", Phys.Rev.Lett. 112 (2014) no.3, 034802 .

[52] N. Blaskovic, R. M. Bodenstein, T. Bromwich, P. N. Burrows, G. B. Christian, M. R. Davis, C. Perry, R. Ramjiawan, D. R. Bett, "Bunch-by-bunch position and angle stabilization at ATF2 based on sub-micron resolution stripline beam position monitors", THPOR034, IPAC16, Busan, Korea.

[53] N. Blaskovic, R. M. Bodenstein, T. Bromwich, P. N. Burrows, G. B. Christian, M. R. Davis, C. Perry, R. Ramjiawan, D. R. Bett, "Development of low-latency, micrometre-level precision, intra-train beam feedback system based on cavity beam position monitors", THPOR035, IPAC16, Busan, Korea.

[54] https://indico.cern.ch/event/336335/contributions/ 789029/attachments/ 657757/904316/ ATF2 ProgressReport.pdf.

[55] M. Patecki, D. Bett, K. Kubo, S. Kuroda, T. Naito, T. Okugi, F. Plassard,T. Tauchi, N. Terunuma, R. Toms, Rogelio, 'Progress in Ultra-Low * Study at ATF2", CERN-ACC-2016-186.

[56] D. Bett, C. Charrondire, M. Patecki, J. Pfingstner, D. Schulte R. Toms, A. Jeremie, "Ground motion compensation using feed-forward control at ATF2", WEPOR005, IPAC16, Busan, Korea.

[57] S. Liu Phd thesis, "ATF2 Acclrateurs d'lectrons Capteur diamant Capteurs Electrons de recul Compton Faisceaux, Dynamique des Halo du faisceau", http://www.theses.fr/18614203X.

[58] R. Kieffer, T. Lefevre, S. Mazzoni, L. Bobb, M. Bergamashi, P. Karataev, T. Aumeyr, M. Billing, J. Conway, J. Shanks, N. terunuma,"Develpment of a versatile OTR-ODR station for Future Linear Colliders", Proceedings of IBIC2015, Melbourne, Australia, TUPB057.

[59] T. Okugi, S. Araki, P. Bambade, K. Kubo, S. Kurado, M. Masuzawa, E. Marin, T. Naito, T. Tauchi, N. Terunuma, R. Tomas, J. Urakawa , G. White, M. Woodley," Linear and second order optics corrections for the KEK Accelerator Test Facility final focus beam line", Phys.Rev.ST Accel.Beams 17 (2014) no.2, 023501 .

[60] T. Suehara, M. Oroku, T. Yamanaka, H. Yoda, T. Nakamura, Y. Kamiya, Y. Honda, T. Kume, T. Tauchi, T. Sanukia, S. Komamiya,"Design of a Nanometer Beam Size Monitor for ATF2", arXiv:0810.5467v1 (30 Oct. 2008).

[61] J. Yan, Y. Yamaguchi, Y. Kamiya, S. Komamiya, M. Oroku, T. Okugi, N. Terunuma, K. Kubo, T. Tauchi, J. Urakawa, "Measurement of nanometer electron beam sizes with laser interference using Shintake Monitor", NIMA. A740 (2014) 131-137.

[62] R.J. Apsimon, D. R. Bett, N. Blaskovic, P. N. Burrows, G. B. Christian, C. I. Clarke, B.D. Constance, H. Dabiri Khah, M. R. Davis, C. Perry, J. Resta-Lopez, C. J. Swinson, "Design and performance of a high resolution, low latency stripline beam position monitor system", PRST-AB, 18, 032803 (2015).

[63] Y. I. Kim, R. Ainsworth, A. Aryshev, S. T. Boogert, G. Boorman, J. Frisch, A. Heo, Y. Honda, W. H. Hwang, J. Y. Huang, E-S. Kim, S. H. Kim, A. Lyapin, T. Naito, J. May, D. McCormick, R. E. Mellor, S. Molloy, J. Nelson, S. J. Park, Y. J. Park, M. Ross, S. Shin, C. Swinson, T. Smith, N. Terunuma, T. Tauchi, J. Urakawa, and G. R. White"Cavity beam position monitor system for the Accelerator Test Facility 2", PRST-AB 15, 042801 (2012).

[64] K.Kubo, "ATF2 recent beam size intensity dependence (wakefield) studies ", LCWS2016, oral presentation, https://agenda.linearcollider.org/event/7371/sessions/4346/#20161206.

[65] J. Snuverink, R. Ainsworth, S. T. Boogert, F. J. Cullinan, A. Lyapin, Y. I. Kim, K. Kubo, S. Kuroda, T. Okugi, T. Tauchi, N. Terunuma, J. Urakawa, G. R. White, 'Measurements and simulations of wakefields at the Accelerator Test Facility 2, PRST-AB 19, 091002 (2016).

[66] O.R. Blanco, P. Bambade, F. Bogard, P. Cornebise, S. Wallon, N. Blaskovic Kraljevic, D.R. Bett, T. Bromwich, P.N. Burrows, G.B. Christian, C. Perry, S. Araki, Y. Honda, K. Kubo, S. Kuroda, T. Naito, T. Okugi, T. Tauchi, N. Terunuma, E.-S. Kim, S. Jang, "Status of ATF2 IP-BPM project, Proceedings of IPAC 2015, Richmond, VA, USA, MOPHA003.

[67] N. Blaskovic Kraljevic , Phd thesis,"Development of a high-precision low-latency position feedback system for single-pass beamlines using stripline and cavity beam position monitors", http//www−pnp.physics.ox.ac.uk/ font/thesis/thesisBlaskovicKraljevic.pdf.

[68] J. Alabau-Gonzalvo, C. Blanch Gutierrez, J.V. Civera, A. Faus-Golfe, J.J. Garcia-Garrigos, J. Cruz, D. McCormick, G. White. "Multi optical transition radiation system for ATF2", MOPE050, IPAC11, San Sebastian, Spain, 2011.

[69] J. Alabau-Gonzalvo, C. Blanch-Gutierrez, J. Cruz, A. Faus-Golfe, J. J. Garcia-Garrigos, D. McCormick, J. Resta-Lopez, G. White, M. Woodley, Optics and Emittance Studies Using the ATF2 Multi-OTR System, IPAC2012, New Orleans, Louisiana, USA, 2012.

[70] J. Alabau-Gonzalvo phd thesis, "Beam size and very low emittance with a Multi-OTR system in ATF2", February 2013.

[71] A. Faus-Golfe, J. Navarro, N. Fuster-Martnez, J. Resta-Lpez, J. Giner- Navarro, " Emittance reconstruction from measured beam sizes in ATF2 and perspectives for ILC", 2016NIMPA.819..122F.

[72] M. Matsuda, S. Nakamura, H. Hayano, "Beam Size Measurements by ø7 m Carbon Wire Scanner", ATF Internal Report (ATF-02-04, 2002).

[73] S. Liu, F. Bogard, P. Cornebise, A. Faus-Golfe, N. Fuster-Martnez, E. Griesmayer, H. Guler, V. Kubytskyi, C. Sylvia, T. Tauchi, N. Terunuma, P. Bambade, "In vacuum Diamond Sensor scanner for beam halo measurements in the beam line at KEK Accelerator Test Facility" NIMA, Volume 832, 1 October 2016, Pages 231-242, ISSN 0168-9002.

[74] R. Yang, P. Bambade, V. Kubytskyi, A. Faus-Golfe, N. Fuster- Martnez, T. Naito, "Modeling and experimental studies of beam halo at ATF2", MOPMB008, IPAC16.

[75] T. Naito, "Beam halo measuremnts utilizing YaG:Ce screen", Proceedings IBIC2015, Melbourne, Australia, TUPB024.

[76] T. Naito, "Beam halo measurements utilizing YAG:CE screen", TUPB024, IBIC15.

[77] S. Liu, P. Bambade, F. Bogard, P. Cornebise, V. Kubytskyi, C. Sylvia, A. Faus-Golfe, N. Fuster-Martinez, T. Tauchi, N. Terenuma, "Investigation of beam halo using in vacuum diamond sensor at ATF2", IPAC15.

[78] D. Wang, P. Bambade, K. Yokoya, J. Gao, "Analytical estimation of ATF beam halo distribution", arXiv:1311.1267v2 (11 Mar. 2014).

[79] Private communication with Dr. T. Okugi.

[80] http://mad.web.cern.ch/mad/.

[81] http://madx.web.cern.ch/madx/doc/ptc_report_2002.pdf.

[82] https://twiki.ph.rhul.ac.uk/twiki/bin/view/PP/JAI/BdSim.

[83] K. Yokoya, "Resistive wall impedance of beam pipes of general cross-section", Part. Acc 41,221 (1993).

[84] G.V. Stupakov, "High-Frequency Impedance of Small-Angle Collimators, SLAC-PUB-9375, August 2002.

[85] G. V. Stupakov,"Impedance of Small-Angle Collimators in High-Frequency Limit", SLAC-PUB-8857.

[86] G. Stupakov, "Advance impedance theory", SLAC-PUB-13661.

[87] A.W.Chao,Physics of Collective Beam Instabilities in High Energy Accelerators (Wiley,NewYork,1993).

[88] K. Bane, M. Sands,"Wakefields of very short bunches in an accelerating cavity", Particle Accelerators 1990, Vol.25 pp73-95.

[89] A. Piwinski, "Wake fields and Ohmic losses in Flat vacuum chambers" DESY-HERA-92-04,1992.

[90] K. Bane and M. Sands, "The Short-Range Resistive wall wakefields",SLAC-PUB-95-7074.

[91] H. Dohlus, I. Zagorodnov, I. Zagodnova, "Impidances and Collimators in European XFEL", TESLA-FEL Report 2012-04, July 2010.

[92] G. Rumolo, A. Latina, D. Schulte, "Effect of wakefield in the CLIC BDS", EUROTeV-Report-2006-026.

[93] I. Zagorodnov, K. Bane, "Wakefield Calculations for 3D Collimator", EPAC 2006.

[94] M.Toader, R.Barlow, "Comparison of Collimator wakefield formulae", WEPP166 , Proceedings of EPAC08 Genoa, Italy.

[95] https://www.3ds.com/products-services/catia/.

[96] http://www.tibtech.com/conductivity.php.

[97] http://www.gdfidl.de/.

[98] K. Kubo, A. Lyapin, J. Snuverink, "Wakefield issue for the Linear Collider", Beam Dynamics Newsletter 61 (2013).

[99] A. Latina, Y. Levinsen, D. Schulte, J. Snuverink, "Evolution of the tracking code Placet", MOPWO053, Proc. IPAC13.

[100] G. Rumolo, A. Latina, W. Bruns, "Tracking with the collimator wake fields through the CLIC-BDS", CLIC meeting (19.05.2006).

[101] A. Latina, R.J. Barlow, G. A. Blair, A. Bungau, S. Malton, G. Rumolo, D. Schulte, J. D. A. Smith, "Wakefiled models for particle tracking codes", CERN-AB-2007-033.

[102] H. Dohlus, I. Zagorodnov, I. Zagodnova, "Impidances and Collimators in European XFEL", TESLA-FEL Report 2012-04, July 2010.

[103] G. Rumolo, A. Latina, D. Schulte, "Effect of wakefield in the CLIC BDS", EUROTeV-Report-2006-026.

[104] Geant4 Users Guide, http://geant4.web.cern.ch/geant4/.

[105] https://root.cern.ch/.

[106] http://proj-clhep.web.cern.ch/proj-clhep/.

[107] J. Snuverink, S. T. Boogert, H. Garcia-Morales, S. M. Gibson, R. Kwee-Hinzmann, L. J. NevayBeam, "Delivery Simulation - Recent Developments and Optimization", CERN-ACC-2015-0191.

[108] http://www.pp.rhul.ac.uk/bdsim/manual/examples/atf2.html.

[109] https://indico.cern.ch/event/614198/contributions/2488860/attachments/1427163/2190168/BDSIM_VerticalCollimator_ASchuetz.pdf.

[110] S. De Barger, S. Metcalfe, C. Ng, T.G. Porter, J. Seeman, M. Sullivan, U. Wienands, "The PEP-II Movable Collimators", SLAC-PUB-11752.

[111] https://www.festo.com/net/SupportPortal/Files/212956/13_1-18%20-%20Stepper%20motors%20EMMS-ST_ENUS.PDF.

[112] https://www.festo.com/net/es_es/SupportPortal/default.aspx?cat=1203.

[113] https://es.mathworks.com/products/matlab.html.

[114] http://www.aps.anl.gov/epics/.

[115] T. Naito,H. Hayano,N.Terunuma,J.Urakawa,Y. Hashimoto, M. Muto, T. Okugi, "SR monitor for the ATF Dampingring, Proc. of PAC97, pp584-586 (1997)".

[116] K.L.F. Bane, T. Naito, T. Okugi, and J. Urakawa, "Bunch Length Measurements at the ATF Damping Ring in April 2000", SLAC-AAS-97, KEK-ATF-11, October 2000.

[117] S. T. Boogert, R. Ainsworth, G. Boorman, S. Molloy, M. Ross, A. Aryshev, Y. Honda, N. Terunuma, J. Urakawa, E-S. Kim, Y. I. Kim, A. E. Heo, A. Lyapin, C. J. Swinson, J.Frisch, D.M.McCormick, J.Nelson,T.Smith,G.R.White,"Cavity beam Position Monitor System for ATF", SLAC-PUB-15177.

Annex 1: Beam transport matrix formalism

The 6D canonical vector $X = (x, p)$ characterizes the movement of a particle in an accelerator in the canonical phase space, being the spatial coordinates $x = (x, y, s)$ and $p = (px, py, ps)$ the momentum vector. The coordinates x and y referred to transverse displacements with respect to the design orbit and the coordinate s is the one along the reference orbit. Usually the so-called trace space is used instead of the canonical phase space, with the geometric coordinates as X=(x, x' , y , y', z, σ_E), with x and y referring to the displacement with respect to the reference orbit, z is the longitudinal displacement with respect to the reference particle, $x' = dx/ds$ and $y' = dy/ds$ the slopes with respect to the reference trajectory and σ_E the momentum variation respect to the reference one. In accelerator physics the beam transport between an initial location, X^i and a second location in the lattice X^f can be expressed formally though a transfer map $\mathcal{M}$.

The transfer map has a Taylor expansion as:

$$X^f = \sum_k R_{jk} X_k^i + \sum_{kl} T_{jkl} X_k^i X_l^i + \sum_{klm} U_{jklm} X_k^i X_l^i X_m^i + \sum_{jklmn} V_{jklm} X_k^i X_l^i X_m^i X_n^i + ... \quad (1)$$

The coefficients R_{jk} ($j, k = 1, 2...6$) are called first order matrix elements corresponding to linear optics, which is composed of drifts, dipoles and quadrupoles. The quantities $T_{jkl}, U_{jklm}, V_{jklmn}, etc.$, are called higher order transfer matrix elements and contain the information about the optics aberrations of the lattice.

When a map $\mathcal{M}$ has a jacobian matrix $\mathbf{M}$ that is symplectic at all points, the map itself it is said it is symplectic which implies that $\mathbf{M}$ satisfies the following matrix relation:

$$\hat{\mathbf{M}}(X^i)\mathbf{J}\mathbf{M}(X^i) = J \quad (2)$$

where $\hat{\mathbf{M}}$ denotes the transpose of $\mathbf{M}$ and $\mathbf{J}$ is a $2n \times 2n$ matrix defined by the equation:

$$J = \begin{pmatrix} 0 & I \\ -I & 0 \end{pmatrix} \quad (3)$$

with I the $n \times n$ identity matrix (n= 3 in our case), and all other entries zero. A symplectic map is equivalent to a canonical transformation.

If we consider the first order matrix elements the transport matrix can be written like:

$$\sigma = \begin{pmatrix} R_{11} & R_{12} & R_{13} & R_{14} & R_{15} & R_{16} \\ R_{12} & R_{22} & R_{23} & R_{24} & R_{25} & R_{26} \\ R_{13} & R_{32} & R_{33} & R_{34} & R_{35} & R_{36} \\ R_{14} & R_{42} & R_{43} & R_{44} & R_{45} & R_{46} \\ R_{15} & R_{52} & R_{53} & R_{54} & R_{55} & R_{56} \\ R_{16} & R_{62} & R_{63} & R_{64} & R_{65} & R_{66} \end{pmatrix} \quad (4)$$

The linear transport matrix elements are calculated by solving the charged particles motion equation considering only the drift spaces, dipoles and quadrupoles, where the magneticl field depends linearly on the deviation of the particle with respect to the reference path. By simply multiplying the transfer matrices corresponding to the

different elements one can calculate the transformation of the coordinates vector X along the whole beamline as:

$$X^f = R_n R_{n-1} ... R_1 X^i \tag{5}$$

For the particular case of considering only the transverse motion and no energy dispersion, the beam matrix elements in term of the Twiss parameters from the initial location (i) to the measurement location (f) could be expressed in the uncoupled case as:

$$R_{f,i} = \begin{pmatrix} R_{11} & R_{12} & 0 & 0 \\ R_{21} & R_{22} & 0 & 0 \\ 0 & 0 & R_{33} & R_{34} \\ 0 & 0 & R_{43} & R_{44} \end{pmatrix} \tag{6}$$

with:

$$R_{11} = \sqrt{\frac{\beta_x^f}{\beta_x^i}}(\cos \Delta\phi_x^{fi} + \alpha_x^i \sin \Delta\phi_x^{fi})$$

$$R_{12} = \sqrt{\beta_x^f \beta_x^i} \sin \Delta\phi_x^{fi}$$

$$R_{21} = \frac{1}{\sqrt{\beta_x^f \beta_x^i}}(\alpha_x^i - \alpha_x^f) \cos \Delta\phi_x^{fi} - (1 + \alpha_x^f \alpha_x^i) \sin \Delta\phi_x^{fi}$$

$$R_{22} = \sqrt{\frac{\beta_x^i}{\beta_x^f}}(\cos \Delta\phi_x^{fi} - \alpha_x^f \sin \Delta\phi_x^{fi})$$

$$R_{33} = \sqrt{\frac{\beta_y^f}{\beta_y^i}}(\cos \Delta\phi_y^{fi} + \alpha_y^i \sin \Delta\phi_y^{fi}) \tag{7}$$

$$R_{34} = \sqrt{\beta_y^f \beta_y^i} \sin \Delta\phi_y^{fi}$$

$$R_{43} = \frac{1}{\sqrt{\beta_y^f \beta_y^i}}(\alpha_y^i - \alpha_y^f) \cos \Delta\phi_y^{fi} - (1 + \alpha_y^f \alpha_y^i) \sin \Delta\phi_y^{fi}$$

$$R_{44} = \sqrt{\frac{\beta_y^i}{\beta_y^f}}(\cos \Delta\phi_y^{fi} - \alpha_y^f \sin \Delta\phi_y^{fi})$$

If one wants to calculate the transfer matrix between the final point and the initial point, the inverse of Eq. (6) has to be calculated. The result of inverting Eq. (6) is:

$$R_{i,f} = \begin{pmatrix} R_{22} & -R_{12} & 0 & 0 \\ -R_{21} & R_{11} & 0 & 0 \\ 0 & 0 & R_{44} & -R_{34} \\ 0 & 0 & -R_{43} & R_{33} \end{pmatrix} \tag{8}$$

Annex 2: ILC and CLIC collimation system

ILC collimation system

In Table 7 the betatron and energy collimation systems main parameters are summarized for the current ILC collimation system implemented on the lattice version ILC2015b describing the values included on the Technical Design Report TDR. The spoilers are indicate as SP^* and the absorbers as AB^*. These systems are based on movable 4-jaws. The protection collimators are defined as PC^* with fixed circular apertures. The photon masks which are vertical fixed slits are named as $MSK1, 2$. Five betatron spoilers are considered, $SP1 - 5$, made of Cu with a 0.6 radiation lengths. The energy spoiler $SPEX$ is 1.0 radiation length made of Titanium. The betatron absorbers,$AB2 - 5$, are 30.0 radiation lengths and are made of Cu while the energy absorber, ABE, $AB7 - 10$, and the muon masks, ,$MSK1 - 2$ are 30.0 radiation lengths and made of Tungsten. Finally the passive collimator,$PC1 - 11$, are 15.0 radiation lengths and made of Cu. In addition, a crab cavity mask, $MSKCRAB$, is included with a fixed circular aperture. In addition to the parameters in Table 7, for the calculation of the wakefield regimes the collimator tapered angle considered is $\alpha = 0.02\ rad$. The aperture on the table refers to the collimation half aperture. A half width of 10 mm is considered in the non collimation plane.

CLIC collimation system

Similar description and collimation system scheme is design for CLIC. The parameters summarized in Table 3 can be found in [46] and corresponds to the CLIC collimation system design parameters for 3 TeV and $L^* = 4.3\ m$ layout. As for the ILC collimation system description the spoilers are indicate as SP^* and the absorbers as AB^* and are also based on movable 4-jaws. The spoilers material is still under study but the best candidate for the moment was Be with a coating of Cu. For the absorbers the proposed material is Ti with also a coating of C. For the calculation of the wakefield regimes the collimator tapered angle considered is $\alpha = 0.02\ rad$. The aperture on the table refers to the collimation half aperture. A half width of 10mm in the non collimation plane.

Table 2: ILC collimation system parameters . For the calculation of the wakefield regimes the collimator tapered angle considered is $\alpha = 0.02 \ rad$. The aperture on the table refers to the collimation half aperture. A half width of 10 mm is considered in the non collimation plane.

s [m]	Name	μ_x [2π]	μ_y [2π]	β_x[m]	β_y[m]	L [m]	a_x [mm]	a_y [mm]	Material	Geometric regime	Resistive regime
342.297	CEBSYE	2.1950	1.8492	10.99	135.15	3.0	2	200	Cu	—	Long
647.352	SP1	3.5616	3.2852	14.03	10.48	0.01	0.5	0.3/0.75*	Cu	Intermediate/Inductive*	Long
732.443	AB2	3.6861	3.6596	1000.01	1000.01	0.43	4	4	Cu	Inductive	Long
732.452	SP2	3.6861	3.6597	1000.01	1000.01	0.01	0.3	0.2/0.75*	Cu	Intermediate/Inductive*	Long
789.643	PC1	3.6983	3.6983	297.01	74.66	0.21	5	5	Cu	Inductive	Long
820.472	AB3	3.7882	4.0040	14.34	10.90	0.43	4	4	Cu	Inductive	Long
820.481	SP3	3.7883	4.0042	14.34	10.89	0.01	0.3	0.3/0.75*	Cu	Intermediate/Inductive*	Long
827.343	PC2	3.8630	4.1048	18.51	10.67	0.21	5	5	Cu	Inductive	Long
900.243	PC3	3.9352	4.4081	1576.40	527.891	0.21	5	5	Cu	Inductive	Long
908.643	AB4	3.9363	4.4098	1000.01	999.99	0.43	4	4	Cu	Inductive	Long
908.652	SP4	3.9363	4.4098	1000.01	999.99	0.01	0.3	0.3/0.75*	Cu	Intermediate/Inductive*	Long
918.143	PC4	3.9377	4.4115	1490.80	614.965	0.21	5	5	Cu	Inductive	Long
964.843	PC5	3.9483	4.4485	300.05	74.05	0.21	5	5	Cu	Inductive	Long
1003.76	AB5	4.4052	4.7120	829680	7774000	0.43	4	4	Cu	Inductive	Long
1003.77	SP5	4.4052	4.7121	299440	49029000	0.01	0.4	0.3/0.75	Cu	Intermediate/Inductive*	Long
1033.24	PC6	4.4206	4.8705	1204.44	65.82	0.21	5	5	Cu	Inductive	Long
1194.44	PC7	4.6015	4.9095	25.26	6935.58	0.21	5	5	Cu	Inductive	Long
1209.28	SPEX	4.6769	4.9010	40.98	4.9010	0.04	3.2	200	Cu	Inductive	Long
1277.61	PC8	4.7640	4.9106	25.3058	6828.84	0.21	5	5	Cu	Inductive	Long
1388.94	ABE	4.9523	4.9467	1231.30	73.05	0.1	1	1	Cu	Inductive	Long
1670.54	AB10	5.9279	5.9070	49.46	689.12	0.1	4.4	4.4	Cu	Inductive	Long
1690.60	AB9	5.9282	5.9071	20838.4	16475.0	0.1	6.6	3	Cu	Inductive	Long
1765.54	AB7	5.9565	5.9101	17.62	135.60	0.1	4.5	3	Cu	Inductive	Long
2224.45	MSK1	6.9282	6.9070	29500.3	15926.7	0.1	8.3	200	Cu	Inductive	Long
2225.35	MSKCRAB	6.9282	6.9070	29763.4	16090.9	0.1	10.5	10.5	Cu	Inductive	Long
2229.26	MSK2	6.9282	6.9071	30918.4	16813.1	0.1	8.5	200	Cu	Inductive	Long

* correspond to the optimized aperture for the doublet octupole tail folding configuration.

Table 3: CLIC collimation system parameters for 3 *TeV* and $L^* = 4.3\ m$. For the calculation of the wakefield regimes the collimator tapered angle considered is $\alpha = 0.02\ rad$. The aperture on the table refers to the collimation half aperture. A half width of 10 *mm* is considered in the non collimation plane.

s [m]	Name	μ_x [2π]	μ_y [2π]	β_x[m]	β_y[m]	L [m]	a_x [mm]	a_y [mm]	Material	Geometric regime	Resistive regime
907.10	ENGYSP	1.6137	1.8600	1406.33	70681.9	0.01	3.51	25.4	Be	Diffractive	Long
1072.10	ENGYAB	1.6257	1.8605	3213.03	39271.5	0.45	5.4	25.4	Ti	Diffractive	Long
1830.87	YSP1	2.2418	2.8149	114.054	483.184	0.01	10	0.102	Be	Intermediate/Diffarctive	Long
1846.69	XSP1	2.2562	2.8263	270.003	101.347	0.01	0.08	10	Be	Diffractive	Long
1923.89	XAB1	2.4735	3.5495	270.102	80.9043	0.45	1	1	Ti	Diffractive	Long
1941.71	YAB1	2.4890	3.5644	114.054	483.184	0.45	1	1	Ti	Diffractive	Long
1943.71	YSP2	2.4919	3.5650	114.014	483.188	0.01	10	0.102	Be	Diffractive/Intermediate	Long
1959.54	XSP2	2.5062	3.5765	270.002	101.361	0.01	0.08	10	Be	Intermediate/Diffractive	Long
2036.72	XAB2	2.7235	4.2993	270.105	80.9448	0.45	1	1	Ti	Diffractive	Long
2054.56	YAB2	2.7390	4.3143	114.055	483.257	0.45	1	1	Ti	Difffractive	Long
2056.56	YSP3	2.7419	4.3150	114.054	483.253	0.01	10	0.102	Be	Diffractive/Intermediate	Long
2072.38	XSP3	2.7562	4.3263	270.003	101.347	0.01	0.08	10	Be	Intermediate/Diffractive	Long
2149.58	XAB3	2.9735	5.0495	270.102	80.9043	0.45	1	1	Ti	Diffractive	Long
2167.40	YAB3	2.9890	5.0644	114.054	483.184	0.45	1	1	Ti	Diffractive	Long
2169.40	YSP4	2.9919	5.0651	114.054	483.188	0.01	10	0.102	Be	Diffractive/Intermediate	Long
2185.22	XSP4	3.0062	5.0765	270.002	101.361	0.01	0.08	10	Be	Intermediate/Diffractive	Long
2262.42	XAB4	3.2235	5.7993	270.105	80.9448	0.45	1	1	Ti	Diffractive	Long
2280.24	YAB4	3.2390	5.8143	114.055	483.257	0.45	1	1	Ti	Diffractive	Long

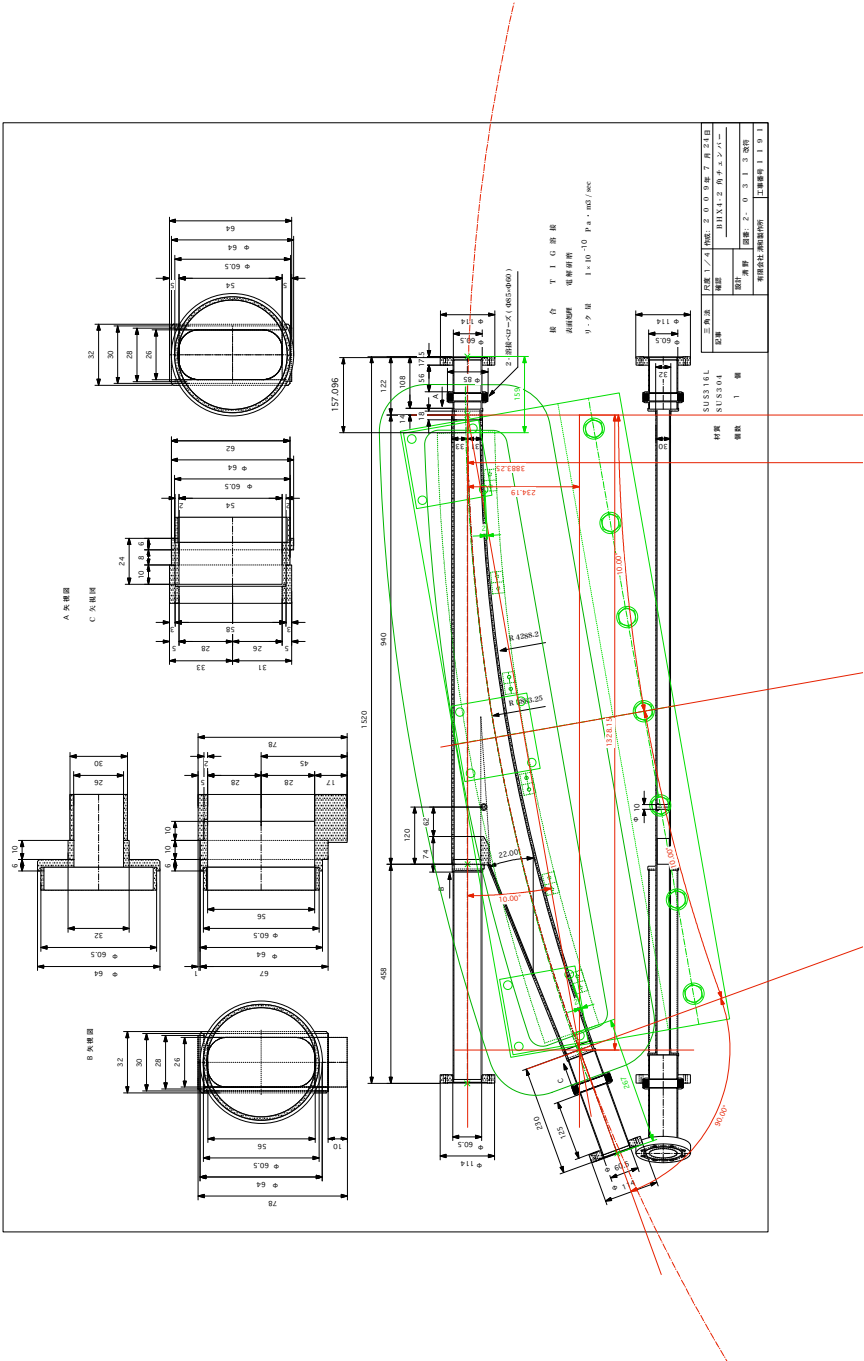# Annex 3: BDUMP mechanical design

Figure 1: BDUMP mechanical scheme

Annex 4: Singular Value Decomposition method (SVD)

The SVD method in linear algebra is a factorization of a real or complex matrix, M, with dimensions $m \times n$ of the form of:

$$M = U S V^T \tag{9}$$

$$
\begin{pmatrix}
M_{11} & \ldots & M_{1n} \\
\ldots & \ldots & \ldots \\
\ldots & \ldots & \ldots \\
M_{m1} & \ldots & M_{mn}
\end{pmatrix}
=
\begin{pmatrix}
U_{11} & \ldots & U_{1m} \\
\ldots & \ldots & \ldots \\
\ldots & \ldots & \ldots \\
U_{m1} & \ldots & U_{mm}
\end{pmatrix}
\begin{pmatrix}
S_{11} & \ldots & \ldots \\
\ldots & S_{22} & \ldots \\
\ldots & \ldots & \ldots \\
\ldots & \ldots & S_{mn}
\end{pmatrix}
\begin{pmatrix}
V_{11} & \ldots & V_{1n} \\
\ldots & \ldots & \ldots \\
\ldots & \ldots & \ldots \\
V_{n1} & \ldots & V_{nn}
\end{pmatrix}^T
\tag{10}
$$

where:

- U is an $m \times m$ unitary matrix .

- S is a diagonal $m \times n$ matrix with non-negative real numbers on the diagonal that give the strength of the correlation modes.

- V^T is the transpose matrix of a $n \times n$ unitary matrix.